U.PORTO

FEUP FACULDADE DE ENGENHARIA UNIVERSIDADE DO PORTO

Smart Structural Health Monitoring Applied to Management and Conservation of Bridges

A thesis submitted for the degree of Doctor of Philosophy in Civil Engineering at the Faculty of Engineering of the University of Porto

by

Emanuel Rodrigues de Sousa Tomé

Supervisors:

Mário Jorge de Seixas Pimentel (Assistant Professor)

Joaquim de Azevedo Figueiras (Full Professor)

June 2019

POPH QUALIFICAR É CRESCER.

QREN QUADRO DE REFERÊNCIA ESTRATÉGICO NACIONAL PORTUGAL 2007.2013

GOVERNO DA REPÚBLICA PORTUGUESA

UNIÃO EUROPEIA Fundo Social Europeu

Doctoral Program in Civil Engineering

Department of Civil Engineering

Tel. +351-22-508 1901

Fax +351-22-508 1446

✉ prodec@fe.up.pt

Edited by

Faculdade de Engenharia da Universidade do Porto

Rua Dr. Roberto Frias

4200-465 PORTO

Portugal

Phone: +351-22-508 1400

Fax: +351-22-508 1440

✉ feup@fe.up.pt

http://www.fe.up.pt

This work was financially supported by: UID/ECI/04708/2019 – CONSTRUCT – Institute of R&D in Structures and Construction funded by national funds through the FCT/MCTES (PIDDAC); POCI-01-0145-FEDER-031355 – "S4Bridges – A smart approach for the maintenance of existing bridges" funded by FEDER funds through COMPETE2020 - Programa Operacional Competitividade e Internacionalização (POCI) and by national funds (PIDDAC) through FCT/MCTES. The support by Fundação para a Ciência e a Tecnologia through the Ph.D. grant SFRH/BD/91536/2012 attributed to the author is also gratefully acknowledged.

To my family.

A Paisagem

Rebrilha na manhã de Primavera
O Sol resplandecente e cintilante
Que transforma num sonho de quimera
Cada gota de orvalho num diamante

Eu olho da janela, além distante
Onde a vegetação rural prospera
E ouço uma pastora carpir cantante
O seu passado amor que perecera

Que formosa manhã! Que doce luz
Que nos entra pela alma e nos seduz
E numa carícia meiga nos afaga…

No meio desta vida há o resplendor
É qual a primavera o próprio amor
Um sonho que nos foge e que se apaga.

Fojo – Castelo de Paiva, 9th January 1949

Delfim de Sousa Tomé
(Emanuel's great-grandfather)

ABSTRACT

The infrastructure systems are drivers of social and economic development in modern societies. Bridges, as part of them, have an essential role since their inefficiency or, in extremis, their collapse has important, and sometimes irreversible, negative consequences to the society and economy. In this context, Structural Health Monitoring (SHM) arises as a tool to ensure the safety, serviceability, durability and sustainability of structures.

Notwithstanding the significant efforts placed on the development of SHM technologies over the last decades, SHM still faces some challenges when transiting from academia to real practical applications. One of these challenges is the interpretation of the structural response under environmental and operational variations. Another challenge is the distinction between the variations due to normal environmental and operational effects and the variations due to structural damage.

Therefore, this work was firstly focused on the development of a methodology for the simulation of the structural response of large concrete bridges under the effects of realistic temperature variations, aiming at the optimum compromise between accuracy and simplicity of the involved procedures. The methodology is validated in a concrete cable-stayed bridge equipped with a permanent structural monitoring system, the Corgo Bridge. The measured and calculated temperatures, bearing displacements, deflections, rotations and stay cable forces are compared during 17 months and good agreement is generally found.

Finally, online data-based methodologies are proposed for damage detection and localisation. They are applied to and validated on the experimental data obtained from the structural monitoring system of the Corgo Bridge. In order to evaluate the effectiveness of the proposed approaches for damage detection and since the bridge is new and sound, the experimental time series are corrupted with numerically simulated damage scenarios. The proposed approaches are demonstrated to be able to detect damage in its early stages.

Keywords: Structural Health Monitoring; Cable-stayed Bridges; Thermomechanical Analysis; Damage Detection; Data-based Approaches.

RESUMO

Os sistemas de infraestruturas são impulsionadores do desenvolvimento social e económico nas sociedades modernas. Como parte integrante desses sistemas, as obras de arte têm um papel essencial uma vez que a sua ineficiência ou, no extremo, o seu colapso tem consequências consideravelmente negativas e por vezes irreversíveis. Neste contexto, a Monitorização da Integridade Estrutural (MIE) surge como uma ferramenta para melhor garantir a segurança, operacionalidade, durabilidade e sustentabilidade das estruturas.

Apesar dos esforços significativos no desenvolvimento de tecnologias de MIE que têm vindo a ser feitos ao longo das últimas décadas, a MIE ainda enfrenta alguns desafios quando transita da academia para aplicações práticas. Um desses desafios é a interpretação da resposta estrutural sob variações ambientais e operacionais. Outro desafio é a distinção entre variações normais devidas aos efeitos ambientais e operacionais e as variações devidas a danos estruturais.

Por conseguinte, este trabalho focou-se em primeiro lugar no desenvolvimento de uma metodologia para a simulação da resposta estrutural de pontes de betão armado de grande vão sob o efeito de variações de temperatura realistas, procurando um compromisso entre exatidão e simplicidade dos procedimentos envolvidos. A metodologia é validada numa obra de arte atirantada de betão armado pré-esforçado na qual foi instalado um sistema de monitorização permanente, o Viaduto do Corgo. As temperaturas, deslocamentos de apoio, flechas, rotações e forças nos tirantes medidas e calculadas são comparadas durante um período de 17 meses e um bom ajuste é geralmente obtido.

Finalmente, são propostas metodologias baseadas em dados para a deteção e localização de dano em tempo real. Essas metodologias são aplicadas e validadas aos dados experimentais obtidos pelo sistema de monitorização contínua do Viaduto do Corgo. Uma vez que o obra de arte escolhida como caso de estudo não tem qualquer dano estrutural, as séries temporais experimentais são corrompidas com danos simulados numericamente. É demonstrado que as metodologias propostas são capazes de detetar dano na sua fase inicial.

Palavras-chave: Monitorização da Integridade Estrutural, Pontes Atirantadas; Análises Termomecânicas; Deteção de Dano; Metodologias baseadas em dados.

ACKNOWLEDGEMENTS

This research work was carried out at the Laboratory of Concrete Technology and Structural Behaviour (LABEST) of the Faculty of Engineering of the University of Porto. I wish to express my sincere gratitude to all persons and institutions that directly or indirectly contributed to this work, namely:

To the supervisor of this thesis, Professor Mário Pimentel, for his support, guidance, patience, encouragement and friendship during this journey. His deep and careful reviews (always the hardest ones) of my work surely contributed not only for a better thesis but also to turn me a better professional and engineer.

To the co-supervisor of this thesis, Professor Joaquim Figueiras, for his valuable and wise comments and reviews of all my works since my master's degree. I am also deeply grateful for his personal confidence in my potential. I hope I had not only fulfilled but also exceeded all the expectations and confidence put on me.

To Professor Luís Lage for the shared knowledge about the LabView programming language and for his patience and disposal to answer to all my naive questions about sensors, electrotechnics and signal processing.

To NewMENSUS for the important collaborations over this journey, interest in my PhD works and all the efforts (sometimes more than what they were contractually compelled to) carried out for being possible to have such great amount of continuous monitoring data of the Corgo Bridge. I would also like to express my personal gratitude to: Engineers Amândio Pinto, José Geraldes and Rémy Faria for their commitment to the design and given instructions during the installation in the field of the structural monitoring system of the stay cables of the Corgo Bridge and their collaboration in the execution of the load test carried out in the Corgo Bridge; Dr Helena Figueiras and Engineer José Carvalhal for the shared information about the structural monitoring system of the Corgo Bridge.

To the LABEST's technicians: to Mr Alberto Monteiro for his careful and competent execution of the accelerometer protections of the stay cable monitoring system of the Corgo Bridge; to Engineer Paula Silva and Mr Cláudio Ferraz for their important and friendly support in the laboratory when required, especially during the development of the structural monitoring system of the stay cables of the Corgo Bridge.

To Professor Ana Maria Sarmento, Professor Carlos Félix, Professor Carlos Sousa and Professor Miguel Ferraz for the shared knowledge in the works where I collaborated with them.

To the Corgo Bridge builder, CAETXXI, and owner/manager, AutoEstradasXXI/Globalvia Transmontana, for the available information about the Corgo Bridge.

To LCW, the Corgo Bridge designer, for the disposal of the design project and interest in the works carried out on the Corgo Bridge.

To Professor Filipe Magalhães and Dr João Santos for the suggested bibliography and wise and valuable comments to my Research Thesis Project.

To Ms Cláudia Correia, Ms Joana Rodrigues and Ms Marta Poínhas for the administrative support.

To Fundação para a Ciência e a Tecnologia for the financial support provided by the PhD grant referenced as SFRH/BD/91536/2012.

To my colleagues for the good environment and cheerful conversations during lunchtimes and breaks, namely to: Alma Sanchez, Ana Mafalda Matos, Aurélio Sine, Bruno Afonso Costa, Cláudia Lemos, Cláudio Ferraz, Cláudio Ferreira, Despoina Skoulidou, Filipe Cavadas, Helena Figueiras, José Carvalhal, José Conceição, Mafalda Amorim, Márcio Buson, Nuno Pereira, Paula Silva, Pedro Gil Ferreira, Rajan Suwal, Rakesh Dumaru, Teresa Stingl, Tiago Ferradosa, Tuba Tatar and Vasco Mano. A special word to Bruno Afonso Costa, Filipe Cavadas and José Conceição for the uninterested and fruitful conversations and discussions about structural health monitoring, bridges, thermomechanical analysis and dams.

Last but not least, to my parents, Delfim and Josélia, for their unconditional love, care, support and sacrifices throughout my entire life and for always believing in me, sometimes more than myself. To my brother, Maximiano, for being my best friend since ever. To my sister-in-law, Ana, and to my nephews, Frederico and Olívia, for their love, care and reasons for so many happy moments in the last years.

TABLE OF CONTENTS

NOTATION AND LIST OF SYMBOLS AND ABBREVIATIONS

Notation

Mathematical equations will use the following notation:

- Scalars: small and capital italic letters: a, b, c, A, B, C
- Vectors: small bold nonitalic letters: $\mathbf{a}, \mathbf{b}, \mathbf{c}$
- Matrixes: capital bold nonitalic letters: $\mathbf{A}, \mathbf{B}, \mathbf{C}$

Roman letters

Uppercase Latin symbols

A	Cross-section area [m^2]
A_e	Finite element area [m^2]
$\mathbf{A}$	M-by-N_r matrix which represents the speed of adjustment to disequilibrium
$\mathbf{B}$	M-by-N_r cointegration matrix
E	Equation of time [min]
	Young's modulus [kPa]
E_{MLR}	n-by-m matrix with the random error of the MLR model

E_{PCA}	n-by-m matrix with the random error of the PCA model
F	Installed force in the stay cable [kN]
G_{on}	Extra-terrestrial solar radiation [W/m^2]
G_{sc}	Solar constant [1367 W/m^2]
I	Total solar radiation on a horizontal plane [W/m^2]
$I(d)$	Time series integrated of order d
I_o	Extra-terrestrial radiation on a horizontal surface for an hour period [W/m^2]
I_b	Beam (or direct) solar radiation on a horizontal plane [W/m^2]
I_d	Diffuse solar radiation on a horizontal plane [W/m^2]
I_M	M-by-M identity matrix
I_T	Total solar radiation on a tilted plane [W/m^2]
I_y	Moment of inertia about the $y - y$ axis [m^4]
I_z	Moment of inertia about the $z - z$ axis [m^4]
$I_{\varepsilon,e}$	Moment of inertia of a finite element e in relation to a generic axis ζ [m^4]
L	Stay cable length [m]
	Likelihood function
L_{loc}	Longitude of the location in question [º]
L_{st}	Standard median for the local time zone [º]
M	Number of time series or variables/sensors (Chapter 6)
M_y	Bending moment about the $z - z$ axis [kN.m]
M_z	Bending moment about the $y - y$ axis [kN.m]
$\mathbf{M}_{ij}$	Product moment matrices
N	Length of the time series (Chapter 3)
	Axial force (Chapter 4)
$\mathbf{N}$	Shape functions
N_p	Moving window size (IQR)
N_r	Number of cointegration vectors and rank of matrix $\mathbf{\Pi}$.
Q_1	First quartile
Q_3	Third quartile
R_b	Geometric factor: ratio of beam radiation on a tilted plane to that on a horizontal plane [-]
RL_α	Ratio between the mean values of the T^2 statistic in the damaged state and the UCL

$RL_{u,\alpha}$	RL_{α} for the undamaged state
RU	Ratio between the mean values of the T^2 statistic in the damaged and undamaged states
$S(\omega)$	Fast Fourier Transform
$\mathbf{S}$	Process covariance matrix in the reference period (for calculation of $\mathbf{T}^2$)
$\mathbf{S}_{ij}$	Residual product-moment matrices
T	Temperature field [ºC]
	Number of observations or data points (Chapter 6)
$\mathbf{T}$	Transformation or loading matrix
T^2	Hotelling T^2 statistic
T_a	Ambient or fluid temperature [K]
$T_{m,e}$	Average temperature of a triangular finite element [ºC]
T_{NL}	Nonlinear temperature component [ºC]
T_s	Surface temperature [K]
T_{sky}	Effective sky temperature [K]
$T_{stay-cable}$	Stay-cable temperature [ºC]
T_{sur}	Surroundings temperature [K]
T_u	Uniform temperature component [ºC]
$T_{u,\,senors}$	Average temperature of the concrete temperature sensors [ºC]
$T_{u,\,sensors}^{Girder}$	Mean temperature of the concrete temperature sensors of a section of the East Sub-Viaduct [ºC]
$T_{u,\,sensors}^{Pier}$	Mean temperature of the concrete temperature sensors of a section of the pier P27 [ºC]
$\hat{\mathbf{U}}$	$(r+1)$-by-m matrix with the estimated coefficients of the MLR model
$\mathbf{X}$	n-by-$(r+1)$ matrix of the predictor variables
$\mathbf{Y}$	n-by-m matrix of the dependent/original variables
$\hat{\mathbf{Y}}$	Prediction of $\mathbf{Y}$
$\mathbf{Z}$	n-by-m matrix of the principal component scores

LOWERCASE LATIN SYMBOLS

c	Specific heat [J/(kg.K)]
d	Distance to the axis ζ [m]
$\mathbf{d}_e$	Vector with the distances between the axis ζ and the nodes i, j and k of the finite element e [m]

e_0	Partial pressure of water vapour [Pa]
f_n	Natural frequency [Hz]
h_c	Convection heat transfer coefficient [W/(m^{3}K)]
h_{solar}	Solar time [h]
h_y	Cross section width [m]
h_z	Cross-section depth [m]
k	Thermal conductivity [Wm^{-1}K^{-1}] (Chapter 4)
	Number of lags (Chapter 6)
k_1	Empirical parameter used to fit the creep curve
k_2	Empirical parameter used to fit the creep curve
k_T	Hourly clearness index
m	Distributed mass per unit length [ton/m] (Chapter 3)
	Number of dependent variables (MLR) (Chapter 5)
	Number of sensors and/or features (PCA, $\mathbf{T}^2$) (Chapter 5 and 6)
n	Mode number (Chapter 3)
	Day of the year; Number of finite elements (Chapter 4)
	Number of observations (Chapters 5 and 6)
p	Number of retained principal components
$q''_{h,conv}$	Convective heat flux [W/m^2]
$q''_{h,rad}$	Heat flux due to longwave radiation [W/m^2]
q''_s	Heat flux due to solar radiation [W/m^2]
r	Number of predictor variables (MLR)
	Number of observations considered for calculation of $\mathbf{T}^2$ (window size)
s	Number of subgroups (or windows) during the reference period ($\mathbf{T}^2$)
v	Wind velocity [m/s]
$\bar{\mathbf{x}}$	Average of the observations inside the window
$\bar{\bar{\mathbf{x}}}$	Process average when it is in control
y_G	Abscissa of the centre of gravity of the section [m]
$y_{G,e}$	Abscissa of the centre of gravity of the finite element e [m]
$\mathbf{y}_t$	Set of M $I(1)$ *time* series (M-by-1)
z_G	Ordinate of the centre of gravity of the section [m]
$z_{G,e}$	Ordinate of the centre of gravity of the finite element e [m]
z_t	Cointegration residual

Greek letters

Uppercase Greek symbols

$\mathbf{\Gamma}_i$	M-by-M short-run impact matrix
Δt	Inverse of the sampling rate [s]
ΔT_y	Linearly varying temperature difference component along the y-y axis or horizontal linear temperature gradient component (for the girder) and transversal linear temperature gradient component (for piers) [ºC]
$\Delta T_{y,\,sensors}$	Differential temperature component about the z – z axis calculated from sensor temperatures [ºC]
ΔT_z	Linearly varying temperature difference component along the z-z axis or vertical linear temperature gradient component (for the girder) and longitudinal linear vertical temperature gradient component (for piers) [ºC]
$\Delta T_{z,\,sensors}$	Differential temperature component about the y – y axis calculated from sensor temperatures [ºC]
$\mathbf{\Lambda}$	Singular values of the matrix $\mathbf{\Sigma}$
$\mathbf{\Pi}$	M-by-M long-run impact matrix
$\mathbf{\Sigma}$	Covariance matrix of the original variables in the training period
$\mathbf{\Phi}$	Matrix with the coefficients of the deterministic terms
$\mathbf{\Psi}$	Matrix consisting of $\mathbf{\Gamma}_1,...,\mathbf{\Gamma}_{k-1}$ and $\mathbf{\Phi}$.
$\mathbf{\Omega}$	Covariance matrix of $\boldsymbol{\varepsilon}_t$

Lowercase Greek symbols

α	Thermal dilatation coefficient
α_s	Solar altitude angle [º]
α_{surf}	Solar absorptivity coefficient of the surface material
β	Surface angle relative to the horizontal plane [º]
$\beta_c(t,t_0)$	Coefficient that describes the development of creep with time after loading
$\boldsymbol{\beta}$	Cointegration vector (*M*-by-*1)*
γ	Surface azimuth angle [º]
γ_s	Solar azimuth angle [º]
δ	Declination [º]
ε	Emissivity
ε_t	Gaussian white noise process
$\boldsymbol{\varepsilon}_t$	Multivariate Gaussian white noise process

ζ	Generic axis
θ	Angle of incidence [º]
θ_z	Zenith angle [º]
λ_i	Eigenvalues of the matrix $\mathbf{\Pi}$
ρ	Specific mass (mass per unit volume) [kg/m^3]
ρ_g	Albedo of the ground [-]
σ	Stefan-Boltzmann constant $[5.67\times10^{-8}\,\mathrm{Wm^{-2}K^{-4}}]$
	Stress field
ϕ	Latitude [º]
$\varphi(t,t_0)$	Creep coefficient, defining creep between times t and t_0
ω	Hour angle [º]
ω_{ss}	Sunset angle [º]

Abbreviations

ADF	Augmented Dickey-Fuller
ANN	Artificial Neural Network
AR	Autoregressive
AutoestradasXXI	Asset manager of the Corgo Bridge
BSS	Blind Source Separation
CAETXXI	Builder of the Corgo Bridge
CONSTRUCT	Institute of R&D in Structures and Construction
CP70	Cumulative percentage of 70%
CP80	Cumulative percentage of 80%
CP90	Cumulative percentage of 90%
CSV	Central Sub-Viaduct of the Corgo Bridge
EOVs	Environmental and Operational Variations
ESV	East Sub-Viaduct of the Corgo Bridge
FFT	Fast Fourier Transform
IQR	Interquartile Range Analysis
LABEST	Laboratory for the Concrete Technology and Structural Behaviour
LI	Localisation Index
LSVs	Lateral Sub-Viaducts of the Corgo Bridge (WSV+ESV)

FEUP	Faculty of Engineering of the University of Porto
HDPE	Extruded high density polyethylene
MLP	Multi-Layer Perceptron
MLR	Multiple Linear Regression
PCA	Principal Component Analysis
PSD	Power Spectral Densities
RH	Relative Humidity [%]
SHM	Structural Health Monitoring
UCL	Upper control limit
VAR	Vector Auto-regression
VECM	Vector Error Correction Model
WSV	West Sub-Viaduct of the Corgo Bridge

Chapter 1

INTRODUCTION

1.1 Motivation

Bridges, as part of the infrastructure systems, are key elements in modern societies. Bridges not only allow the transposition of a valley, a transport link or a watercourse, but are also a driver of social and economic development. The structural inefficiency of these structures or, in extremis, their collapse has important, and sometimes irreversible, negative consequences to the society and to the economy. Therefore, the monitoring of these structures both during the constructive stages and their service life is of particular relevance.

Structural health monitoring (SHM) technologies can be defined as a tool to ensure the safety, serviceability, durability, and sustainability of structures by employing long-term real-time monitoring [125] with the aim of assisting and informing operators about the structures condition under gradual or sudden changes to their state [15]. The use of SHM technologies is envisaged as a way to rationalise the maintenance procedures of important bridges, allowing a continuous follow-up of the structural condition, complementing the visual inspections with quantitative information. Proactive conservation strategies based on long-term monitoring are increasingly recommended for special structures as long-span

bridges [68]. SHM should ideally be implemented in order to detect damage in real-time and in its early stage and before it becomes critical, enabling early preventive action to be taken to minimise the ownership costs [68].

In the last decades several bridges have been provided with structural monitoring systems in Portugal [39, 54, 86, 87, 132, 165, 187] and all over the world [1, 17, 122, 123, 125, 211]. However, notwithstanding the large efforts placed on the development of SHM technologies, it has been argued that in only a few cases SHM systems have clearly demonstrated their value to operators and owners [206, 209]. These systems often include a large number of sensors and generate big amounts of data which in many circumstances is of difficult interpretation and usability by the asset managers [15, 105, 176, 209, 229]. The implementation of automatic and real-time data processing algorithms in order to bring the big amounts of data down to a human and useful scale is often pointed out as a key step for increasing the value of SHM. In particular, algorithms enabling the robust detection of small structural damages and thereby supporting decision-making on asset management are still a challenge to be addressed.

Two distinct and complementary approaches have been followed towards this objective: model-based and data-based. The model-based approaches require the development of a behavioural model of the structure, which is continuously updated based on measured data from the real structure in order to follow the mechanical and material properties of the structure [27, 66]. The data-based approaches are based on statistical analyses of data and do not require the development of an analytical model, being the structural condition estimated without information of the physical processes [27, 66, 170]. There are pros and cons in both approaches and they complement each other. A more detailed discussion can be found in Chapter 2.

In general, the robustness and accuracy of the damage detection algorithms depend on how successfully the changes in the structural response due to damage can be discerned from the normal environmental and operational effects. In the scope of SHM, the process of removing the environmental and operational effects from the structural response is usually termed as data normalisation. Depending on the type of structure, this process can be complex and constitutes one of the main reasons for the slow transition of SHM from academia to real

practical applications [41, 66, 184].

SHM technology also faces cultural issues. The low probability of collapse of civil engineering structures (essentially due to the high safety margins adopted in design) leads to the erroneous perception that the investments involved in the structural maintenance activities are small and not necessary. Moreover, since in general the investment in an SHM system presents only medium or long term return, convincing the involved stakeholders of the benefits of the SHM is not an easy task. The present PhD works intend to be a contribution towards the solution of technical issues that SHM technologies still face.

1.2 Objectives

So far, academics have been the greatest beneficiaries of the structural health monitoring systems [16], having had the opportunity of increasing and deepening their knowledge about the performance of several special structures. On the other hand, bridge managers primary objective is to ensure that the structure is safe and operational for the long term with minimal costs of conservation [16]. Therefore, it is essential to implement and develop methodologies for detecting structural changes associated with damages occurrences, providing to the bridge manager real-time information about the real condition of the structure.

As stated before, one of the main challenges that SHM technology faces in practical applications is the removal of the operational and environmental effects from the measured responses. Although data-based methodologies have been proposed to remove these effects from the measured data, the full understanding of the structural response to environmental actions of the bridges is often overlooked, being the statistical techniques usually applied without this prior knowledge. In this context, the first objective of the present work is the understanding of the structural response of cable-stayed bridges under environmental loads, in particular of the Corgo Bridge (the case study of the present work). Besides allowing the interpretation and validation of the data being acquired by the structural monitoring system, the simulated datasets are expected to provide insights on the selection of variables/sensors to be adopted in the data-based approaches to be employed for damage detection and localisation.

The second objective is the application of input-output and output-only data-based methodologies for damage/anomaly detection and localisation. Those methodologies will be implemented on the real datasets obtained from the sensing system installed in the Corgo Bridge. Therefore, those methodologies should be able to suppress the effects due to environmental, operational and long-term variations. Moreover, the implemented methodologies should be able to flag anomalies in an online manner in order to support the decision-making process related to the maintenance and conservation strategies of bridges.

To sum up, the main goal is the transformation of the big amount of data being acquired by the sensing system into useful data to assist the bridge management. The present PhD work is expected to be a meaningful contribution to the transition of the SHM technology from academia to industry.

1.3 Overview

In Chapter 2, the reader is introduced to the key concepts and definitions of SHM technology needed to follow the thesis. The strategy followed in this thesis for structural health monitoring is also presented.

In Chapter 3, the case study (Corgo Bridge) that will be used throughout this work is presented. The installed monitoring system is described in detail, with a particular focus on the structural monitoring system of the stay cables. The numerical model that was developed to follow the construction stages, to analyse the structural behaviour during the load test and to follow the results collected by long-term monitoring system, which are examined in Chapter 4, is also described. Finally, the behaviour of the bridge during the load test is discussed.

In Chapter 4, a methodology is proposed for the simulation of the structural response of large concrete bridges under the effects of realistic temperature variations, aiming at the optimum compromise between accuracy and simplicity of the involved procedures. The transient temperature field in a set of representative cross-sections is obtained from the available meteorological data via two-dimensional thermal analyses. The temperature field is decomposed into uniform, linear and non-linear components, the former two being introduced in a mechanical model of the bridge to obtain the transient structural response.

The methodology is applied to a concrete cable-stayed bridge equipped with a permanent structural monitoring system. The measured and calculated hourly temperatures, deflections, bearing displacements, rotations and stay cable forces are compared during a period of 17 months and good agreement is generally found. The consideration of the radiative cooling effects is demonstrated to be essential in other to obtain a good estimation of the thermal field of the bridge. The behaviour of the bridge is discussed and the relative contribution of each temperature component to a given structural response is disclosed. A discussion on the optimal deployment location of a minimum set of embedded temperature sensors in order to achieve the best estimators of the temperature components (uniform and linear) is also presented.

In Chapter 5, an online data-based methodology for early damage detection and localisation under the effects of environmental and operational variations (EOVs) is proposed. The methodology is described in detail and implemented in the Corgo Bridge, of which 3½ years of data are available. The effects of EOVs are suppressed by the combined application of two well-established multivariate data analysis methods: multiple linear regression and principal component analysis. Criteria for the systematic choice of the predictor variables and the number of principal components to retain are proposed. Since the bridge is new and sound, the experimental time series are corrupted with numerically simulated damage scenarios in order to evaluate the damage detection ability. It is demonstrated that the sensitivity to damage is increased when daily, two-day or three-day averaged data is used instead of hourly data. The effectiveness of the proposed methodology is also demonstrated with the detection of a real, small and temporary sensor anomaly. The implemented methodology has revealed to be robust and efficient, presenting a contribution to the transition of structural health monitoring from academia to industry.

In Chapter 6, a strategy for real-time early damage detection based on multivariate cointegration analysis and statistical process control is proposed. The effects of environmental and operational variations are suppressed using cointegration analysis, being the cointegrating vector estimated following the multivariate Johansen procedure. The cointegrated residuals are then used for novelty detection by means of the Hotelling T^2 control chart. The proposed strategy is systematised and is applied to the Corgo Bridge,

being the stay cable forces used as damage sensitive-features. Several damage scenarios are studied involving increasing section loss of the stay cables. The damage intensities that can be detected using the proposed methodology and the available sensory system are quantified.

Finally, Chapter 7 summarises and discusses the results obtained and concludes with recommendations for future research.

Chapter 2

STRUCTURAL HEALTH MONITORING

2.1. General

This chapter introduces the reader to the key concepts and definitions of Structural Health Monitoring (SHM). Therefore, an extensive review of the SHM field was not intended, but a short and general overview of the main concepts necessary to follow the thesis. One is referred to [8, 12, 32, 66, 211, 218, 221] for extensive and deeper reviews on SHM. The strategy followed in this thesis for structural health monitoring is also presented.

2.2. Structural Health Monitoring systems

Several civil engineering structures have been provided with SHM systems in the last decades, namely bridges, dams, wind turbines, sports facilities, buildings, offshore platforms and underground facilities [1, 17, 121-123, 125, 211]. They are generally envisaged to [104, 121, 127, 222]:

- Monitor the construction phase and loading tests;
- Monitor repairs and reconstruction with the view of evaluating the effectiveness of maintenance, retrofit and repair works;

- Provide a detailed understanding of the structural mechanisms and loadings;
- Obtain massive amounts of in situ data for leading-edge research in structural engineering, such as wind- and earthquake-resistance designs, new structural types and smart material applications;
- Validate design assumptions and structural analysis methodologies with the potential benefit of improving design specifications and guidelines for similar structures in the future.
- Ensure structural and operational safety by means of real-time information about anomalies in loading and response at an early stage;
- Provide a decision support tool for safety assessment and residual capacity immediately after disasters and extreme events;
- Provide evidence and instruction for planning and prioritizing the structure inspection, maintenance, repair and rehabilitation;
- Predict the remaining life of the structure.

However, as discussed in the previous chapter, for several reasons the SHM technology is not yet in a state of maturity able to fully accomplish all the listed items. Since SHM is an interdisciplinary research field, in order to achieve the listed goals collaboration between civil, mechanical, electrical and computer engineering (among others) are mandatory [104].

An SHM system should ideally be composed of [122, 144, 151]:

i. Sensory and data acquisition systems;
ii. Transmission and database systems;
iii. Data validation and interpretation;
iv. Real-time diagnostics (i.e., data normalisation, anomaly detection and localisation) and alert system;
v. Retrieval of information as required for posterior analyses such as safety evaluation and reliability analysis.

With regards to the first subset, sensory and data acquisition systems, a huge sort of sensors can be employed. Examples of typical measurements in bridges are accelerations, deflections, strains, rotations and temperatures. The number, the type and the layout of

the sensors should be chosen taking into consideration the goal or goals of the SHM system. However, an architecture that allows some redundancy is always recommended.

The data transmission is nowadays usually made by means of an internet connection. In order to reduce the amount of data to be transmitted, the data can be pre-processed before being transmitted to the location where it will be analysed and stored.

Data should be then validated for each sensor individually. Abnormal values outside the range of measurement of the sensors and outliers should be removed using, for instance, techniques from statistical process control. A more in-depth interpretation of the data can be made by means of a physical model of a structure (usually a finite element model) by comparison of the measured responses with long-term predictions [189] and/or daily variation predictions due to environmental loads [198].

Concerning real-time diagnosis, since data gathered by SHM systems is usually sensitive to environmental and operational effects, these should be first suppressed. In the scope of SHM, this process is usually termed as data normalisation. After data normalisation and extraction of damage sensitive features, anomaly/damage detection and localisation techniques can be employed. When an anomaly is flagged, an alert should be automatically sent to the bridge and/or SHM system managers.

Finally, the information should be stored for posterior analyses, such as safety evaluation and reliability analysis, and for implementation of future new and more effective damage feature extraction and/or damage detection and localisation algorithms. Obviously, a fair equilibrium of what is stored in raw or processed should be set since a huge amount of data of difficult management can be easily gathered by a continuous SHM system in just a few hours.

2.3. Anomaly/damage detection approaches

2.3.1. General remarks

Damage can be defined as a change in the material and/or geometric properties of a structural system, including changes to the boundary conditions, that adversely affects the present and/or future performance of that system [66]. Implicit in the definition of damage

is a comparison between two different states of the system. Therefore, and as states the second fundamental axiom of SHM [215], the identification of damage always requires a comparison between two system states.

Concerning damage identification, an SHM system can be classified on a five-level scale according to the level of information that can be delivered [167, 214]:

- **Level 1: damage detection:** the SHM system gives only qualitative information about the presence, or not, of damage;
- **Level 2: damage localisation:** there is information about the probable position of the damage;
- **Level 3: damage classification:** there is information about the type of damage;
- **Level 4: damage assessment:** there is an estimate of the extent of damage;
- **Level 5: remaining lifetime prediction:** there is information about the safety of the structure. For instance, the methodology estimates the residual life of the structure.

The vertical structure is clear: each level requires that all lower-level information is available [214]. While the first two levels can be accomplished using unsupervised data-based approaches alone, the levels 3 and 4 may require the use of model-based approaches or supervised data-based approaches* [170, 214] (third fundamental axiom of SHM). The last level may also require complementary information and analysis such as visual inspections, non-destructive testing and structural and material failure analyses [169, 183]. In other words, level 5 cannot be accomplished without an understanding of the physics of damage [214].

2.3.2. Model-based and data-based approaches

Two distinct and complementary approaches have been followed towards damage detection: model-based and data-based. The model-based approaches, also termed in the technical literature as physics-based, law-based, inverse approach or structural identification, require the development of a behavioural model of the structure, usually a finite element model.

* The definitions of supervised and unsupervised approaches are introduced in section 2.3.3.

Once the model is built, measured data from the real structure is used to update the model. Damage detection is then possible by comparison of data form subsequent monitoring phase with the model predictions. If any deviations from the normal condition are observed, a further update of the model will indicate the location and extent of where structural changes have occurred, providing damage diagnosis [66].

Although several model-based approaches have been proposed over the last years [90, 94, 95, 140, 143, 203], model-based approaches are often ill-conditioned and non-unique due to measurement and modelling errors [73, 217]. Moreover, the modelling of damage can be done by means of a broad variety of approaches, ranging from simply reducing the stiffness of an element to complex and highly parameterised crack models [10, 72]. Building refined models that truly reflect the real structural behaviour can be very expensive since they could require months of engineering time [180].

The data-based approaches, also termed in the technical literature as non-physics based, data-driven, model-free, forward or pattern recognition approaches, are based on statistical analysis of data and do not require the development of an analytical model, being the structural condition estimated without information of the physical processes [27, 66, 170]. Instead, a model is constructed applying a machine learning or pattern recognition approach to the data gathered by the structural monitoring system. Moreover, these data-based approaches have the advantages of accommodating the uncertainty of the measured variability and of being usually faster than model-based approaches since they usually are less computer-intensive.

However, as already referred in 2.3.1, damage diagnosis cannot be addressed by data-based approaches. That is, only level 1 up to and including level 4 in the scale of damage identification can be achieved using data-based approaches [216]. Moreover, data-based approaches usually can only be used to interpolate, that is, they usually should only be used when the input data do not depart dramatically from those used for training the model [10].

In Table 2.1 the strengths and weakness of both approaches are summarised. Since they complement each other, their domains of application are problem-dependent. They also share some commonality that is usually overlooked. Indeed, both approaches can be said

model-based. The difference is in the type of model. If the models are classified in white, grey and black-box models according to their degree of *a priori* physical content, the model-based approaches seek to establish a white-box model while the data-based approaches seek to establish a grey or black-box model [10]. Moreover, they both require measured damage-sensitive features from the structure.

Table 2.1 – Strengths and weaknesses of data-based and model-based data interpretation (adapted from ASCE [8]).

Interpretation types	**Strengths**	**Weaknesses**
Model-based Most appropriate when: ▪ Design model is not accurate ▪ Structure has strategic importance ▪ Damage is suspected ▪ There are structural management challenges	▪ Interpretation is easy when links between measurements and potential causes are explicit ▪ The effects of changes in loading and use can be predicted ▪ Guidance for further inspection and measurement ▪ Consequences of future damage can be estimated ▪ Support for planning rehabilitation and repair ▪ May help justify replacement avoidance	▪ Modelling is expensive and time consuming ▪ Errors in models and in measurements can lead to identification of the wrong model ▪ Large numbers of candidate models are hard to manage ▪ Identification of the right model could require several interpretation-measurement cycles ▪ Complex structures with many elements have combinatorial challenges ▪ Typically highly-parameterised ▪ Generally do not accommodate uncertainty
Data-based Most appropriate when: ▪ Many structures need to be monitored ▪ There is time for training the system	▪ No modelling costs ▪ May not need for damage scenarios ▪ Many options for signal analysis ▪ Incremental training can track damage accumulation ▪ Good for long-term use on structures for early detection of situations requiring model-based interpretation ▪ May be parsimoniously parameterised ▪ Naturally accommodate uncertainty	▪ Physical interpretation of the signal may be difficult ▪ Weak support for decision on rehabilitation and repair ▪ Indirect guidance for structural management activities such as inspection and further measurement ▪ Cannot be used to justify replacement avoidance ▪ Usually cannot be used to extrapolate

As data-based approaches are usually less computationally complex, they are better suited for early damage detection. Moreover, in civil engineering structures the most important question to answer is “Is there damage?”. The questions about location and severity are usually less important in civil engineering structures since the simple existence of damage will trigger other procedures [211]. For those reasons, data-based approaches are followed in the present thesis. However, physic-based models are still used in order to understand and interpret the structural behaviour of the studied structure. In Figure 2.1 is depicted a schematic representation of the strategy for structural health monitoring proposed and followed in this thesis. As represented in Figure 2.1, the methodologies used for data validation and interpretation, such as finite element models of the structure, can give valuable insights in the establishment of the algorithms for data normalisation,

anomaly/damage detection and localisation, even when data-based approaches are used. For instance, finite element models can be used to simulate damage scenarios that are not possible to obtain in any other way. These data can be then used to test the validity and effectiveness of the methodologies applied for damage detection and localisation. This approach is followed in Chapters 5 and 6, where damage scenarios simulated using a validated finite element model of the Corgo Bridge are used to demonstrate the effectiveness of the proposed methodologies. With regards to data validation and interpretation, in Chapters 3 and 4 the data obtained experimentally is compared to the predictions obtained by the developed finite element models. This process allows the validation of the developed finite element models (thermal and mechanical) and the interpretation of the structural behaviour of the case study, enabling also a better understanding of the readings continuously being acquired by the structural monitoring system. Moreover, since the experimental data has a high resemblance with the calculated data, it can be inferred that any abnormal event took place during the analysed period. Concerning the rectangles "sensory and data acquisition systems" and "data storage and visualisation", they are addressed in Chapter 3 too, where the developed software for data acquisition, processing and storage of the stay cable monitoring system is described. It should also be noted that the scheme depicted in Figure 2.1 represents also the components of an SHM system listed in section 2.2 until the bullet iv.

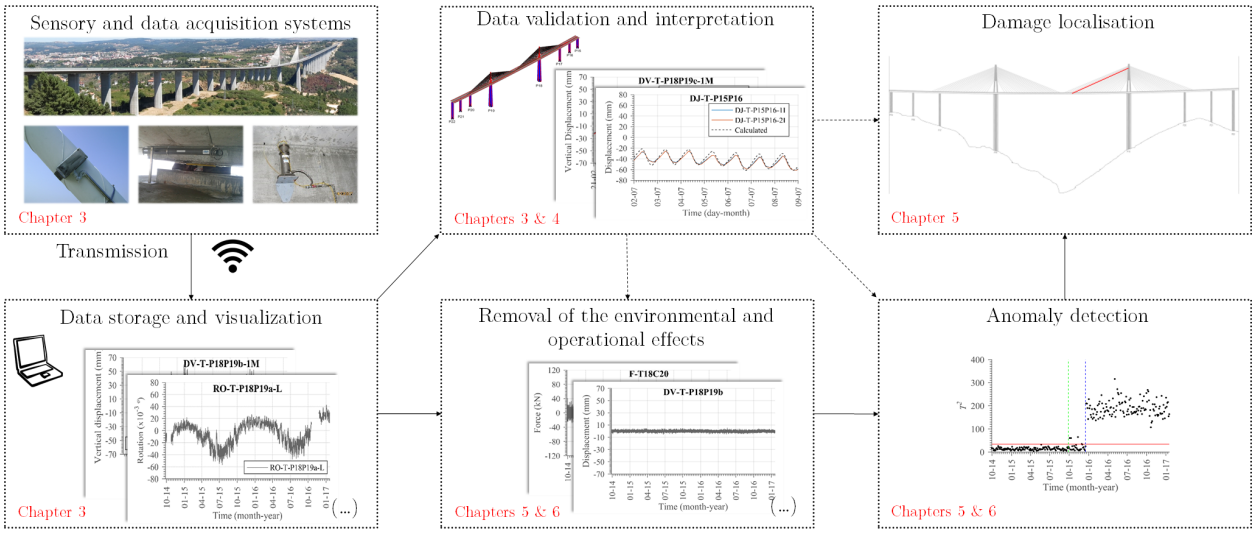

Figure 2.1 – Schematic representation of the proposed strategy for structural health monitoring.

2.3.3. Literature review on data-based approaches

2.3.3.1. General

Data-based approaches usually rely on three main steps: feature extraction and data compression, data normalisation and feature classification. Feature extraction can be defined as the process of extracting damage-sensitive features from the measured structural system response data. The extracted damage-sensitive features are expected to be more sensitive to damage than the raw data. Data compression is the process of reducing the dimension of the measured data [66]. As feature extraction and data compression are usually carried out together, being their distinction sometimes not straightforward, they are here merged into one step.

Data normalisation is the process of filtering out the environmental and operation effects (EOVs) from the measured structural response. In general, the robustness and accuracy of the damage detection algorithms depend on how successfully the benign variations due to EOVs are discerned from the variations due to damage. Feature classification is the stage where the features are labelled. Statistical strategies are used to classify the features related to known or novel structural conditions.

Data-based approaches can be supervised or unsupervised. When data is available from both the undamaged and damaged structure, the statistical pattern recognition algorithms fall into the general classification referred to as supervised learning. Unsupervised learning refers to algorithms that are applied to data not containing examples from the damaged structure [66]. The ability to perform damage detection in an unsupervised learning mode is very important because data from damaged structures are typically not available for most real-world civil engineering structures [182]. These procedures are known as novelty detection or anomaly detection within the machine learning community or as outlier detection methods within the statistics community [66].

2.3.3.2. Feature extraction and data compression

In the feature extraction/data compression stage, the measured data is transformed into a different type of information, whose changes are expected to be more informative about the structural condition [170]. Since the learning algorithm will have many more adjustable

parameters the higher is the dimension of the feature vector, feature extraction/data compression is considered a critical step in any data-based approach [218].

The most used feature extraction method is, by far, modal analysis. Modal frequencies, mode shape coordinates or damping ratios [79, 88, 124, 133, 147] are used as damage-sensitive features. They are usually extracted from the measured accelerations by means of operational modal analysis techniques [14]. Alternatively to modal analysis, wavelet transforms has been used, being the wavelet coefficients used as damage sensitive features [29, 96, 152, 156, 157, 202]. Time series models have also been used as an alternative to modal analysis. Time series models, such as autoregressive (AR) models, have been adjusted to acceleration or strain measurements and the coefficients of the adjusted models are used as damage-sensitive features [34, 70, 108, 150].

Basic signal statistics, as the first four statistical moments (mean, standard deviation, skewness and kurtosis), have been used for feature extraction [66, 71, 83, 136]. They are usually applied for feature extraction on the residuals obtained from the data normalisation under the assumption that the residuals follow a normal distribution. Principal Component Analysis (PCA) has also been widely used for feature extraction, being the eigenvalues, the eigenvectors or the angle between subspaces used as damage sensitive features [26, 115, 116, 156, 162]. PCA has also been widely used for data compression in the scope of SHM [63, 89].

The Mahalanobis distance or multivariate control charts such as the Hotelling T^2 control chart can also be seen as feature extraction and data compression methodology, although their ultimate goal is feature classification. They transform a multivariate dataset in a univariate dataset. Examples of their application can be found in [11, 48, 86, 133, 145].

Recently, Symbolic Data Analysis (SDA) have been proposed for feature extraction [43]. In comparison to classical data, the symbolic data objects have the advantage of being richer and less voluminous [170]. Symbolic data analysis has been used for feature extraction of acceleration measurements, modal frequencies and coordinates [5, 43] and displacement and rotation measurements [169, 172].

According to their localisation within the work-flow of the data-based approach, feature

extraction/data compression can be classified as centralised (Figure 2.2 (a)), pattern-level (Figure 2.2 (b)) or combinations of both (Figure 2.2 (c)) [170, 201, 218]. Obviously, the divisions depicted in Figure 2.2 in reality are not always so well defined, being sometimes feature extraction and data compression achieved along with the same algorithm used for data normalisation or feature classification.

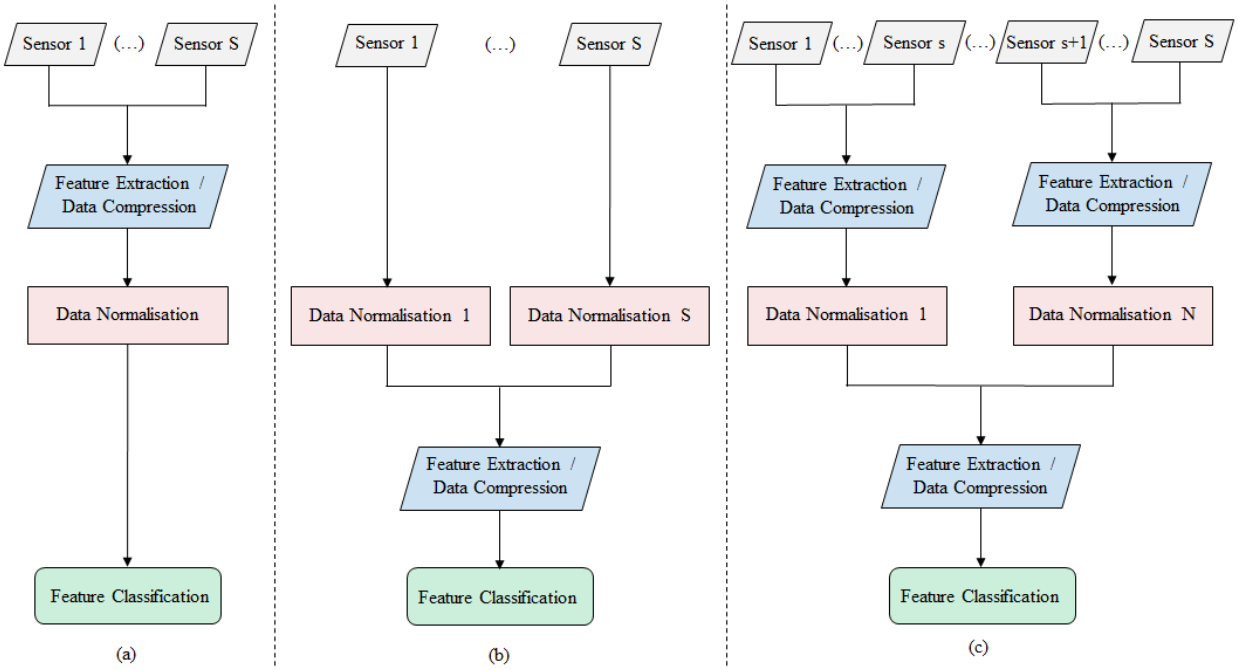

Figure 2.2 – Classification of feature extraction/data fusion according to its localisation within the work-flow of the data-based approach ([170]): (a) centralised-level; (b) pattern-level and (c) both.

2.3.3.3. DATA NORMALISATION

General

The changes in structural response caused by small damages can be easily masked by the environmental and operational effects [184, 223]. Therefore, data normalisation is very important in order to detect damage. Depending on the type of structure, this process can be complex and constitutes one of the main reasons for the slow transition of SHM from academia to real practical applications [41, 66, 184]. Among all EOVs that affect the structural responses, daily and seasonal temperature variations are by far the most reported in the technical literature. Several long-term monitoring studies have reported that temperature variations can produce strains, displacements or rotations of the same order of magnitude, or even larger, than those due to dead or live loads [2, 18, 24, 106, 112, 118,

159, 198]. Other environmental and operational effects that generate changes in the measured structural responses have been reported, such as traffic [113, 133] and wind [124, 133].

Data normalisation is usually achieved by training a machine learning model in the normal structural response, being then the estimates compared to the measured responses in order to detect abnormal behaviours. Two complementary approaches can be followed: input-output or output-only. The input-output methods, also called regression-based, aim to remove the EOVs by means of the establishment of relationships between the measured actions (temperature, traffic, wind, humidity and so on) and the measured structural responses. The output-only methods, also called normalisation approaches based on latent-variables, can characterise the effects generated by the EOVs without measuring them [71], which allows the study of complex structural responses generated by actions of expensive and challenging quantification and characterisation [170]. The input-output and output-only methods can be combined in order to take advantage of the benefits of the two approaches [133, 233] since there is no evidence that one should be preferred over the other [170].

Input-output methods

The simplest and probably the most used input-output approach for data normalisation is Multiple Linear Regression (MLR). MLR assumes that the relationship between the EOVs and the structural response is linear. Examples of the used of MLR in order to supress EOVs can be found in [55, 88, 110, 227]. Robust linear regression [26, 49, 110], which takes into account the presence of outliers, and Bayesian linear regression [77, 84, 208] have also been used for data normalisation.

However, when the relationships between the measured EOVs and structural responses are not linear, methods with the ability to model nonlinear relationships between variables have been used. The nonlinear relationship between the input and the output can be due to a nonlinear behaviour of the structure or due to the fact that the measured EOVs are not representative of the truly EOVs acting on the structure [198]. The Artificial Neural Networks named Multi-Layer Perceptron (MLP) has been the most used machine learning algorithm to model nonlinear relationships in the scope of SHM [218]. Examples of their

application can be found in [7, 107, 110, 135, 147, 172, 230, 231]. Another machine learning algorithm with the capacity of modelling nonlinear relationships successfully applied in the field of SHM is Support Vector Regression (SVR). Examples of applications of SVR within the scope of SHM can be found in [89, 109, 110, 148].

Output-only methods

Within output-only methods for data normalisation, Principal Component Analysis (PCA) is probably the most used linear output-only approach in the scope of SHM. PCA has been used alone [11, 156, 164, 169, 224] and combined with input-output methods [133]. Nonlinear versions such as local PCA [37, 225], Kernel PCA [149, 164] and Auto-Associative Neural Networks [78, 85, 232] have also been used in the scope of SHM.

Recently, Cointegration Analysis – from the field of econometrics [61] – has been proposed as a new output-only approach to suppress the effects of EOVs in SHM [40, 44]. The basic idea behind Cointegration Analysis is to establish linear relationships between nonstationary time series in order to create a stationary residual. Applications of Cointegration Analysis to SHM data can be found in [36, 37, 120, 128, 129]. Nonlinear cointegration analysis has also been proposed for SHM applications [177, 240].

Some applications of algorithms from the family of Blind Source Separation (BSS) such as Independent Component Analysis [226, 236, 237] and Second-Order Blind Identification [161] have also been made. BSS algorithms are able to recover the underlying set of signals, called sources, from the records of their mixture [161].

2.3.3.4. Feature classification

The feature classification stage is intrinsically associated with the type of data-based approach adopted: supervised or unsupervised. Supervised classification in real practical applications of civil engineering structures are scarce or inexistent. Since civil engineering structures are usually unique and very expensive, data from the damage states are usually not available for training supervised models. Even though, some works can be found in the literature using supervised data-based approaches. They are usually applied to numerically simulated data. Examples of supervised algorithms used for feature classifications are artificial neural networks [6, 57, 105, 160, 228] and support vector machines [6].

With regards to unsupervised feature classification algorithms, procedures known as novelty detection or anomaly detection within the machine learning community or as outlier detection methods within the statistics community have been applied [66]. Unsupervised statistical classification has been conducted by means of statistical process control, using univariate control charts [26, 55, 91, 213], multivariate control charts such the Hotelling T^2 control chart [47, 114, 133] or metrics such as the Euclidean distance [78, 233] or the Mahalanobis distance [11, 88, 224]. Applications using cluster analysis for feature classification, such as partitioning methods [4, 52, 172], hierarchical methods [43, 169, 171] or Gaussian Mixture Models [108, 168], can also be found. Recently, principal component analysis has also been used for feature classification [186, 237].

2.3.3.5. Additional remarks

The previous sections summarised, with special focus in civil engineering applications, the most applied algorithms for data-based damage detection by the SHM community. As can be easily perceived, the division of the data-based approach in feature extraction/data compression, data normalisation and feature classification is not always straightforward. Moreover, the same algorithm can be used in any of the three stages. For that reason, some authors state that the data normalisation procedure is usually present in the data acquisition, feature extraction, statistical modelling and feature classification phases [168]. Even though, this organization was chosen since the author believes that is the most pedagogical way to transmit the key concepts of any data-based approach for damage detection.

Chapter 3

CORGO BRIDGE

3.1 Introduction

In this chapter the Corgo Bridge is presented. This bridge will be used as case study throughout this work. The installed monitoring system is described, with a particular focus on the structural monitoring system of the stay cables. The numerical model that was developed to follow the construction stages, to analyse the structural behaviour during the load test and to follow the results collected by long-term monitoring system, which are examined in Chapter 4, is also described. Finally, the behaviour of the bridge during the load test is discussed.

3.2 Description of the bridge

The Corgo Bridge (Figure 3.1) is a prestressed concrete box-girder bridge with a total length of 2790m, divided into three continuous sub-viaducts: the West Sub-Viaduct (WSV), the Central Sub-Viaduct (CSV) and the East Sub-Viaduct (ESV) with, respectively, 855m, 768m and 1167m length. The West and East Sub-Viaducts are continuous frame bridges with the majority of the spans being 60m long and were constructed using movable scaffolding systems. The Central Sub-Viaduct is a cable-stayed bridge with a 300m long

central span balanced by 126m long adjacent spans and two continuous end spans with 48m and 60m on each side (see Figure 3.3). The suspension system consists of one single central plane with four symmetric semi-fans of 22 stay-cables each. The central span and the adjacent spans were built using the balanced cantilever method, while the continuous end spans were constructed using the same movable scaffolding systems of the Lateral Sub-Viaducts* (LSV). The construction of the bridge started in March 2010 and was finished in March 2013. The load test was performed on July 2013 and the bridge was opened to traffic on September 2013.

Figure 3.1 – Corgo Bridge: (a) general view, (b) general perspective of the deck and (c) side elevation.

* Lateral Sub-Viaducts refer to the West and East Sub-Viaducts.

The deck is constituted by a unicellular box-girder of constant height (3.5m) with overhangs supported by prefabricated concrete struts spaced at regular intervals of 3m. The deck holds two carriageways with two traffic lanes each. While the width of the Lateral Sub-Viaducts is 25.30m, the Central Sub-Viaduct is 28.00m wide in order to provide space for the pylons and anchorages of the stay-cables (see Figure 3.2). The top slab of the bridge-girder of the Central Sub-Viaduct is also transversally prestressed for complementing the transmission of the cable forces to the box-girder.

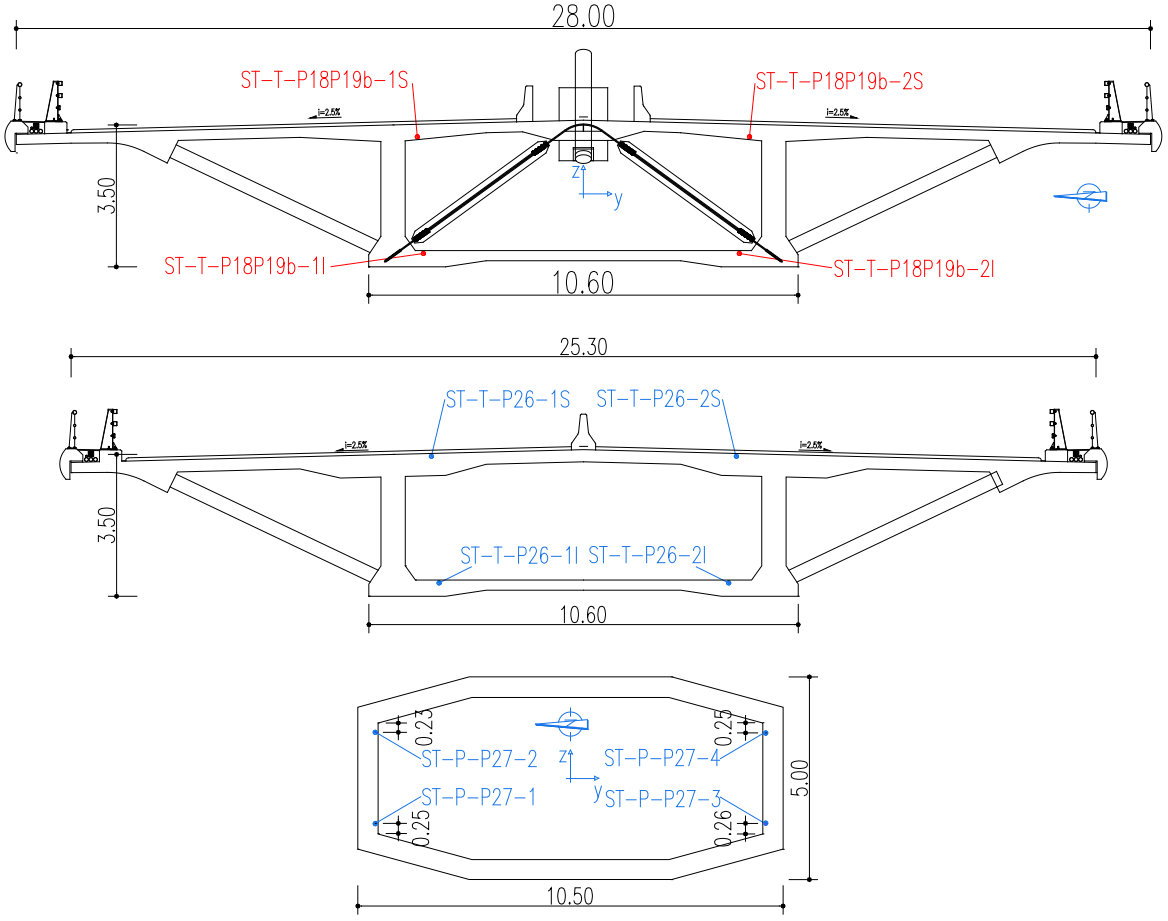

Figure 3.2 – Typical cross-sections with the location of the concrete temperature sensors: (a) Central Sub-Viaduct; (b) Lateral Sub-Viaducts; (c) typical pier.

The piers have a constant octagonal-shaped box cross-section. Below the deck the pylons have also an octagonal-shaped box cross-section but with variable transversal dimension along with the height. The pylon part above the deck has an inverted "V" shape along the longitudinal direction of the bridge. The pylons have a total length of about 193m, of which 130m are between the foundations and the deck. The height of the piers varies between

18.23m and 113.02m. While the pylons are monolithically connected to the box-girder, the connection between the piers and the deck is carried out using pot bearings which are fixed in both longitudinal and transversal directions, or only transversely fixed (see Table 3.1). Further information about the Corgo Bridge can be found in Barata [9].

Table 3.1 – Pier-girder connections of the Corgo Bridge.[†]

Pot bearings		**Monolithic connection**
Transversely fixed	**Transversely and lengthwise fixed**	
E1 to P4	P5 to P12	Pylons P18 and P19
P13 to P16	P17	
P21 to P22	P20	
P35 to E2	P23 to P34	

3.3 Structural monitoring system

A comprehensive structural monitoring system was implemented in the Corgo Bridge, with a particular focus on the Central Sub-Viaduct due to its higher structural complexity. The schematic layout of the structural monitoring system is shown in Figure 3.3. The system contemplates the measurement of bearing relative displacements, span deflections, rotations, cable forces, average concrete strains, strains in the steel diagonals, ambient and concrete temperatures, ambient and concrete humidity and durability indicators. For the measurement of these magnitudes both fibre-optic sensors (span deflections, steel and concrete strains of the Central Sub-Viaduct) and electric sensors (relative bearing displacements, rotations, cable forces, concrete strains of the East Sub-Viaduct, temperature, humidity and durability indicators) were used [146]. It should also be referred that in the transition piers (P15 and P22) there are two pairs of bearings, one supporting the girder of the Central Sub-Viaduct and other supporting the girder of one of the Lateral Sub-Viaducts. Therefore, the relative bearing displacements are measured between the transition pier and the corresponding girder (see Figure 3.4). With the exception of the cable forces, which have 2 readings per hour, all the sensors have 4 readings per hour. The raw readings of the temperatures, span deflections and stay cable forces can be found in Appendix A. These are the sensors used for damage detection and localisation in Chapters 5 and 6. Examples of the readings of bearing displacements and rotations can be found in

[†] The pot bearings of the piers P17 and P20 are also provided with anti-lifting devices.

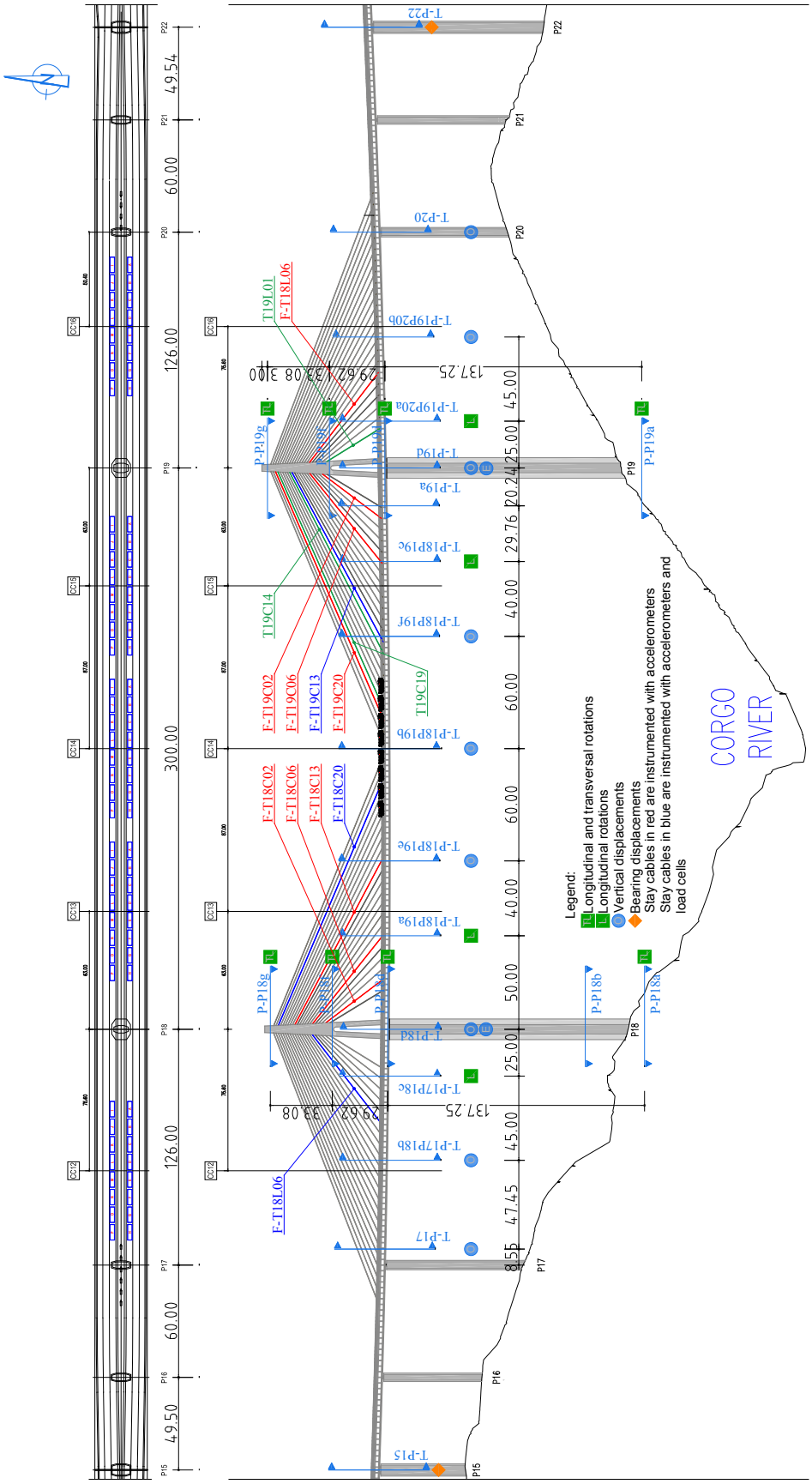

Figure 3.3 – Side elevation of the Central Sub-Viaduct, location of the instrumented sections of the CSV and vehicles position during the route II of the load test.

Chapter 4. Further details about the implemented structural monitoring system may be

found in Félix *et al.* [67].

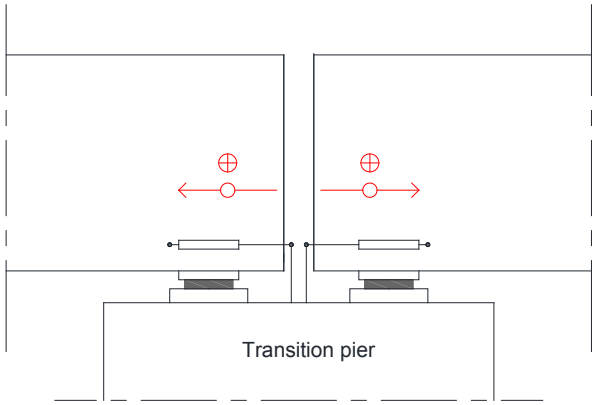

Figure 3.4 – Schematic representation of the installed bearing displacement transducers (LVDTs) in the transition piers.

3.3.1 Structural monitoring system of the stay cables

3.3.1.1 General remarks

The safety of cable-supported bridges is closely related to the cable integrity [23, 90, 130, 163] since these structures are considered to be safe if no important variations in the stay cable forces are observed [31, 130]. The existing methods for the determination of the forces in stay cables can be classified as direct and indirect. Examples of direct methods are load cells and electric or optic strain gages bonded to the steel wires of the prestressing strands. Examples of indirect methods are the ones based on the identified natural frequencies and subsequent estimation of the installed force using the taut string theory. The natural frequencies are usually estimated from the measurement of accelerations. Other indirect techniques such as interferometry laser systems [42], sensors based on the magneto-elastic effect [22] and guided stress waves [173] have also been used to indirectly estimate the installed force in stay cables.

In this context, a monitoring system of the stay cables was installed in the Corgo Bridge. It is a mixed system using 3 load cells and 10 accelerometers. This section describes the implemented structural monitoring of the stay cables of the Corgo Bridge, including the installation details and the software for automatic processing of the acceleration readings and estimation in real-time of the installed force in the stay cables.

3.3.1.2 DETERMINATION OF THE STAY CABLE FORCE USING ACCELEROMETERS

Identification of the natural frequencies of the stay cables

Among the existing output-only methods for modal parameter identification, the Peak-Picking frequency-domain technique is one of the most used due to its simplicity and fastness. The basic idea of the Peak-Picking technique is that a structure will have stronger responses near its natural frequencies when subjected to ambient excitations [14]. The frequencies are then identified by simply selecting the peaks of in the power spectral densities (PSD) computed from the measured outputs. The PSD can then be determined from:

$$PSD(\omega) = \frac{S(\omega)^* \cdot S(\omega)}{N \cdot \Delta t} \tag{3.1}$$

where $S(\omega)$ is the Fast Fourier Transform (FFT) of the accelerations time series, $(\bullet)^*$ is the complex conjugate, N is the length of the time series and Δt is the inverse of the sampling rate.

However, two errors are associated with the application of FFT to discrete-time signals: aliasing and leakage [134]. The former is due to the fact that the signal is sampled, having as a consequence the overlap of energy associated to frequencies higher than half of the sampling rate (the Nyquist frequency) to the energy associated to frequencies lower than the Nyquist frequency [19, 134]. The latter is due to the finite nature of the time series. The impossibility of indefinitely observe a signal leads to the distribution of energy associated with a particular frequency by the neighbour frequencies [19, 134].

In order to avoid aliasing errors, a low-pass filter with a cut-off frequency of 0.4 of the sampling rate should be used [14, 166]. The leakage error can be minimized by means of application of time windows to the signal before the determination of the signal FFT. Therefore, a segmentation of the time series with an overlap of 50% is usually made, being the Hanning window applied to each segment before the determination of its FFT. Then an average PSD of the segments is obtained. In order to not change the energy content of the signal, the ordinates of the signal should be divided by the root mean squared value of the window [134]. This methodology is usually referred to as Welch's Methodology [210] and

was the one implemented in the software STayMensus.

Estimation of the installed cable force

After the determination of the natural frequencies of the cables, the installed force (F) can be estimated by means of the taut string theory:

$$F = 4mL^2\left(\frac{f_n}{n}\right)^2 \tag{3.2}$$

where m is the distributed mass per unit length [ton/m], L is the cable length [m] and f_n is the natural frequency [Hz] associated with the mode n. The taut string theory assumes that [23]:

- The flexural stiffness of the cable is negligible. Therefore, a perfect hinge can be assumed as the bearing condition at the cable ends;
- There is no relative displacement of the points where the cable is anchored, that is, there is not coupling between the pylon, or deck, and the cable;
- The transverse in-plane deflections of symmetrical modes do not generate additional tension in the cable (the cable is inextensible).

These simplifications are not strictly valid in civil engineering structures and several improvements to accounting for the bending stiffness and cable sag have been proposed [64, 76, 137, 163]. Methodologies combining numerical finite element modelling with experimental data was also been proposed [20, 102]. However, the accuracy of the force estimations for continuous monitoring is not so important as in periodic inspections since in continuous monitoring one can just look for changes in the natural frequencies of the cable instead of the installed force. For that reason, the forces in the stay cables of the Corgo Bridge are estimated using the equation (3.2).

3.3.1.3 Instrumented stay cables and accelerometer fixing system

The stay cables instrumented with accelerometers are listed in Table 3.2 and their location is shown in Figure 3.3. The instrumented cables are evenly distributed in the central span to ensure maximum representativeness. The used accelerometers are the PCB *Piezotronics*

393B12 and they were placed 5m above the deck, measuring vibrations in the vertical plane of the fan. The acquisition system, a National Instruments cDAQ-9188 with three modules NI-9234, was placed at the midspan of the main span of the bridge in order to reduce the electric cable length between the acquisition system and accelerometers.

Table 3.2 – Instrumented stay cables.

Stay cable	**L [m]**	**m [kg/m]**	**Observations**
T18L06	62.16	64.06	Stay cable instrumented with a load cell
T18C02	40.22	52.88	
T18C06	62.74	64.06	
T18C13	104.1	84.71	
T18C20	147.5	89.95	
T19C20	144.9	89.95	Stay cable instrumented with a load cell
T19C13	102.9	84.71	Stay cable instrumented with a load cell
T19C06	61.86	64.06	
T19C02	39.67	52.88	
T19L06	63.04	64.06	

The accelerometers were fixed to the stay cables using stainless steel clamps, facing north in order to reduce the sun exposure (see Figure 3.5). The electric cables are led inside stainless steel pipes along the stay cable towards the interior of the box-girder until the acquisition system and the computer with the *STayMensus* software [192, 193].

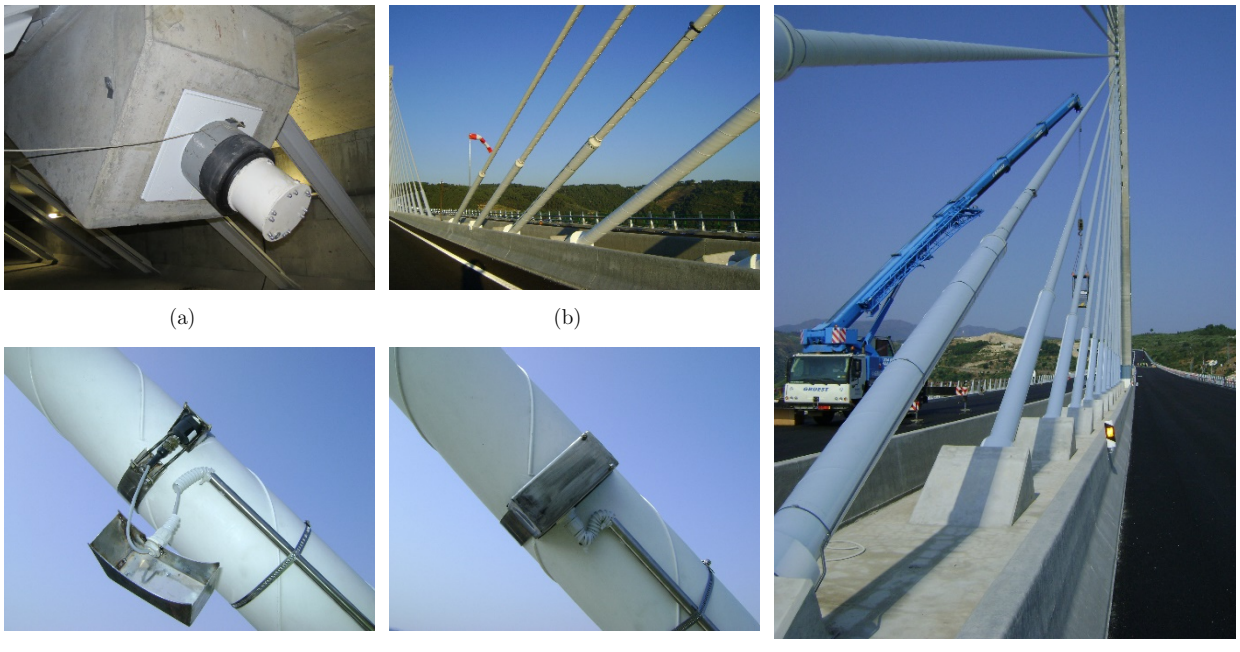

(a) (b) (d) (e) (c)

Figure 3.5 – Stay cable monitoring system of the Corgo Bridge: (a) load cell, (b) and (c) stay cable instrumented with an accelerometer, (d) and (e) installation details of the accelerometers.

3.3.1.4 STAYMENSUS: A TOOL FOR ACQUISITION AND ANALYSIS OF TENSION FORCES IN STAY CABLES

STayMensus is a standalone software developed in the LabView environment. It can be installed on any computer without the need of pre-installing LabView. *STayMensus* autonomously manages all the process of data collection, pre-processing, processing and storage. The flowchart of the *STayMensus* software is presented in Figure 3.6. First, the signal is collected. Second, the signal is pre-processed: the signal is filtered and decimated. Third, the PSD is determined using Welch's Methodology. Fourth, the natural frequencies of the stay cables are estimated by selecting the peaks of the PSD. Fifth, the stay cable force is estimated by means of the taut string theory. Finally, the data is stored.

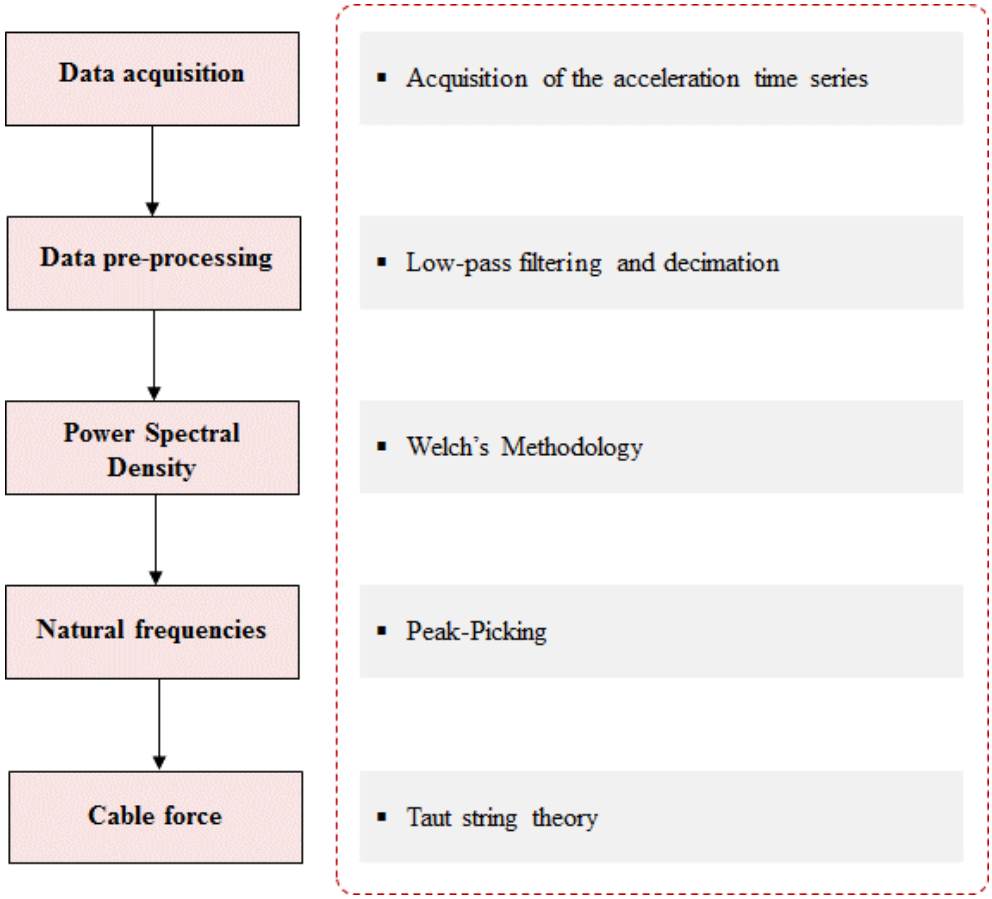

Figure 3.6 – Flowchart of the algorithm of the *STayMensus*.

STayMensus should ideally be installed on a computer with an internet connection and be executed continuously in order to take advantage of all its functionalities. It should be noted that all of the functionalities are available to the final users, which does not need to have any knowledge about the LabView programming language. The main functionalities of

STayMensus are now enumerated:

- Real-time estimation of the power spectrum densities and installed cable forces;
- Creation of an organised database with all the results;
- Automatic sending of an email when a pre-established acceleration threshold is exceeded;
- Automatic sending of an email when there is some problem with the acquisition configurations and human intervention is necessary;
- Scheduled and non-scheduled acquisition;
- Definition of the acquisition time of each event;
- Definition of the periodicity of each scheduled event;
- Definition of the sampling rate and decimating factor;
- Definition of the number of natural frequencies to estimate;
- Output of error logs;

The continuous record of acceleration time series can lead to a big amount of stored data. Wherefore, the acceleration time series may or may not be saved after they are processed. In Figures 3.7 and 3.8 are depicted two screenshots of the *STayMensus* software: one with the real-time determination of the PSD for the stay cable T18C20 and another with the menu of options.

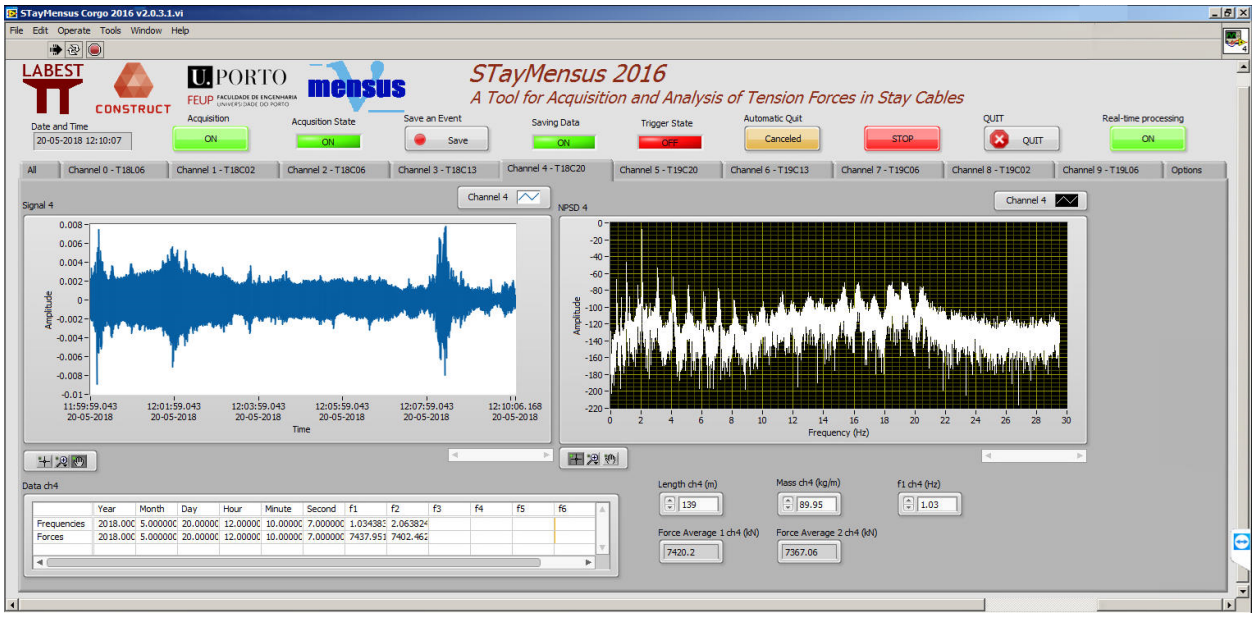

Figure 3.7– Real-time estimate of the force installed in the stay cable T18C20.

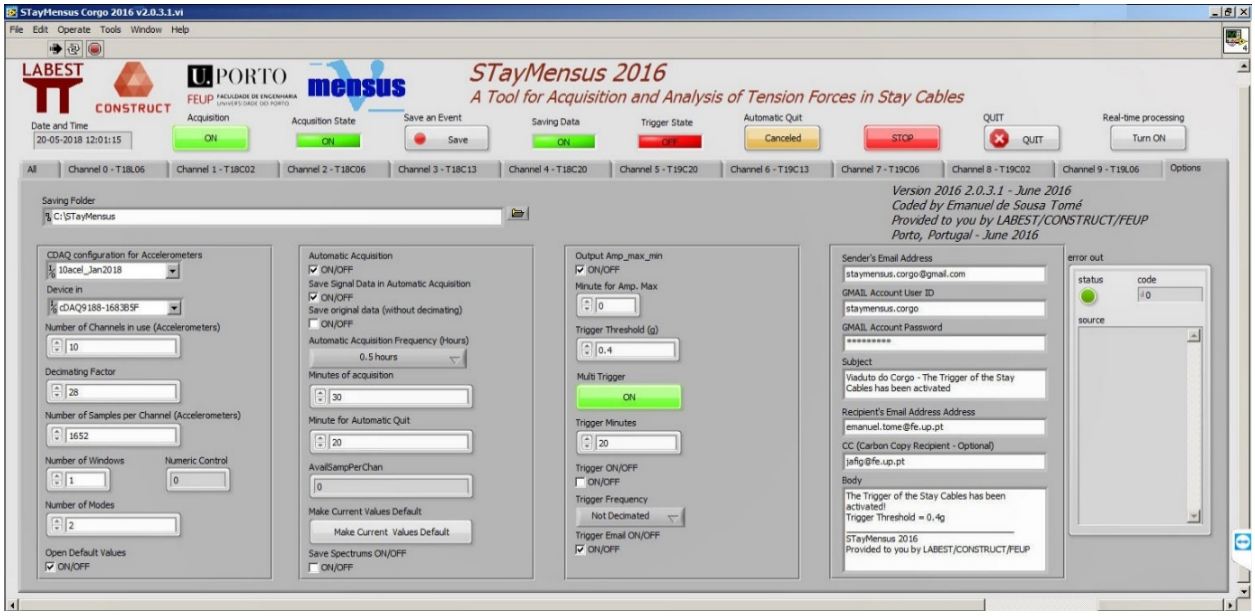

Figure 3.8 – Options menu of the *STayMensus*.

In Appendix A the obtained outputs of the *STayMensus* software can be found (Figures A.5 and A.6). As can be seen in those Figures, there are few gaps in the data during the period of data used in this Thesis (3.5 years). The existing gaps are essentially due to power outages. This demonstrates the robustness of the developed monitoring system.

3.4 Finite element model of the Central Sub-Viaduct of the Corgo Bridge

The structural response of the bridge to thermal loads and vehicle loads is determined using a three-dimensional beam finite element model [190, 191], see Figure 3.9. Fully numerically integrated 3-node Timoshenko beam elements are adopted. All the post-tensioning tendons and bars are included in the model as embedded truss elements, initially unbounded during the tensioning operations and bonded afterwards. The stay cables are modelled using truss elements. A total of 1064 3-node Timoshenko beam elements and 560 truss elements were used. The construction schedule was available and strictly followed in the analysis, including all the re-tensioning stages of the stay cables. A total of 335 construction stages were simulated, with a total duration of 1012 days since casting of the first segments of pylon P19 up to complete closure of the deck.

Concrete creep and shrinkage, and prestress steel relaxation models according to the EN1992-1 where selected. Two concrete mixes were adopted according to the design

specifications: C40 concrete for the piers; and C50 for the girder and pylon segments above the deck. The creep curves, $\varphi(t,t_0)$, for the C50 concrete in the deck where fitted to 200 days of experimental data acquired on prismatic specimens cast during the construction. The curve fitting was performed using two empirical parameters k_1 and k_2:

$$\phi(t,t_0) = k_1 \cdot \phi_0 \cdot \beta_c(t,t_0)^{k_2} \tag{3.3}$$

where φ_0 is the notional creep coefficient and $\beta_c(t,t_0)$ is the coefficient describing the development of creep with time after loading, both according to the EN1992-1. The best fit was obtained with $k_1 = 1.72$ and $k_2 = 0.85$. The remaining input data for defining the creep and shrinkage curves were defined as follows: average relative humidity RH=60%, ambient temperature T=15ºC (both based on the measured yearly average values) and cement type R. As for the prestressing steel, EN1992-1 relaxation class 2 was adopted for the strands and class 3 for the bars. The coefficient of thermal expansion was assumed to be $10\times10^{-6}\,°C^{-1}$ both for concrete and steel.

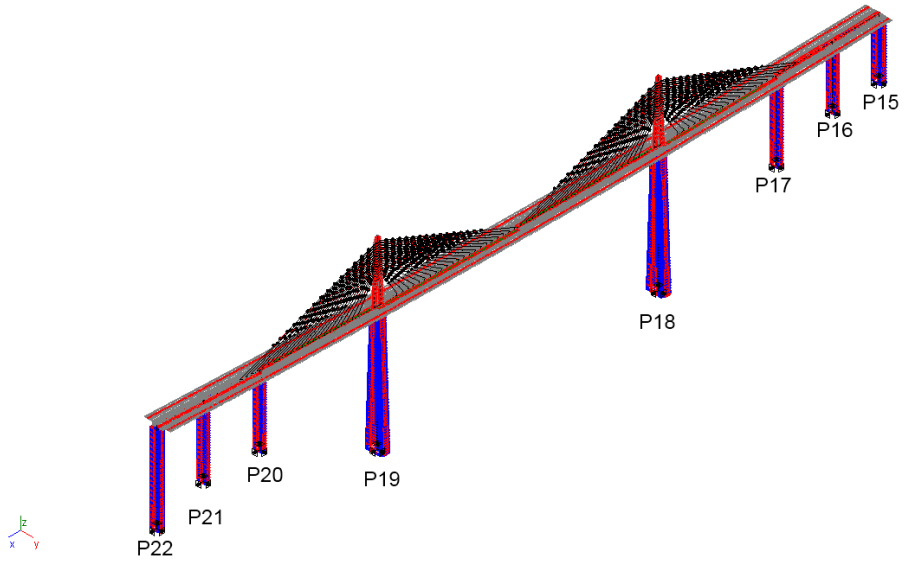

Figure 3.9 – Mechanical finite element model of the Central Sub-Viaduct of the Corgo Bridge [190, 191].

The developed model was validated with experimental data both during the construction stages [190, 191] and during the load test [194-196]. A good fit between the experimental and calculated results was obtained. It is however noted that the west part of the bridge is slightly stiffer than predicted by the model (see next section).

The predicted time-dependent response of the bridge for two sensors (one cable force and

one girder deflection) are depicted in Figure 3.10. The vertical dashed lines mark the beginning and end of the experimental data used in this thesis (from January 2015 to July 2018). As can be inferred from Figure 3.10, some sensors have a time-dependent response that cannot be simplified by a logarithmic function. Moreover, some sensors such as the girder displacements are still in considerable evolution over the next years. Therefore, the suppression of these long-term effects are of vital importance when damage detection methodologies are applied in Chapter 5 and 6 since their disregard could lead to a considerable amount of false positives.

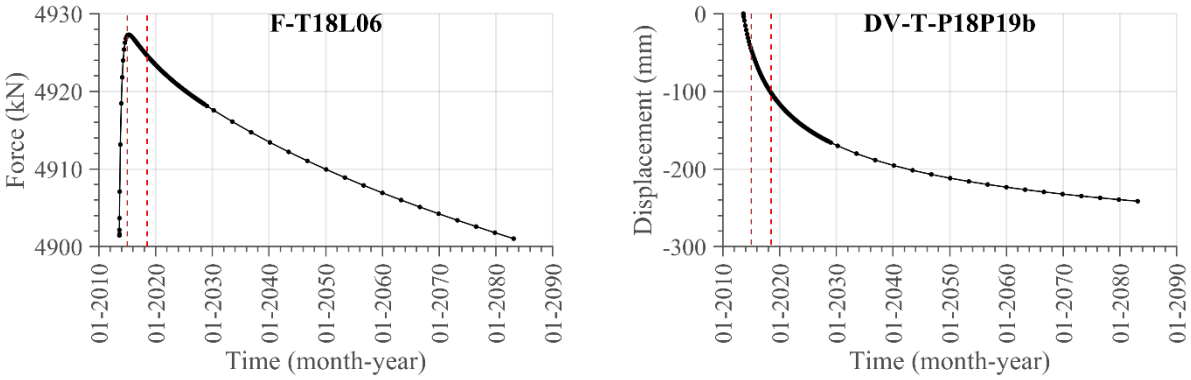

Figure 3.10 – Predicted time dependent response of the bridge for sensors: (a) F-T18L06 and (b) DV-T-P18P19b. The vertical red dashed lines correspond to January 2015 and July 2018.

3.5 Load test

3.5.1 General remarks

It is generally recommended to perform load tests in complex bridges before opening to traffic in order to evaluate the condition of the as-built structure and to establish the reference state of the bridge. Through these field tests, it is possible to obtain important features of bridge structural behaviour under controlled loads and the comparison between the experimental data and numerical simulations provides an important insight on the effective behaviour of the bridge. This will be exemplified in the following sections. Load tests are also referred as an important tool for the safety evaluation of bridges [155], for the assessment of the effective structural behaviour after a retrofit intervention [25] and for validation and calibration of indirect methods for estimation of structural physical quantities which were not directly measured [188].

In this section, the most relevant results obtained during the load test of the Central Sub-Viaduct of the Corgo Bridge are presented. The experimental results are compared to the numeric results obtained from the finite element model described in the previous section. In this particular case, the main objectives of the performed load test were to:

- Assess the bridge condition and structural behaviour under controlled loads;
- Evaluate the conformity of the constructed structure with the design assumptions;
- Validate and calibrate numerical models for further studies during the service state of the bridge;
- Establish a reference state of the bridge before its opening to traffic;
- Validate and check the implemented structural monitoring system.

3.5.2 Description of the field load test

The load test of the Corgo Bridge occurred in July 2013 and was as much comprehensive as possible, comprising several load cases and load levels in order to assess the linearity and repeatability of the structural response of the bridge. Eighteen static load cases (load cases CC1 to CC18) and three crossings of the bridge by two and four trucks at low speed to trace the experimental influence lines [194-196] were performed. Due to the large quantity of experimental data, only the results of 4 static load cases (CC12 to CC16) with 16 trucks each, and of the low-speed crossing with 4 trucks are discussed (see Figure 3.11). The vehicles used in the load test have an average mass of approximately 30 tons distributed by three axles (see Figure 3.12 and Table 3.3).

(a) (b)

Figure 3.11 – Position of the vehicles during the load case CC14 (a) and during the crossing for obtaining the centred influence line.

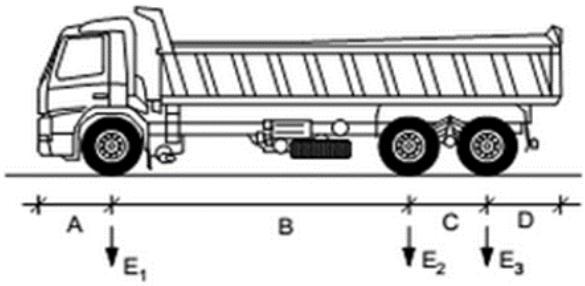

Figure 3.12 – Schematic representation.

Table 3.3 – Averaged mass of the used vehicles.

	Mass (ton)
μ	29.889
σ	0.974
Max	31.44
Min	28.36

Besides the sensors of the structural monitoring system, provisory sensors were additionally used during the load test for ensuring redundancy in the measurements of the vertical deflections. Also, topographic measurements of the horizontal displacements of the pylons and of the vertical displacements of the girder were performed [193, 194]. In order to support the interpretation of the presented results, the deformed meshes for the load cases CC12 to CC16 are depicted in Figure 3.13.

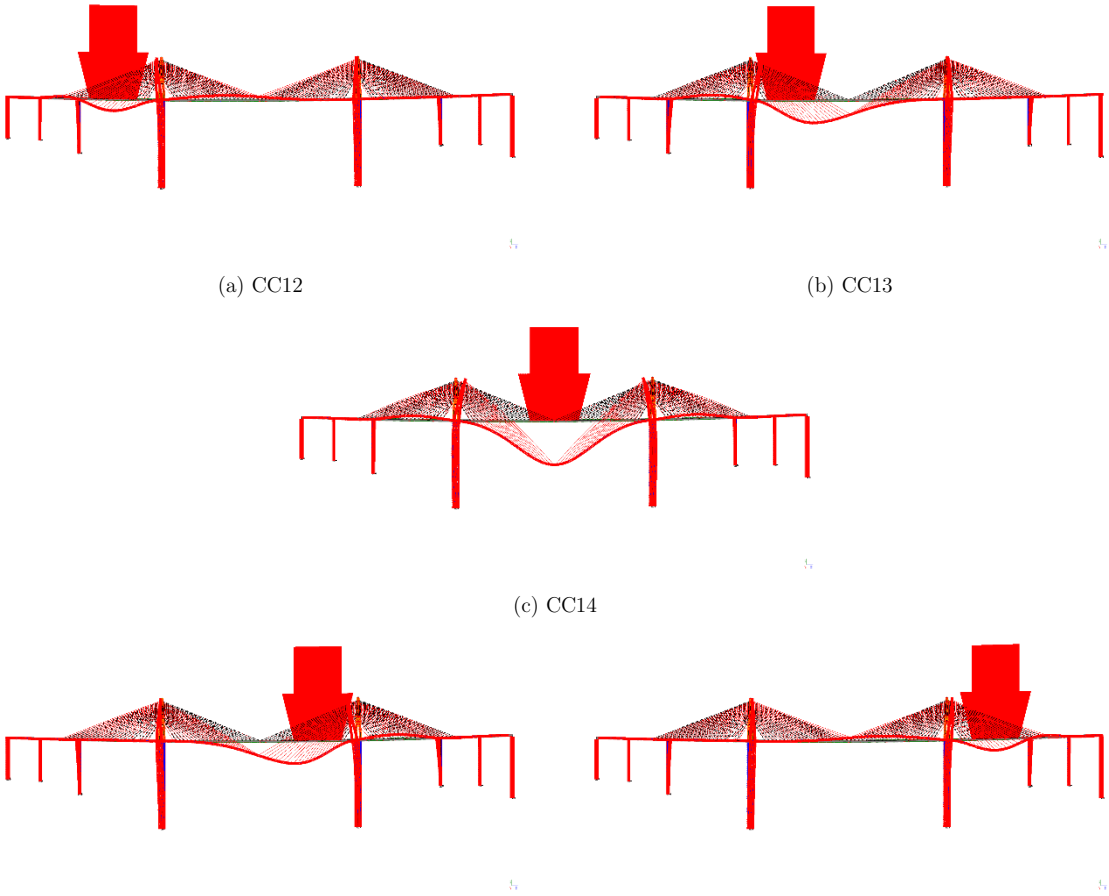

(a) CC12 (b) CC13

(c) CC14

(d) CC15 (e) CC16

Figure 3.13 –Deformed meshes for the load cases CC12 to CC16 (*Evolution* screenshots) [191].

3.5.3 Results

3.5.3.1 Deck

The calculated and measured girder deflections obtained during the load cases CC12 to CC16 are depicted in Figure 3.14. On the whole, the obtained results using the different measurement systems are consistent between them and agree well with the calculated results. A maximum downward deflection of about 128mm was observed at the midspan of the main span for load case CC14 and a maximum upward deflection of about 16mm in section T-P18P19e (located in the main span, 90m away from pylon P18) for load case CC12. Generally, a stiffer behaviour of the girder was observed near the pylon P18, where the observed girder deflections for the influence lines are smaller than the those calculated (see Figure 3.15) and the vertical displacements for the symmetrical load cases CC12 and CC16 are also smaller.

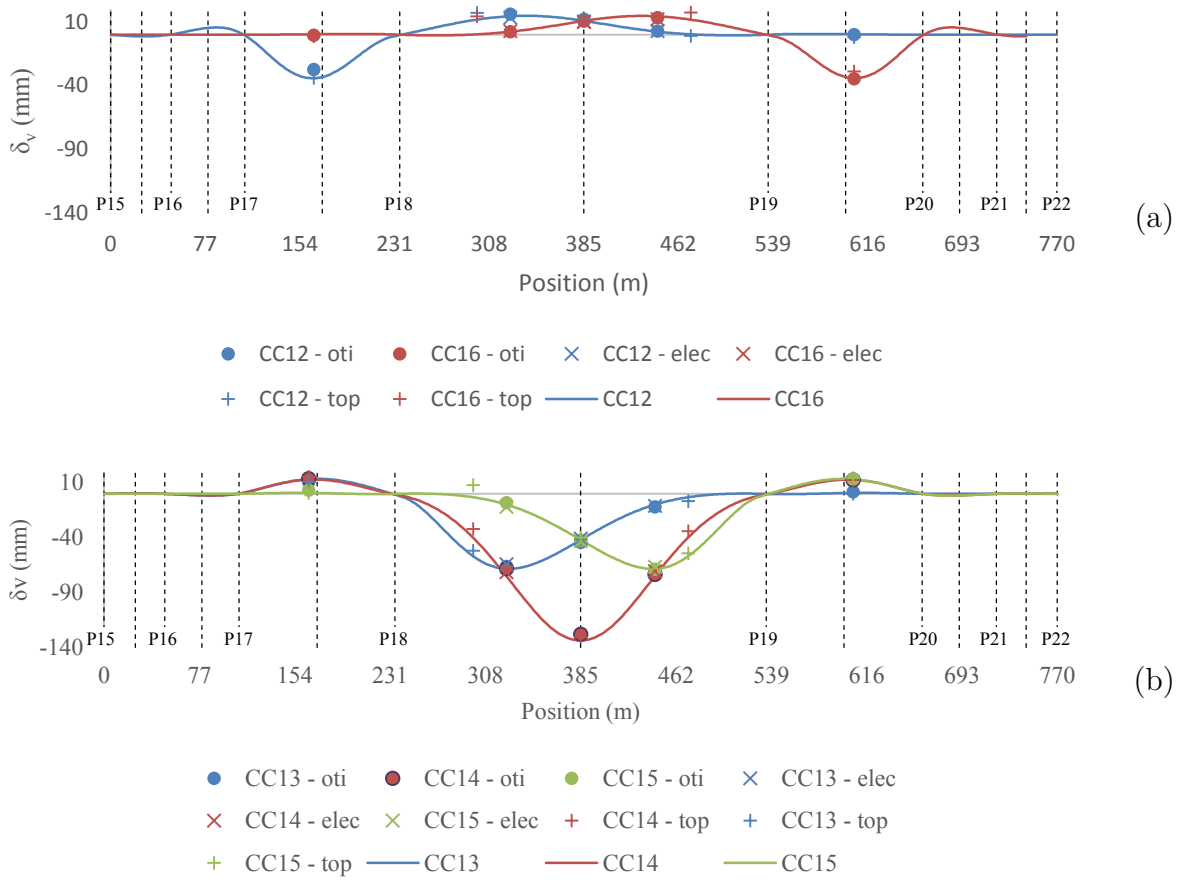

Figure 3.14 – Calculated (lines) versus measured (dots and crosses) vertical displacements of the girder for load cases: (a) CC12 and CC16; (b) CC13 to CC15.

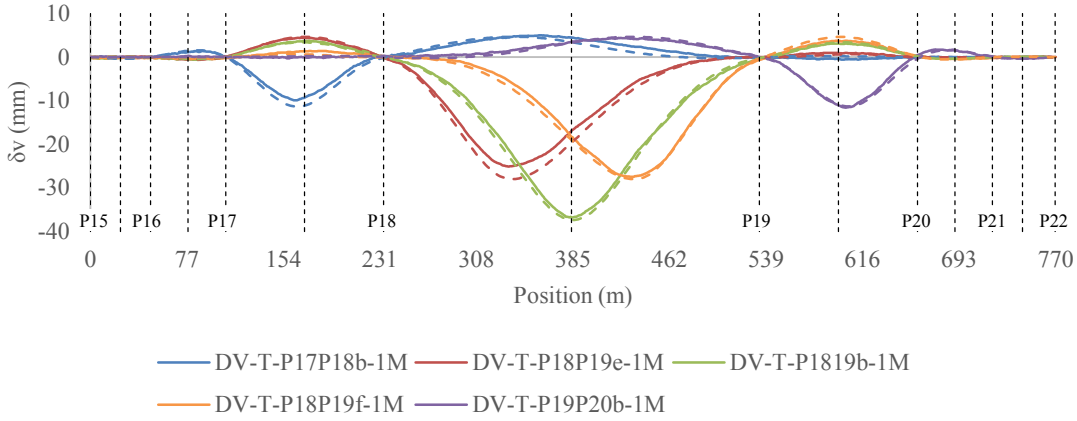

Figure 3.15 – Calculated (dashed lines) versus measured (lines) influence lines of the vertical displacements. The influence lines refer to two pairs of 30ton trucks crossing the bridge side by side.

Regarding the rotations of the girder corresponding to the static load cases and to the influence lines, a good agreement is also achieved between the measured and calculated values. Likewise the deflections, the calculated rotations show a slight tendency to overestimate the measured values (see Figures 3.16 and 3.17). The highest longitudinal rotation observed was of about 58×10^{-3} degrees for load case CC15 in cross-section T-P18P19c. Naturally, a rotation of the same order of magnitude was observed in cross-section T-P18P18a for the symmetric load case CC13.

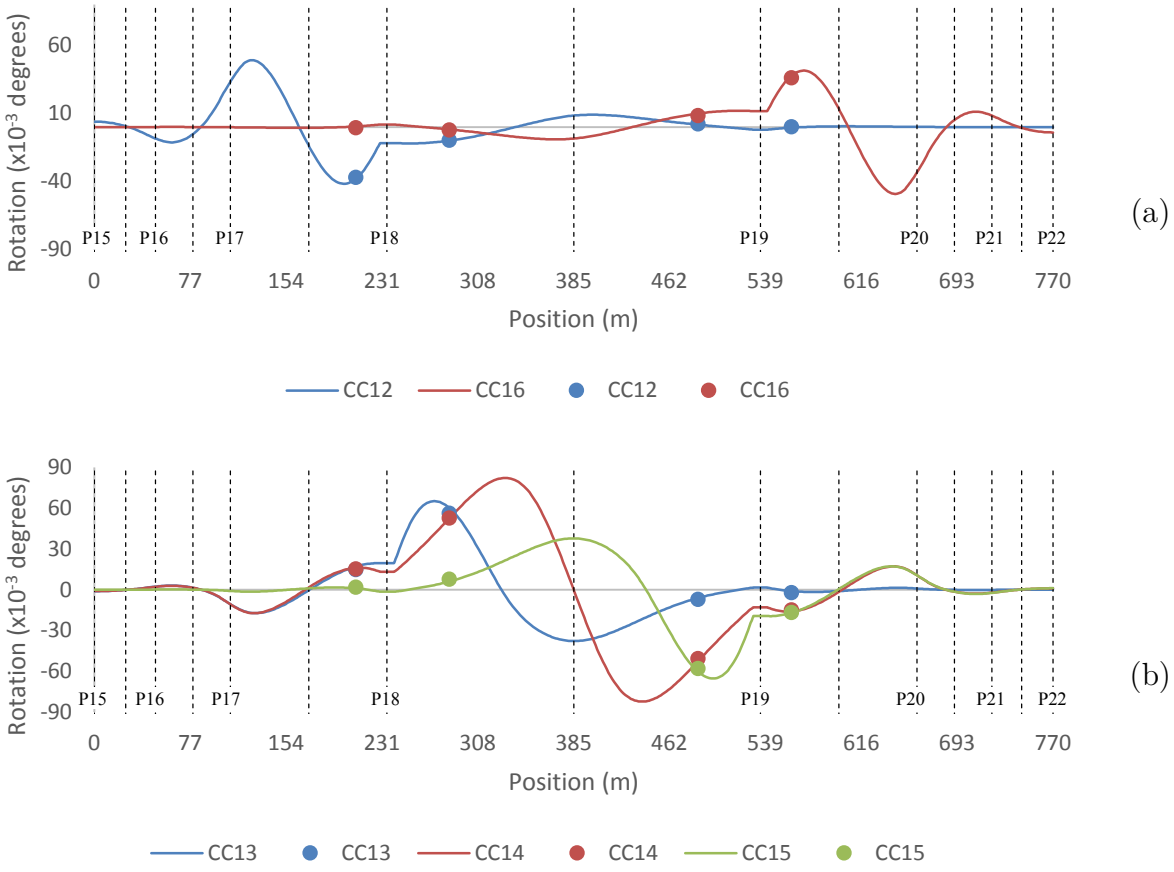

Figure 3.16 – Calculated (lines) versus measured (dots) rotations of the girder for load cases: (a) CC12 and CC16; (b) CC13 to CC15.

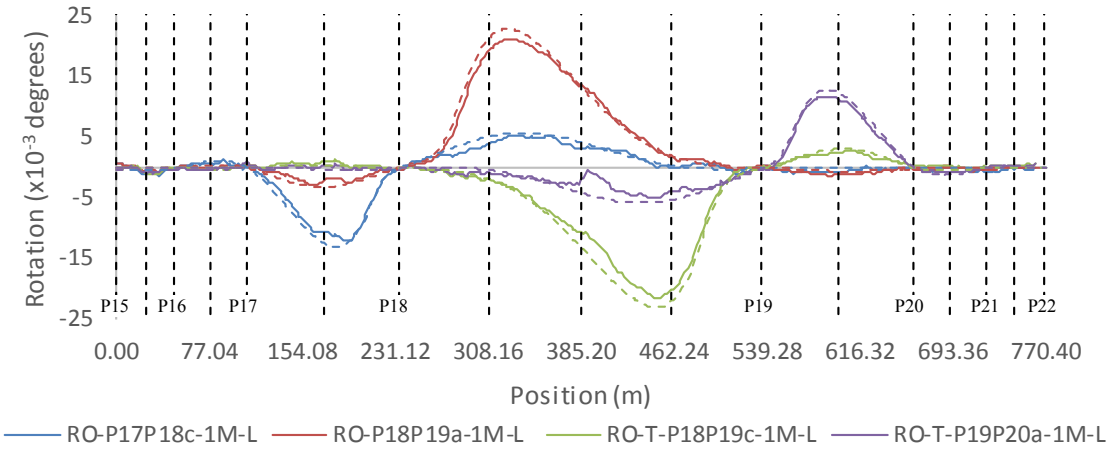

Figure 3.17 – Calculated (dashed lines) versus measured (lines) influence lines of the girder rotations. The influence lines refer to two pairs of 30ton trucks crossing the bridge side by side.

3.5.3.2 PYLONS

The pylons are the structural elements where the biggest differences between the experimental and calculated values were obtained, for both horizontal displacements and rotations, as can be seen in Figure 3.18. For the load cases with non-symmetrical load layout, the observed structural behaviour is significantly stiffer than that modelled, while for symmetric load cases a good agreement is obtained. As discussed in section 3.5.3.4, this can be explained by an anomalous behaviour of the bearings, probably related to unexpected friction in the bearings, or another sort of malfunctioning, leading to a restraint to the relative displacement between the deck and the piers along the longitudinal direction. This restraint was not considered in the finite element model and does not affect the pylon displacements and rotations under symmetric loading, since for those load cases the relative longitudinal displacements at the bearing are negligible [197].

Two scenarios were considered for studying the effect of the longitudinal restraint in the measured pylon displacements and rotations [197]:

- Scenario 1: Connection between the piers and the girder as designed (see Table 3.1);
- Scenario 2: All relative longitudinal movements blocked.

It is noted that even when the bearings are blocked the deck can still move in the longitudinal direction due to the flexibility of the piers. As can be seen in Figure 3.18, a good approximation between the calculated and the experimental results is only achieved

when all bearings are blocked (scenario 2).

However, it should be noted that there is also an important interaction between Central Sub-Viaduct and the Lateral Sub-Viaducts when it comes to the relative displacements at the transition piers P15 and P22, an effect which was not modelled in the considered scenarios. Finally, it should be stressed that the blocking of the relative longitudinal movements in the bearings does not introduce significant changes in the calculated displacements and rotations of the girder presented before and in the cable forces presented in next section.

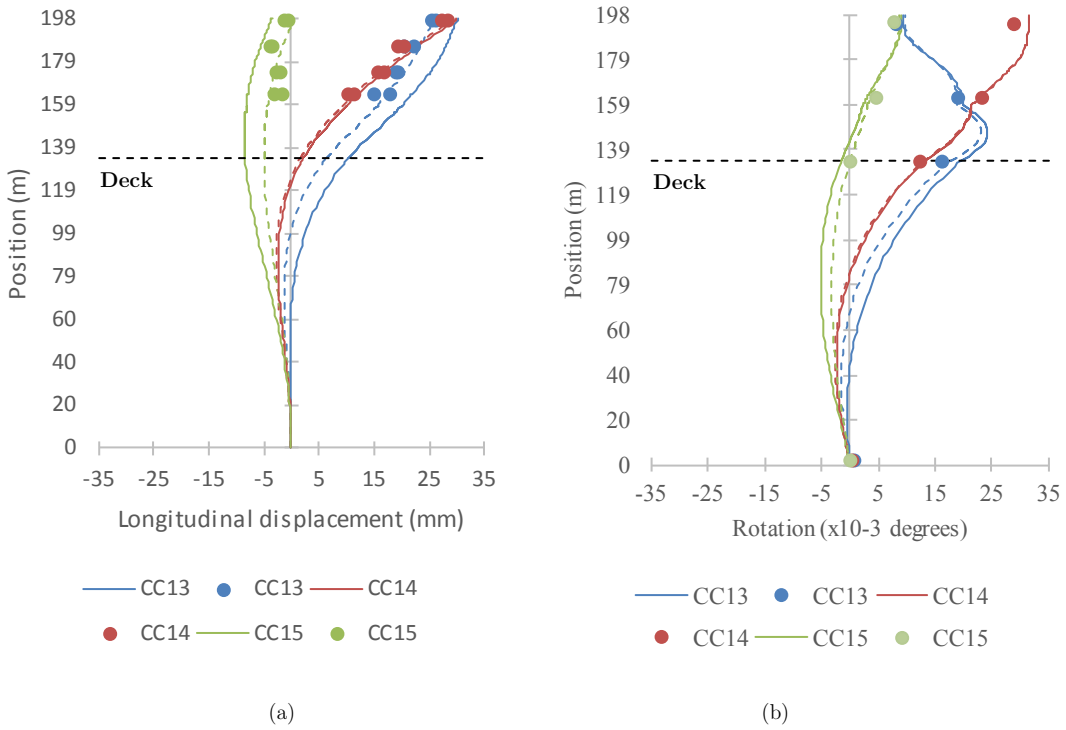

Figure 3.18 – Calculated (lines – scenario 1; dashed lines – scenario 2) versus measured (dots) (a) lengthwise horizontal displacements and (b) rotations for pylon P18: load cases CC13 to CC15.

3.5.3.3 CABLE FORCES

In general, the calculated cable forces variations follow the observed cable force variations (see Figure 3.19). However, for some of the load cases the observed cable forces variations are slightly smaller than those calculated. This behaviour becomes more evident in the influence lines of the cable stay forces presented in Figure 3.20. Although the experimental and the calculated cable force influence lines have a similar shape, the variations in the cable forces predicted by the finite element model overestimate the measured values.

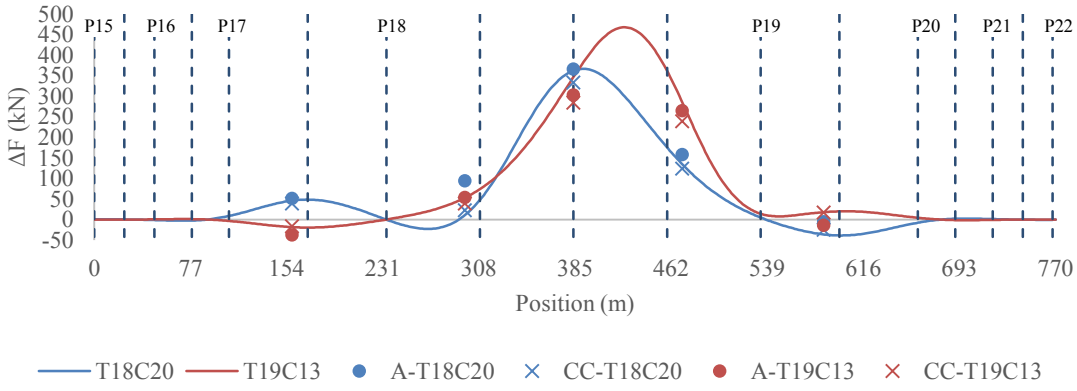

Figure 3.19 – Calculated (lines) versus experimental (dots and crosses) cable forces variations for stay-cables T18C20 and T19C13.

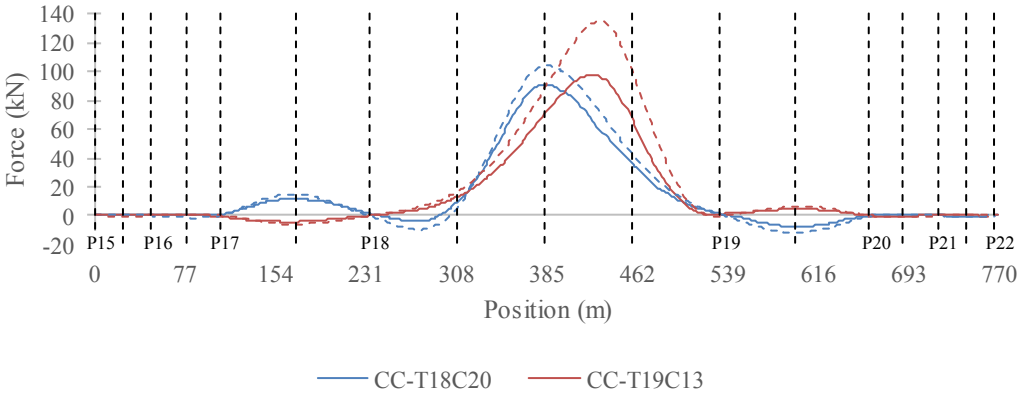

Figure 3.20 – Calculated (dashed lines) versus measured (lines) influence lines for cable forces. The influence lines refer to two pairs of 30ton trucks crossing the bridge side by side.

3.5.3.4 BEARING DISPLACEMENTS

The observed bearing displacements in the transition piers of the Corgo Bridge during the static load cases CC12 to CC16 are presented in Figure 3.21 where a comparison is made with the expected relative displacements considering the theoretical unrestrained behaviour of the bearings in piers P15, P16, P21 and P22 as obtained from the numerical analysis. Therefore, the following unexpected behaviours were observed:

- The measured relative longitudinal displacements at both expansion joints are significantly smaller than those calculated, which confirms that in fact the longitudinal movement at the bearings is restrained. This confirms the findings reported in section 3.5.3.2 where the longitudinal displacements and rotations of the piers during the load test are examined and shown to depend on the restraint

provided by the supports;

- Looking in more detail the measured relative displacements shown in Figure 3.21 and Figure 3.22 (c) and (d), it is possible to observe an interdependency between the relative displacements measured at the bearings of the Central sub-viaduct and the Lateral sub-viaducts. As the latter was not being loaded, this can only be due to the fact that the bearings are partially restrained, possibly due to friction, thereby leading to longitudinal displacements of the piers over which the expansion joints are located. In this case, the force required to move the piers P15 and P22 is smaller than that required to overcome the friction at the bearings. It is noted that in the case of the joints over pier P22, the relative displacements of the East sub-viaduct (unloaded) are even larger than those of the central sub-viaduct (under loading) (see Figure 3.21 (b));

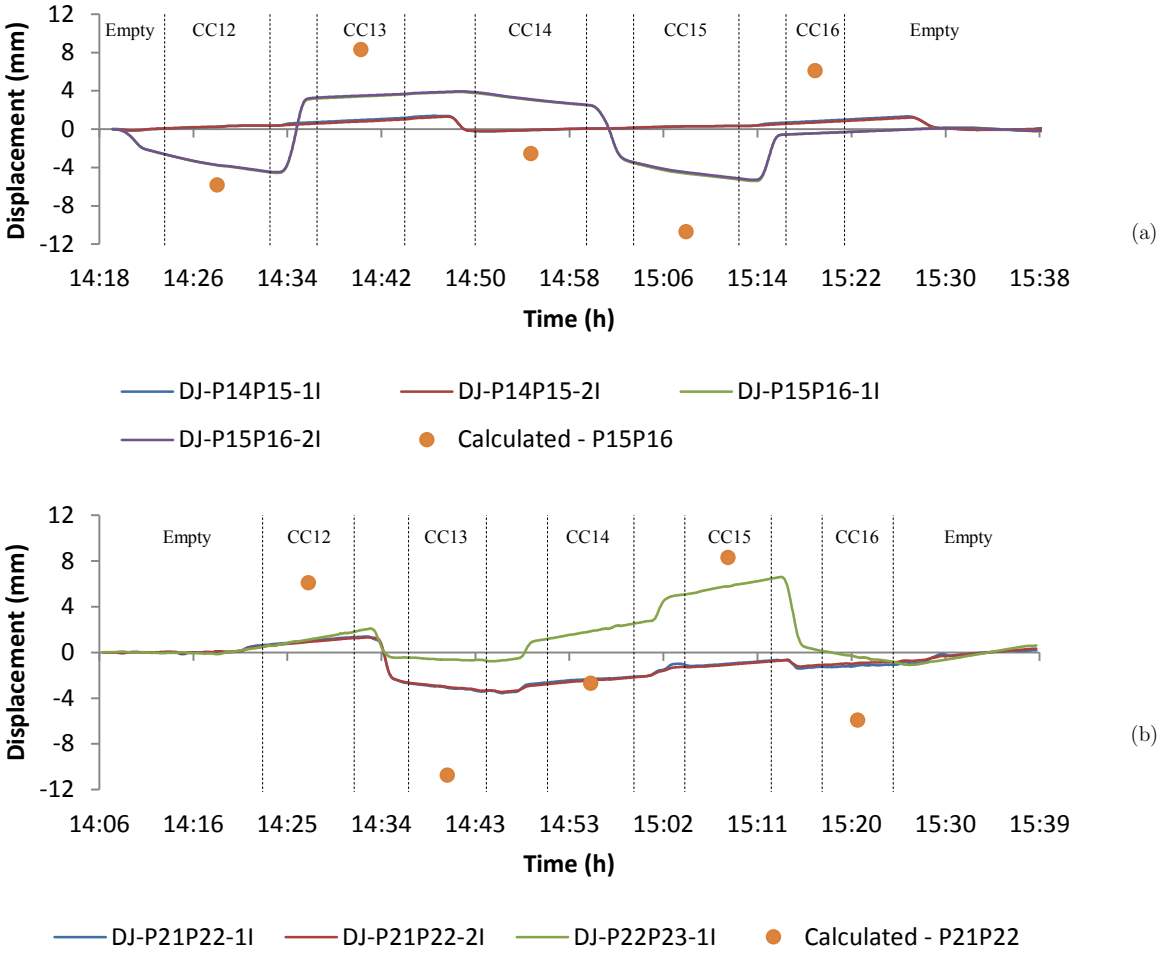

Figure 3.21 – Bearing displacements during the load test: (a) pier P15; (b) pier P22.

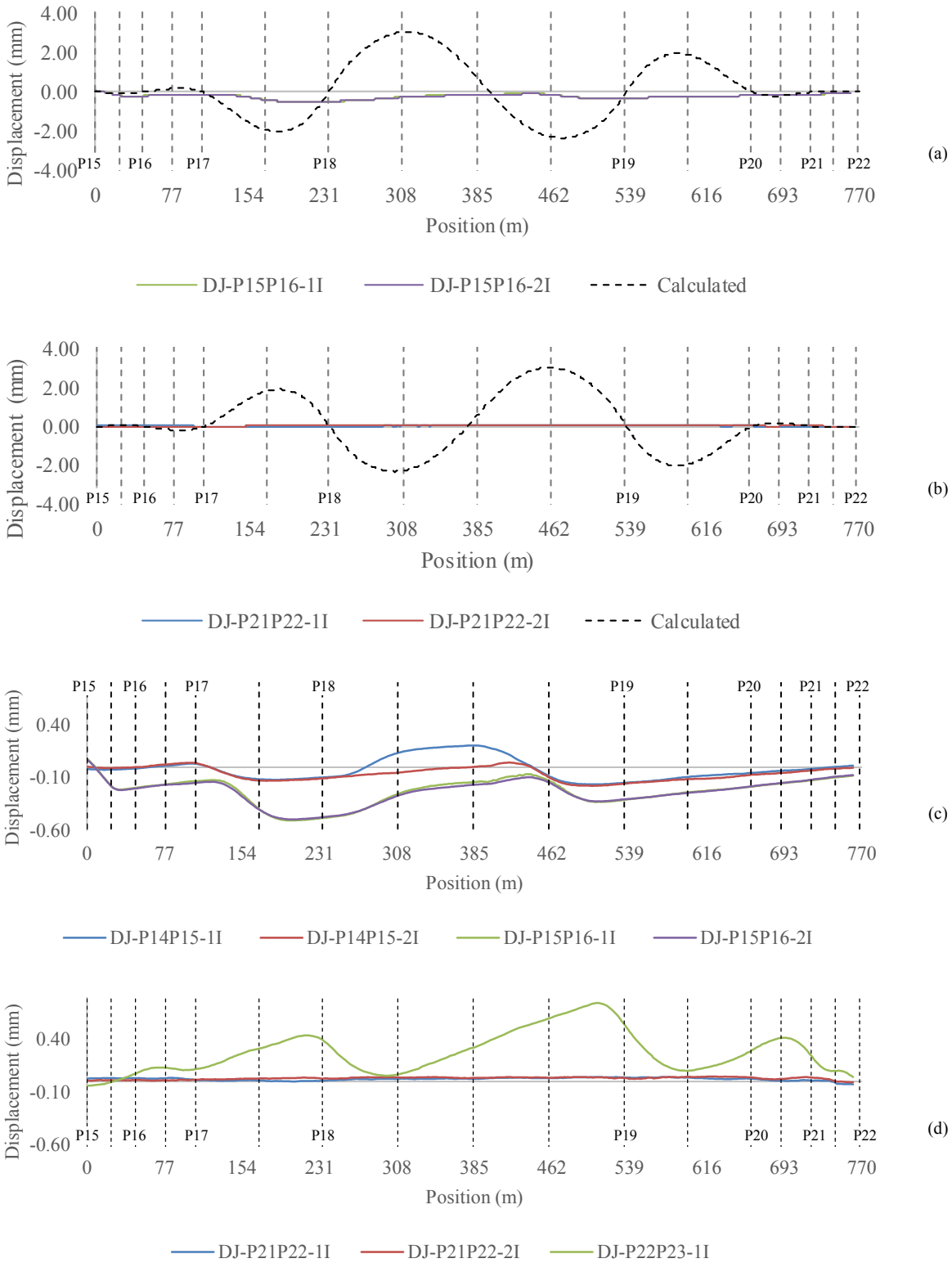

Figure 3.22 – Influence lines of the bearing displacements: (a) experimental versus calculated for DJ-T-P15P16; (b) experimental versus calculated for DJ-T-P21P22 (c) pier P15 (experimental), (d) pier P22 (experimental). The influence lines refer to two pairs of 30ton trucks crossing the bridge side by side.

Finally, corrective measures were taken in the pot bearings in order to correct the detected anomalies. However, it should be borne in mind that a restriction to traffic loads does not mean that the same level of restriction in the bearings exists for thermal loads since they have a slow evolution in time and lead to larger longitudinal movements.

3.6 Concluding remarks

This chapter briefly presented the Corgo Bridge, used as case study in this thesis. The structural monitoring system installed to follow the construction stages and the long-term behaviour of the bridge was described. A special focus on the dynamic structural monitoring system of the stay cables was given for two reasons. First, it is the part of the structural monitoring system where the author had an active intervention, leading the process of design, development and implementation. Second, the data gathered from this sub-system was revealed to be the most important for damage detection and localisation (at least in the simulated damaged scenarios on Chapters 5 and 6). The developed structural monitoring system of the stay cables was demonstrated to be robust since there are few gaps in the data during 3.5 years and they are essentially due to power outages.

The developed mechanical finite element model of the Corgo Bridge was presented. This model was used to follow the construction stages, to analyse the structural behaviour during the load test, to follow the results collected by long-term monitoring system, which are examined in Chapter 4, and to simulate damage scenarios in order to test the damage detection and localisation methodologies developed in Chapters 5 and 6.

A good fit between the experimental and calculated values for the different load cases of the load test was generally obtained for girder deflections and rotations. Major differences between the calculated and measured values were found for the rotations and horizontal displacements of the pylons, especially for non-symmetric load cases. Moreover, it was found that for those load cases, the pylon displacements and rotations are highly dependent on the level of longitudinal restraint conferred by the piers, namely the level of friction on their bearings. This longitudinal restraint was confirmed by the observed bearing displacements during the load test. Moreover, interdependency between the relative displacements measured at the bearings of the Central sub-viaduct and the Lateral sub-viaducts was

observed. As the latter was not being loaded, this can only be due to the fact that the bearings are partially restrained, possibly due to friction, thereby leading to longitudinal displacements of the piers over which the expansion joints are located. Corrective measures were taken after the load test in order to correct the identified anomalies.

The calculated cable forces variations were generally larger than those measured, although the shape of both experimental and calculated results are similar. It should be referred that the cable forces as well as the girder deflections and rotations revealed to be insensitive to the level of longitudinal restraint provided by the piers. This means that those sensors are insensitive to damages or abnormal levels of friction in the bearings.

Chapter 4*

STRUCTURAL RESPONSE OF THE CORGO BRIDGE UNDER THERMAL LOADS

4.1 Introduction

The characterization of the structural response to daily and seasonal temperature variations has an important role in the assessment of the structural condition of bridges. Several long-term monitoring studies have reported that temperature variations can induce strains, displacements or rotations of the same order of magnitude, or even larger, than those due to dead or live loads [2, 18, 24, 106, 112, 118, 159]. Taking the example of the Corgo Bridge, the vertical mid-span displacement measured during the load test when four 30ton trucks crossed the bridge side by side is similar to the daily fluctuations that are consistently measured during the summer period due to the sole effect of the daily temperature variations. Additionally, and contrary to traffic or wind loads, the temperature variations act continuously and the continuous observation of the corresponding structural response provides abundant data that can be used to detect the occurrence of modifications in the

* This chapter is based on the paper: Sousa Tomé, E., M. Pimentel, and J. Figueiras (2018). *Structural response of a concrete cable-stayed bridge under thermal loads.* Engineering Structures. Vol. 176: p. 652-672.

structural behaviour, enabling the timely adoption of proactive conservation measures.

Besides a good understanding of the temperature effects [230], the detection of changes in the structural response due to small damages requires suitable algorithms for filtering out the environmental and operational effects from the monitoring data [184, 223]. In the scope of structural health monitoring (SHM) this is usually designated as data normalisation [66]. One of the commonly adopted approaches relies on regression-based algorithms, which aim to remove the environmental and operational effects by means of relationships between the measured actions and the measured structural responses [91, 231]. The effectiveness of these methods relies on the proper characterization of the thermal action on the bridge. The temperature components (uniform and differential) and structural parts that contribute more to a given structural response have to be identified and temperature sensors have to be judiciously placed to obtain the best possible estimates of the relevant temperature components. Moreover, even if the application of the data normalisation methods may not strictly require the physical interpretation of the bridge structural behaviour, in many instances it is desirable to have a critical assessment of the data, with a physical and quantified interpretation of the measurements.

As reported in [21, 111], the temperature distributions inferred from in-situ measurements can be used as input into mechanical finite element models for the simulation of the structural behaviour of real bridges under transient thermal loading. However, this may require a sufficiently dense network of temperature sensors, which is seldom available. In general, the temperature field needs to be computed if an accurate representation is to be achieved.

Many studies can be found focusing on the characterization of the temperature fields at the cross-section level using transient thermal analyses [13, 53, 59, 75, 103, 117, 139, 159, 185, 234]. The two-dimensional transient temperature field in a cross-section can be computed using numerical methods – most often the finite difference or the finite element method – to solve the heat balance differential equation considering the boundary conditions defined by the ambient temperature, wind velocity, solar and longwave radiation. Fewer studies can be found where the thermal and the structural analysis of the bridge are integrated to provide an insight on the effects of the temperature variations on the structural behaviour.

In this case, coupled thermo-mechanical analyses can be performed. This coupling is one-directional in the sense that the thermal field can be assumed to be independent of the state of stress, and the latter can be directly determined from the former via an appropriate mechanical model of the bridge. Following this line of thinking, Westgate *et al.* [212] studied the temperature distribution and the associated structural response of a steel suspension bridge, the Tamar Bridge. They developed a 3D finite element model of the entire bridge, in which both thermal and mechanical analyses were performed. The thermal boundary conditions were defined using the readings from the structural monitoring system, being the solar radiation estimated from the cloud cover. Recently, Zhu and Meng [235] presented thermo-mechanical analysis of a steel cable-stayed bridge, the Qingling Meng Bridge. A three-dimensional sunlight-sheltering algorithm was used to model complex sheltering effects, being the solar radiation estimated using an empirical model.

In many bridges it is sufficient to perform a 2D thermal analysis of the different cross-sections and to assume that the temperature field is invariant along the longitudinal axis of the elements, thus largely simplifying the problem. Xia *et al.* [220] presented a study of the temperature distribution and associated structural response of a long-span steel suspension bridge, the Tsing Ma Bridge. A 2D thermal analysis of the main structural elements was developed. The boundary conditions of the thermal problem were established using the ambient temperature and the wind velocity obtained from the monitoring system of the bridge and an empirical solar radiation model. The structural response (strains and displacements) of the bridge was obtained using a global finite element model wherein the calculated temperature distributions were introduced.

No study similar to those referred above could be found in the literature concerning concrete bridges. Given the lower thermal conductivity and higher specific heat of concrete when compared to steel, the spatial distribution and the time evolution of the temperatures within each cross-section are rather complex. The direct use of the temperature readings to characterize the thermal action is not possible unless an unrealistic large number of thermometers is adopted. In this context, an efficient procedure for a detailed and realistic analysis of the structural response of concrete bridges subjected to thermal loads is proposed. The thermal and mechanical problems are solved in a sequential manner and

resorting to independent numerical models. Accurate models for the conductive, convective and radiative heat transfer mechanisms are described and guidance is provided for the selection of the relevant material properties and definition of the boundary conditions based on field data. The obtained transient temperature fields are decomposed into uniform, differential and nonlinear components. The first two components are introduced into the finite element model of the bridge to obtain the time-histories defining the structural response to the temperature variations, which can be superposed to that due to the long term effects such as concrete creep, shrinkage and relaxation.

In order to demonstrate the effectiveness of the proposed procedure, it is applied to the Corgo Bridge. The measured and calculated hourly temperatures, deflections, bearing displacements, rotations and stay-cable forces are compared during a period of 17 months. The long-term behaviour of the bridge is discussed and the relative contribution of each temperature component to a given structural response is disclosed. A discussion on the optimal deployment location of the embedded temperature sensors – considering a few number of sensors per section – in order to have better estimators of the temperature components using the temperature readings is also presented.

4.2 Methodology

One of the objectives of this work is the systematization of a methodology that is generally applicable to large concrete bridges, with a reasonable balance between accuracy and simplicity of the involved procedures. In general, the global structural analysis of large span concrete bridges is made resorting to beam finite element models. The use of this type of model for the mechanical analysis becomes very attractive, not only due to the reduced number of degrees of freedom, but also because it is generally available from previous design /assessment stages. The thermal analysis is performed separately, as shown in Figures 4.1 and 4.2 , which schematically summarize the proposed methodology.

In a first stage, a set of representative cross-sections is selected and the thermal problem is solved as illustrated in Figure 4.1 to find the corresponding time histories of the uniform, $T_u(t)$ and differential, $\Delta T(t)$, temperature components. These are used as inputs into the mechanical model. The transient temperature distribution within each cross-section is

determined by solving the thermal problem through two-dimensional finite element analyses. The number of analysed cross-sections depends on the geometry of the bridge, on the variation of the geometrical properties along the longitudinal axes of the structural elements (girder, piers, etc.) and on the sheltering effects governing the solar radiation reaching the surfaces of the structural element. The boundary conditions of the thermal problem are defined by the air temperature, effective sky temperature, wind speed and solar radiation on tilted planes. The latter is computed from the solar radiation on the horizontal plane, usually available from meteorological stations, through a solar radiation model. The effective sky temperature is obtained through an empirical model of the longwave radiation. The temperature inside the box girder was considered equal to the readings of the air

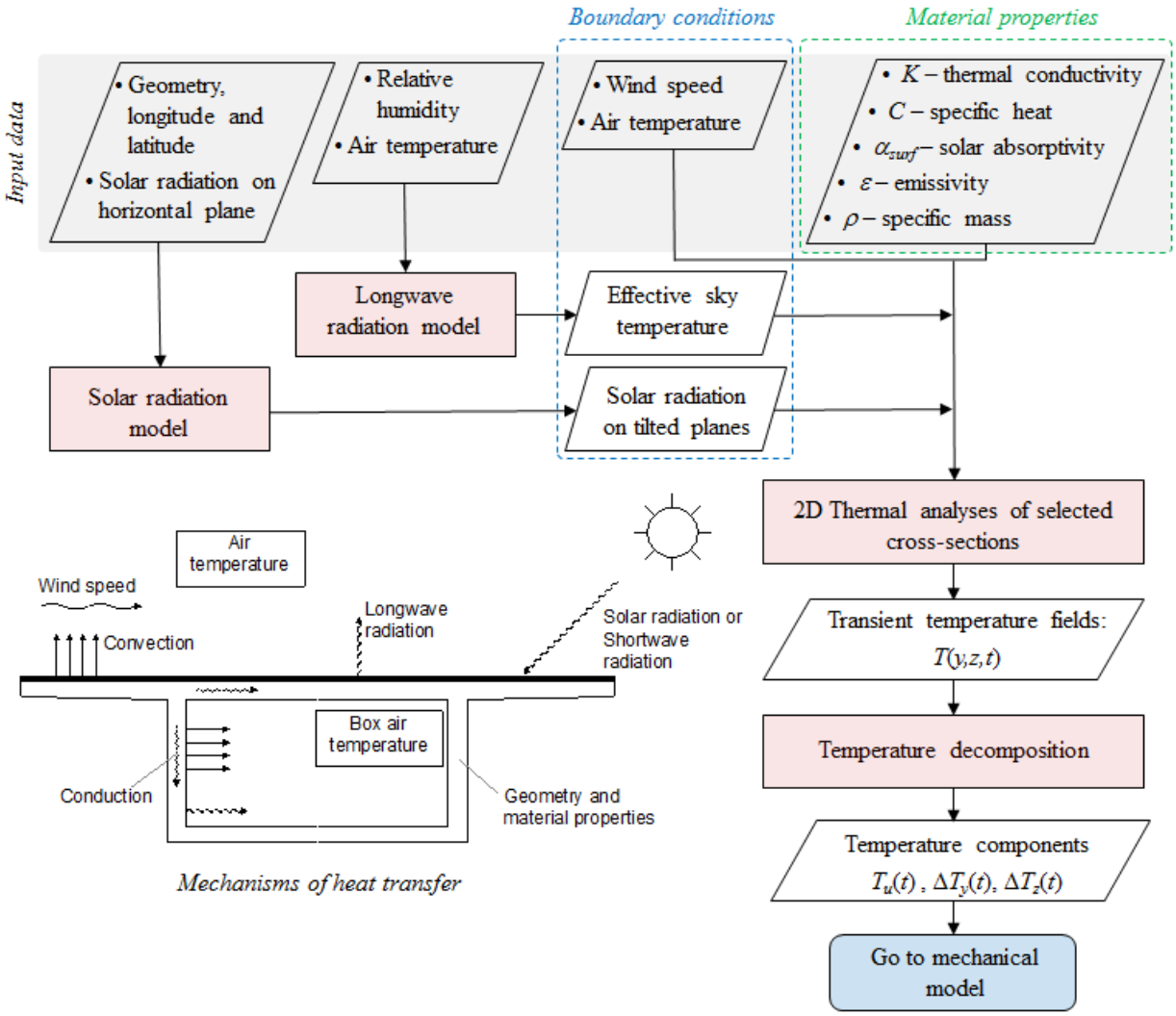

Figure 4.1 – Flowchart showing the methodology adopted to solve the thermal problem and obtaining the time histories of the uniform, $T_u(t)$, and differential, $\Delta T(t)$, temperature components.

temperature inside the box girder obtained from the structural monitoring system. However, in case these are not available, the air inside the box girder can be simulated with finite elements as discussed in [74, 159, 234].

The mechanical problem is solved in a second stage, as illustrated in Figure 4.2. The time-dependent rheological behaviour of the materials – concrete creep and shrinkage, the evolution of the elasticity modulus and prestress steel relaxation – and the construction process must be taken into account and included in the model. If linear structural behaviour is assumed, the principle of superposition of effects can be applied as schematically indicated in the figure. Therefore, the calculated structural responses can be determined based on unit temperature loadings, which are multiplied by the previously obtained uniform and vertical linear temperature gradient components.

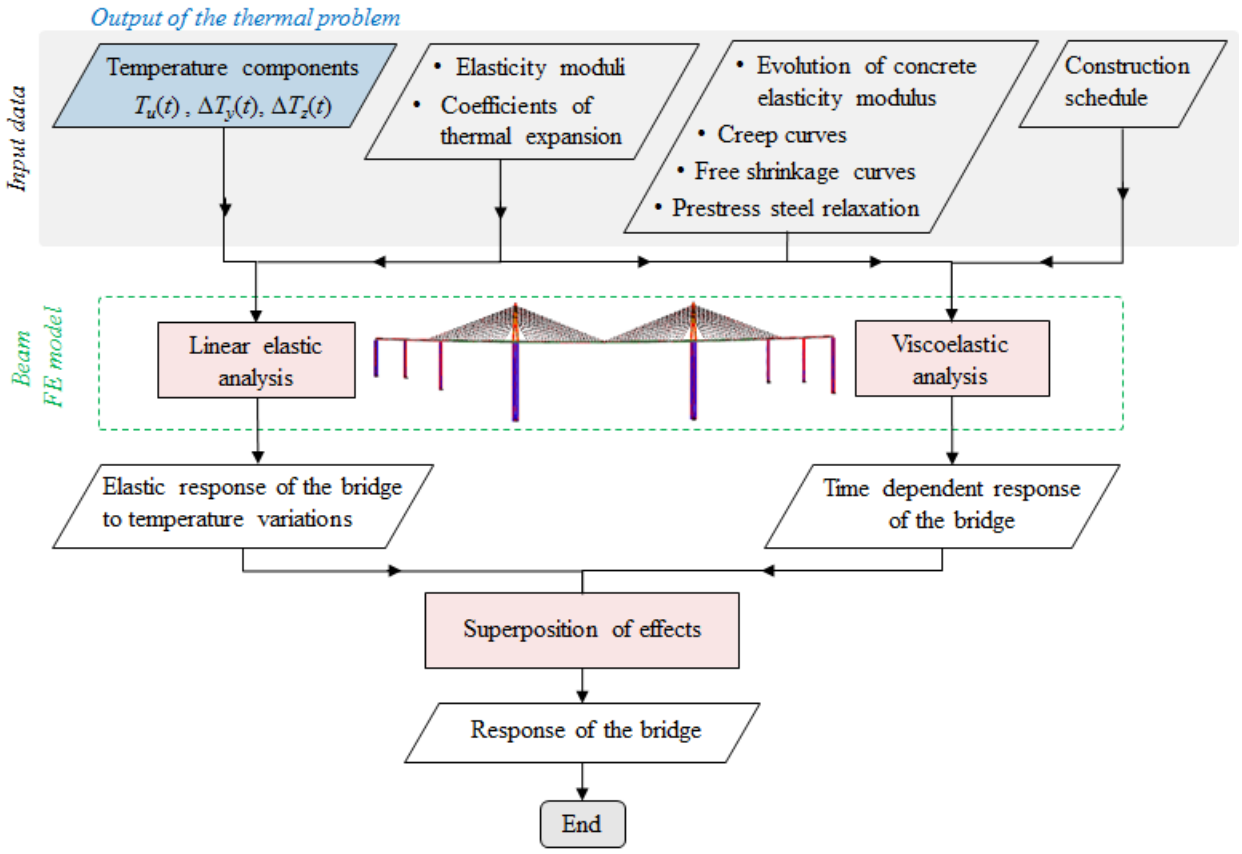

Figure 4.2 – Flowchart showing the methodology adopted to solve the mechanical problem.

In this procedure, the mechanical properties - most notably the elasticity modulus of concrete - are considered independent of the temperature. If this simplification is not

acceptable and reliable models relating the elasticity modulus with the temperature are available, this effect can be easily introduced. In addition, if the temperature fields are simulated since the construction, it is possible to refine the calculation of the maturity variable (usually the equivalent time, t_{eq}, determined using the Arrhenius equation) governing the kinetics of creep, shrinkage and elasticity modulus. This level of refinement was not adopted in the analysis presented herein.

4.3 THERMAL PROBLEM

4.3.1 GENERAL

Heat can be defined as the energy transfer owing to temperature differences between different systems in communication. Usually, and for the sake of simplicity, the heat transfer problem is split in three main mechanisms, - conduction, convection and radiation - , schematically illustrated in Figure 4.1. The thermodynamic equilibrium of hardened concrete is expressed by the heat balance equation

$$k\nabla\cdot(\nabla T)=\rho c\dot{T} \tag{4.1}$$

where k is the thermal conductivity [W.m^{-1}K^{-1}], T is the temperature [K], ρ is the material-specific mass [kg/m^3] and c is the specific heat [J/(kg.K)], being the product ρc usually termed as the volumetric heat capacity. The convective and radiative heat transfer occurring at the surfaces define the boundary conditions.

The Newton's law of cooling can express the convective heat transfer between a surface and the environment [92]:

$$q''_{h,conv}=h_c(T_s-T_a) \tag{4.2}$$

where $q''_{h,conv}$ is the convective heat flux [W/m^2], h_c is the convection heat transfer coefficient [W/(m^{3}K)], and T_s and T_a are the surface and fluid temperatures [K], respectively. The radiative heat transfer is usually divided into longwave radiation and solar (or shortwave) radiation. The former is due to the temperature differences between two bodies, as for instance the concrete and the air [65], and is expressed by:

$$q''_{h,rad} = \varepsilon\sigma(T_s^4 - T_{sur}^4) \tag{4.3}$$

where $q''_{h,rad}$ is the heat flux due to longwave radiation [W/m²], ε is the emissivity of the surface [-], σ is the Stefan-Boltzmann constant ($\sigma = 5.67\times10^{-8}$ $Wm^{-2}K^{-4}$) and T_{sur} is the surroundings temperature [K]. For a horizontal surface facing the sky, the surroundings temperature can be assumed as the effective sky temperature T_{sky}, which can be obtained directly from measurements of the downward atmospheric longwave radiation or from empirical models [126, 205]. The adopted empirical model to determine T_{sky} is described in Appendix B. For non-horizontal surfaces (such pier walls), T_{sur} can be assumed to be equal to T_a since those surfaces are mainly influenced by longwave radiation emitted by the ground and adjacent obstacles such as vegetation and buildings.

Even though being governed by the same mechanisms as the longwave radiation, the solar radiation is usually considered as a heat source depending on the time of the day, the day of the year, cloudiness of the sky, orientation, longitude and altitude of the surface [221]. The heat flux due to solar radiation, i.e., the total amount of solar radiation absorbed by a surface is determined as:

$$q''_s = -\alpha_{surf} I_T \tag{4.4}$$

where I_T is the total solar radiation on a tilted plane, α_{surf} is the solar absorptivity coefficient of the surface material ($0 \le \alpha_{surf} \le 1$). The coefficients $\alpha_{surf} = 0.5$ and $\alpha_{surf} = 0.9$ are usually adopted for concrete and asphalt, respectively [118]. I_T can be calculated from the measured solar radiation on a horizontal plane, *I*, as described in Appendixes C and D, or using empirical models of solar radiation.

4.3.2 Temperature distribution decomposition

As depicted in Figure 4.3, the nonlinear temperature distribution over a cross-section can be split into a uniform component (T_u), a linearly varying temperature difference component along the *y*-*y* axis (ΔT_y), a linearly varying temperature difference component along the *z*-*z* axis (ΔT_z), and a nonlinear temperature difference component (T_{NL}),. While the uniform component produces an elongation along the longitudinal axis of the beam, the differential

components induce curvatures. The nonlinear temperature difference component originates a self-equilibrated stresses distribution due to the fact that the cross-section is restrained from warping and remains plane. These stresses occur even in statically determined structures.

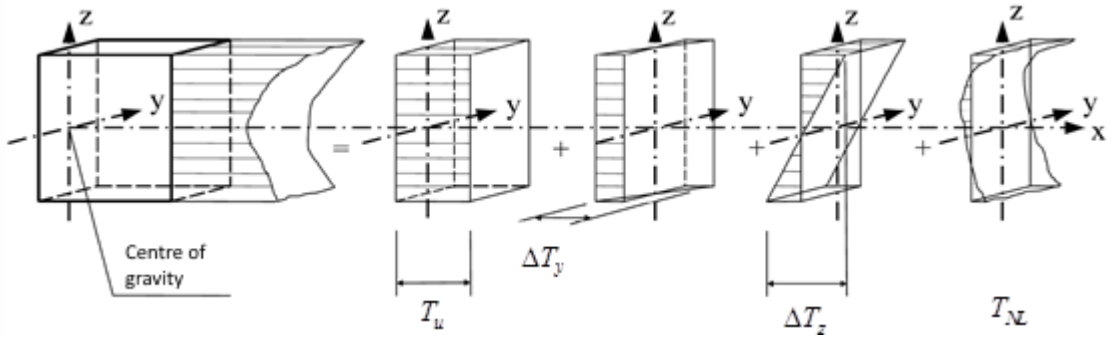

Figure 4.3 – Temperature components of a temperature profile in a generic section. Taken and adapted from [28].

While the uniform temperature component is mainly affected by the seasonal air temperature variations, the linear and nonlinear temperature components are mainly governed by short-term variations governed by solar radiation and daily temperature variations [119].

For a generic and fully restrained section with area A submitted to a temperature distribution T originating a stress field σ, the axial force N and the bending moments M_y and M_z are:

$$N = \int_A \sigma \, dA = E\alpha \int_A T \, dA \tag{4.5}$$

$$M_y = \int_A \sigma z \, dA = E\alpha \int_A Tz \, dA \tag{4.6}$$

$$M_z = \int_A \sigma y \, dA = E\alpha \int_A Ty \, dA \tag{4.7}$$

where E is the Young's modulus and α is the thermal dilatation coefficient. As $N = E\alpha T_u A$ and $\frac{1}{\rho} = \frac{M_y}{EI} = \frac{\alpha \Delta T_z}{h_y}$ the following equations can be derived:

$$T_u = \frac{1}{A} \int_A T \, dA \tag{4.8}$$

$$\Delta T_y = \frac{h_y}{I_z}\int_A Ty\, dA \tag{4.9}$$

$$\Delta T_z = \frac{h_z}{I_y}\int_A Tz\, dA \tag{4.10}$$

where h_y and h_z are the cross section width and depth, and I_y and I_z are the moments of inertia of the section about the y and z axes (assumed a set of principal axes). The nonlinear temperature component is then obtained by:

$$T_{NL} = T - T_u - \Delta T_y \frac{y}{h_y} - \Delta T_z \frac{z}{h_z} \tag{4.11}$$

In general the calculation of the integrals in equations (4.8)-(4.10) over a generic section requires the adoption of numerical methods, such as the finite element method. The formulation for triangular finite elements can be found in Appendix **E**.

4.4 Thermal finite element models

Considering that the air temperature, solar radiation, wind velocity and geometry of the cross-section are constant along the longitudinal direction of the deck [13, 60, 74, 75, 221, 234], only one cross-section of the box-girder needs to be modelled. For the pylons and piers, a similar assumption is made, i.e., the temperature variation along the longitudinal axis of the pylons and piers it is assumed to be negligible. As a result, seven representative cross-sections were modelled (see Figure 4.4):

- One cross-section of the girder.
- Three sections for the pylons: one representative of the bottom part of the pylon (below the deck), the second one of the "legs" above deck, and the third one of the top part of the pylon.
- Three sections for the piers: the first one of piers P15 and P22, the second one of piers P16 and P21 and the last one of piers P17, P20.

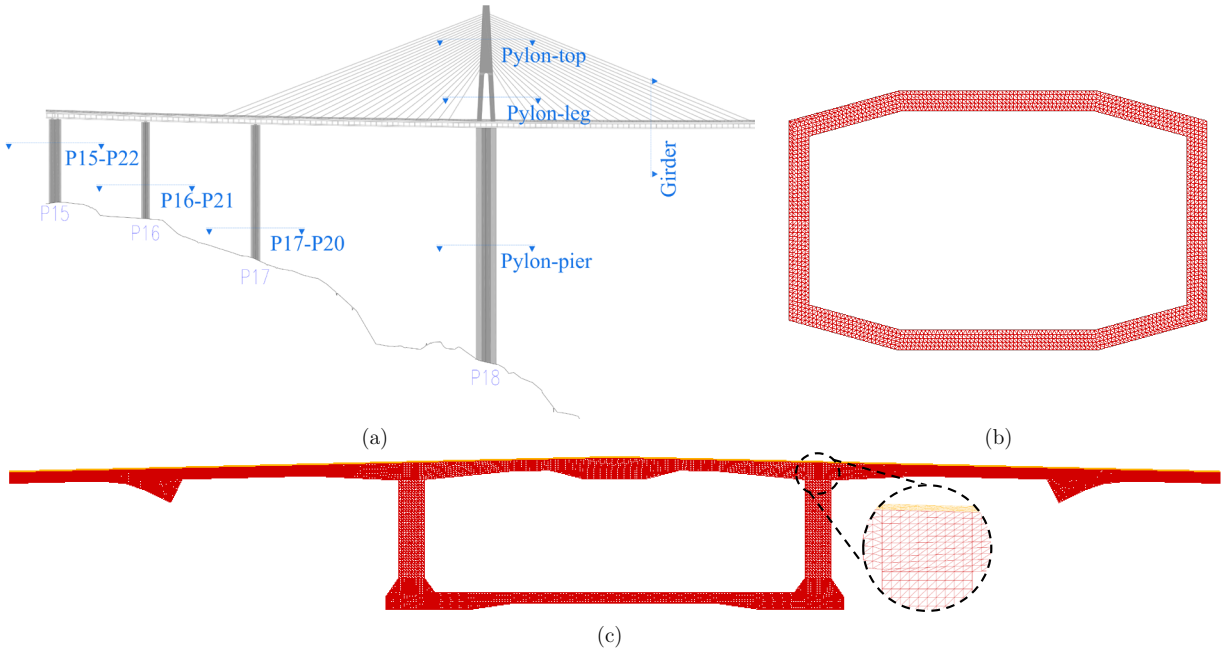

Figure 4.4 – Thermal analysis: (a) Location of the representative sections; (b) Finite element model of the cross-section of the piers P15 and P22; (c) Finite element model of the box-girder. A 4cm thick asphalt layer is included.

The thermal properties of concrete depend on the properties and proportions of its constituents. The concrete conductivity and specific heat were determined considering the concrete mixture adopted in the Corgo Bridge. As for the 4cm thick asphalt layer on top of the deck, values commonly recommended in the literature were adopted, as summarized in Table 4.1.

Table 4.1 – Adopted material properties.

Parameter	Symbol	Unit	Concrete	Asphalt
Conductivity	k	$W.m^{-1}K^{-1}$	2.5	0.83
Specific heat	c	$J.kg^{-1}.K^{-1}$	836	880
Specific mass	ρ	kg/m^3	2364	2200
Solar absorptivity	α_{surf}	-	0.50	0.90
Emissivity	ε	-	0.88	0.92

Concerning the boundary conditions, the air temperatures T_a were taken directly from the monitoring system of the Corgo Bridge: the external air temperature and the air temperature inside the box-girder are both measured at sections T-P17P18d and T-P19d; and the air temperature inside the pylons and piers was assumed equal to the readings obtained from the thermometers located inside the pylon P18 (section P-P18a). Since the monitoring system of the Corgo Bridge provides no data concerning wind velocity, v, and

solar radiation on horizontal plane, I, the measurements from Folgares [181] meteorological station were adopted. This station is located 40 kilometres east from the Corgo Bridge. The total solar radiation on a title plane I_T was determined according to the surface solar exposure and the solar geometric relations presented in Appendix C using the isotropic diffuse model (see Appendix D). The longwave radiation was considered according to equation (4.3). In the case of horizontal surfaces facing the sky, the effective sky temperature T_{sky} was determined using the model described in Appendix B, using the air temperature and relative humidity values measured by the bridge monitoring system. The convection heat transfer coefficient was assumed to vary with the wind velocity, v, according to the equation proposed by Jonasson [101]:

$$h_c = \begin{cases} 5.6 + 3.95v, & v \leq 5\text{m/s} \\ 7.6v^{0.78}, & v > 5\text{m/s} \end{cases} \tag{4.12}$$

Inside the box-girder, piers and pylons the convection heat transfer coefficient was assumed equal to 5.6 W/(m.K) (which, according to the equation above is equivalent to consider a null wind velocity inside the box-girder). The transient thermal analyses were performed in the finite element code TNO DIANA [204] using the three-node triangular finite isoparametric elements T3HT, with an average width of 6cm, and a time step of one hour, which is the smallest time step of the data available from the meteorological station.

The stay cables of the Corgo Bridge are parallel strand cables, being each individual strand protected by an extruded high density polyethylene (HDPE) sheath. The strand bundle is still protected by a polyethylene cylindrical pipe, being the individual strands surrounded by air. This makes the numerical simulation of the corresponding thermal field an extremely complex task. Therefore, the measured temperature on the stay cable T19C13 was assumed to be representative of the temperature of all the stay cables of the suspension system.

4.5 Results and discussion

4.5.1 Comparison with measured temperatures

The validation of the thermal finite element models was made comparing the temperature time series measured in the sensors embedded in the concrete with the corresponding calculated values, during a period of 17 months. The results obtained for the deck cross-

section T-P26 are here discussed and depicted in Figure 4.5. The temperature sensors are located 7cm from the nearest concrete face, as shown in Figure 3.1 (b).

A good fit between the calculated and the experimental temperatures was obtained, particularly for the sensors placed in the bottom slab of the box-girder (Figure 4.5 (b)), where the differences between the calculated temperature and the readings are generally below 1°C. For the sensors placed on the top slab of the box-girder, the differences are mostly below 2°C. In order to explain the differences, the influence of eventual deviations between real and planned temperature sensor position was analysed. The results obtained shifting the position of the temperatures sensors 3cm up and down are shown in Figure 4.6 for typical summer and winter weeks. It can be seen that while the differences remain during winter, a better fit is achieved during summer when the sensor is assumed to be shifted 3cm up the planned position. However, larger differences between experimental and calculated values should always be expected for the sensors ST-T-P26-1S/2S since they are placed near to the upper surface of the top slab and are more sensitive to boundary conditions of difficult definition, such as the radiative heat transfer. In particular, the consideration of the longwave radiative heat transfer was crucial to obtain accurate estimations of the temperatures measured in the top slab during wintertime. The simulations with $T_{sur} = T_a$ instead of $T_{sur} = T_{sky}$ in eq. (3) are shown in Figure 4.7, clearly depicting the importance of the accurate simulation of radiative cooling effects occurring on the top surface of the slab.

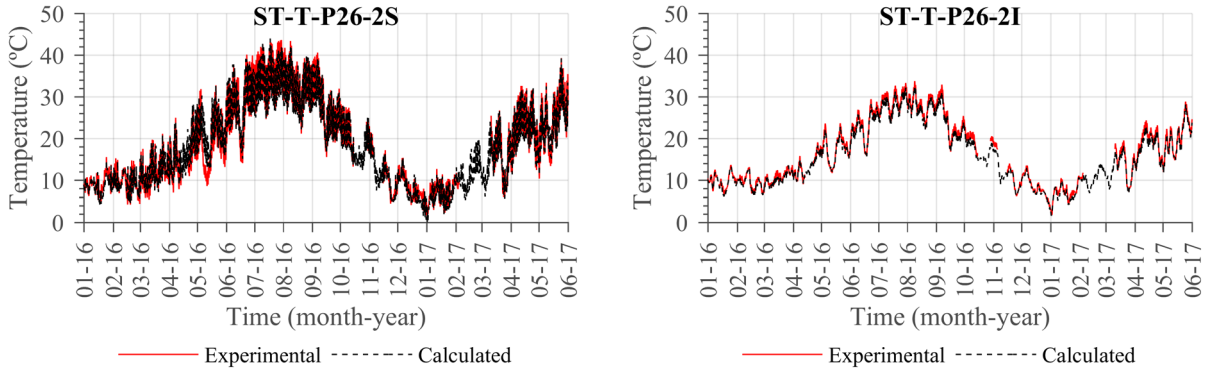

(a) (b)

Figure 4.5 – Calculated versus experimental temperatures in cross-section T-P26: (a) sensor ST-T-P26-2S, (b) sensor ST-T-P26-2I.

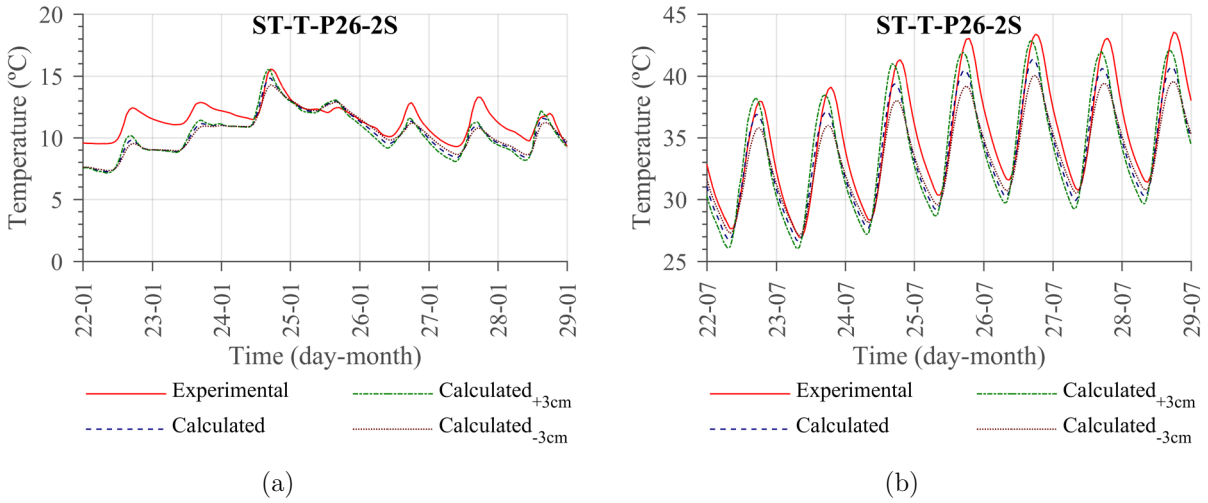

Figure 4.6 – Calculated versus experimental temperatures in sensor ST-T-P26-2S: (a) detail for a typical winter week – 22-29/1/2016 and (b) detail for a typical summer week – 22-29/7/2016).

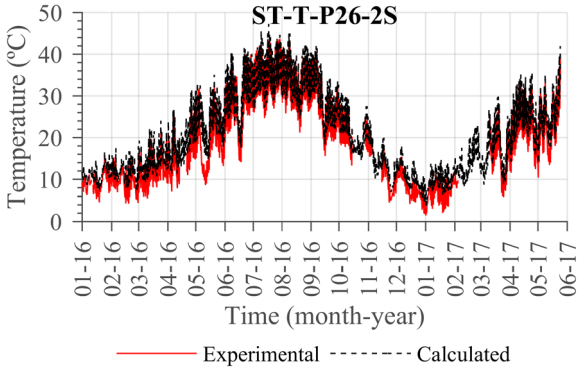

Figure 4.7 – Effect of radiative cooling on the top slab. When Tsky is not considered in eq. (3) the fit between the measured and calculated temperatures is clearly affected.

4.5.2 Temperature components

4.5.2.1 Girder

The uniform temperature component T_u and the vertical linear temperature gradient component ΔT_z for the box-girder are depicted in Figure 5.8. Both temperature components exhibit clear daily and seasonal trends. As expected, the daily temperature variations and the daily mean values are larger during the summertime.

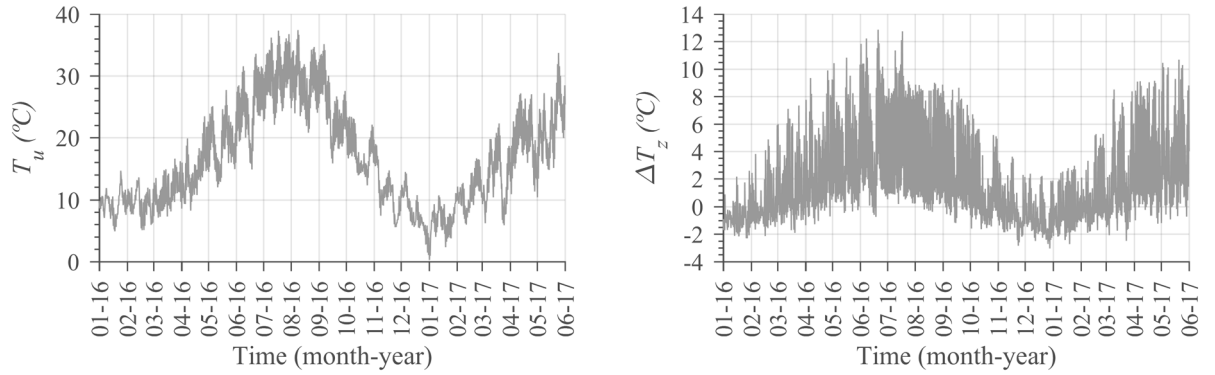

(a) (b)

Figure 4.8 – Uniform temperature component (a) and vertical linear temperature gradient component (b) for the box-girder.

The average of the uniform temperature component for the first year of data is $T_{u,mean}$=17.4ºC. In the analysed period, the uniform temperature component variation $\Delta T_u = T_u - T_{u,mean}$ of the box-girder reaches the minimum of -17.1ºC in the winter (1th January 2017) and the maximum of 20.0ºC in the summer (8th August 2016), while the minimum and maximum vertical linear temperature gradient are, respectively, -3.0ºC (28th December 2016) and 12.9ºC (20th June 2016). The daily variations of both temperature components reach the maxima and minima generally at the same time instants. These values indicate that the characteristic values of the temperature components in the deck girder considered in the design have already been punctually exceeded during the analysed period.

In the context of the interpretation of the results from a structural health monitoring system, the uniform temperature component T_u is usually estimated with the average temperature of the sensors ($T_{u,sensors}$). Likewise, the vertical linear temperature gradient component ΔT_z is estimated with the difference between the temperature readings from the sensors placed in the top and bottom fibres of the cross-section ($\Delta T_{z,sensors}$). The accuracy of these estimators is examined here.

The position of the sensors in the cross-section has a significant influence on the quality of the obtained estimators. The optimal location of the sensors to estimate a given quantity is here proposed to be determined by minimisation of the mean squared differences between the standardised values of the target and estimated time-series, the latter depending on the coordinates of the sensors within the cross-section. The use of the standardised series is

justified because the estimate of the shape of the series is more relevant that its scale. Considering the girder cross-sections T-P18P19b and T-P26, each having the top slab temperature sensors placed in different positions (see Figure 3.1 (b)), considerably different estimations for T_u and ΔT_z are obtained. This is shown in Figure 4.9 where the results obtained with the optimal sensor locations are also presented. It can be concluded that the estimators obtained using the temperature readings of section T-P26 have higher quality both for the uniform temperature component and vertical linear temperature gradient component. This information is confirmed by the surface contour lines of the mean squared difference between the standardized temperature components and their estimators for different sensor positions (see Figure 4.10). The best estimator for T_u would be obtained if the pair of sensors had been placed, respectively, at a distance of 35cm and 23cm from the interior surface of the bottom and top flanges of the box-girder. In respect to ΔT_z, the best estimation would be obtained if the pair of sensors would have been placed, respectively, at a distance of 2cm and 23cm from the interior surface of the bottom and top flanges of the box-girder. This points towards the conclusion that using only two sensors it is not possible to obtain the best estimates of both T_u and ΔT_z. Ideally, it would be necessary two sensors to have the optimal estimate of T_u and another two for the estimator of ΔT_z. In both cases, between the available sensor coordinates, better estimators can be obtained using section T-P26. For this reason, hereafter the analysis is made considering only the results of section T-P26 in order to evaluate the quality of the available estimators.

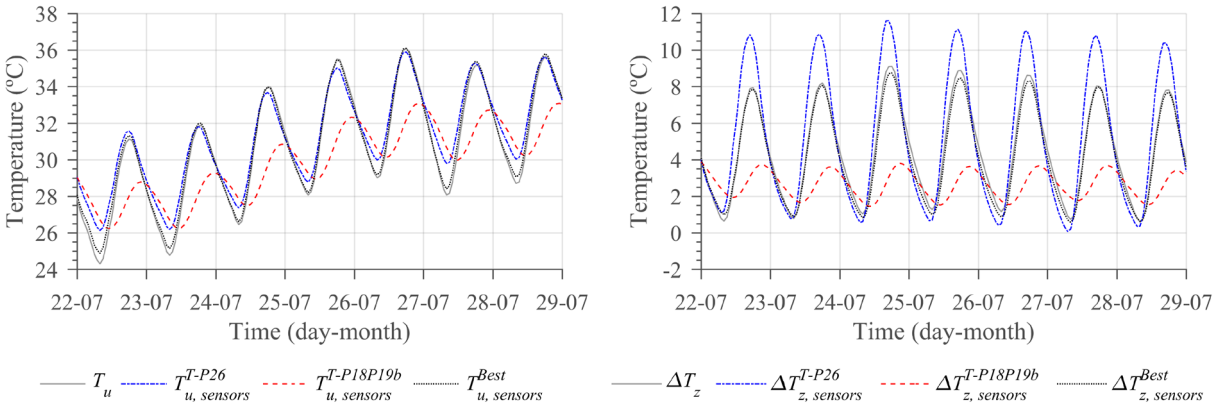

(a) (b)

Figure 4.9 – Uniform (a) and linear vertical gradient (b) temperature components for a week in summer (22nd-29th July 2016). Comparison between the values calculated with those obtained from the sensors readings of the sections T-P26 and T-P18P19b.

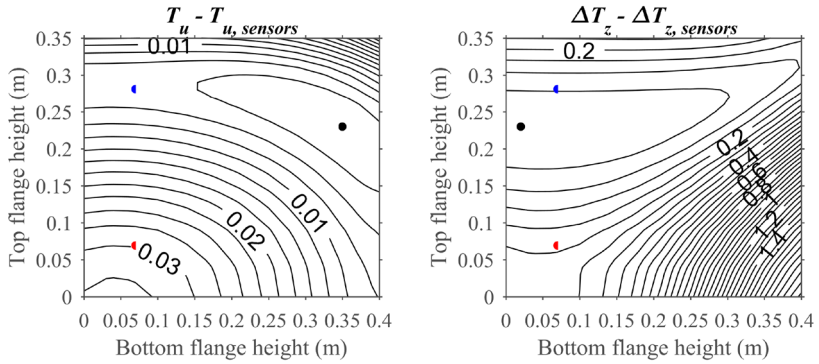

(a) (b)

Figure 4.10 – Surface contour lines of the mean squared difference between the standardised series of: (a) T_u and $T_{u,\,sensors}$; (b) ΔT_z and $\Delta T_{z,\,sensors}$ during the year of 2016. Black, blue and red points correspond, respectively, to the surface minimum (best position of the sensors), section T-P16 and section T-P18P19b. Zero height corresponds to the interior surface (box) of the flanges.

The uniform temperature component T_u is plotted as a function of its estimator $T_{u,\,sensors}$ during the year of 2016 in Figure 4.11. The first conclusion is that the hysteresis is small, pointing out the good correlation between T_u and $T_{u,\,sensors}$. Moreover, the range of the variation of T_u and $T_{u,\,sensors}$ is also very similar. As a result, and for the particular case of the deck cross-section, $T_{u,\,sensors}$ can be considered a reasonable estimator of T_u.

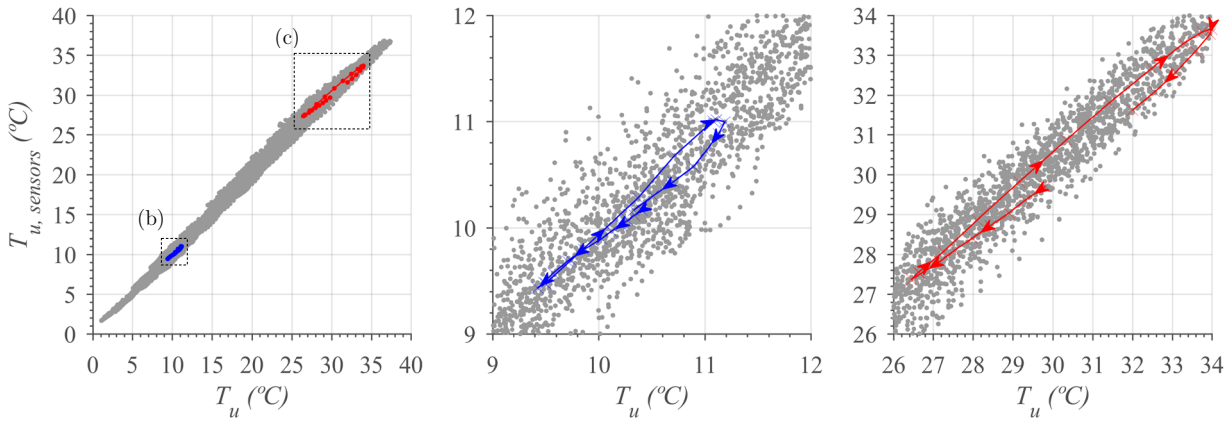

(a) (b) (c)

Figure 4.11 – Uniform temperature component (T_u) versus average temperature of the sensors for the year of 2016: (a) general perspective; (b) detail for a winter day (28th January 2016); and (c) detail for a summer day (24th July 2016).

The linear vertical temperature gradient ΔT_z is plotted in Figure 4.12 as a function of its

estimator $\Delta T_{z,\,sensors}$. In contrast to the uniform temperature component, here the hysteresis between ΔT_z and $\Delta T_{z,\,sensors}$ is larger and the ranges of variation are also different. The hysteresis can be reduced if a lag of one or two hours is considered between ΔT_z and $\Delta T_{z,\,sensors}$. However, this lag depends on the location of the sensors in the cross-section and is not constant over the time. This results clearly show that for this sensor layout $\Delta T_{z,\,sensors}$ is not a good estimator of ΔT_z and is not a good explanatory variable when it is used in regression-based models to explain the variations of the monitored data due to environmental actions.

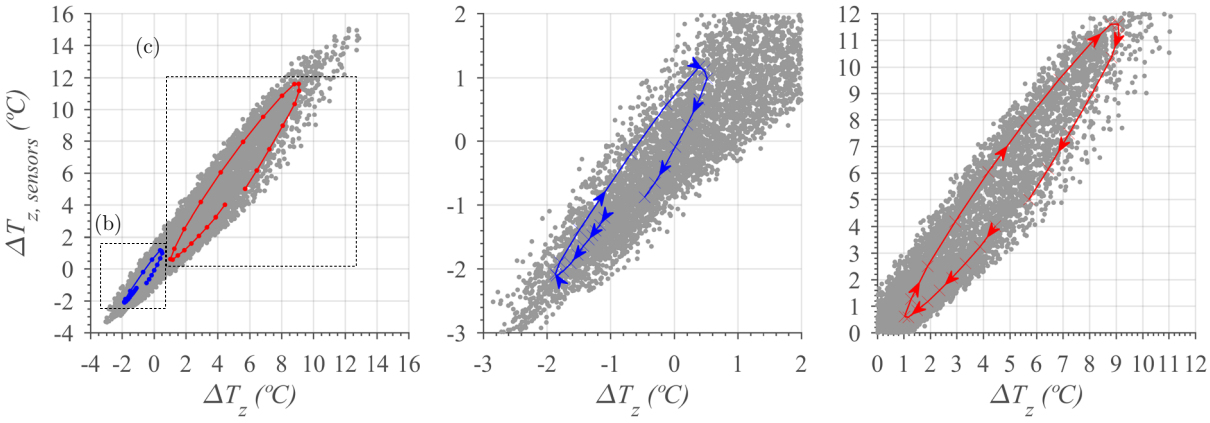

Figure 4.12 – Vertical linear temperature gradient (ΔT_z) versus linear vertical temperature gradient of the sensors $(\Delta T_{z,\,sensors})$: (a) general perspective; (b) detail for a winter day (28th January 2016); and (c) detail for a summer day (24th July 2016).

4.5.2.2 PIER

The temperature distribution decomposition obtained for a typical pier is depicted in Figure 4.13. The uniform temperature component T_u has a daily and seasonal variation similar to the shape of the ambient temperature. On the contrary, the evolution in time of the linear temperature gradients shows a different pattern, being the ΔT_y time evolution similar to the time evolution of the difference between the incident solar radiation on the south and north faces of the pier. It is interesting to confirm that the solar radiation I_T reaching the south surface of the piers is minimal during summer since the solar altitude angle is higher during this time of the year. During winter, the solar altitude angle is lower but the solar

radiation on the horizontal plane I is also lower. The maximum values end up occurring during spring and autumn. In the same way, the time evolution of ΔT_z is similar to the time evolution of the difference between the incident solar radiation on the east and west faces of the pier. In this case, the maximum values occur during late spring and summer.

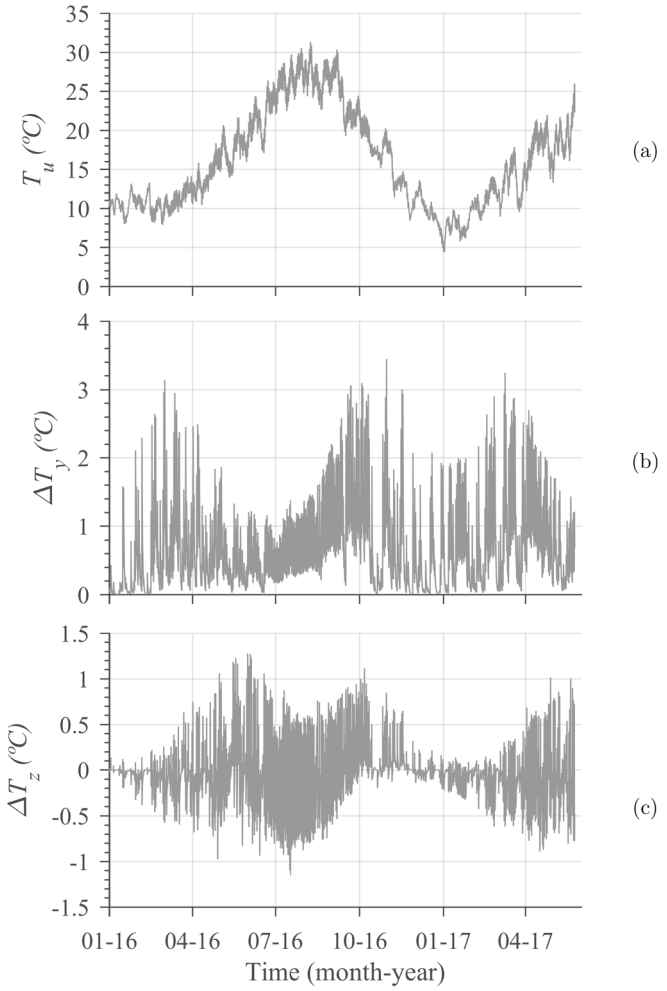

Figure 4.13 – Temperature distribution decomposition of the pier P27: (a) uniform temperature component (T_u), (b) Transversal linear temperature gradient component (ΔT_y) and (c) Longitudinal linear temperature gradient component (ΔT_z).

The detail of the model can be exemplified by the analysis of the daily variation of ΔT_y in two consecutive days of July 2016. Its value tends to zero until 9:00. Then the sun starts reaching the south surface of the piers and ΔT_y starts increasing until 15:00, one hour after the maximum of the incident solar radiation on the south surface. As for the evolution of the linear temperature gradient component ΔT_z on a summer day, a sharp variation on the slope of the curve is seen around 8:00 corresponding to the effect of the incident solar

radiation on the east face. The maximum is reached at 12:00 and the minimum at 18:00. This behaviour is clearly related to the fact that after 11:00 there is no more direct solar radiation in the east face of the pier and with the beginning of direct solar radiation on the West face at 13:00.

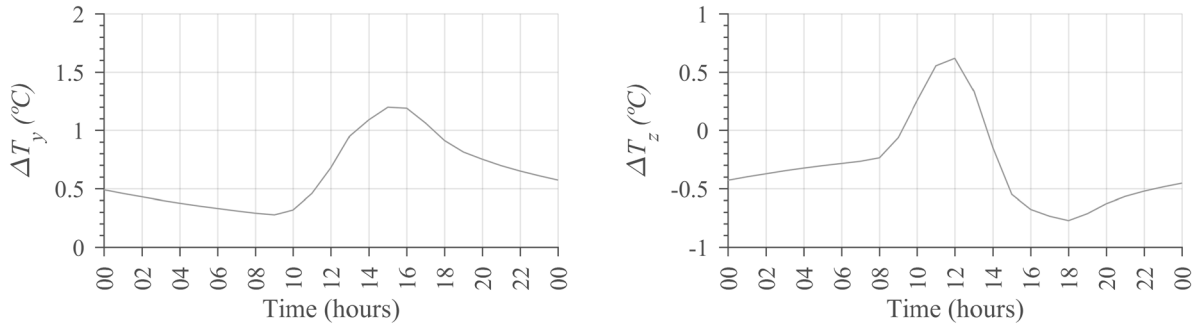

(a) (b)

Figure 4.14 – Temperature distribution decomposition of the pier P27 on 24th July 2016: (a) transversal linear temperature gradient component (ΔT_y) and (b) longitudinal linear temperature gradient component (ΔT_z).

With regards to the optimal positioning of the sensors, the uniform temperature component is best estimated when the temperature sensors of the south/north walls and east/west walls are placed 41cm and 12cm away, respectively, from the interior surface of the corresponding walls (see Figure 4.15 (a)). Concerning the differential temperature components ΔT_y and ΔT_z, the best location for the sensors is symmetric: 35cm from the interior surface of the east and west walls, in the case of ΔT_y, and 37cm from the interior surface of the south and north walls, in the case of ΔT_z. Therefore, for the present case study, in order to have good estimators for all the temperature components eight sensors would be needed: four for $T_{u,sensors}$, two for $\Delta T_{y,sensors}$ and another two for $\Delta T_{z,sensors}$.

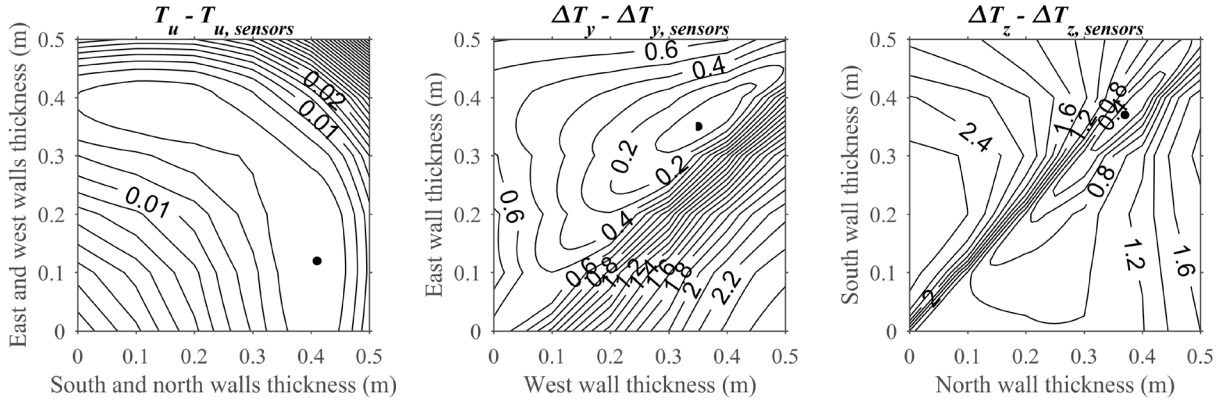

(a) (b) (c)

Figure 4.15 – Surface contour lines of the mean squared difference between the standardized series of: (a) T_u and $T_{u,\,sensors}$, (b) ΔT_y and $\Delta T_{y,\,sensors}$, (c) ΔT_z and $\Delta T_{z,\,sensors}$ during the year of 2016. Black points correspond to the surface minimum (best position of the sensors). Zero thickness corresponds to the interior surface (box) of the pier walls.

4.5.3 Comparison of the calculated structural response with experimental data

Here the results obtained from the mechanical model are compared to experimental evidence. In order to obtain comparable results, both the experimental and calculated time series are plotted after subtracting the corresponding annual mean value.

4.5.3.1 Bearing displacements

The calculated and experimental series of the relative longitudinal bearings displacements with respect to pier P15 (west bearing) are quite similar, as shown in Figure 4.16. The model predicts that during the analysed 17 month period the long term effects are responsible for a 14mm drift of the relative longitudinal displacement, corresponding to an opening movement, which agrees satisfactorily with the available experimental data since no drift can be clearly noticed between the experimental and calculated values. Looking in more detail at two typical weeks of data, one in winter and another in summer, as shown in Figure 4.16 (b) and (c), it is possible to assess the accuracy that is possible to obtain in this type of simulation. The maximum errors reach 10mm during summer, which is about 6.6% of the 150mm yearly amplitude. The daily amplitude is generally well reproduced.

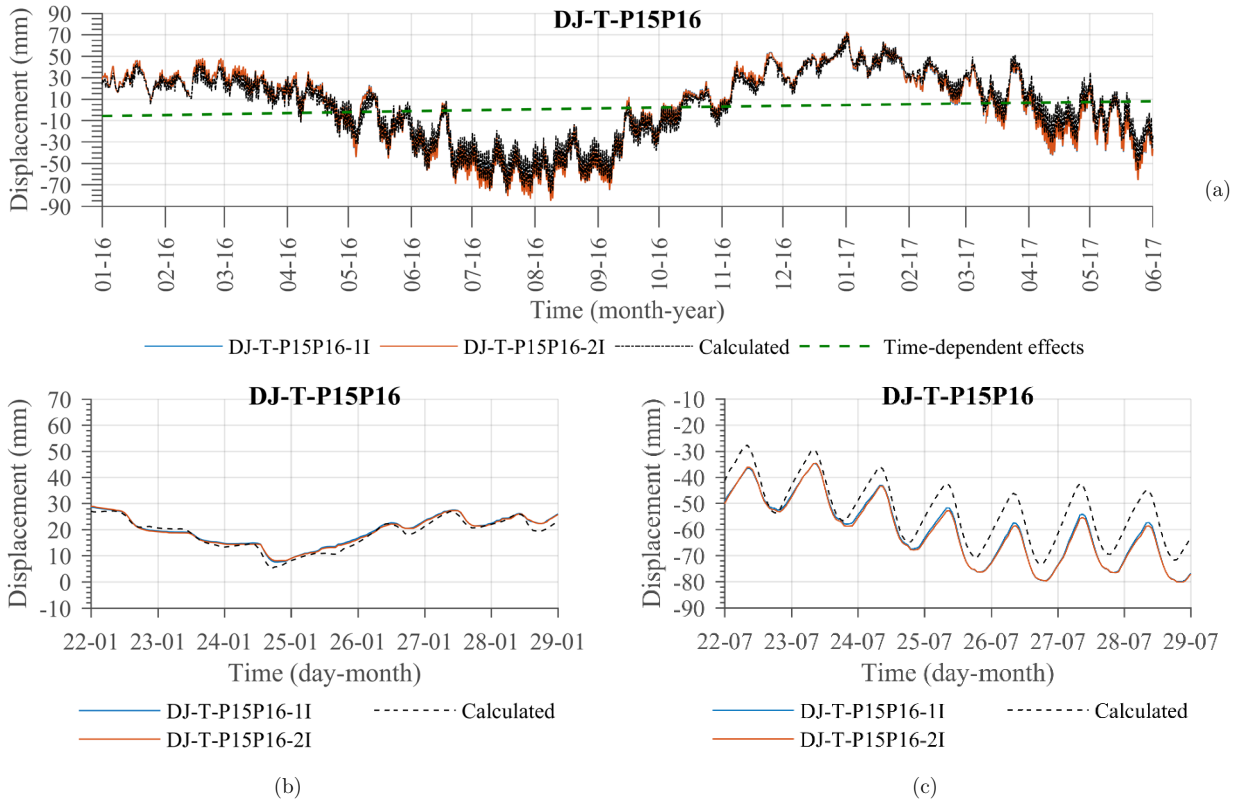

Figure 4.16 – Experimental and calculated bearing displacements of the Central Sub-Viaduct – DJ-T-P15P16 (West) (a), winter 2015/2016 detail (c) and summer 2016 detail (c).

It is interesting to analyse the contribution of each temperature component or structural element to the total measured displacement. The relative contribution of each temperature component/structural element has been determined as the ratio between the absolute value of the corresponding contribution to the sum of the absolute values of the individual contributions. As expected, the model predicts that the relative bearing displacements are mostly explained by the uniform temperature component of the deck girder, as summarized in Table 4. It is also worth noting the contribution of the longitudinal differential temperature gradient ΔT_Z of the piers and pylons. In the case of the east bearings the contribution of the piers increases. Noting that the relative longitudinal bearing displacements are obtained by the difference between the longitudinal movement of the deck and the flexural displacement at the top of the transition piers (see Figure 3.4), this result is explained by the fact that the east transition pier (P22) is taller than the west transition pier P15. The contribution of the piers varies along the year, being larger between mid-April and the end of September, as depicted in Figure 4.17. As discussed in section 6.2.2, this is due to the fact that the solar radiation in the east and west faces of the piers

and pylons is higher during this period. For instance, for 24th July 2016 the ΔT_z of about 1.40ºC represented in Figure 4.14 (b) induces a horizontal displacement of 9.0mm in the top of the pier, which is about 30% of the displacement amplitude for that day.

Table 4.2 – Annual average contribution of each structural element to the bearing displacements.

Structural Element	**DJ-P15P16**			**DJ-P21P22**		
	T_u	ΔT_z	**Total**	T_u	ΔT_z	**Total**
Girder	89.3%	0.0%	89.4%	85.2%	0.2%	85.3%
Pylons	1.1%	4.0%	5.1%	1.2%	3.7%	4.9%
Piers	0.5%	4.4%	4.9%	1.2%	7.9%	9.2%
Stay cables	0.6%	-	0.6%	0.6%	-	0.6%
Total	91.6%	8.4%	100.0%	88.2%	11.8%	100.0%

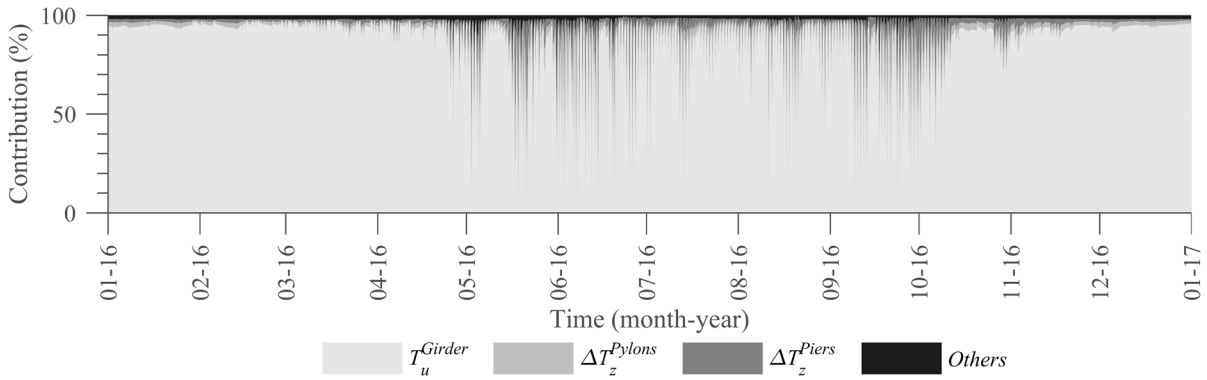

Figure 4.17 – Relative contribution of each structural element for the bearing displacement DJ-T-P21P22 during the year of 2016.

4.5.3.2 Vertical displacements

In Figure 4.18 the experimental and calculated time series of the vertical mid-span displacement are depicted. In general, a good resemblance between the experimental and numerical series was obtained. The time-dependent effects are estimated to contribute to a downward displacement at midspan of about 22mm during the analysed 17 month period, as shown by the green dashed curve. Again, this tendency seems to be confirmed by the experimental data. It is also worth noting that this value is still smaller than vertical displacement amplitude observed during a typical summer day, as can be seen in Figure 4.18 (b).

In Table 4.3 the annual average contribution of each structural element for the vertical

deflections measured by the sensors in the central (DV-T-P18P19b) and side (DV-T-P17P18b) spans is presented, being possible to conclude that the uniform temperature component is responsible for more than 95% of the vertical displacements for all sensors, reaching almost 100% in the case of DV-T-P18P19b. Moreover, while the vertical displacements in the central span are mainly governed by the uniform temperature component of the girder and the stay cables, the vertical displacements in the adjacent spans are less influenced by the stay cables and more by the uniform temperature of the piers and pylons. The weights of each structural element present in Table 4.3 vary throughout the year as shown in Figure 4.17. This figure indicates that the contribution of the stay cables for the vertical deflection in the central span increases during summer.

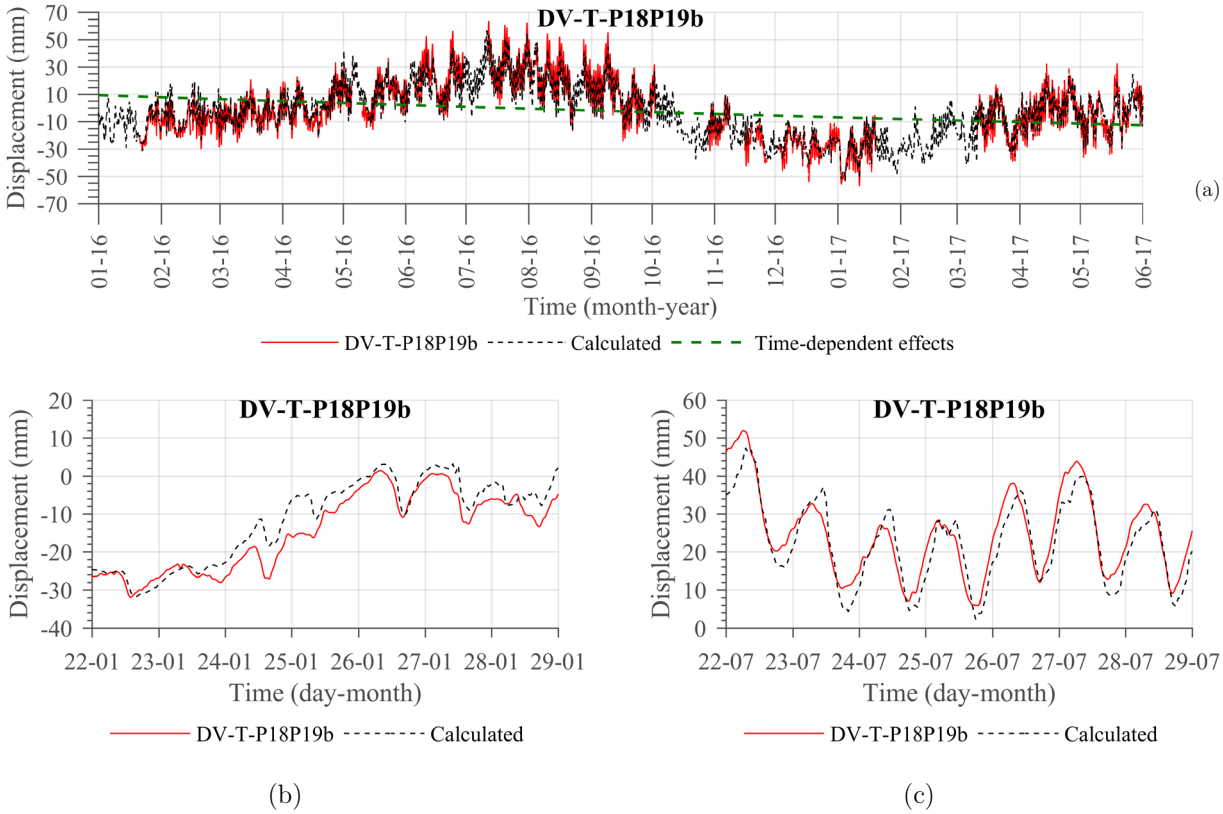

Figure 4.18 – Vertical displacements of the girder: DV-T-P18P19b (central span – see Figure 3.3 for sensor location) (a), winter 2015/2016 detail (b) and summer 2016 detail (c).

Table 4.3 – Annual average contribution of each structural element for two relative vertical displacements.

Structural Element	**DV-T-P17P18b**			**DV-T-P18P19b**		
	T_u	ΔT_z	**Total**	T_u	ΔT_z	**Total**
Girder	19.89%	0.37%	20.25%	42.89%	0.00%	42.90%
Pylons	37.46%	3.23%	40.70%	16.87%	0.00%	16.87%
Piers	33.16%	0.65%	33.81%	5.58%	0.00%	5.58%
Stay cables	5.24%	-	5.24%	34.65%	-	34.65%
Total	95.75%	4.25%	100.00%	99.99%	0.01%	100.00%

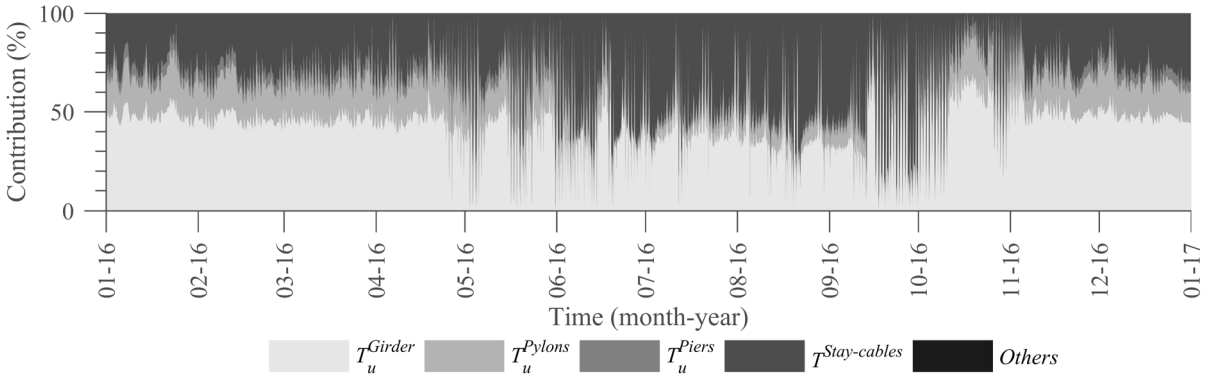

Figure 4.19 – Relative contribution of each structural element for the vertical displacement DV-T-P18P19b during the year of 2016.

4.5.3.3 Rotations

The experimental and the calculated time series for the sensor RO-P-P18d-L located at the pylon P18 and RO-T-P18P19c-L located in the deck, 50m away from pylon P19 are shown in Figure 4.20. The fit between the experimental and calculated time series is clearly better for the rotations of the deck. The time-dependent effects are expected to contribute to a rotation of the pylons towards the central span, being estimated a variation of about 5×10^{-3} degrees and -1.5×10^{-3} degrees for, respectively, RO-P-P18d and RO-T-P18P19c during the analysed 17 month period. Concerning the contribution of each structural element for the rotation responses, once again the uniform temperature component T_u governs more than 99% of the rotation calculated in the deck and about 93% of that measured in the pier, as shown in Table 4.4.

Table 4.4 – Annual average contribution of each structural element for two rotations.

Structural Element	RO-T-P18P19c-L			RO-P-P18d-L		
	T_u	ΔT_z	Total	T_u	ΔT_z	Total
Girder	40.95%	0.05%	41.00%	51.83%	0.00%	51.83%
Pylon	18.14%	0.58%	18.72%	14.51%	5.64%	20.15%
Piers	5.39%	0.12%	5.52%	8.25%	1.08%	9.34%
Stay cables	34.77%	-	34.77%	18.68%	-	18.68%
Total	99.25%	0.75%	100.00%	93.28%	6.72%	100.00%

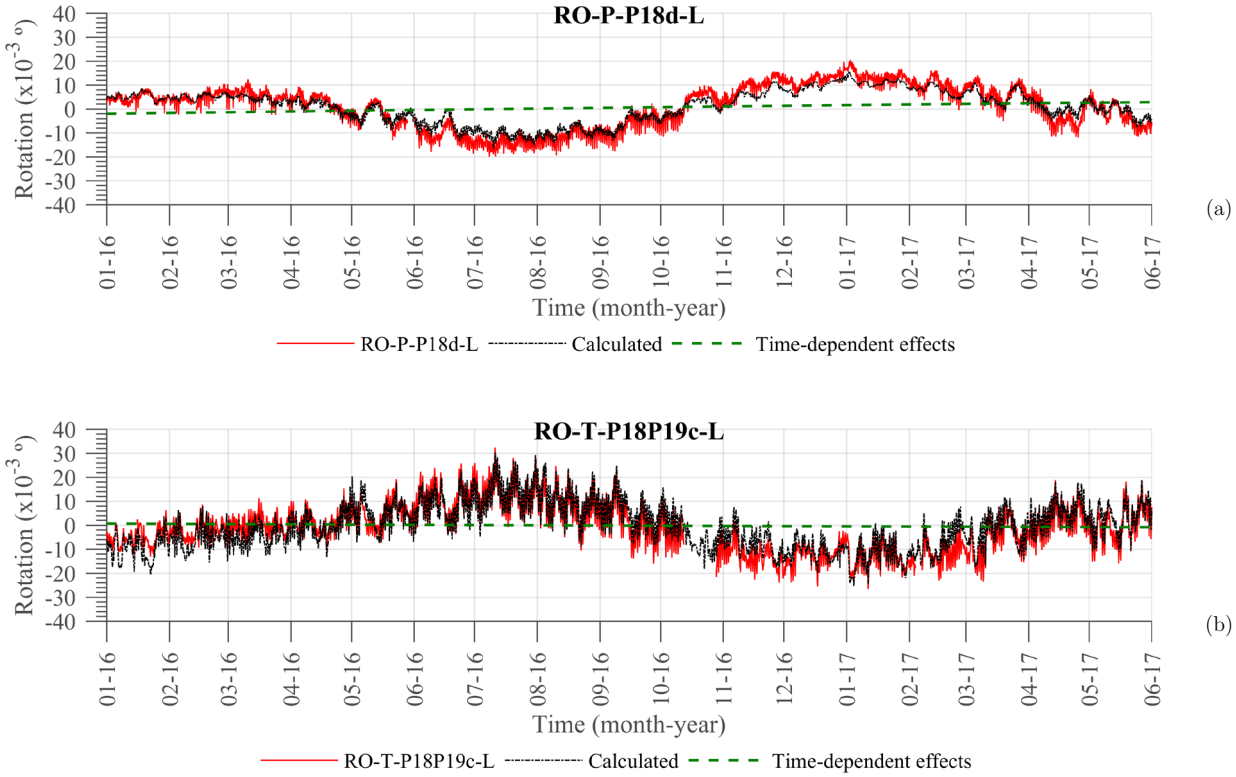

Figure 4.20 – Rotations of the girder: (a) RO-P-P18d-L (located in the interception of the pylon P18 with the girder) and (b) RO-T-P18P19c-L (located in the central span).

4.5.3.4 STAY CABLE FORCES

The variations in the stay cable forces due to the temperature effects are very small, generally around 1% of the installed force. This may explain why the resemblance between the measured and calculated time series is lower when compared to the remaining sensors. The stay cable T18C20 (the location of which is defined in Figure 3.3) is taken as an example and the corresponding time series are depicted in Figure 4.21. The force installed in this stay cable is approximately $7500kN$ with a variation of approximately $\pm 40kN$ during

the year, the largest amongst the monitored cables. Likewise, the force variation due to the time-dependent effects is predicted to be small, leading to an estimated force decrease of about 24kN (approximately 0.3% of the installed force) during 17 months.

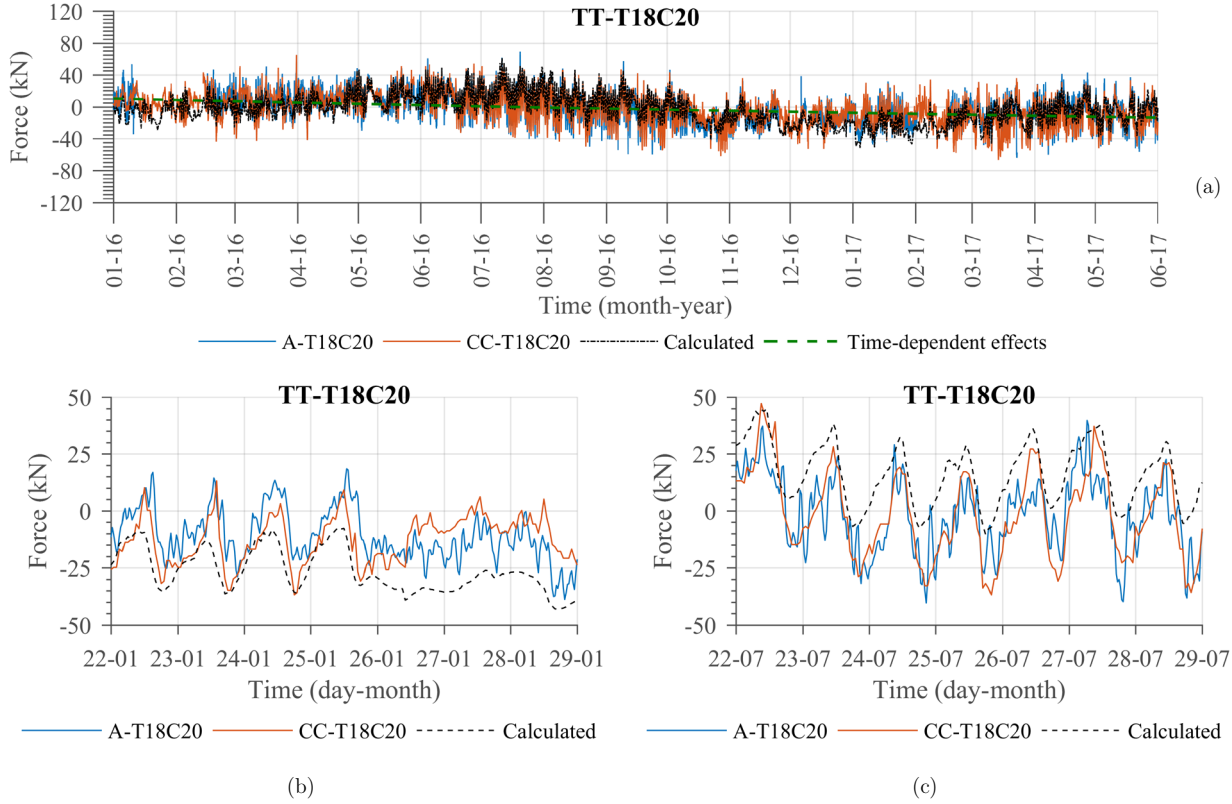

Figure 4.21 – Cable forces: T18C20 (a), winter 2016/2017 detail (b) and summer 2016 detail (c). A-T18C20 refer to the forces determined with accelerometers and CC-T18C20 to the forces directly measured with a load cell.

The contribution of each structural element for the cable force variations of the stay cable T18C20 is presented in Table 4.5. Once again, the uniform temperature component governs the force variation in all instrumented stay cables. The uniform temperature component of the girder and stay cables are the main responsible for the force variations in the stay cables located near to the mid-span of the central span, while the uniform temperature component of the pylons takes more relevance for the shorter stay cables.

Table 4.5 – Annual average contribution of each structural element to the force in the stay cable T18C20.

Structural Element	**F-T18C20**		
	T_u	ΔT_z	**Total**
Girder	46.49%	0.07%	46.56%
Pylons	9.76%	3.44%	13.21%
Piers	5.01%	0.63%	5.64%
Stay cables	34.59%	0.00%	34.59%
Total	95.85%	4.15%	100.00%

4.6 Concluding remarks

A methodology is proposed for the simulation of the structural response of large concrete cable-stayed bridges under the effects of temperature variations, aiming at the optimum compromise between accuracy and simplicity of the involved procedures. The methodology is general and can be used to determine the structural response to thermal loads of other types of bridges, irrespective of the material.

The obtained results were compared against the readings of the permanent structural monitoring system installed at the Corgo Bridge, providing the validation of the developed methodology, as well as an indication of the accuracy that can be achieved. The structural behaviour of the bridge under the effects of temperature variations could be disclosed, enabling a better understanding of the readings continuously being acquired by the structural health monitoring system. For the large majority of the sensors, the variation of the uniform temperature component was demonstrated to be responsible of about 90% of the structural response.

The detailed simulation of the radiative heat transfer mechanisms revealed to be essential for the accuracy of the results. The agreement between the measured and calculated temperatures provides a confirmation of the adequacy of the adopted models and material properties. It is also noted that only after the consideration of the effective sky temperature in the longwave radiation model the temperatures measured in the top slab during wintertime could be accurately reproduced, highlighting the importance of the consideration of this physical phenomenon (which is usually disregarded) in order to obtain accurate estimates of the thermal field.

In the context of the interpretation of the readings provided by structural monitoring

systems, the uniform and differential temperature components have to be estimated from the discrete temperature readings. A discussion on the optimal deployment location of the embedded temperature sensors in order to have better estimates was presented for the girder and a pier of the Corgo Bridge. However, other types of sections and boundary conditions (namely solar exposure) should be further considered in order to be possible to give more general recommendations for localisation of the temperature sensors.

The comparison between the measured and calculated structural response in terms of longitudinal bearing displacements, vertical deflections, rotations and stay-cable force variations yielded a satisfactory agreement. The assumption of constant temperature distribution along the longitudinal direction of the girder, piers and pylons, did not compromise the validity of the results, demonstrating the validity of this assumption. The analysis enabled the quantification of the contribution of each temperature component to the calculated structural response. It is concluded that the differential temperature component contributes very little to the response of the analysed cable-stayed bridge, except in the case of the longitudinal bearing displacements were it contributes, on average, to about 10% of the total displacement. This is due to the flexural displacement of the tall piers, which are dictated by the differential temperature between the east and west vertical surfaces. The trend due to the long term effects (creep, shrinkage and prestress steel relaxation) could be clearly detected in the monitoring readings and could be satisfactorily reproduced by the numerical model. This confirms the adequacy of the adopted models for the long term effects during the 17 month observation period.

Chapter 5*

ONLINE EARLY DAMAGE DETECTION AND LOCALISATION USING MULTIVARIATE DATA ANALYSIS

5.1 Introduction

Albeit the extensive research made in SHM, successful in-situ implementations of long-term SHM systems that are proven to be able to deal with EOVs are still scarce [37, 84, 133, 233]. In many of the damage detection techniques that have been proposed, the EOVs on the structural response are often disregarded and validation of the related algorithms is still performed using either numerical simulations on simple structural elements or experimental results obtained in a well-controlled laboratory environment [66].

In this context, this work intends to be a contribution to the transition of SHM technology from academia to industry. A data-based methodology for online damage detection and localisation is proposed and validated using real data gathered by a long-term continuous

* This chapter is based on the paper: Sousa Tomé, E., M. Pimentel, and J. Figueiras (2019). *Online early damage detection and localisation using multivariate data analysis – application to a cable-stayed bridge.* Structural Control and Health Monitoring. [Accepted].

monitoring system installed in the Corgo Bridge. Two well-established multivariate statistical tools – multiple linear regression analysis (MLR) and principal component analysis (PCA) – are employed for data normalisation. Anomaly detection is performed using the Hotelling T^2 Control Chart. The damage detection ability is evaluated considering damage scenarios involving the reduction of the cross-section area of the stay-cables. Since the selected bridge is new and sound, the structural response due to the damage events is numerically simulated and superposed to the real data being acquired by the SHM system. Finally, the methodology is applied to the dataset composed by the girder deflections and a real, small and temporary sensor anomaly is detected, further demonstrating its effectiveness.

5.2 Methodology

One of the main objectives of this work is to propose a systematic methodology to process and interpret in real-time the readings from a bridge monitoring system. This methodology should generally be applicable to any type of bridge and structural monitoring system architecture and should entail pre-processing of the raw data (for outlier removal), data normalisation and finally a novelty index sensitive to damage but insensitive to operational and environmental effects, as schematized in Figure 5.1. When damage is flagged, some indication regarding the location of the damage should be given. Finally, the methodology should be able to process new data in real-time, that is, in an online manner.

Due to problems in the measuring devices or due to external factors, data collected from any continuous monitoring system has always missing values and abnormal values (outliers) [157]. As illustrated in Figure 5.1, the first stage of the proposed methodology concerns the removal of the existing outliers and suppression of the wind and traffic effects. For outlier removal, the Interquartile Range Analysis (IQR) is used. For the suppression of the wind and traffic effects, the daily, two-day or three-day average values are used. Indeed, the process of averaging data works as a low-pass filter removing the sudden changes, such as the ones due to wind and traffic effects, which are challenging to model. This is discussed in more detail in section 5.4.2.4, where a comparison with the results obtained with hourly data is presented.

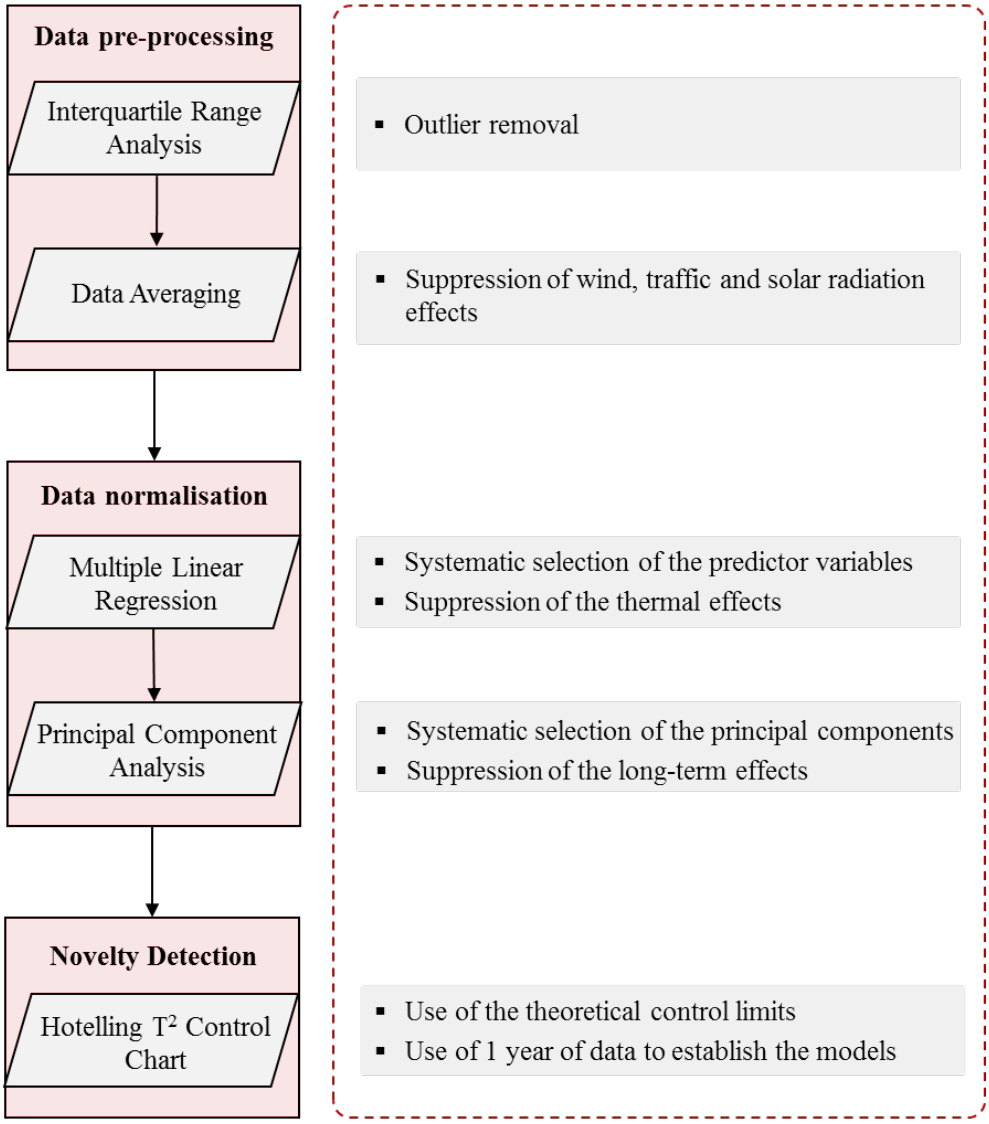

Figure 5.1 – Flowchart showing the methodology adopted for data pre-processing, data normalisation and novelty detection.

The second stage corresponds to the suppression of the thermal and long-term effects, that is, the data normalisation. The adopted methods should be able to handle missing data. This is made through the sequential combination of two well-established multivariate statistical tools as proposed by Magalhães *et al.* [133]: multiple linear regression (MLR) and principal component analysis (PCA). The MLR is used to remove the measured actions on the bridge, in this case the temperature, from the data. In the present case study, the relationship between the measured temperatures and structural responses is linear. However, in case this relationship between predictor variables and dependent variables is nonlinear, the use of methods that have the ability to model nonlinearities between

variables, such as the artificial neural networks, may be recommended instead. The selection of the predictor variables to include in the model is made by means of the Pearson correlation coefficient. Predictor variables with a Pearson correlation coefficient with the dependent variable lower than a pre-established threshold are excluded. The sensitivity to this threshold is evaluated in section 5.4.2.1.

The PCA model is applied to the residuals of the MLR model. The goal of the PCA is to suppress the EOVs not suppressed by the MLR model, namely the remaining temperature effects and the long-term behaviour due to rheological effects of the concrete. One should note that long-term behaviour is nonlinear in time. For that reason, a black-box method such as Auto-Associative Neural Networks is not recommended to remove this effect since that kind of methods do not extrapolate well due to the fact that the training data must span the full range of the input space [80]. When the PCA is used to remove the long-term effects, it is being assumed that the relationship in time between the different sensors is linear. The number of principal components to retain is chosen based on the cumulative percentage of the total variation. This is discussed in detail in section 5.4.2.2.

In order to illustrate the data normalisation process, Figure 5.2 shows the vertical displacement at the midspan of the cable-stayed bridge used as case study in the present work before the normalisation (Figure 5.2 (a)) and after the MLR (Figure 5.2 (b)) and MLR-PCA (Figure 5.2 (c)) models. In Figure 5.2 (a) the variations due to temperature and long-term effects are noticeable. In Figure 5.2 (b) where the residuals of the MLR model are shown, the variations induced by temperature were considerably suppressed, as expected, being now the trend due to long-term effects more evident. The PCA model removes this trend and eventually other effects not removed by the MLR model. In Figure 5.2 (c) the residuals after the MLR-PCA model are presented, being noticeable that all the variations due to operational and environmental effects were removed.

After the data is normalised, the Hotelling T^2 multivariate control chart is used for novelty detection. However, as in any multivariate control chart, after an abnormal behaviour is flagged, it is not possible to know which sensor(s) is(are) responsible for that behaviour. Therefore, it is not possible to give a clue where the damage is localised. To circumvent this, one can look to the residuals of the sensors or construct control charts with sub-

datasets of the data. The last approach is the one followed in the present work. After the damage is flagged, sub-datasets of data are constructed from the original dataset. The sensors more affected by damage should be in the sub-dataset where the variation in the T^2 statistic is higher.

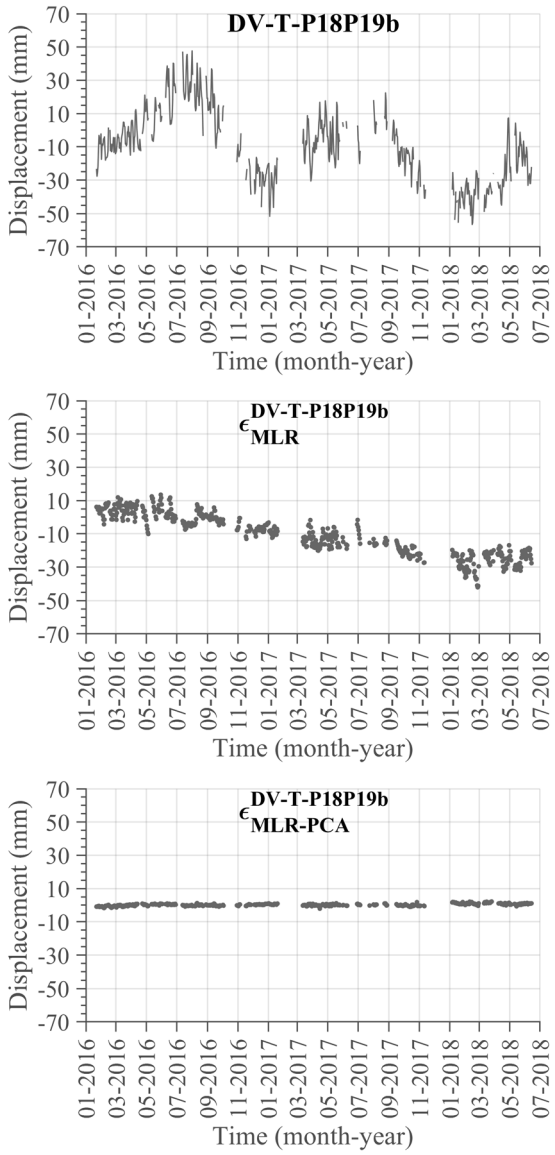

Figure 5.2 – Vertical deflection of the central span (sensor DV-T-P18P19b located at section T-P18P19b in Figure 3.3): (a) pre-processed data – daily averaged data; (b) residuals of the MLR model; and (c) residuals of the MLR-PCA model.

5.3 Data normalisation and novelty detection: theoretical background

5.3.1 Data pre-processing: Interquartile Range Analysis (IQR) and data averaging

The Interquartile Range Analysis (IQR) is used to remove outliers from the data obtained by the monitoring system. The effectiveness, robustness and simplicity of this method in datasets from civil engineering structures were demonstrated by Posenato [157]. The IQR states that a value is an outlier if it is not inside the interval:

$$[Q_1 - 1.5 \times IQR, Q_3 + 1.5 \times IQR] \tag{5.1}$$

where Q_1 and Q_3 are, respectively, the first and third quartiles of the sample with N_p points, and IQR is the interquartile range $(Q_3 - Q_1)$ for the same sample. A moving window of size N_p centred in each point defines the considered sample. When an outlier is detected, that point is removed and substituted by the average of the neighbouring points. An N_p corresponding to one day of data was considered in the present work.

Concerning data averaging, daily, two-day and three-day averaged series are used in this work. Days with more than six hours of missing data were not taken into account.

5.3.2 Data normalisation

5.3.2.1 Multiple linear regression (MLR)

Linear regression analysis is the simplest multivariate statistical tool to relate the observed environmental and/or operational factors with the observed structural responses and/or features. This statistical tool can be used to predict one or more responses (dependent variables) from a collection of predictors (usually called as the predictor, the regressor or the independent variables) and to assess the influence of the predictors on the dependent variables [99]. The multilinear regression model is expressed by [99]:

$$\mathbf{Y} = \mathbf{X}\hat{\mathbf{U}} + \mathbf{E}_{MLR} \tag{5.2}$$

where $\mathbf{Y}$ is an *n-by-m* matrix of the dependent variables, being n the number of observations

and m the number of dependent variables, $\mathbf{X}$ is an n-by-$(r+1)$ matrix with the corresponding n values of r selected predictor variables, $\hat{\mathbf{U}}$ is an $(r+1)$-by-m matrix with the estimated model parameters that weight the contribution of each predictor variable, and $\mathbf{E}_{MLR}$ is an n-by-m matrix with the random error of the MLR model.

The estimates of the model parameters $(\hat{\mathbf{U}})$ are obtained through the least squares method and are given by:

$$\hat{\mathbf{U}} = (\mathbf{X}^{\mathrm{T}}\mathbf{X})^{-1}\mathbf{X}^{\mathrm{T}}\mathbf{Y} \tag{5.3}$$

The model can be used to obtain predictions of the dependent variables $(\hat{\mathbf{Y}})$, being the error of the forecasts the difference between $\mathbf{Y}$ and $\hat{\mathbf{Y}}$.

5.3.2.2 Principal component analysis (PCA)

Principal Component Analysis (PCA) can be defined as a statistical tool for explaining the variance-covariance structure of a set of variables through linear combinations of these variables [99]. PCA has been extensively used in the scope of SHM, namely for the recognition of patterns in the data, data cleansing and data compression [69]. The fact that PCA is a latent-variable method, that is, a method that is able to remove the environmental effects using only the structural responses, without any knowledge about the input, is usually pointed out as its most attractive feature [11, 169, 224].

Considering an *n-by-m* matrix $\mathbf{Y}$ with the original variables, where m is the number of sensors or/and features and n is the number of observations in time, a transformation to another set of m variables $\mathbf{Z}$, the principal component scores, can be made by:

$$\mathbf{Z} = \mathbf{Y} \cdot \mathbf{T} \tag{5.4}$$

where $\mathbf{T}$ is the transformation (or loading) matrix, an m-by-m orthonormal matrix that applies a rotation to the original coordinate system [133]. The covariance matrix of the original variables in the training period, $\mathbf{\Sigma}$, is related to the covariance matrix of the principal component scores, $\mathbf{\Lambda}$, by the following equation,

$$\mathbf{\Sigma} = \mathbf{T} \cdot \mathbf{\Lambda} \cdot \mathbf{T}^{\mathrm{T}} \tag{5.5}$$

being the $\mathbf{T}$ and $\mathbf{\Lambda}$ matrixes obtained by the singular value decomposition of the covariance matrix $\mathbf{\Sigma}$ of the original variables. The columns of $\mathtt{T}$ are the singular vectors and the diagonal matrix $\mathbf{\Lambda}$ contains the singular values of the matrix $\mathbf{\Sigma}$ in descending order. The singular values stored in $\mathbf{\Lambda}$ are the variances of the components of $\mathtt{Z}$. Moreover, the matrix $\mathbf{\Lambda}$ can be split into a matrix with the first p singular values and in a matrix with the remaining m-p singular values, which are not relevant to explain the variability of $\mathtt{Y}$.

After the choice of p, the first p components of the matrix $\mathbf{Z}$ can be calculated using equation (5.4) and a transformation matrix $\hat{\mathbf{T}}$ built with the first p columns of $\mathtt{T}$. Those first p components can be re-mapped to the original space [224] using the following equation:

$$\hat{\mathbf{Y}} = \hat{\mathbf{Z}} \cdot \hat{\mathbf{T}}^{\mathrm{T}} = \mathbf{Y} \cdot \hat{\mathbf{T}} \cdot \hat{\mathbf{T}}^{\mathrm{T}} \tag{5.6}$$

being then the residual error matrix estimated from:

$$\mathbf{E}_{PCA} = \mathbf{Y} - \hat{\mathbf{Y}} \tag{5.7}$$

The residual error matrix $\mathbf{E}_{PCA}$ is expected to be insensitive to the effects modelled by the PCA and can be used to detect damage.

On the choice of the number of principal components to retain

One of the critical steps of the PCA is the choice of the number of p components to retain. Although several approaches, many of them *ad hoc*, have been proposed for determining p [93, 100, 153], still there is not a definitive answer [99]. However, in the context of SHM "the selection of an appropriate dimension p is not so critical as it appears" [224] since what is being looked for is a change in the hyperplane defined by the p principal components adopted from the reference state to the current state. Therefore, stable results can be obtained using different p principal components [224].

The determination of the number of components to retain should be made in a systematic way. Therefore, a criterion based on the cumulative percentage of the total variation is adopted, where p is the smallest value for which the chosen percentage is exceeded. Cumulative percentages of 70% (CP70), 80% (CP80) and 90% (CP90) are evaluated in the present work.

5.3.3 Classification: Hotelling T^2 control chart

After removing the environmental factors from the measured structural response, a control chart can be used to track the existence of abnormal values, which can be related to the presence of damage. The so-called control limits define the accepted process variability. If an observation exceeds those control limits, the observation is said to be an out-of-control observation. In the context of SHM, this out-of-control observation may be associated with the presence of damage in the structure.

In order to have only one control-chart instead of having one for each variable/sensor, the multivariate Hotelling T^2 control chart was adopted, being the T^2-statistic calculated as [141]:

$$T^2 = r(\bar{\mathbf{x}} - \bar{\bar{\mathbf{x}}})^{\mathrm{T}} \mathbf{S}^{-1} (\bar{\mathbf{x}} - \bar{\bar{\mathbf{x}}}) \tag{5.8}$$

where r is the number of observations considered (window size), $\bar{\mathbf{x}}$ is the average of the observations inside the window, $\bar{\bar{\mathbf{x}}}$ is the process average when it is in control and $\mathbf{S}$ is the process covariance matrix, also estimated in the training period. The lower control limit is zero and if $r > 1$ the upper control limit (UCL) is obtained from:

$$UCL = \frac{m(s+1)(r-1)}{s \cdot r - s - m + 1} F_{m,\, s \cdot r - s - m + 1}(\alpha) \tag{5.9}$$

where $F_{m,\, s \cdot r - s - m + 1}(\alpha)$ is the α percentage point of the F distribution with m and $s \cdot r - s - m + 1$ degrees of freedom, being m the number of sensors and/or features and s the number of subgroups (or windows) collected during the training period. If $r = 1$, the UCL is obtained from:

$$UCL = \frac{m(s+1)(s-1)}{s^2 - s \cdot m} F_{m,\, s-m}(\alpha) \tag{5.10}$$

This statistic, as all the multivariate control charts, has the advantage of condensing all sensors responses into a scalar indicator, working in the context of SHM as a damage indicator. However, after an abnormal behaviour is flagged, it is not possible to know which sensor(s) is(are) responsible for that behaviour.

5.3.4 PERFORMANCE INDICATORS

In order to evaluate the ability for data normalisation and novelty detection of the proposed methodology, three performance indicators are used. The first is the number of false positives, that is, the number of points above the UCL when the structure is in control and no damage was introduced in the time series. This is used to evaluate the ability of the methodology to suppress the EOVs. The lower the number of false positives is, the more effective is the suppression of the EOVs.

Two other indicators are used to evaluate the sensitivity to damage since a given model can produce a very low number of false positives, but be poorly sensitive to damage. The first is the ratio between the mean values of the T^2 statistic in the damaged and undamaged states (RU):

$$RU = \frac{mean\left(T^2_{damaged}\right)}{mean\left(T^2_{undamaged}\right)} \tag{5.11}$$

The second is the ratio between the mean values of the T^2 statistic in the damaged state and the UCL (RL_α):

$$RL_\alpha = \frac{mean\left(T^2_{damaged}\right)}{UCL(\alpha)} \tag{5.12}$$

A high value of RU means that there is a clear distinction between the undamaged and damaged states. Values of RL_α higher than one means that on average the points are above the UCL. The higher RL_α, the higher is the distance between the points and the UCL. When the data is not well-normalised, low values of RU and high values of RL_α are obtained. On the other hand, when an overfitted model is used to normalize the data, high values of RU and low values of RL_α are obtained. The best data normalisation methodology will be that simultaneously providing a low number of false positives and high values of both RU and RL_α. The indicator RL_α can also be calculated for the undamaged state ($RL_{u,\alpha}$), providing a measure of the quality of the data normalisation process.

5.4 Application to the case study

The present section describes the parametric studies that were developed to determine the best parameters for the proposed methodology. This analysis is undertaken using a dataset constituted by the ten stay cable forces estimated from the measured accelerations, which revealed to be the most sensitive features to the damages in the stay cables. In section 5.4.2.5 the results obtained for a dataset composed by the vertical deflections are presented.

5.4.1 Pre-processing and damage simulation

In order to exemplify the data being used, the time series of the stay cable force F-T19C13 (see Figure 3.3 for sensor location) with the raw data, after the application of the IQR and after daily averaging are presented in Figure 5.3 (a), (b) and (c), respectively. The outlier removal due to the application of the IQR algorithm with a time window of one day can be observed comparing Figure 5.3 (a) to (b). The suppression of the variations due to daily temperature variations can be noted comparing Figure 5.3 (b) to (c).

Damage scenarios involving cross-section area reduction of the stay-cables are numerically simulated to evaluate the damage detection ability. The numerical simulation is performed using the finite element model previously validated in Chapters 3 and 4. The damage is introduced in the model and the obtained numerical variations in the sensors are superposed to the real data being acquired by the SHM system. Figure 5.3 (d) shows the corrupted time series for the sensor F-T19C13 corresponding to the damage scenario involving the loss of 2.5% of the cross-section area of the neighbouring stay-cable T19C14. This introduces a variation of 12kN in the stay-cable T19C13.

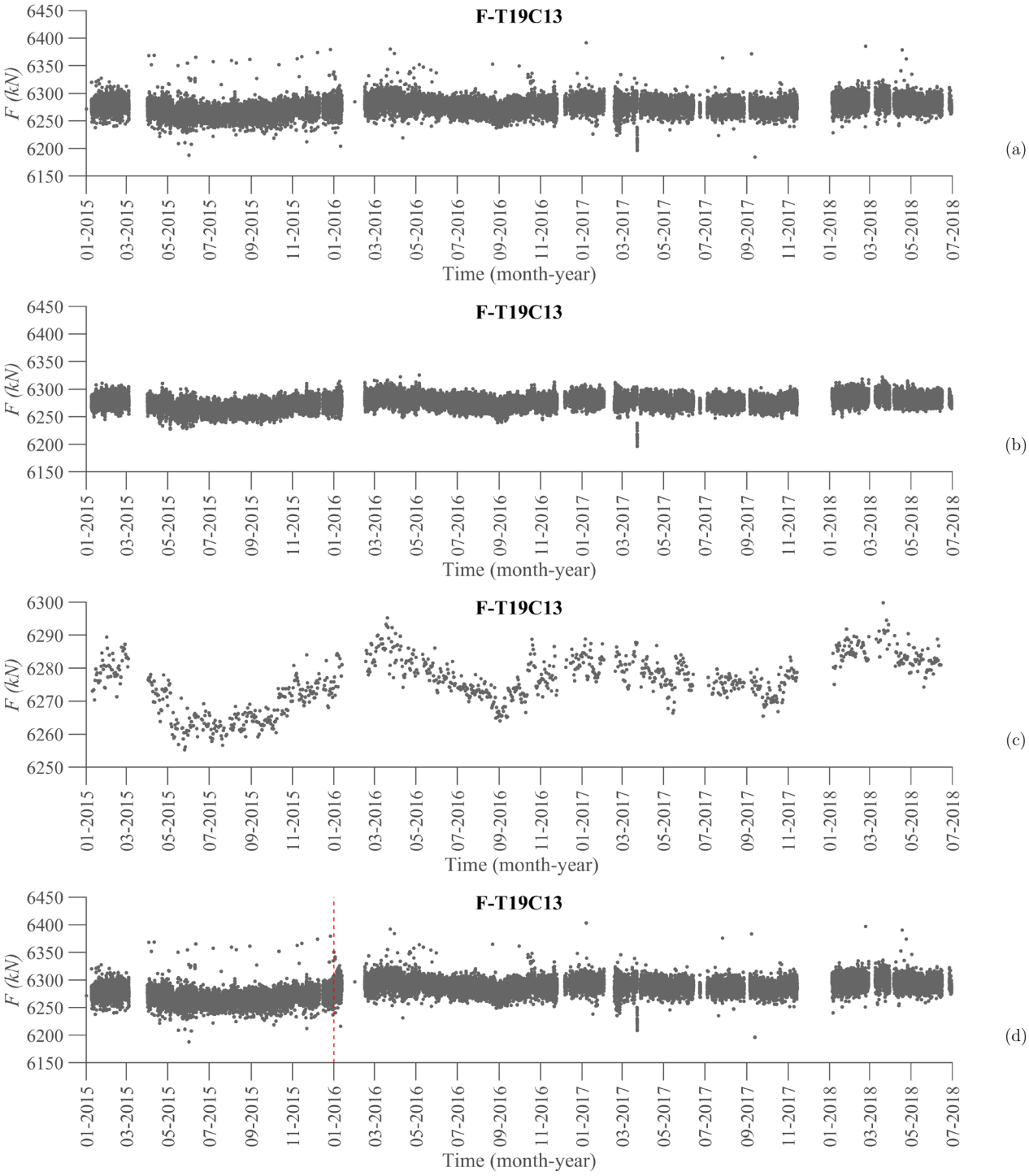

Figure 5.3 – Time series of the cable force F-T19C13: (a) raw; (b) after IQR; (c) after IQR and daily average; (d) raw data with a simulated damage scenario corresponding to 2.5% of area loss in the stay-cable T19C14 introduced in January 2016 (vertical dashed line). See Figure 3.3 for stay-cable location.

5.4.2 Data normalisation

5.4.2.1 Choice of the predictor variables

The linear regression is used to suppress, or at least minimize, the thermal effects from the measured structural response. The selection of an appropriate set of dependent variables is a crucial step. The bridge is expected to respond linearly to the uniform and linear components of the thermal field in its structural elements. However, the concrete temperatures can only be measured in a few discrete locations and on a limited number of cross-sections. These local temperature readings are not linearly correlated with the structural responses. In the previous chapter, it was demonstrated that the mean of the readings of the four temperature sensors embedded in the monitored cross-sections are good estimators of the uniform temperature component (the location of the temperature sensors in one of the reference cross-sections can be found in Figure 3.1 (c) and (d)). Although it was demonstrated that it is not possible to obtain good estimators of the linear temperature components using the available sets of temperature sensors, the linear temperature component has shown to have a low weight in the structural response of the Corgo Bridge [198]. Indeed, the uniform temperature component is shown to be responsible for more than 90% of the structural response to thermal loads. For those reasons, the mean of the concrete temperature sensors of a cross-section in the girder $\left(T_{u,\,sensors}^{Girder}\right)$, the mean of the concrete temperature sensors in a pier cross-section $\left(T_{u,\,sensors}^{Pier}\right)$ and the stay-cable temperature readings $\left(T_{stay-cable}\right)$ were considered as candidates to predictor variables in the fitted regression models. They are expected to be, respectively, representative of the uniform temperature component of the girder, of the uniform temperature component of the pylons and piers and of the temperature of the stay cables.

However, each measured structural response shows different degrees of correlation with the considered predictors. The consideration of an unimportant predictor variable in the model can actually decrease the fit to the data, causing an increase of the error mean square [142]. With this in mind, the predictors that have an absolute value of the Pearson correlation coefficient with the dependent variable below a pre-established threshold were not considered in the model.

The influence of the threshold value is evaluated in terms of the ability for data normalisation and damage detection sensitivity. Three different levels were then considered: 0.3, 0.4 and 0.5. The number of false positives, RU and RL (due to an area reduction damage of 10% in the stay cable T19C19) during the years of 2017 and 2018 are presented in Table 5.1 for the three thresholds. A more permissible threshold $\left(|R| \geq 0.3\right)$ leads to a larger amount of false positives (eight) and a lower sensitivity to damage (lower RU and RL), indicating that excessive predictor variables were considered in the models. However, if the threshold is too high, sensitivity to damage is also lost and the number of false positives increases again. For these reasons, a threshold of 0.4 was set for the absolute value of the Pearson coefficient, $|R|$, when choosing the predictor variables among the available candidates.

Table 5.1 – Number of false positives $(\alpha = 99.9\%)$, RU and RL for the years of 2017 and 2018 (Considered damaged: 10% of area loss in the stay-cable T19C19; Daily averaged series; Training period size: 365 days; Principal components were chosen using CP80).

$\|R\|$	No. positives $(\alpha = 99.9\%)$		No. positives (%) $(\alpha = 99.9\%)$		RU	$RL_{99.9\%}$	
	Undamaged	Damaged	Undamaged	Damaged		Undamaged	Damaged
0.3	8	351	2.28	100	7.83	0.38	2.99
0.4	2	351	0.57	100	11.62	0.42	4.87
0.5	7	351	1.99	100	8.75	0.44	3.84

In Table 5.2 the Pearson correlation coefficients between predictors and dependent variables are presented. For sensors F-T18C20 and F-T19L06, no MLR model was considered when the used training period is the year of 2015 since $|R|$ is lower than 0.4 for all the predictor candidates.

Table 5.2 – Pearson correlation coefficient (R) between predictors and dependent variables for 2015 for daily averaged data.

	$T_{u,\,sensors}^{Girder}$	$T_{u,\,sensors}^{Pier}$	$T_{stay-cable}$
F-T18L06	-0.62	-0.65	-0.70
F-T18C02	-0.67	-0.65	-0.83
F-T18C06	-0.76	-0.74	-0.72
F-T18C13	-0.81	-0.84	-0.70
F-T18C20	0.16	0.03	-0.11
F-T19C20	-0.39	-0.53	-0.54
F-T19C13	-0.76	-0.78	-0.67
F-T19C06	-0.60	-0.47	-0.51
F-T19C02	-0.35	-0.33	-0.56
F-T19L06	-0.37	-0.32	-0.33

5.4.2.2 Choice of the number of principal components

The PCA models are fitted to the residuals of the MLR models, as referred in section 5.2. The main goal of fitting a PCA model after the MLR model is to remove EOVs not measured and not considered in the regression model, such as the differential temperature components and the long-term behaviour of concrete and prestressing steel. However, the choice of the number of principal components p to retain is not straightforward. The choice of a low number of principal components could lead to an excessive number of false positives. On the other hand, the choice of too many principal components could lead to the reduction of the sensitivity to damage/novelties.

The adopted method to select the number of principal components to retain is based on the cumulative percentage of the variance of the components. Three cut-off levels (70%, 80% and 90%) are evaluated here in terms of data normalisation ability and damage/novelty sensitivity, leading to the models designated as CP70, CP80 and CP90, respectively. The number of false positives, RU and RL obtained for the three cut-off levels during the years of 2017 and 2018 are presented in Table 5.3. The obtained results show that CP70 has the worst performance since it shows more false-positives and a lower value of RU. The obtained value for RL is higher for CP70 since the normalisation of the data is less effective (note that RL is also higher for the undamaged state). Concerning CP80 and CP90, the latter leads to fewer false-positives and a higher value of RU. However, CP80 leads to a higher RL, which means that it is more sensitive to damage. This is confirmed by the control

charts presented in Figure 5.4. For this reason, CP80 is selected, presenting the best compromise between normalisation and sensitivity to damage.

Table 5.3 – Number of false positives ($\alpha = 99.9\%$), RU and RL for the years of 2017 and 2018 (Considered damaged: 10% of area loss in the stay-cable T19C19; Daily averaged series; Training period size: 365 days; Cut-off of R set to 0.4).

Criterion	No. positives ($\alpha = 99.9\%$)		No. positives (%) ($\alpha = 99.9\%$)		RU	$RL_{99.9\%}$	
	Undamaged	Damaged	Undamaged	Damaged		Undamaged	Damaged
CP70	8	351	2.28	100	9.81	0.50	4.91
CP80	2	351	0.57	100	11.62	0.42	4.87
CP90	0	347	0	98.86	13.75	0.18	2.50

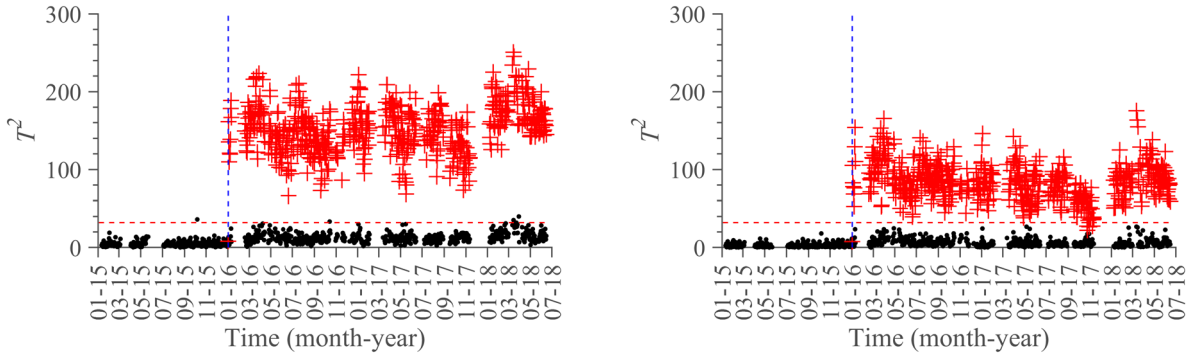

(a) (b)

Figure 5.4 – Hotelling T^2 control chart for undamaged (black points) and damaged (red points - 10% of area loss in stay-cable T19C19) state: (a) the principal components are chosen using CP80; (b) the principal components are chosen using CP90. UCL determined for $\alpha = 99.9\%$. Training period size: 365 days. The vertical blue dashed line indicates the end of the training period.

5.4.2.3 Sensitivity to the training period size

A key issue when fitting any model to remove the EOVs is the choice of the training period size. It is usually suggested to use at least one year of data to fit the models in order to capture the full range of EOVs. In order to evaluate this effect, the training period size is changed from 56 days to 730 days (2 years) and the evolution of the performance indicators is analysed.

The evolution of the number of false positives, RU and $RL_{\alpha=99.9\%}$ with the training period size are presented, respectively, in Figures 5.5,5.6 and 5.7. As expected, when the training period is increased, both the number of false positives and $RL_{\alpha=99.9\%}$ decrease while RU increases. However, more relevant than that is the fact that all the performance indicators

tend to stabilise around acceptable values only after the training period goes beyond one year, irrespective of the adopted criterion to choose the number of principal components to retain.

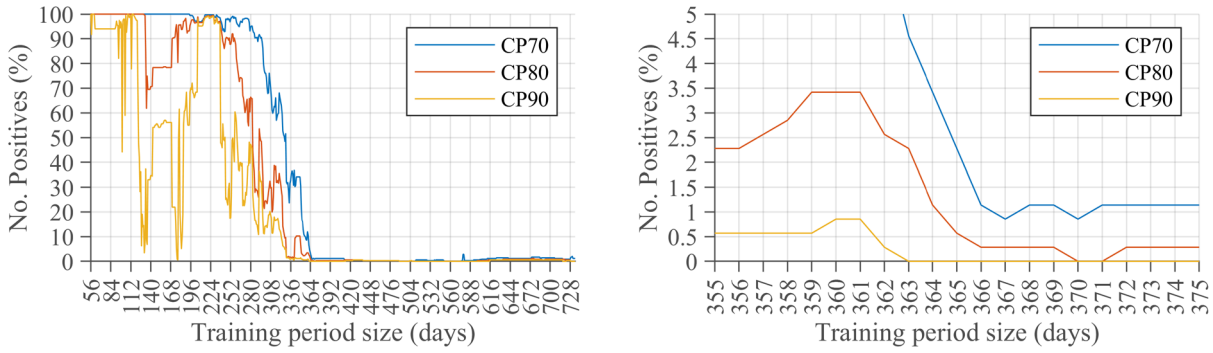

(a) (b)

Figure 5.5 – Evolution with the training period size of the number of positives ($\alpha = 99.9\%$) for the data of the years 2017 and 2018: (a) 56 to 730 days; (b) 355 to 375 days.

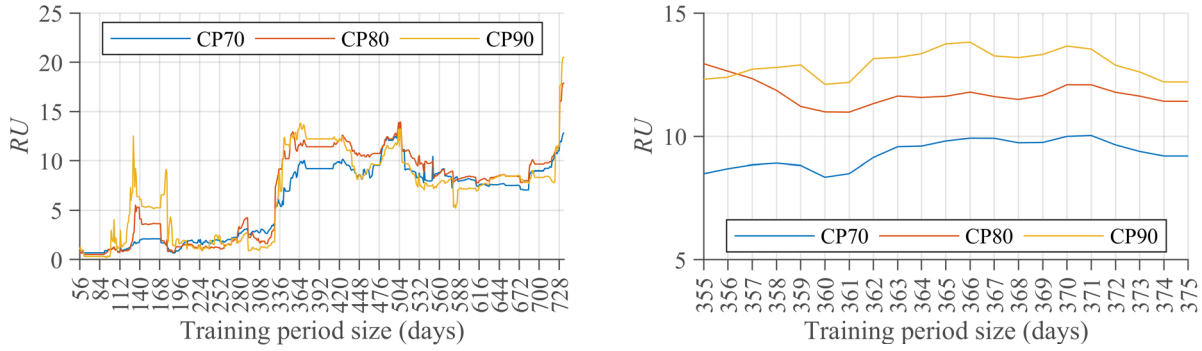

(a) (b)

Figure 5.6 – Evolution with the training period size of the performance indicator RU for the data of the years 2017 and 2018: (a) 56 to 730 days; (b) 355 to 375 days.

For CP80 the percentage of false positives stabilises at 0.28%, which is higher than 1-α = 0.1% (see Figure 5.5 (b)) but is only due to one point above the UCL. As expected and shown in the previous section, RU becomes higher when more principal components are retained (see Figure 5.6 (b)) because the denominator of RU becomes lower. To evaluate the sensitivity to damage, one should consider RL_α (Figure 5.7). Similar values of RL_α are obtained for CP70 and CP80, meaning that similar sensitivities to damage are obtained, although CP80 has a lower number of false positives (see Figure 5.7 (d)). Significantly lower values are obtained for CP90 (see Figure 5.7 (b) and (d)), which indicates that in this case the model is less sensitive to anomalies. Irrespective of the size of the training period, CP80

appears again as the optimum model.

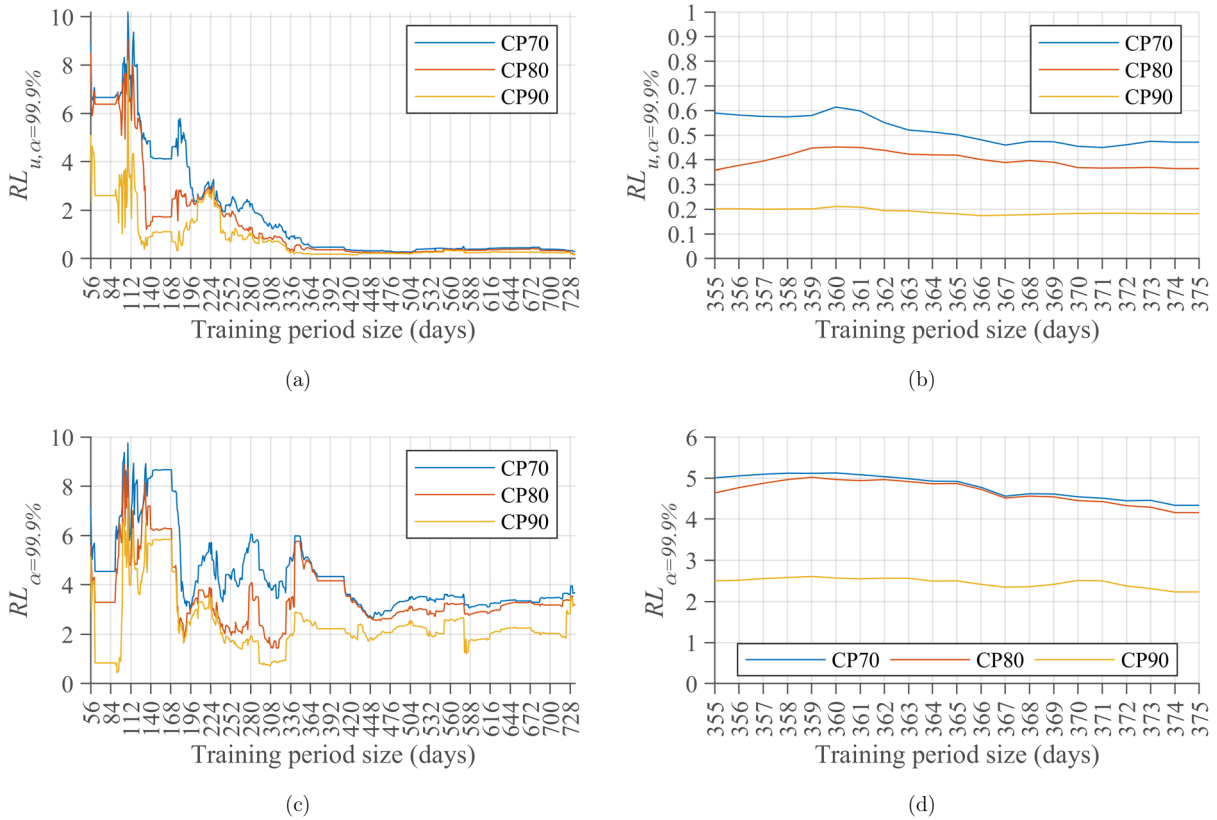

Figure 5.7 – Evolution with the training period size of the performance indicator RL ($\alpha = 99.9\%$) for the data of the years 2017 and 2018: (a) 56 to 730 days (undamaged); (b) 355 to 375 days (undamaged); (c) 56 to 730 days (damaged); (d) 355 to 375 days (damaged).

5.4.2.4 *Effect of the data averaging and window size (r)*

Until now, only the results corresponding to daily averaged series with the T^2 statistic computed using a window size (r) of one day have been presented. Therefore, the number of false positives and the performance indicators RU and RL are presented in Table 5.4 for hourly data, daily averaged data, two-day averaged data and three-day averaged data. The first conclusion that can be taken is that when the hourly data is used, it is not possible to achieve both an efficient suppression of the EOVs and a high sensitivity to damage. However, when the averaged data is used, the situation improves significantly. This happens due to the following reasons: first, the process of data averaging works as a low-pass filter removing the sudden changes, such as those due to solar radiation, wind and traffic, that are difficult to model; second, the correlation between the predictor variables and the dependent variables increases with the averaging process. Therefore, no relevant information

is lost and the ability for detecting a change in the structural response of the bridge is increased with the process of data averaging.

Table 5.4 – Number of false positives $(\alpha = 99.99\%)$, RU and RL for different number of points per day and window sizes (r) in the computation of the T^2 statistic (Data from the years 2017 and 2018; considered damage scenario: 10% of area loss in the stay-cable T19C19; Training period size: 365 days (year of 2015); Cut-off of $|R|$ set to 0.4).

No. points per day	r	No. positives		No. positives (%)		RU	$RL_{u,\alpha=99.99\%}$	$RL_{\alpha=99.99\%}$
		Undamaged	Damaged	Undamaged	Damaged		Undamaged	Damaged
24 (8760)	1	11	35	0.13	0.41	1.46	0.19	0.28
	6	294	902	21.46	65.84	1.72	0.73	1.26
	12	439	624	68.27	97.05	1.81	1.32	2.39
	24	270	293	92.15	100	1.93	2.39	4.60
	48	118	120	98.33	100	1.97	4.56	8.99
	72	64	64	100	100	1.96	6.67	13.07
1 (365)	1	1	351	0.28	100	11.62	0.34	4.00
	2	10	168	5.95	100	12.78	0.56	7.12
	3	33	103	32.04	100	13.11	0.85	11.08
1/2 (183)	1	1	172	0.58	100	13.70	0.34	4.68
	2	1	78	1.28	100	15.19	0.48	7.33
	3	13	48	27.08	100	15.98	0.75	11.91
1/3 (122)	1	0	117	0.00	100	16.47	0.32	5.35
	2	0	53	0.00	100	19.68	0.36	7.14
	3	3	33	9.09	100	20.44	0.58	11.91

Concerning the window size r used to compute the T^2 statistic, as expected the sensitivity to damage increases along with the window size (higher values of RU and RL). However, the number of false positives also increases. Analysing the obtained values of RL_u (undamaged state) and the percentage of false positives, it can be concluded that, generally, the suppression of the EOVs was effective when RL is lower than 0.5 (shaded lines in Table 5.4). It can also be concluded that is better to increase the window over which the data is averaged instead of augmenting r because the suppression of the EOVs becomes more effective, as can be assessed by the values of RU and RL_u (compare the values in blue and green in Table 5.4).

5.4.2.5 Application to another set of data

In order to evaluate the effectiveness of the proposed methodology when applied to other types of data, an application to the dataset constituted by the six girder vertical deflections (the localisation of the sensors is depicted in Figure 3.1) is presented in Figure 5.8. It can

be seen that the methodology is effective in suppressing the EOVs and that nothing relevant happened in the bridge except for the period between January and March 2018. Indeed, the detected anomaly in that period was due to an irregularity in water pressure of the liquid levelling system, which was fixed in one of the inspections to the structural monitoring system. Note that the differences in the time series before and after the anomaly is fixed are not noticeable with the unaided eye (see Figure 5.9). Thus, the effectiveness of the proposed methodology for anomaly detection is demonstrated.

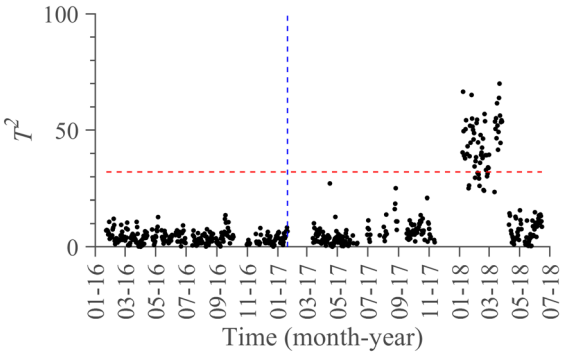

Figure 5.8 – Hotelling T^2 control chart for six vertical deflections (The cut-off of $|R|$ is set to 0.4; The principal components are chosen using CP80; UCL determined for $\alpha = 99.99\%$; Training period size: 365 days; Daily averaged values. The vertical blue dashed line indicates the end of the training period).

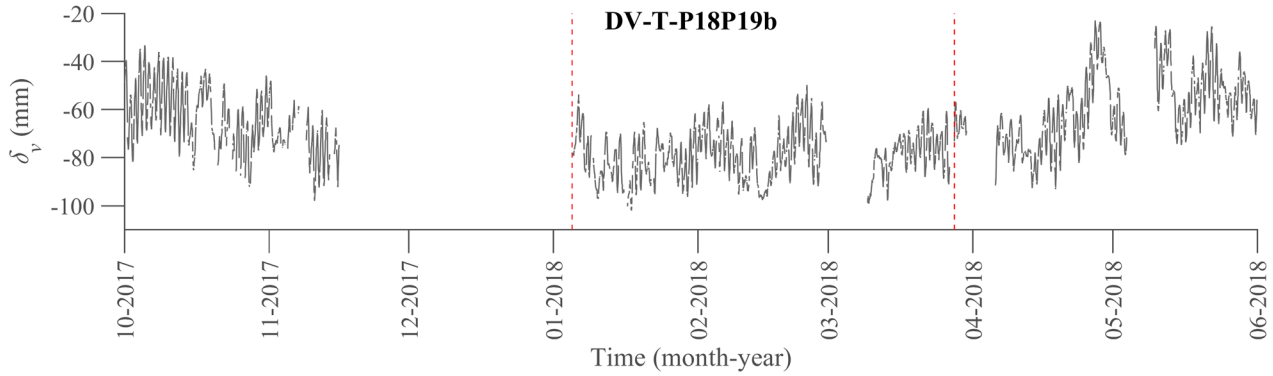

Figure 5.9 – Time series of the sensor DV-T-P18P19b between March and May 2018. The vertical dashed lines comprise the period of sensor malfunctioning.

5.4.3 Damage detection

The main goal of the present section is to evaluate the sensitivity of the proposed methodology to damages in the suspension system of the Corgo Bridge. For that propose, area reductions of 30% are sequentially and individually considered in all the stay cables. In Figure 5.10, the ratio $RL_{\alpha=99.99\%}$ determined for the 88 damage scenarios is presented.

Since the methodology is very sensitive to damages in the instrumented stay cables, where damages smaller than 1% can be detected, these cables are not represented in Figure 5.10. Assuming that damage is unambiguously flagged when $RL \geqslant 1.0$, the most difficult damages to detect are those in the stay-cables near the pylons and in the stay cables in the side spans further away from the pylons.

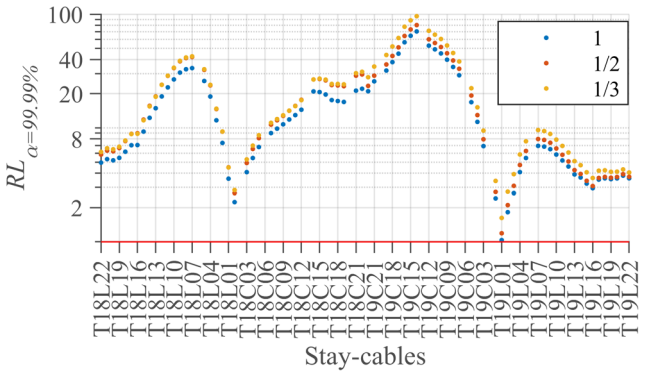

Figure 5.10 – Performance indicator $RL_{\alpha=99.99\%}$ obtained for 88 damage scenarios (30% of area loss individually in each stay-cable). Horizontal red line: $RL=1$. Daily averaged values; $r=1$; training period size: 366 days (year of 2016); The cut-off of $|R|$ is set to 0.4; The principal components are chosen using CP80. 1, 1/2 and 1/3 refer to daily, two-day and three-day averaged data, respectively.

Although the bridge is nearly symmetric and the introduced damages are also symmetric, the obtained sensitivities are not symmetric. The methodology is more sensitive when the damages are located in the central span near to the pylon P19 and in the side span of the pylon P18. This is due to the standard deviation of the time series: the lower the standard deviation is, the higher is the sensitivity to damage. Therefore, different sensitivities for symmetric damages are due to the effectiveness of the data normalisation process, which is not equal for all the sensors. Within the non-instrumented stay cables, from Figure 5.10 it is also possible to conclude that damage is more easily flagged in the stay cable T19C14. On the other side, the stay-cable T19L01 is the one where damage is more difficult to detect. In order to determine the minimum damages that can be detected in each of the stay cables, the intensity of damage (section loss) was varied from 0.5% to 100%, the latter corresponding to the loss of a stay-cable. The evolution of $RL_{\alpha=99.99\%}$ with the intensity of damage in the stay-cable T19C14 is presented in Figure 5.11. It can be concluded that the minimum damage that can be detected with the selected dataset is an area reduction of 2.5% when a window of size one is used ($r=1$) for the computation of the T^2 statistic. If a window of size two is used ($r=2$), an $RL_{\alpha=99.99\%}$ above the unit is obtained for an area

reduction between 1.5% and 2.5% (see Figure 5.11 (b)).

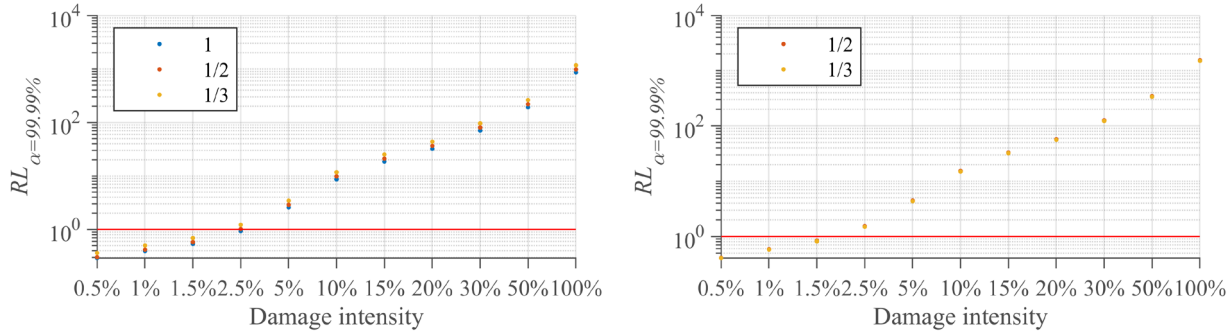

(a) (b)

Figure 5.11 – Variation of $RL_{\alpha=99.99\%}$ with the intensity of damage in stay-cable T19C14: (a) *r=1*; (b) *r=2*. The numbers 1, 1/2 and 1/3 refer to daily, two-day and three-day averaged data, respectively. Training period size: 366 days; the cut-off of $|R|$ is set to 0.4; The principal components are chosen using CP80.

If the same analysis is performed for the stay-cable T19L01, as depicted in Figure 5.12, it is concluded that the minimal damage that can be detected corresponds to an area reduction of 30% if a window of size one is used (*r=1*) for the computation of the T^2 statistic. However, when two-day or three-day averaged data and a window size of two (*r=2*) are adopted (Figure 5.12 (b)), it is possible to flag an area reduction of 20% in the stay-cable T19L01. Bearing in mind that the accidental loading scenario corresponding to the loss of one stay-cable was considered in the design of the Corgo Bridge [175], the proposed methodology can flag damage in the suspension system of the bridge in its early stage.

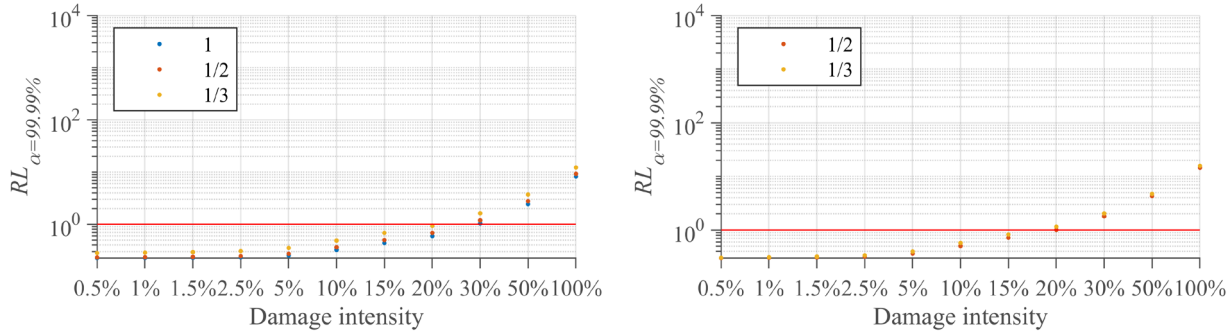

(a) (b)

Figure 5.12 – Variation of $RL_{\alpha=99.99\%}$ with the intensity of damage in stay-cable T19L01: (a) *r=1*; (b) *r=2*. 1, 1/2 and 1/3 refer to daily averaged data, two-day averaged data and three-day averaged data, respectively. Training period size: 366 days; the cut-off of $|R|$ is set to 0.4; the principal components are chosen using CP80.

5.4.4 Damage localisation

After the damage is flagged, an insight on its localisation should be given. Bearing this in

mind, subsets of the original dataset can be constructed in order to evaluate its sensitivity to the flagged damage. For this propose, two subsets were considered: the forces in the stay-cables of the pylon P18 (F-T18L06, F-T18C02, F-T18C06, F-T18C13 and F-T18C20) and those of the pylon P19 (F-T19C20, F-T19C13, F-T19C06, F-T19C02 and F-T19L06). The corresponding performance indicator values $RL_{\alpha=99.99\%}$ obtained for the 88 damage scenarios are depicted in Figure 5.13.

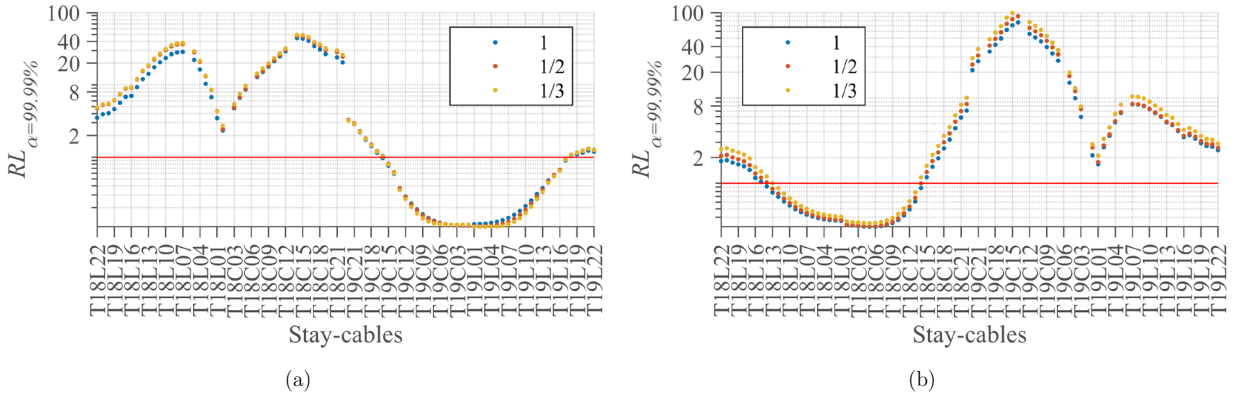

Figure 5.13 – Performance indicator $RL_{\alpha=99.99\%}$ obtained for 88 damage scenarios (30% of area loss individually in each stay-cable) for subsets: (a) stay-cables of the pylon P18; and (b) stay-cables of the pylon P19. Horizontal red line: $RL=1$. Daily averaged values; $r=1$; training period size: 366 days (year of 2016); the cut-off of $|R|$ is set to 0.4; the principal components are chosen using CP80. 1, 1/2 and 1/3 refer to daily, two-day and three-day averaged data, respectively.

As expected, the sub-datasets are more sensitive to damages located near the selected sensors. Defining the Localisation Index (LI) as the difference between the performance indicator RL of the dataset containing the instrumented stay cables of the pylon P18 $\left(RL^{P18}_{\alpha=99.99\%}\right)$ and the performance indicator RL of the dataset containing the instrumented stay cables of the pylon P19 $\left(RL^{P19}_{\alpha=99.99\%}\right)$,

$$LI = RL^{P18}_{\alpha=99.99\%} - RL^{P19}_{\alpha=99.99\%} \tag{5.13}$$

the Figure 5.14 is obtained. If $LI > 1.0$, the damage is located near the pylon P18. Otherwise, if $LI < 1.0$, the damage is located near the pylon P19. Naturally, if more instrumented stay-cables were available, a finer damage localisation would be possible. Even though, the indication provided with the available array of sensors can already be very useful for the inspection of the bridge after the damage is detected.

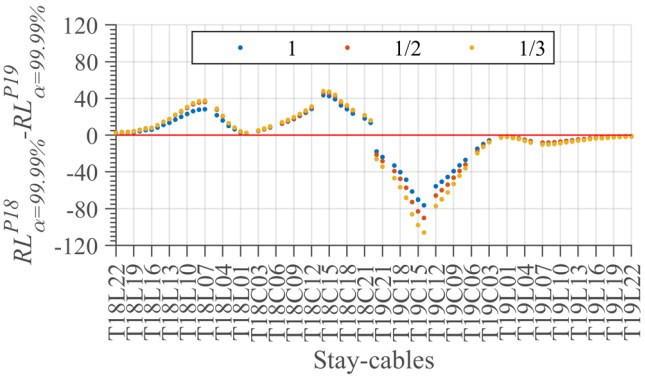

Figure 5.14 – Localisation Index (LI) for 88 damage scenarios (30% of area loss individually in each stay-cable).

5.5 Concluding remarks

An online data-based methodology for early damage detection and localisation under the effects of EOVs is proposed. Its application to 3½ years of data gathered from the SHM system of a large prestressed cable-stayed bridge is described and the performance is evaluated.

A pre-processing strategy is proposed prior to the application of data normalisation models. Outliers are first removed using the IQR and then the data is averaged on a daily, two-day or three-day basis in order to suppress the high-frequency changes due to, for instance, traffic, wind and solar radiation effects. It is demonstrated that this strategy considerably improves both the suppression of the EOVs and the sensitivity to damage.

The temperature and long-term effects are removed by combining two well-established multivariate statistical tools: MLR and PCA. The use of the MLR is justified by the expected linear relationship among the selected predictor and dependent variables. The PCA is applied to the residuals of the MLR model in order to suppress the EOVs not suppressed by the MLR model, namely the remaining temperature effects and the long-term behaviour due to rheological effects of the concrete. The use of PCA implies a nearly linear relationship between the sensors readings. This assumption is demonstrated to be valid during the observed period since the process is in control for 3½ years. This assumption may cease to be valid in the long-term and a slow drift in the T^2 values may start being observed.

The criteria guiding the choice of the predictor variables in the MLR models, the number

of principal components to retain in the PCA models and the training period size were evaluated by means of a parametric analysis. A trade-off between sensitivity to damage and robustness to false positives was identified. With regards to the training period size, stable results are only obtained when the training period size is equal to, or greater than, one year.

The methodology was applied to two distinct datasets: girder deflections and cable forces. The former was used to demonstrate the detection of a real and small temporary anomaly in the sensing system. The latter served to exemplify the ability for early-damage detection in the suspension system. Considering the available sensor layout, the proposed methodology is shown to unambiguously detect a reduction of the cross-section area of 2.5% and 20% in the most sensitive and least sensitive non-instrumented stay-cables, respectively. Area reductions smaller than 1% can be flagged in all the instrumented stay cables.

Finally, an approach based on the relative variation of the T^2 statistic on sub-datasets is proposed for damage localisation. The available sensor layout allows determining in which of the pylons the damaged stay cable is anchored.

Chapter 6*

ONLINE EARLY DAMAGE DETECTION USING COINTEGRATION ANALYSIS

6.1 Introduction

Recently, cointegration analysis – from the field of econometrics [61] – has been proposed as a new output-only approach to suppress the effects of EOVs in process monitoring [33] and SHM [40, 44]. The basic idea behind cointegration analysis is to establish relationships between nonstationary time series in order to create a stationary residual. When the established relationship ceases being stationary, the structure is no longer operating under normal behaviour [44].

Notwithstanding the increasing research in cointegration analysis applied to SHM and of the proposed enhancements and derivatives in the last few years [45, 177-179, 219, 239, 240], few case studies involving real civil engineering structures using cointegration analysis can still be found in the technical literature [36, 37, 120, 128, 129]. Moreover, all the

* This chapter is based on the paper: Sousa Tomé, E., M. Pimentel, and J. Figueiras (20xx). *Real-time damage detection under environmental and operational effects using cointegration analysis – application to experimental data from a cable-stayed bridge.* Mechanical Systems and Signal Processing. [Submitted].

available applications use the Engle-Granger procedure [61] for determining the cointegration vectors, which is suitable only for bivariate datasets [40, 46]. In the present chapter, a multivariate cointegration methodology based on the Johansen procedure [97], which is a maximum-likelihood multivariate estimation procedure, is systematised. The methodology is applied to real datasets obtained from the structural monitoring system of the Corgo Bridge. The measured stay cable forces of the suspension system of the bridge are chosen as damage sensitive-features.

The EOVs, such as temperature and long-term behaviour due to rheological effects of the concrete, are expected to be suppressed in an output-only manner, that is, by the establishment of relationships between the cable forces. Indeed, as demonstrated in Chapter 4, the long-term effects due to the concrete rheology and prestress relaxation have an important role in the structural response of the bridge, inducing non-stationarity in the sensor readings.

After the EOVs are suppressed using cointegration analysis, the Hotelling T^2 control chart is used for anomaly/damage detection. To evaluate the damage detection ability of the proposed methodology, damage scenarios involving cross-section area reduction of the stay-cables are numerically simulated. The real data being acquired by the SHM system is superposed with the structural response due to damage events obtained via the finite element model of bridge previously validated in Chapters 3 and 4. The damage scenarios involving section loss of the stay-cables were considered since the safety of cable-supported bridges is closely related to the cable integrity [35]. In this context, the present Chapter proposes a strategy for early damage detection in civil engineering structures and intends to be a contribution to the transition of SHM technology from academia to engineering practice.

6.2 Data normalisation and novelty detection: theoretical background

6.2.1 Data normalisation: cointegration analysis

6.2.1.1 Stationarity, non-stationarity and order of integration

A process is said to be stationary if it has time-invariant statistical moments. In practice,

the weak definition of stationarity is often used. This definition states that a process is stationary if the first two statistical moments (mean and variance) are constant in time [30].

A common way to describe a non-stationary process is by means of the order of integration. If a non-stationary process becomes stationary after differencing d times, it is said to be integrated of order d, denoted as $I(d)$ [82]. The order of integration can be achieved by means of a unit root test, such as the augmented Dickey-Fuller (ADF) test [50, 51]. The ADF test tests the null hypothesis that a unit root is present in the time series $(\rho = 1)$ against the alternative hypothesis that the time series is stationary $(\rho < 1)$ using the model:

$$y_t = \rho y_{t-1} + \xi_1 \Delta y_{t-1} + ... + \xi_k \Delta y_{t-k} + \mu + \nu t + \varepsilon_t \tag{6.1}$$

where Δ is the differencing operator, such that $\Delta y_t = y_t - y_{t-1}$, k is the number of lagged difference terms, ξ_i is the ith autoregressive coefficient, μ is a drift coefficient, ν is a deterministic trend coefficient and ε_t is a Gaussian white noise process. The inclusion of a drift and/or deterministic trend is optional. In the present work, only the drift was considered. The number of lagged difference terms k can be determined using an information criterion such as the Hannan-Quinn information criterion [81], which is adopted in the present work. The null hypothesis $\rho = 1$ is assessed via the test statistic:

$$t_\rho = \frac{\hat{\rho} - 1}{\sigma_\rho} \tag{6.2}$$

where $\hat{\rho}$ is the ordinary least squares estimate of ρ and σ_ρ is the standard error of ρ. The null hypothesis is rejected if $t_\rho < t_\alpha$, being t_α the critical value for the statistics at the significance level α. A significance level of 1% is adopted in this work. If the null hypothesis is rejected, the time series is stationary. If the null hypothesis is not rejected, the ADF test should be repeated for Δy_t. If the null hypothesis is then rejected, y_t is an $I(1)$ nonstationary sequence. This process can be continued until the order of integration of the time series is found.

6.2.1.2 COINTEGRATION AND JOHANSEN PROCEDURE

Two or more non-stationary time series are said to be cointegrated if there exists at least a linear combination of them that is stationary. Considering a set of M $I(1)$ time series $\mathbf{y}_t = [y_{1,t}, y_{2,t}, ..., y_{M,t}]^T$, $\mathbf{y}_t$ is cointegrated if there exists a vector $\boldsymbol{\beta} = [\beta_1, \beta_2, ..., \beta_M]^T$ such that:

$$\boldsymbol{\beta}^T \mathbf{y}_t = \beta_1 y_{1,t} + \beta_2 y_{2,t} + ... + \beta_M y_{M,t} = z_t \sim I(0) \tag{6.3}$$

where the vector $\boldsymbol{\beta}$ is called a cointegrating vector and z_t the cointegration residual or long-run equilibrium relationship between time series. Since $\mathbf{y}_t$ is M-dimensional, there may exist at most $M-1$ linearly independent cointegrating vectors. It should be noted that for the time series to be cointegrated, they must have shared/common trends and the same order of integration [40].

If $\mathbf{y}_t$ is cointegrated with N_r cointegrating vectors, where $0 < N_r < M$, the cointegration relationship given by equation (6.3) can be extended to multiple cointegration:

$$\mathbf{B}^T \mathbf{y}_t = \begin{bmatrix} \boldsymbol{\beta}_1^T \mathbf{y}_t \\ \vdots \\ \boldsymbol{\beta}_{N_r}^T \mathbf{y}_t \end{bmatrix} = \begin{bmatrix} z_{1,t} \\ \vdots \\ z_{N_r,t} \end{bmatrix} \sim I(0) \tag{6.4}$$

where the M-by-N_r matrix $\mathbf{B}$ is the cointegration matrix. Two approaches have been followed to estimate the cointegration vector(s). The first one is the Engle-Granger procedure [61] which is suitable only for bivariate data sets [40, 46]. The second one is the Johansen procedure [97] which is a maximum-likelihood multivariate estimation procedure. The Johansen procedure is a combination of cointegration and error correction models in a Vector Auto-regression (VAR) model [46]. Consider the following VAR(k) model for the M-by-1 vector $\mathbf{y}_t$:

$$\mathbf{y}_t = \mathbf{A}_1 \mathbf{y}_{t-1} + ... + \mathbf{A}_k \mathbf{y}_{t-k} + \boldsymbol{\Phi} \mathbf{d}_t + \boldsymbol{\varepsilon}_t \tag{6.5}$$

where $\boldsymbol{\Phi} \mathbf{d}_t$ contains the deterministic terms (e.g. no constant, constant only or constant plus time trend). The VAR(k) model is stable (note that stability implies stationarity, that is, a stable process is one that will not diverge to infinity) if the roots of

$$\left|\mathbf{I}_M - \mathbf{A}_1 z - ... - \mathbf{A}_k z^k\right| = 0 \tag{6.6}$$

lie outside the complex unit circle [238]. If equation (6.6) has a root on the unit circle (which implies that the VAR model is not stable) then some or all of the variables in $\mathbf{y}_t$ are $I(1)$ and they may also be cointegrated [238].

However, the cointegration relationships are not explicitly apparent in the VAR representation. They become apparent when the VAR model is transformed to the Vector Error Correction Model (VECM) which takes the form [46]:

$$\Delta\mathbf{y}_t = \mathbf{\Pi}\mathbf{y}_{t-1} + \mathbf{\Gamma}_1\Delta\mathbf{y}_{t-1} + ... + \mathbf{\Gamma}_{k-1}\Delta\mathbf{y}_{t-k+1} + \mathbf{\Phi}\mathbf{d}_t + \boldsymbol{\varepsilon}_t \tag{6.7}$$

where $\mathbf{\Gamma}_i = -(\mathbf{I}_M - \mathbf{A}_1 - ... - \mathbf{A}_i)$ with $i = 1,...,k-1$ and $\mathbf{\Pi} = -(\mathbf{I}_M - \mathbf{A}_1 - ... - \mathbf{A}_k)$. The M-by-M matrixes $\mathbf{\Pi}$ and $\mathbf{\Gamma}_i$ contain, respectively, information on the long-run and short-run adjustments to changes in $\mathbf{y}_t$. The term $\mathbf{\Pi}\mathbf{y}_{t-1}$ is the only one which includes potential $I(1)$ variables and for $\Delta\mathbf{y}_t$ to be $I(0)$, $\mathbf{\Pi}\mathbf{y}_{t-1}$ must also be $I(0)$. Therefore, if the cointegration relationships exist, they are contained in $\mathbf{\Pi}\mathbf{y}_{t-1}$ [238]. If the VAR(k) has unit-roots then from equation (6.6) and taking as example the root $z = 1$, it becomes clear that $\mathbf{\Pi}$ is a singular matrix since

$$\left|\mathbf{I}_M - \mathbf{A}_1 - ... - \mathbf{A}_k\right| = \left|\mathbf{\Pi}\right| = 0 \tag{6.8}$$

If $\mathbf{\Pi}$ is singular then it has reduced rank $rank(\mathbf{\Pi}) = N_r < M$. There are three cases to consider [238]:

- $rank(\mathbf{\Pi}) = M$ (full rank), which implies that all the variables in $\mathbf{y}_t$ are $I(0)$ and there is no cointegration relationships.
- $rank(\mathbf{\Pi}) = 0$ which implies that $\mathbf{\Pi} = 0$ and $\mathbf{y}_t$ is $I(1)$ and not cointegrated. The VECM in equation (6.7) reduces to a VAR(k-1) model in first differences:

$$\Delta\mathbf{y}_t = \mathbf{\Gamma}_1\Delta\mathbf{y}_{t-1} + ... + \mathbf{\Gamma}_{k-1}\Delta\mathbf{y}_{t-k+1} + \mathbf{\Phi}\mathbf{d}_t + \boldsymbol{\varepsilon}_t \tag{6.9}$$

- $0 < rank(\mathbf{\Pi}) = N_r < M$ which implies that $\mathbf{y}_t$ is $I(1)$ with N_r linearly independent cointegration vectors and $M - N_r$ common stochastic trends (or unit-roots). Since

$\mathbf{\Pi}$ has rank N_r, it can be written as the product $\mathbf{\Pi} = \mathbf{A}\mathbf{B}^T$, where $\mathbf{A}$ is an M-by-N_r matrix which represents the speed of adjustment to disequilibrium, that is, the elements of $\mathbf{A}$ distribute the impact of the cointegration vectors to the evolution of $\Delta\mathbf{y}_t$, and $\mathbf{B}$ is an M-by-N_r matrix with the long-run coefficients, that is, the cointegration matrix [82, 238].

Determination of the cointegration vectors

Johansen's procedure applies maximum likelihood to the VAR model, assuming that the errors are Gaussian [131]. Defining $\mathbf{u}_{0,t} = \Delta\mathbf{y}_t$, $\mathbf{u}_{1,t} = \mathbf{y}_{t-1}$, $\mathbf{u}_{2,t} = \left[\Delta\mathbf{y}_{t-1}{}^T, \Delta\mathbf{y}_{t-2}{}^T, ..., \Delta\mathbf{y}_{t-k}{}^T, \mathbf{d}_t{}^T\right]^T$ and $\mathbf{\Psi} = \left[\mathbf{\Gamma}_1, \mathbf{\Gamma}_2, ..., \mathbf{\Gamma}_{k-1}, \mathbf{\Phi}\right]$, equation (6.7) can be rewritten as [40]:

$$\mathbf{u}_{0,t} - \mathbf{A}\mathbf{B}^T\mathbf{u}_{1,t} = \mathbf{\Psi}\mathbf{u}_{2,t} + \boldsymbol{\varepsilon}_t \tag{6.10}$$

The short-run dynamics can be taken out by regressing $\mathbf{u}_{0,t}$ and $\mathbf{u}_{1,t}$ separately on the right-hand side of equation (6.10) [82]. The residual vectors $\mathbf{r}_{0t}$ and $\mathbf{r}_{1t}$ are then obtained from:

$$\mathbf{u}_{0,t} = \mathbf{C}_1\mathbf{u}_{2,t} + \mathbf{r}_{0,t} \tag{6.11}$$

$$\mathbf{u}_{1,t} = \mathbf{C}_2\mathbf{u}_{2,t} + \mathbf{r}_{1,t} \tag{6.12}$$

being the coefficient matrixes $\mathbf{C}_1$ and $\mathbf{C}_2$ obtained by ordinary least squares. The residual vectors $\mathbf{r}_{0t}$ and $\mathbf{r}_{1t}$ can be used to form residual product-moment matrixes:

$$\mathbf{S}_{ij} = \frac{1}{T}\sum_{t=1}^{T}\mathbf{r}_{it}\mathbf{r}_{jt}^{\mathrm{T}} \qquad i, j = 0,1 \tag{6.13}$$

where T is the number of observations or data points. Finally, the cointegrating vectors $\mathbf{B}$ are found as the eigenvectors of the eigenvalue problem,

$$\left|\lambda\mathbf{S}_{11} - \mathbf{S}_{10}\mathbf{S}_{00}^{-1}\mathbf{S}_{01}\right| = 0 \tag{6.14}$$

The cointegrating vector associated with the highest eigenvalue corresponds to the most stationary linear combination of the original variables. Indeed, the eigenvalues λ_i are a measure of how strongly the cointegrated relations are correlated with the stationary part

of the process [40, 82]. The cointegrated relation is 'more stationary' the larger the eigenvalue is. Readers are referred to Appendix F for the explanation of the theory behind the Johansen's cointegration procedure.

On the choice of the number of lags

One important step in the Johansen procedure is the choice of number of lags k. In this work the number of lags k was chosen using the stationarity-based approach proposed by Dao *et al.* [46]. It can be summarized in the following steps:

i. Define the maximum and the minimum number of lags, k_{min} and k_{max} respectively. k_{min} was set to 3 and k_{max} was set according to the following equation [174]:

$$k_{max} = \left[12 \left(\frac{T}{100} \right)^{1/4} \right] \tag{6.15}$$

where the square brackets denote the integer part of the result.

ii. Determine $\mathbf{B}$ and calculate the M-1 cointegration residuals for all lag lengths between k_{min} and k_{max}.

iii. Calculate the ADF statistic for all cointegration residuals.

iv. Calculate the average ADF statistic for each lag length. The lag length with the most negative average ADF statistic is the lag length that produces the most stationary residuals obtained for the undamaged condition.

In the context of SHM, the cointegrating vectors of a set of variables are established using data from the undamaged state of the structure (usually called the training period). It is expected that the projection of the new data will remain stationary if the structure continues in its normal behaviour. Otherwise, if a damage is introduced, the projection of the new data is expected to become non-stationary.

6.2.1.3 ON THE CHOICE OF THE COINTEGRATION VECTORS

After the cointegration matrix $\mathbf{B}$ is determined, only the cointegration vectors that produce stationary cointegration residuals should be retained and used to project new data in the cointegration space. Thus, damage can be detected in real-time. The determination of the cointegration vectors is made by means of a likelihood ratio statistic test proposed by Johansen, the trace test [97]. For *I(1)* variables, in order to the product $\mathbf{\Pi y}_{t-1}$ in equation (6.7) to be stationary, the matrix $\mathbf{\Pi}$ is required to be rank deficient [40, 82]. If $\mathbf{\Pi}$ has full rank, the *I(1)* variables cannot be cointegrated. The trace test tests the null hypothesis $\mathbf{\Pi}$ having rank N_r against the alternative hypothesis of $\mathbf{\Pi}$ having full rank. Recalling that the rank of $\mathbf{\Pi}$ is equal to the number of non-zero eigenvalues of $\mathbf{\Pi}$, this test is based on the estimated eigenvalues λ_i of the matrix $\mathbf{\Pi}$ [238]. The trace statistic λ_{trace} used to test the hypothesis that there are at most r cointegration vectors is:

$$\lambda_{trace} = -T \sum_{i=r+1}^{M} \ln(1-\lambda_i) \; for \; N_r = 0,1,...,M-1 \tag{6.16}$$

The asymptotic distribution of this test statistic depends on the type of determinist trend considered in the model of equation (6.7) [40]. The normal procedure is to first test the hypothesis of no cointegration (N_r=0). If the null hypothesis is rejected, then test for N_r=*1*. One should continue increasing N_r until the null hypothesis is not rejected. When the null hypothesis of rank N_r is not rejected, then it is concluded that there are N_r cointegration vectors. These N_r cointegration vectors are used to project new data in the cointegration space.

6.2.2 CLASSIFICATION: HOTELLING T^2 CONTROL CHART

After the data is normalised, a control chart can be used to track the existence of abnormal values, which can be related to the presence of damage. The so-called control limits define the accepted process variability. The observation is said to be an out-of-control observation if an observation exceeds the control limits. In the context of SHM, this out-of-control observation may be associated with the presence of damage in the structure.

In order to have only one control-chart instead of having one for each monitored feature, the multivariate Hotelling T^2 control chart was adopted, being the T^2-statistic calculated

using the expression (5.8) [141]. In the present chapter, r was always set to be 1. Therefore, the lower control limit is zero and the upper control limit (UCL) is computed from equation (5.10). The T^2-statistic condensates all monitored features into a scalar indicator, working in the context of SHM as a damage indicator.

6.2.3 Summary of the proposed approach

To sum up, the followed procedure to suppress the environmental and operational effects from the data can be summarized in the following steps:

i. Evaluate the order of integration $I(d)$ of each monitored variable using the ADF test. Only variables integrated of order one $I(1)$ should be selected;

ii. Determine the number of k lags using the stationary-based approach proposed by Dao *et al.* [46];

iii. Calculate the M-1 cointegration residuals using the cointegration matrix $\mathbf{B}$ obtained for the lag length k chosen in the previous step;

iv. Choose the cointegration vectors to retain using the trace test;

v. Project new data in the cointegration space using the cointegration vectors selected in the previous step. Thus, damage can be detected in real-time;

vi. Compute the T^2 statistic.

6.2.4 Performance indicators

The ability for data normalisation and novelty detection of the proposed methodology is evaluated by means of three performance indicators. The first is the number of false positives, that is, the number of points above the UCL when the structure is in control and no damage was introduced in the bridge. This indicator is used to evaluate the ability of the methodology to suppress the environmental and operational effects. The lower the number of false positives is, the more effective was the suppression of the environmental and operational effects.

Since a data normalisation model can have a very low number of false positives but be poorly sensitive to damage, two other indicators were used to evaluate the sensitivity to damage. The first is the ratio between the mean values of the T^2 statistic in the damaged and undamaged states (RU) and is computed using equation (5.11). The second is the ratio between the mean values of the T^2 statistic in the damaged state and the UCL (RL_α) and is computed using equation (5.12). A high value of RU means that there is a clear distinction between the undamaged and damaged states. Values of $RL_\alpha > 1.0$ means that on average the points are above the UCL. The higher RL_α, the higher is the distance between the points and the UCL. When the data is not well-normalised, low values of RU and high values of RL_α are obtained. If low values of RL_α are obtained, the model is not damage sensitive. The best data normalisation methodology will be that simultaneously providing a lower number of false positives and higher values of both RU and RL_α.

6.3 Application to the case study

The present section describes the application of the proposed methodology to the experimental datasets obtained from the structural monitoring system of the Corgo Bridge.

6.3.1 Experimental time series and damage simulation

The half-hourly cable forces are pre-processed with the Interquartile Range Analysis algorithm [158] in order to remove the existing outliers and then daily averaged. The process of daily averaging can be seen as a low-pass filter, where the sudden changes due to traffic, wind and solar radiation are suppressed. The daily averaged experimental time series of the cable forces used in the present work are depicted in Figure 6.1. There are variations in cable forces not only due to the temperature changes, but also time trends due to the long-term effects of the concrete and prestress steel, as already discussed in Chapters 3 and 4.

For training period sizes larger than 171 days (starting in January 2015), all the cable forces time series are integrated of order one. Therefore, the conditions that the time series must have shared/common trends and must be integrated of the same order are fulfilled.

To evaluate the damage detection ability of the proposed methodology, damage scenarios involving the cross-section area reduction of the stay-cables are numerically simulated. The

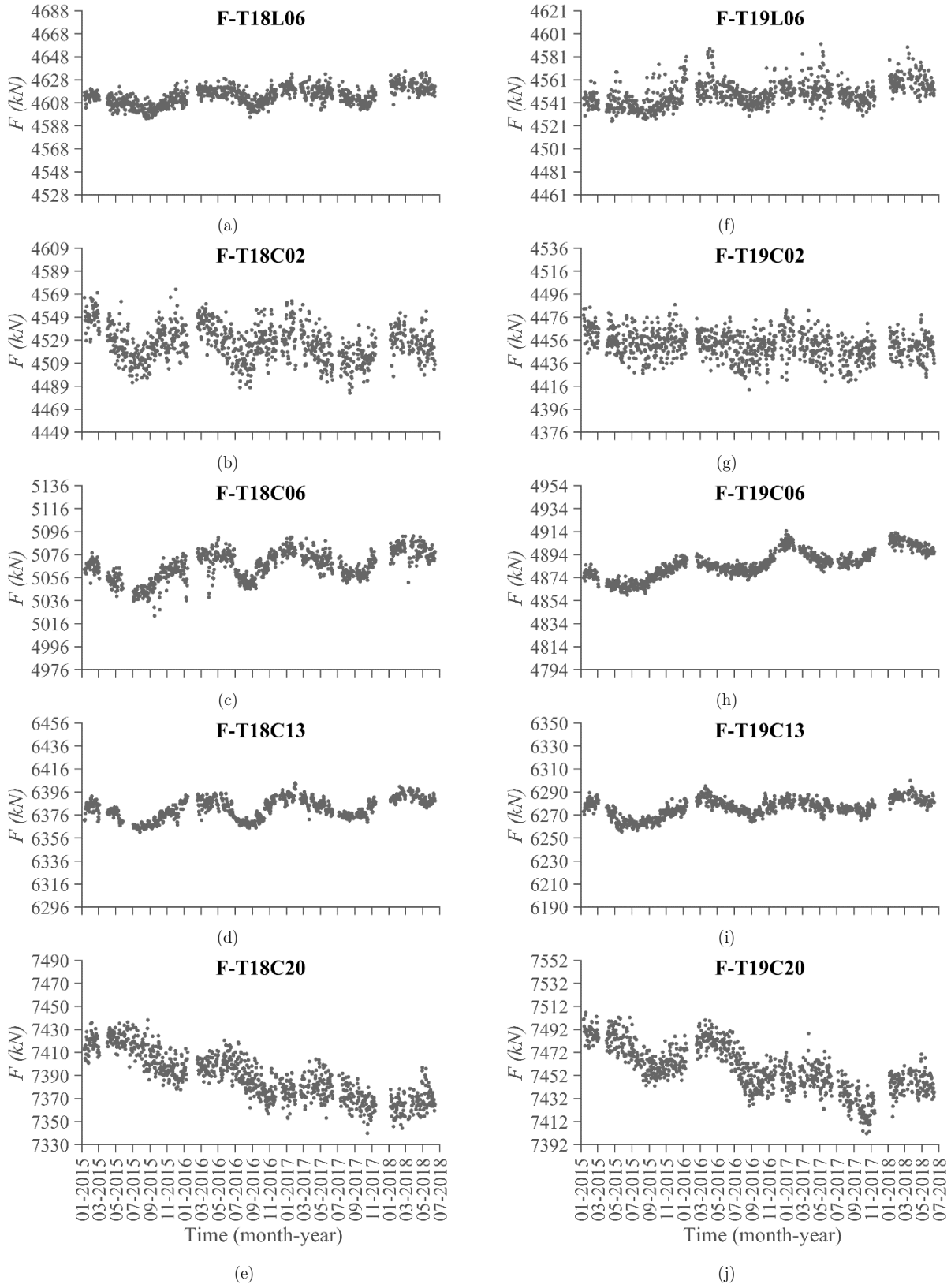

Figure 6.1 – Daily averaged experimental time series of the cable forces: (a) F-T18L06, (b) F-T18C02, (c) F-T18C06, (d) F-T18C13, (e) F-T18C20, (f) F-T19L06, (g) F-T19C02, (h) F-T19C06, (i) F-T19C13, (j) F-T19C20.

real data being acquired by the SHM system is superposed with the structural response due

to damage events obtained via the finite element model of the bridge previously validated in Chapters 3 and 4. The variations in the sensor responses due to the simulated damage scenarios are used to introduce a shift in the experimental time series. This is illustrated in Figure 6.2, where the corrupted experimental time series of the sensors F-T19C13 and F-T19C20 are presented for a damage scenario corresponding to 3.5% of area reduction in the stay cable T19C14. The calculated force variations are presented in Table 6.1 for the instrumented stay cables in two damage scenarios. These force variations are the shift values introduced in the experimental time series.

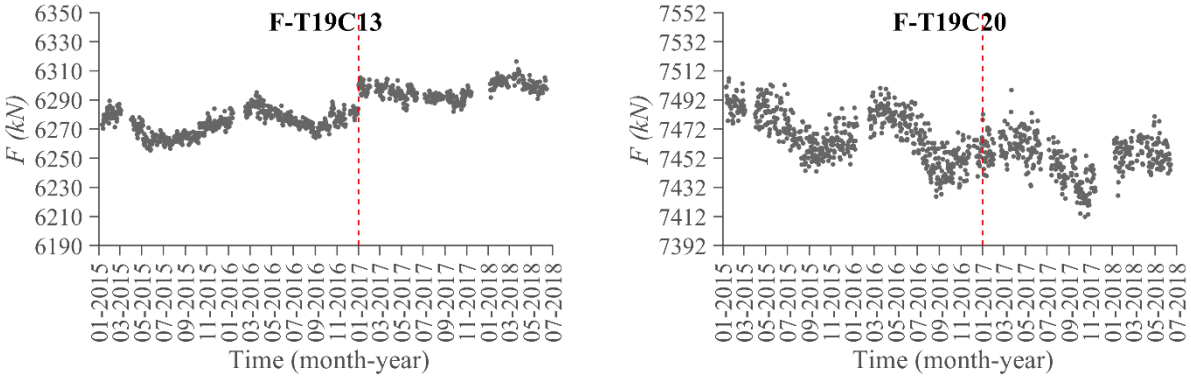

(a) (b)

Figure 6.2 – Daily averaged experimental time series with a simulated damage scenario corresponding to 3.5% of area reduction in the stay cable T19C14 introduced in January 2017 (vertical dashed line): (a) F-T19C13 and (b) F-T19C20.

Table 6.1 – Force variation in the stay cables in two damage scenarios.

	$\Delta F\ (kN)$	
Sensor	3.5% of area reduction in the stay cable T19C14	10% of area reduction in the stay cable T19C19
F-T18L06	0.5	2.6
F-T18C02	-0.3	-0.5
F-T18C06	-0.1	2.3
F-T18C13	1.4	9.6
F-T18C20	3.5	13.0
F-T19C20	10.2	44.7
F-T19C13	16.6	34.0
F-T19C06	9.0	10.0
F-T19C02	3.4	2.6
F-T19L06	-0.7	-3.2

6.3.2 Data normalisation

6.1.1.1. Cointegration residuals

The cointegration residuals obtained for a training period size of 730 days corresponding to the years of 2015 and 2016 are depicted in Figure 6.3. Eight cointegration vectors are determined using the trace test since the null hypothesis that $R = 8$ is accepted. Therefore, the cointegration residuals $z_{1,t}$ to $z_{8,t}$ are the cointegration residuals used to construct the Hotelling T^2 control chart depicted in Figure 6.4 (a). The UCL was computed for a significance level of 99.99% in order to reduce as much as possible the number of false positives. Even though, the number of false positives is superior to 0.01%. As discussed in the next section, the number of false positives is reduced when the training period size is increased. For instance, if a training period size of 365 days is considered (Figure 6.4(b)), the number of false positives is higher (about 5%). This happens since the data does not strictly respect the assumptions of the Hotelling T^2 control chart of independence between samples (no autocorrelation) and that the samples are multivariate normal. Alternatively, the UCL could be defined by the analysis of the histogram of T^2-statistic in the training period. However, the use of the theoretical limits was kept since this is established independently of the data. In Figure 6.4, along with the obtained control charts for the undamaged state is also presented the computed T^2-statistic for the same dataset corrupted with a simulated damage scenario (an area loss of 10% in stay-cable T19C19, identified in green in Figure 3.3). Since the introduced damaged is flagged for both the training period sizes, it can be concluded that the chosen cointegration residuals are insensitive to EOVs but still sensitive to damage.

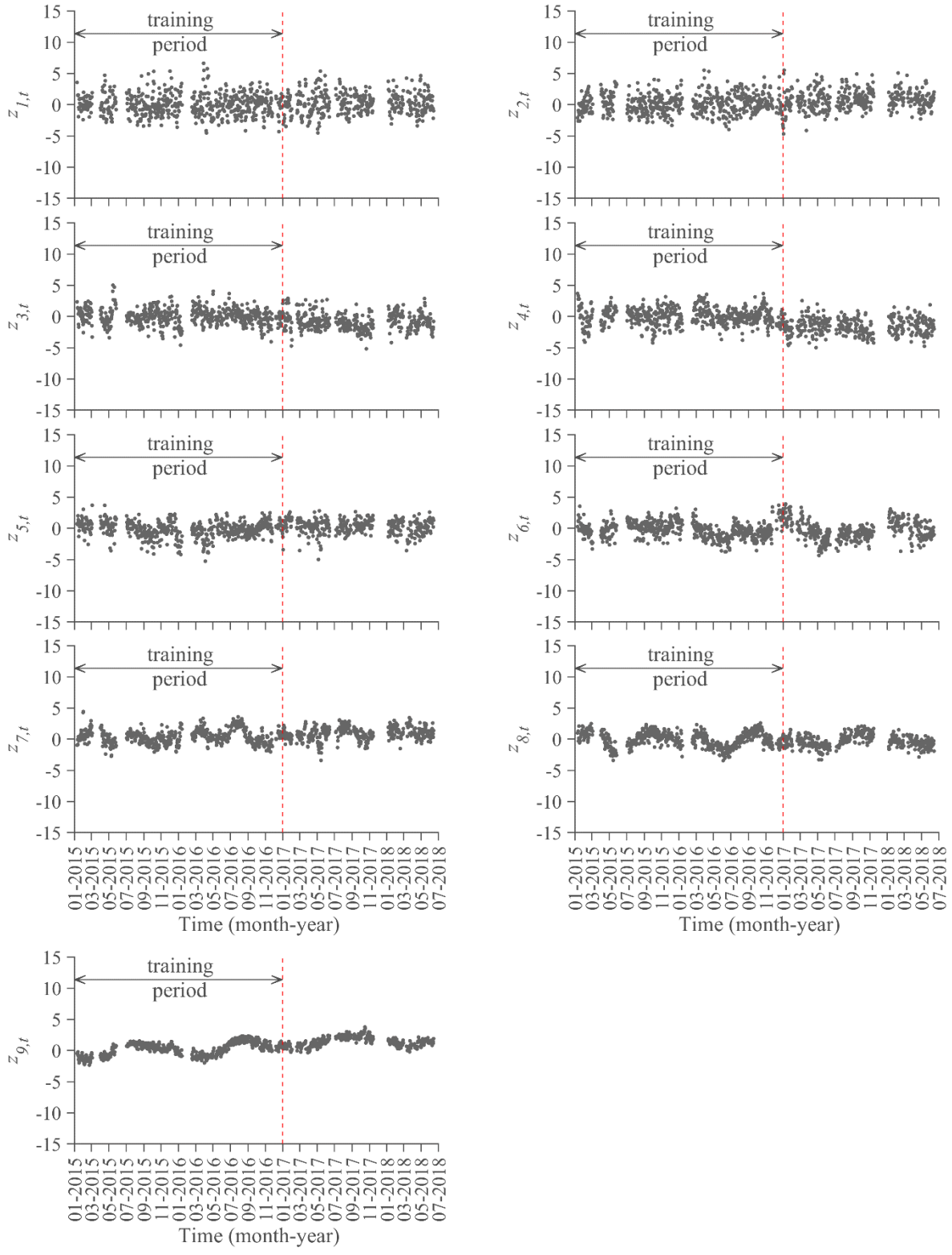

Figure 6.3 – Cointegration residuals. Training period size: 730 days (years of 2015 and 2016).

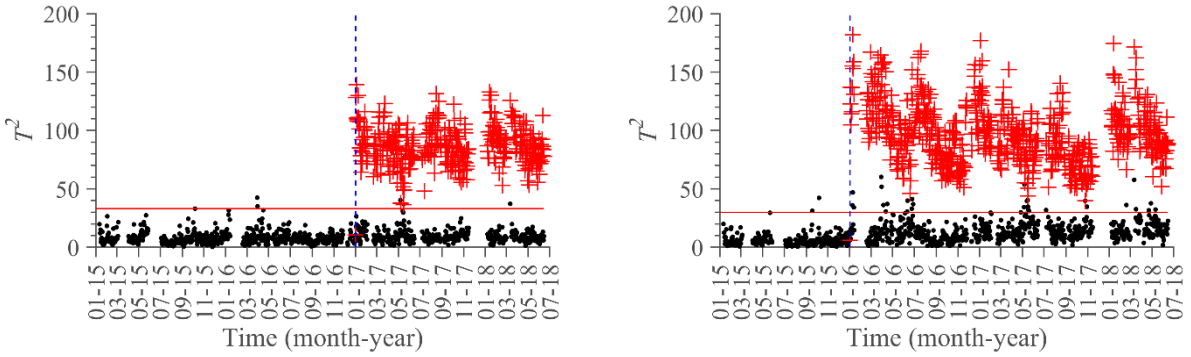

(a) (b)

Figure 6.4 – Hotelling T^2 control chart for a training period size of: (a) 730 days and (b) 365 days. Black points correspond to the undamaged state and red points to the simulated damaged scenario (10% of area loss in the stay cable T19C19). UCL determined for α=99.99% (horizontal red line). The vertical blue dashed line indicates the end of the training period.

6.1.1.2. Sensitivity to the training period size

An important issue when fitting a model with the aim of suppressing the environmental and operational effects is the choice of the training period size. In order to capture the full range of the environmental and operational variations, a minimum training period size of one year is usually adopted to fit the data normalisation models. To evaluate the influence of the training period size on the quality of the data normalisation and ability for damage detection, the training period size was varied between 172 days and 730 days (2 years). The performance indicators presented in section 6.2.4 were computed when the models are in control during a common period of 1.5 years (January 2017 to June 2018). Two significance levels also considered in the trace test: 5% and 1%.

Concerning the number of false positives (Figure 6.5), low values of false positives are only obtained for training period sizes larger than 500 days for both the significance levels considered in the trace test. The percentage of false positives is generally around 5% for training period sizes larger than 308 and 365 days when significance levels of 1% and 5%, respectively, are used in the trace test.

Concerning the sensitivity to damage, it can be concluded that the distinction between undamaged and damage states increases as the training period size increases. This can be inferred from the evolution of the performance indicator RU with the training period size shown in Figure 6.6 (a). Moreover, more stable values are obtained when using a

significance level of 5% in the trace test. The sharp variations in the graphs are due to the fact that sometimes a different set of cointegration vectors is selected for similar training period sizes (see Figure 6.7 (a)). This becomes more frequent when the significance level in the trace test is stricter. As shown in Figure 6.6(b), the indicator $RL_{\alpha=99.99\%}$ tends to stabilize for training period sizes larger than 365 days. Likewise the performance indicator RU, more stable values are obtained when using a significance level of 5% in the trace test. For this particular damage scenario, and unlike the performance indicator RU, the performance indicator $RL_{\alpha=99.99\%}$ does not increase with training period size. This is due to de fact that the number of retained cointegration residuals increases (see Figure 6.7 (a)), which causes an increase in the UCL (see Figure 6.7 (b)).

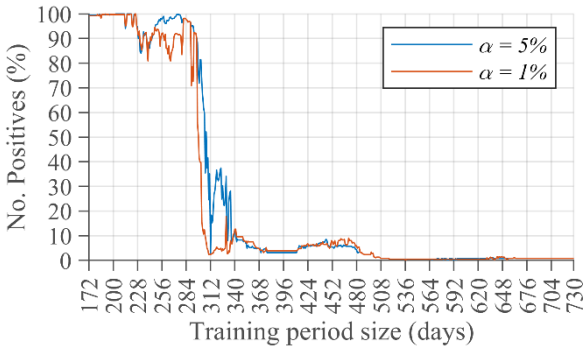

Figure 6.5 - Evolution with the training period size of the number of false positives (UCL computed for α= 99.99%).

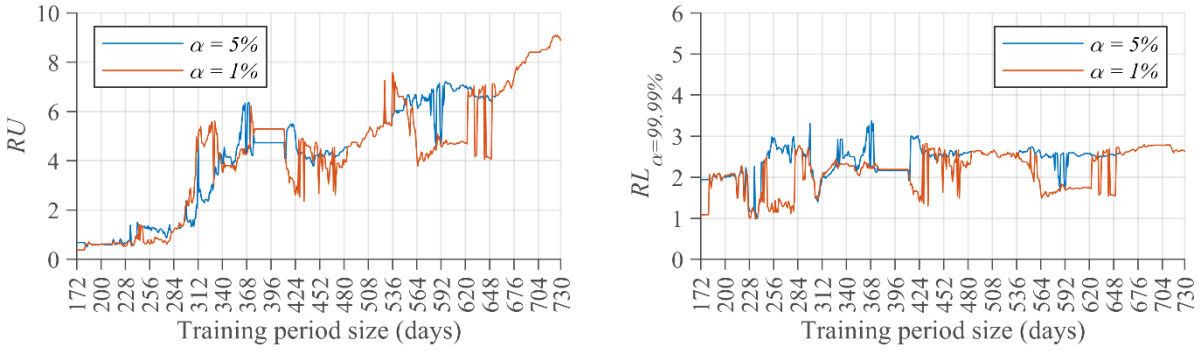

(a) (b)

Figure 6.6 — Evolution with the training period size of the performance indicators: (a) RU and (b) RL for α=99.99%. Considered damage scenario: 10% of area reduction in the stay cable T19C19.

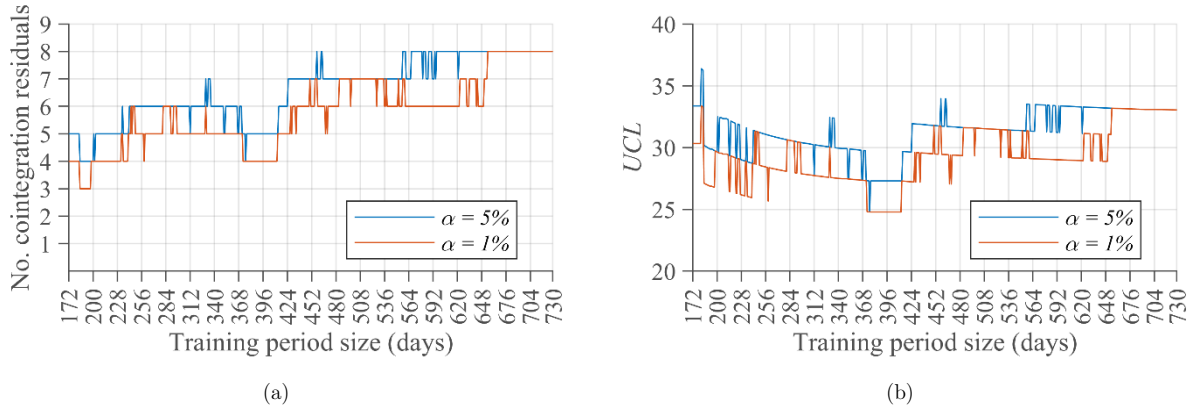

(a) (b)

Figure 6.7 – Evolution with the training period size of: (a) number of cointegration residuals retained by the trace test for a significance level of 5%, and (b) UCL of the Hotelling T^2 control chart.

6.3.3 Damage detection

To evaluate the sensitivity of the proposed approach to damage in the suspension system of the Corgo Bridge, area reductions from 0% up to 100% are sequentially and individually considered in all stay cables. Assuming that damage is unambiguously flagged when RL≥1.0, the minimum detectable damage for each stay cable is presented in Figure 6.8. Excluding the instrumented stay cables (where area variations smaller than 1% can be flagged), the short stay-cables anchored close to the pier are those where the damages are more difficult to detect since a small area reduction induces negligible force variations in the remaining cables.

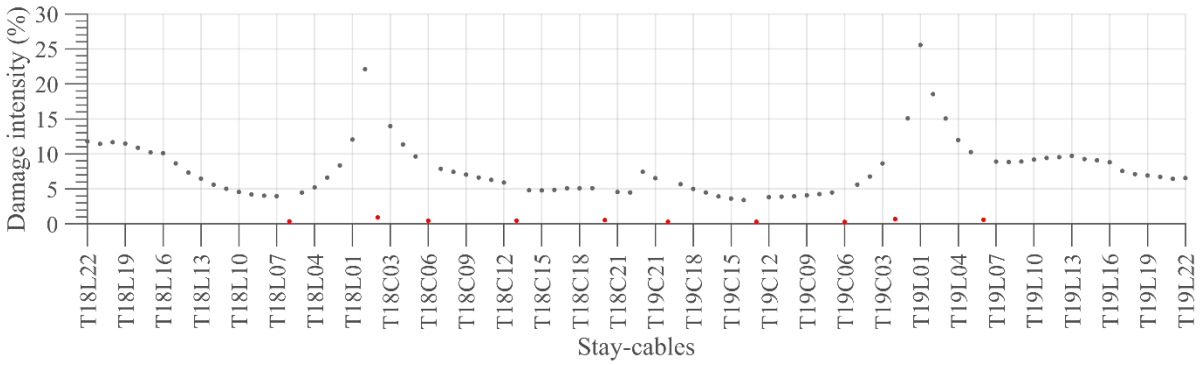

Figure 6.8 –Minimum detectable damage in each stay cable considering that a damage is unambiguously detected when $RL_{\alpha=99.99\%} \geq 1$. Significance level of the trace test: 5%. UCL computed using a significance level of α=99.99%. Training period size: 730 days. The instrumented stay cables are in red.

The results in Figure 6.8 show that the damages in stay-cables T19L01 and T19C14 are, respectively, the most difficult and the easiest to detect in the non-instrumented stay cables.

The stay-cables are identified in green in Figure 3.3. The minimum damage that can be unambiguously detected using the selected dataset is an area reduction of about 3.5% in stay-cable T19C14. In the worst scenario, at least an area reduction of about 25% can be unambiguously flagged in the most difficult stay cable of the suspension system. It should be stressed that if more stay cables were instrumented, possible smaller damages would be detectable using the proposed strategy. Even though, for the majority of the stay cables at least area reductions of about 5% are unambiguously flagged, with only four stay cables where damages bigger than 15% are not unambiguously detectable. Moreover, bearing in mind that the accidental loading scenario corresponding to the loss one stay-cable was considered in the design of the Corgo Bridge [175], damage in the suspension system of the bridge can be considered to be unambiguously flagged in its early stage.

6.3.4 Comparison with the MLR-PCA methodology

In Figure 6.9 is depicted minimum detectable damage in each stay cable considering that a damage is unambiguously detected when $RL_{\alpha=99.99\%} \geq 1$ for MLR-PCA and Cointegration Analysis. In both methods a training period size of 2 years was considered for the construction of Figure 6.9. The performance of both models is comparable, with a small advantage for the Cointegration Analysis. Moreover, besides being more consistent from the theoretical point of view, the Cointegration Analysis model is an output-only method and requires less user-defined parameters.

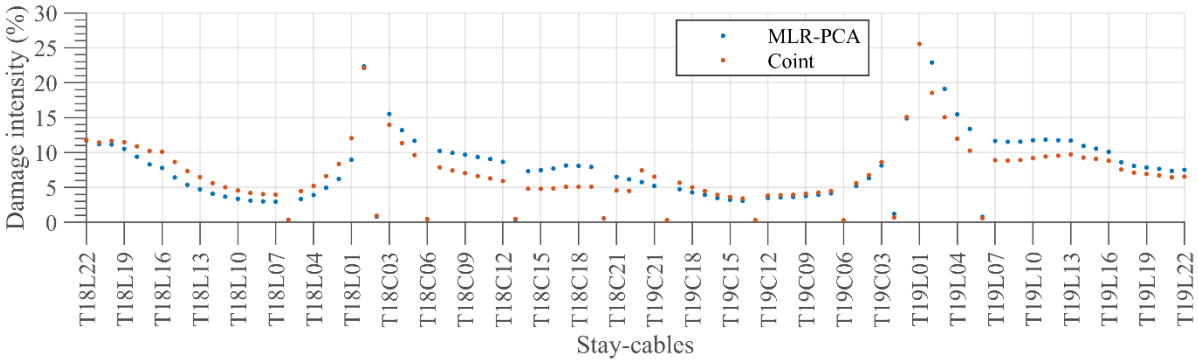

Figure 6.9 – Minimum detectable damage in each stay cable considering that a damage is unambiguously detected when $RL_{\alpha=99.99\%} \geq 1$ for MLR-PCA and Cointegration Analysis. Significance level of the trace test: 5%. UCL computed using a significance level α=99.99%. Training period size: 730 days.

6.4 Concluding remarks

This chapter describes a practical application of an online data-based strategy to detect early damage under environmental, operational and long-term effects. The proposed approach is based on multivariate cointegration analysis and statistical process control. Its application to data gathered from the structural monitoring system of a cable-stayed bridge is described and the performance is evaluated.

The proposed strategy was systematised and applied to the measured cable forces of the Corgo Bridge. This dataset was chosen since the safety of cable-supported bridges is closely related to the cable integrity and because all the measured forces share common trends, an important condition for the time series to be cointegrated. A parametric analysis was conducted to evaluate the effect of training period size on the effectiveness of data normalisation and sensitivity to damage. It was demonstrated that increasing the training period size improves the distinction between the undamaged and damaged states and decreases the number of false positives.

Numerically simulated damage scenarios were used to corrupt the experimental time series in order to evaluate the ability of the proposed strategy for damage detection. In the instrumented stay cables, an area reduction smaller than 1% can be easily flagged. In the stay cables that are not instrumented, an area reduction of about 3.5% and of about 25% can be unambiguously detected in the most and least sensitive stay cables, respectively. The latter corresponds to the two-pairs of short stay cables anchored close to the pier. It should be stressed that if more stay cables were instrumented, or if an improved post-processing strategy was adopted for determining the cable forces from the measured accelerations, smaller damages would be detectable using the proposed strategy. Even though, for the majority of the non-instrumented stay cables at least area reductions of about 5% are unambiguously flagged. Moreover, since the accidental loading scenario corresponding to the failure of one stay-cable was considered in the design of the Corgo Bridge [175], damage in the suspension system of the bridge can be considered to be flagged in its early stage.

Finally, it should be stressed that the set of sensors/damage sensitive-features should always

be selected with the aim of detection a particular damage or malfunction. Moreover, any approach for damage detection should always be complemented with other approaches and analysis of other complementary datasets/sensors, as well as with periodic visual inspections. For instance, the structural response of the bridge, such as the evolution of the long-term effects, should be followed up using methodologies like the one proposed in chapter 4. In this work the damage detection was based on numerical simulations of damage superposed to the measured time series. The proposed strategy should now be further validated in order case studies, preferably in structures where damage was already identified.

Chapter 7

CONCLUSIONS AND FUTURE RESEARCH

7.1 Conclusions

This thesis was focussed on the development of modern smart tools to support bridge asset management. It includes the design, development and implementation of a structural monitoring system, the thermomechanical study of a cable-stayed bridge for interpretation of the data gathered from structural monitoring systems and the development and implementation of data-based approaches for real-time damage detection using structural monitoring data. The main achievements are summarised in the following paragraphs.

Chapter 2

In Chapter 2, the main definitions and concepts related to structural health monitoring and damage detection approaches are given. The main goals and components of an SHM system were defined and the advantages and disadvantages of model-based and data-based approaches for damage/anomaly detection were discussed. The strategy followed in this thesis for structural health monitoring was also presented. Finally, a literature review on data-based approaches was presented.

Chapter 3

In Chapter 3, the Corgo Bridge, used as case study in this thesis, was presented. The structural monitoring system installed to follow the construction stages and the long-term behaviour of the bridge was described. A special focus on the dynamic structural monitoring system of the stay cables was given for two reasons. First, it is the part of the structural monitoring system where the author had an active intervention, leading the process of design, development and implementation. Second, the data gathered from this sub-system was revealed to be the most important for damage detection and localisation (at least in the simulated damaged scenarios on Chapters 5 and 6). The developed structural monitoring system of the stay cables was demonstrated to be robust since there are few gaps in the data during 3.5 years and they are essentially due to power outages.

The developed mechanical finite element model of the Corgo Bridge was presented. This model was used to follow the construction stages, to analyse the structural behaviour during the load test, to follow the results collected by long-term monitoring system, which were examined in Chapter 4, and to simulate damage scenarios in order to test the damage detection and localisation methodologies developed in Chapters 5 and 6.

A good fit between the experimental and calculated values for the different load cases of the load test was generally obtained. However, some results suggested that the bearings are partially restrained, possibly due to friction, thereby leading to longitudinal displacements of the piers over which the expansion joints are located. Corrective measures were taken after the load test in order to correct the identified anomalies.

Chapter 4

In Chapter 4, a methodology is proposed for the simulation of the structural response of large concrete cable-stayed bridges under the effects of temperature variations, aiming at the optimum compromise between accuracy and simplicity of the involved procedures. The methodology is general and can be used to determine the structural response to thermal loads of other types of bridges, irrespective of the material.

The obtained results were compared against the readings of the permanent structural

monitoring system installed at the Corgo Bridge, providing the validation of the developed methodology, as well as an indication of the accuracy that can be achieved. The structural behaviour of the bridge under the effects of temperature variations could be disclosed, enabling a better understanding of the readings continuously being acquired by the structural health monitoring system. For the large majority of the sensors, the variation of the uniform temperature component was demonstrated to be responsible for about 90% of the structural response.

The detailed simulation of the radiative heat transfer mechanisms revealed to be essential for the accuracy of the results. The agreement between the measured and calculated temperatures provides a confirmation of the adequacy of the adopted models and material properties. It is also noted that only after the consideration of the effective sky temperature in the longwave radiation model the temperatures measured in the top slab during wintertime could be accurately reproduced, highlighting the importance of the consideration of this physical phenomenon (which is usually disregarded) in order to obtain accurate estimates of the thermal field.

In the context of the interpretation of the readings provided by structural monitoring systems, the uniform and differential temperature components have to be estimated from the discrete temperature readings. A discussion on the optimal deployment location of the embedded temperature sensors in order to have better estimates was presented for the girder and a pier of the Corgo Bridge. However, other types of sections and boundary conditions (namely solar exposure) should be further considered in order to be possible to give more general recommendations for localisation of the temperature sensors.

The comparison between the measured and calculated structural response in terms of longitudinal bearing displacements, vertical deflections, rotations and stay-cable force variations yielded a satisfactory agreement. The assumption of constant temperature distribution along the longitudinal direction of the girder, piers and pylons, did not compromise the validity of the results, demonstrating the validity of this assumption. The analysis enabled the quantification of the contribution of each temperature component to the calculated structural response. It is concluded that the differential temperature component contributes very little to the response of the analysed cable-stayed bridge, except

in the case of the longitudinal bearing displacements were it contributes, in average, to about 10% of the total displacement. This is due to the flexural displacement of the tall piers, which are dictated by the differential temperature between the east and west vertical surfaces. The trend due to the long term effects (creep, shrinkage and prestress steel relaxation) could be clearly detected in the monitoring readings and could be satisfactorily reproduced by the numerical model. This confirms the adequacy of the adopted models for the long term effects during the 17-month observation period.

Chapter 5

In Chapter 5 an online data-based methodology for early damage detection and localisation under the effects of EOVs is proposed. Its application to 3½ years of data gathered from the SHM system of a large prestressed cable-stayed bridge is described and the performance is evaluated.

A pre-processing strategy is proposed prior to the application of data normalisation models. Outliers are first removed using the IQR and then the data is averaged on a daily, two-day or three-day basis in order to suppress the high-frequency changes due to, for instance, traffic, wind and solar radiation effects. It is demonstrated that this strategy considerably improves both the suppression of the EOVs and the sensitivity to damage.

The temperature and long-term effects are removed by combining two well-established multivariate statistical tools: MLR and PCA. The use of the MLR is justified by the expected linear relationship among the selected predictor and dependent variables. The PCA is applied to the residuals of the MLR model in order to suppress the EOVs not suppressed by the MLR model, namely the remaining temperature effects and the long-term behaviour due to rheological effects of the concrete. The use of PCA implies a nearly linear relationship between the sensors readings. This assumption is demonstrated to be valid during the observed period since the process is in control for 3½ years. This assumption may cease to be valid in the long-term and a slow drift in the T^2 values may start being observed.

The criteria guiding the choice of the predictor variables in the MLR models, the number of principal components to retain in the PCA models and the training period size were

evaluated by means of a parametric analysis. A trade-off between sensitivity to damage and robustness to false positives was identified. With regards to the training period size, stable results are only obtained when the training period size is equal to, or greater than, one year.

The methodology was applied to two distinct datasets: girder deflections and cable forces. The former was used to demonstrate the detection of a real and small temporary anomaly in the sensing system. The latter served to exemplify the ability for early-damage detection in the suspension system. Considering the available sensor layout, the proposed methodology is shown to unambiguously detect a reduction of the cross-section area of 2.5% and 20% in the most sensitive and least sensitive non-instrumented stay-cables, respectively. Area reductions smaller than 1% can be flagged in all the instrumented stay cables.

Finally, an approach based on the relative variation of the T^2 statistic on sub-datasets is proposed for damage localisation. The available sensor layout allows determining in which of the pylons the damaged stay cable is anchored.

Chapter 6

In Chapter 6, a practical application of an online output-only data-based strategy to detect early damage under environmental, operational and long-term effects is described. The proposed approach is based on multivariate cointegration analysis and statistical process control. Its application to data gathered from the structural monitoring system of the Corgo Bridge is described and the performance is evaluated.

The proposed strategy was systematised and applied to the measured cable forces of the Corgo Bridge. This dataset was chosen since the safety of cable-supported bridges is closely related to the cable integrity and because all the measured forces share common trends, an important condition for the time series to be cointegrated. A parametric analysis was conducted to evaluate the effect of training period size on the effectiveness of data normalisation and sensitivity to damage. It was demonstrated that increasing the training period size improves the distinction between the undamaged and damaged states and decreases the number of false positives.

Numerically simulated damage scenarios were used to corrupt the experimental time series

in order to evaluate the ability of the proposed strategy for damage detection. In the instrumented stay cables, an area reduction smaller than 1% can be easily flagged. In the stay cables that are not instrumented, an area reduction of about 3.5% and of about 25% can be unambiguously detected in the most and least sensitive stay cables, respectively. The latter corresponds to the two-pairs of short stay-cables anchored close to the pier. It should be stressed that if more stay cables were instrumented, or if an improved post-processing strategy was adopted for determining the cable forces from the measured accelerations, smaller damages would be detectable using the proposed strategy. Even though, for the majority of the non-instrumented stay cables at least area reductions of about 5% are unambiguously flagged. Moreover, since the accidental loading scenario corresponding to the failure of one stay-cable was considered in the design of the Corgo Bridge [175], damage in the suspension system of the bridge can be considered to be flagged in its early stage.

7.2 Recommendations for future research

Structural monitoring system of the stay cables of the Corgo Bridge

Although the quality of the obtained data, the developed software (*STayMenusus*) uses the peak-picking method for the determination of the modal frequencies. In the near future, state-of-the-art methodologies for operational modal analysis should be implemented in the STayMensus software. This improvement in the identification of the modal frequencies of the stay cables may improve the damage detectability of the methodologies proposed in Chapters 5 and 6. Moreover, since the modal frequencies of the Corgo Bridge are detectable in the PSD of the accelerations measured in the stay cables, it could be interesting to analyse their long-term evolution.

Thermomechanical analysis of bridges

The determination of the thermal field of stay cables was not addressed in this thesis. Instead, a temperature reading from the structural monitoring system was used. Usually, the stay-cables of new cable-stayed bridges are parallel strand cables, being each individual strand protected by an extruded high density polyethylene (HDPE) sheath. The strand bundle is still protected by a polyethylene cylindrical pipe, being the individual strands

surrounded by air. This makes the numerical simulation of the corresponding thermal field an extremely complex task and should be addressed in future in order to make the methodology applicable in case temperature readings of the stay cables are not available.

The presented study on the optimal deployment location of the embedded temperature sensors should be extended for other types of cross-sections and boundary conditions (namely solar exposure) in order to be possible to give more general recommendations for localisation of temperature sensors. Ideally, a platform that promptly indicates the best sensor positions given only the geometry of the cross-section should be created.

Finally, the presented thermomechanical study focused on the static response of the bridge. However, the study of the variation of dynamic proprieties, such as modal frequencies and damping ratios, under thermal loads could be interesting. Indeed, that kind of studies are barely found in the technical literature.

Data-based approaches for damage detection and localisation

The data-based approaches developed in Chapters 5 and 6 revealed great potential for damage detection and localisation and they are a significant contribution for the transition of SHM from academia to industry. However, some further improvements and developments should be considered in the future. For that propose, the existing database of the Corgo Bridge could be used to perform benchmark studies to evaluate other algorithms for feature extraction, data normalisation and feature classification. Between the most used methodologies for data normalisation in the scope of SHM, the author believes that algorithms from the field of Blind Source Separation have still a great potential to explore, namely for the suppression of long-term effects.

In both of the proposed approaches for damage detection, the Hotelling T^2 control chart was used for feature classification. However, the residuals of the data normalisation usually do not strictly respect the assumptions of the Hotelling T^2 control chart of independence between samples (no autocorrelation) and that the samples are multivariate normal. Therefore, the UCL could be defined, for instance, by the analysis of the histogram of the T^2-statistic or using extreme value analysis. Other algorithms for feature classification, such as Cluster Analysis, should also be implemented and tested in the near future.

With regards to damage localisation, other approaches should be developed and implemented. Namely, methodologies that use a library of numerically simulated damage scenarios could be of great interest. Once damage is flagged, the similarity between the measured and simulated datasets can be used to localise and maybe classify the damage. Since that kind of methodologies is difficult to validate in real structures, its application to a laboratory model can give valuable insights for the implementation of that kind of methodologies in full-scale bridges.

Another important issue to be addressed is the definition of different alert levels. The alert levels can be defined, for instance, on the basis of the values of the T^2-statistic (or other statistic computed by the algorithm used for feature classification). These alerts levels may be defined by means of the simulation of typical damage scenarios in a finite element model of the structure. The correspondent corrective measures and immediate actions to take after a certain alert is trigged should be defined in collaboration with the bridge manager and designer.

Finally, the proposed approaches for damage detection are essentially suited for new bridges or bridges where there is some considerable amount of structural monitoring data (at least one year for training the models). However, in some cases that amount of data is not available. For that reason, other approaches that enable to extract valuable information from smaller datasets should be studied and their performance evaluated, even if they are less sensitive to damage than the approaches proposed in Chapters 5 and 6.

REFERENCES

[1] Abé, M. and Y. Fujino (2017). *Monitoring of long-span bridges in Japan.* Proceedings of the Institution of Civil Engineers - Civil Engineering. **Vol. 170**(3): p. 135-144.

[2] Aktan, A.E., F.N. Catbas, K.A. Grimmelsman, and C.J. Tsikos (2000). *Issues in Infrastructure Health Monitoring for Management.* Journal of Engineering Mechanics. **Vol. 126**(7): p. 711-724.

[3] Alduchov, O.A. and R.E. Eskridge (1996). *Improved Magnus Form Approximation of Saturation Vapor Pressure.* Journal of Applied Meteorology. **Vol. 35**(4): p. 601-609.

[4] Almeida Cardoso, R., A. Cury, F. Barbosa, and C. Gentile (2019). *Unsupervised real-time SHM technique based on novelty indexes.* Structural Control and Health Monitoring. **Vol. 26**(7): p. e2364.

[5] Alves, V., A. Cury, N. Roitman, C. Magluta, and C. Cremona (2015). *Novelty detection for SHM using raw acceleration measurements.* Structural Control and Health Monitoring. **Vol. 22**(9): p. 1193-1207.

[6] Alves, V., A. Cury, N. Roitman, C. Magluta, and C. Cremona (2015). *Structural modification assessment using supervised learning methods applied to vibration data.* Engineering Structures. **Vol. 99**: p. 439-448.

[7] Arangio, S. and F. Bontempi (2014). *Structural health monitoring of a cable-stayed bridge with Bayesian neural networks.* Structure and Infrastructure Engineering. **Vol. 11**(4): p. 575-587.

[8] ASCE (2013). *Structural Identification of Constructed Systems: Approaches, Methods, and Technologies for Effective Practice of St-Id*, Reston, Virginia. 249 p.

[9] Barata, V. (2012). *Viaduto do Corgo da A.E. Transmontana*. in *Encontro Nacional Betão Estrutural 2012*. Porto: FEUP/GPBE.

[10] Barthorpe, R.J. (2011). *On Model- and Data-based Approaches to Structural Health Monitoring*. University of Sheffield, Doctoral Thesis.

[11] Bellino, A., A. Fasana, L. Garibaldi, and S. Marchesiello (2010). *PCA-based detection of damage in time-varying systems.* Mechanical Systems and Signal Processing. **Vol. 24**(7): p. 2250-2260.

[12] Boller, C., F.K. Chang, and Y. Fujino (2009). *Encyclopedia of Structural Health Monitoring*: Wiley.

[13] Branco, F. and P. Mendes (1993). *Thermal Actions for Concrete Bridge Design.* Journal of Structural Engineering. **Vol. 119**(8): p. 2313-2331.

[14] Brincker, R. and C. Ventura (2015). *Introduction to Operational Modal Analysis*: Wiley.

[15] Brownjohn, J.M. (2007). *Structural health monitoring of civil infrastructure.* Philos Trans A Math Phys Eng Sci. **Vol. 365**(1851): p. 589-622.

[16] Brownjohn, J.M.W., P. Moyo, P. Omenzetter, and S. Chakraborty (2005). *Lessons from monitoring the performance of highway bridges.* Structural Control and Health Monitoring. **Vol. 12**(3-4): p. 227-244.

[17] Brownjohn, J.M.W., A. De Stefano, Y.-L. Xu, H. Wenzel, and A.E. Aktan (2011). *Vibration-based monitoring of civil infrastructure: challenges and successes.* Journal of Civil Structural Health Monitoring. **Vol. 1**(3-4): p. 79-95.

[18] Brownjohn, J.M.W., K.-Y. Koo, A. Scullion, and D. List (2014). *Operational deformations in long-span bridges.* Structure and Infrastructure Engineering. **Vol. 11**(4): p. 556-574.

[19] Caetano, E.d.S. (1992). *Identificação experimental de parâmetros dinâmicos em sistemas estruturais*. Faculdade de Engenharia da Universidade do Porto, Master Thesis.

[20] Caetano, E.d.S., R. Bartek, F. Magalhães, C. Keenan, and G. Trippick (2013). *Assessment of Cable Forces at the London 2012 Olympic Stadium Roof.* Structural Engineering International. **Vol. 23**(4): p. 489-500.

[21] Cao, Y., J. Yim, Y. Zhao, and M.L. Wang (2011). *Temperature effects on cable stayed bridge using health monitoring system: a case study.* Structural Health Monitoring. **Vol. 10**(5): p. 523-537.

[22] Cappello, C., D. Zonta, H.A. Laasri, B. Glisic, and M. Wang (2018). *Calibration of Elasto-Magnetic Sensors on In-Service Cable-Stayed Bridges for Stress Monitoring.*

Sensors (Basel). **Vol. 18**(2).

[23] Casas, J.R. (1994). *A Combined Method for Measuring Cable Forces: The Cable-Stayed Alamillo Bridge, Spain.* Structural Engineering International. **Vol. 4**(4): p. 235-240.

[24] Catbas, F.N., M. Susoy, and D.M. Frangopol (2008). *Structural health monitoring and reliability estimation: Long span truss bridge application with environmental monitoring data.* Engineering Structures. **Vol. 30**(9): p. 2347-2359.

[25] Cavadas, F., C. Rodrigues, C. Félix, and J. Figueiras (2013). *Post-rehabilitation assessment of a centenary steel bridge through numerical and experimental analysis.* Journal of Constructional Steel Research. **Vol. 80**: p. 264-277.

[26] Cavadas, F., I.F.C. Smith, and J. Figueiras (2013). *Damage detection using data-driven methods applied to moving-load responses.* Mechanical Systems and Signal Processing. **Vol. 39**(1-2): p. 409-425.

[27] Cavadas, F. (2016). *Structural Health Monitoring of Bridges: Physics-based Assessment and Data-driven Damage Identification.* University of Porto, Doctoral Thesis.

[28] CEN (2009). *Eurocode 1 - Actions on structures - Part 1-5: General action - Thermal actions*, Caparica: IPQ. 48 p.

[29] Cha, Y.-J. and Z. Wang (2018). *Unsupervised novelty detection–based structural damage localization using a density peaks-based fast clustering algorithm.* Structural Health Monitoring: An International Journal. **Vol. 17**(2): p. 313-324.

[30] Chatfield, C. (1975). *The Analysis of Time Series: Theory and Practice*, London: Chapman and Hall.

[31] Chen, C.-C., W.-H. Wu, and C.-Y. Liu (2012). *Effects of Temperature Variation on Cable Forces of an Extradosed Bridge.* in *6th European Workshop on Structural Health Monitoring.* Dresden/Germany.

[32] Chen, H.P. (2018). *Structural Health Monitoring of Large Civil Engineering Structures*: Wiley.

[33] Chen, Q., U. Kruger, and A.Y.T. Leung (2009). *Cointegration Testing Method for Monitoring Nonstationary Processes.* Industrial & Engineering Chemistry Research. **Vol. 48**(7): p. 3533-3543.

[34] Cheung, A., C. Cabrera, P. Sarabandi, K.K. Nair, A. Kiremidjian, and H. Wenzel (2008). *The application of statistical pattern recognition methods for damage detection to field data.* Smart Materials and Structures. **Vol. 17**(6).

[35] Cho, S., J. Yim, S.W. Shin, H.-J. Jung, C.-B. Yun, and M.L. Wang (2013). *Comparative Field Study of Cable Tension Measurement for a Cable-Stayed Bridge.* Journal of Bridge Engineering. **Vol. 18**(8): p. 748-757.

[36] Coletta, G., G. Miraglia, M. Pecorelli, R. Ceravolo, E. Cross, C. Surace, and K. Worden (2019). *Use of the cointegration strategies to remove environmental effects from data acquired on historical buildings.* Engineering Structures. **Vol. 183**: p. 1014-1026.

[37] Comanducci, G., F. Magalhães, F. Ubertini, and Á. Cunha (2016). *On vibration-based damage detection by multivariate statistical techniques: Application to a long-span arch bridge.* Structural Health Monitoring. **Vol. 15**(5): p. 505-524.

[38] Cooper, P.I. (1969). *The absorption of radiation in solar stills.* Solar Energy. **Vol. 12**(3): p. 333-346.

[39] Costa, B.J.A. and J.A. Figueiras (2012). *Fiber optic based monitoring system applied to a centenary metallic arch bridge: Design and installation.* Engineering Structures. **Vol. 44**: p. 271-280.

[40] Cross, E.J., K. Worden, and Q. Chen (2011). *Cointegration: a novel approach for the removal of environmental trends in structural health monitoring data.* Proceedings of the Royal Society A: Mathematical, Physical and Engineering Sciences. **Vol. 467**(2133): p. 2712-2732.

[41] Cross, E.J., G. Manson, K. Worden, and S.G. Pierce (2012). *Features for damage detection with insensitivity to environmental and operational variations.* Proceedings of the Royal Society A: Mathematical, Physical and Engineering Sciences. **Vol. 468**(2148): p. 4098-4122.

[42] Cunha, A. and E. Caetano (1999). *Dynamic measurements on stay cables of cable-stayed bridges using an interferometry laser system.* Experimental techniques. **Vol. 23**(3): p. 38-43.

[43] Cury, A., C. Crémona, and E. Diday (2010). *Application of symbolic data analysis for structural modification assessment.* Engineering Structures. **Vol. 32**(3): p. 762-775.

[44] Dao, P.B. and W.J. Staszewski (2013). *Cointegration approach for temperature effect compensation in Lamb-wave-based damage detection.* Smart Materials and Structures. **Vol. 22**(9).

[45] Dao, P.B. and W.J. Staszewski (2014). *Lamb wave based structural damage detection using cointegration and fractal signal processing.* Mechanical Systems and Signal Processing. **Vol. 49**(1-2): p. 285-301.

[46] Dao, P.B., W.J. Staszewski, and A. Klepka (2017). *Stationarity-Based Approach for the Selection of Lag Length in Cointegration Analysis Used for Structural Damage Detection.* Computer-Aided Civil and Infrastructure Engineering. **Vol. 32**(2): p. 138-153.

[47] Deraemaeker, A., E. Reynders, G. De Roeck, and J. Kullaa (2008). *Vibration-based structural health monitoring using output-only measurements under changing*

environment. Mechanical Systems and Signal Processing. **Vol. 22**(1): p. 34-56.

[48] Deraemaeker, A. and K. Worden (2018). *A comparison of linear approaches to filter out environmental effects in structural health monitoring.* Mechanical Systems and Signal Processing. **Vol. 105**: p. 1-15.

[49] Dervilis, N., K. Worden, and E.J. Cross (2015). *On robust regression analysis as a means of exploring environmental and operational conditions for SHM data.* Journal of Sound and Vibration. **Vol. 347**: p. 279-296.

[50] Dickey, D.A. and W.A. Fuller (1979). *Distribution of the Estimators for Autoregressive Time Series With a Unit Root.* Journal of the American Statistical Association. **Vol. 74**(366): p. 427-431.

[51] Dickey, D.A. and W.A. Fuller (1981). *Likelihood Ratio Statistics for Autoregressive Time Series with a Unit Root.* Econometrica. **Vol. 49**(4): p. 1057-1072.

[52] Diez, A., N.L.D. Khoa, M. Makki Alamdari, Y. Wang, F. Chen, and P. Runcie (2016). *A clustering approach for structural health monitoring on bridges.* Journal of Civil Structural Health Monitoring. **Vol. 6**(3): p. 429-445.

[53] Dilger, W.H., A. Ghali, M. Chan, M.S. Cheung, and M.A. Maes (1983). *Temperature Stresses in Composite Box Girder Bridges.* Journal of Structural Engineering. **Vol. 109**(6): p. 1460-1478.

[54] Dimande, A., M. Pimentel, C. Félix, and J. Figueiras (2012). *Monitoring system for execution control applied to a steel arch footbridge.* Structure and Infrastructure Engineering. **Vol. 8**(3): p. 277-294.

[55] Ding, Y. and A. Li (2011). *Assessment of bridge expansion joints using long-term displacement measurement under changing environmental conditions.* Frontiers of Architecture and Civil Engineering in China. **Vol. 5**(3): p. 374-380.

[56] Duffie, J.A. and W.A. Beckman (2013). *Solar Engineering of Thermal Processes*. 4th Edition edition ed, Hoboken: John Wiley & Sons. 936.

[57] Eftekhar Azam, S., A. Rageh, and D. Linzell (2018). *Damage detection in structural systems utilizing artificial neural networks and proper orthogonal decomposition.* Structural Control and Health Monitoring. **Vol. 0**(0): p. e2288.

[58] Eisenberg, M.A. and L.E. Malvern (1973). *On finite element integration in natural co-ordinates.* International Journal for Numerical Methods in Engineering. **Vol. 7**(4): p. 574-575.

[59] Elbadry, M. and A. Ghali (1983). *Temperature Variations in Concrete Bridges.* Journal of Structural Engineering. **Vol. 109**(10): p. 2355-2374.

[60] Elbadry, M.M. and A. Ghali (1983). *Nonlinear Temperature Distribution and its Effects on Bridges.* IABSE Periodica. **Vol. 3/1983**.

[61] Engle, R.F. and C.W.J. Granger (1987). *Co-Integration and Error Correction: Representation, Estimation, and Testing.* Econometrica. **Vol. 55**(2): p. 251-276.

[62] Erbs, D.G., S.A. Klein, and J.A. Duffie (1982). *Estimation of the diffuse radiation fraction for hourly, daily and monthly-average global radiation.* Solar Energy. **Vol. 28**(4): p. 293-302.

[63] Fallahian, M., F. Khoshnoudian, and V. Meruane (2018). *Ensemble classification method for structural damage assessment under varying temperature.* Structural Health Monitoring. **Vol. 17**(4): p. 747-762.

[64] Fang, Z. and J. Wang (2012). *Practical Formula for Cable Tension Estimation by Vibration Method.* Journal of Bridge Engineering. **Vol. 17**(1): p. 161-164.

[65] Faria, R., M. Azenha, and J.A. Figueiras (2006). *Modelling of concrete at early ages: Application to an externally restrained slab.* Cement and Concrete Composites. **Vol. 28**(6): p. 572-585.

[66] Farrar, C.R. and K. Worden (2013). *Structural Health Monitoring: A Machine Learning Prespective*, ed. Wiley, Chichester.

[67] Félix, C., C. Rodrigues, R.d. Faria, J. Figueiras, L. Afonso, and V. Barata (2012). *Conceção e implementação do sistema de monitorização estrutural do Viaduto do Corgo.* in *Encontro Nacional Betão Estrutural 2012*. Porto: FEUP/GPBE.

[68] fib (2013). *Fib Model Code for Concrete Structures 2010*: Ernst & Sohn, a Wiley brand.

[69] Figueiredo, E., G. Park, J. Figueiras, C. Farrar, and K. Worden (2009). *Structural Health Monitoring Algorithm Comparisons Using Standard Data Sets*: Los Alamos National Laboratory.

[70] Figueiredo, E., J. Figueiras, G. Park, C.R. Farrar, and K. Worden (2011). *Influence of the Autoregressive Model Order on Damage Detection.* Computer-Aided Civil and Infrastructure Engineering. **Vol. 26**(3): p. 225-238.

[71] Figueiredo, E.J.F. (2010). *Damage identification in civil engineering infrastructure under operational and environmental conditions*. Faculdade de Engenharia da Universidade do Porto, Doctoral Thesis.

[72] Friswell, M.I. and J.E.T. Penny (2002). *Crack Modeling for Structural Health Monitoring.* Structural Health Monitoring. **Vol. 1**(2): p. 139-148.

[73] Friswell, M.I. (2007). *Damage identification using inverse methods.* Philos Trans A Math Phys Eng Sci. **Vol. 365**(1851): p. 393-410.

[74] Froli, M., N. Hariga, G. Nati, and M. Orlandini (1996). *Longitudinal Thermal Behaviour of a Concrete Box Girder Bridge.* Structural Engineering International. **Vol. 6**(4): p. 237-242.

[75] Fu, H., S. Ng, and M. Cheung (1990). *Thermal Behavior of Composite Bridges.*

Journal of Structural Engineering. **Vol. 116**(12): p. 3302-3323.

[76] Fu, Z., B. Ji, Q. Wang, and Y. Wang (2017). *Cable Force Calculation Using Vibration Frequency Methods Based on Cable Geometric Parameters.* Journal of Performance of Constructed Facilities. **Vol. 31**(4).

[77] Goulet, J.-A. (2017). *Bayesian dynamic linear models for structural health monitoring.* Structural Control and Health Monitoring. **Vol. 24**(12): p. e2035.

[78] Gu, J., M. Gul, and X. Wu (2017). *Damage detection under varying temperature using artificial neural networks.* Structural Control and Health Monitoring. **Vol. 24**(11): p. e1998.

[79] Guo, H.Y. (2006). *Structural damage detection using information fusion technique.* Mechanical Systems and Signal Processing. **Vol. 20**(5): p. 1173-1188.

[80] Hagan, M.T., H.B. Demuth, M.H. Beale, and O. De Jesús (2014). *Neural network design*: Martin Hagan.

[81] Hannan, E.J. and B.G. Quinn (1979). *The determination of the order of an autoregression.* Journal of the Royal Statistical Society: Series B (Methodological). **Vol. 41**(2): p. 190-195.

[82] Harris, R.I.D. (1995). *Using Cointegration Analysis in Econometric Modelling*: Harvester Wheatsheaf, Prentice Hall.

[83] He, Q., F. Kong, and R. Yan (2007). *Subspace-based gearbox condition monitoring by kernel principal component analysis.* Mechanical Systems and Signal Processing. **Vol. 21**(4): p. 1755-1772.

[84] Hedegaard, B.D., C.E.W. French, and C.K. Shield (2017). *Long-Term Monitoring Strategy for Time-Dependent Deflections of Posttensioned Concrete Bridges.* Journal of Bridge Engineering. **Vol. 22**(11).

[85] Hsu, T.-Y. and C.-H. Loh (2010). *Damage detection accommodating nonlinear environmental effects by nonlinear principal component analysis.* Structural Control and Health Monitoring. **Vol. 17**(3): p. 338-354.

[86] Hu, W.-H., C. Moutinho, E. Caetano, F. Magalhães, and Á. Cunha (2012). *Continuous dynamic monitoring of a lively footbridge for serviceability assessment and damage detection.* Mechanical Systems and Signal Processing. **Vol. 33**: p. 38-55.

[87] Hu, W.-H., E. Caetano, and Á. Cunha (2013). *Structural health monitoring of a stress-ribbon footbridge.* Engineering Structures. **Vol. 57**: p. 578-593.

[88] Hu, W.-H., Á. Cunha, E. Caetano, R.G. Rohrmann, S. Said, and J. Teng (2017). *Comparison of different statistical approaches for removing environmental/operational effects for massive data continuously collected from footbridges.* Structural Control and Health Monitoring. **Vol. 24**(8): p. e1955.

[89] Hua, X., Y. Ni, J. Ko, and K. Wong (2007). *Modeling of Temperature–Frequency Correlation Using Combined Principal Component Analysis and Support Vector Regression Technique.* Journal of Computing in Civil Engineering. **Vol. 21**(2): p. 122-135.

[90] Hua, X., Y. Ni, Z. Chen, and J. Ko (2009). *Structural Damage Detection of Cable-Stayed Bridges Using Changes in Cable Forces and Model Updating.* Journal of Structural Engineering. **Vol. 135**(9): p. 1093-1106.

[91] Huang, H.-B., T.-H. Yi, H.-N. Li, and H. Liu (2018). *New Representative Temperature for Performance Alarming of Bridge Expansion Joints through Temperature-Displacement Relationship.* Journal of Bridge Engineering. **Vol. 23**(7).

[92] Incropera, F.P., D.P. Dewitt, T.L. Bergman, and A.S. Lavine (2013). *Principles of Heat and Mass Transfer*: Wiley.

[93] Jackson, D.A. (1993). *Stopping Rules in Principal Components Analysis: A Comparison of Heuristical and Statistical Approaches.* Ecology. **Vol. 74**(8): p. 2204-2214.

[94] Jaishi, B. and W. Ren (2005). *Structural Finite Element Model Updating Using Ambient Vibration Test Results.* Journal of Structural Engineering. **Vol. 131**(4): p. 617-628.

[95] Jesus, A., P. Brommer, R. Westgate, K. Koo, J. Brownjohn, and I. Laory (2019). *Modular Bayesian damage detection for complex civil infrastructure.* Journal of Civil Structural Health Monitoring. **Vol. 9**(2): p. 201-215.

[96] Jian, G., C. Yong, and S. Bing-nan (2005). *Experimental study of structural damage identification based on WPT and coupling NN.* Journal of Zhejiang University-SCIENCE A. **Vol. 6**(7): p. 663-669.

[97] Johansen, S. (1988). *Statistical analysis of cointegration vectors.* Journal of Economic Dynamics and Control. **Vol. 12**(2): p. 231-254.

[98] Johansen, S. (1995). *Likelihood-based Inference in Cointegrated Vector Autoregressive Models*: Oxford University Press.

[99] Johnson, R.A. and D.W. Wichern (2013). *Applied Multivariate Statistical Analysis*. 6 edition ed, Harlow: Pearson. 776.

[100] Jolliffe, I.T. (2002). *Principal Component Analysis*: Springer.

[101] Jonasson, J.-E. (1994). *Modelling of temperature, moisture and stresses in young concrete*. Luleå University of Technologyy, Doctoral thesis.

[102] Kim, B. and T. Park (2007). *Estimation of cable tension force using the frequency-based system identification method.* Journal of sound and vibration. **Vol. 304**(3-5): p. 660-676.

[103] Kim, S.-H., S.-J. Park, J. Wu, and J.-H. Won (2015). *Temperature variation in steel*

box girders of cable-stayed bridges during construction. Journal of Constructional Steel Research. **Vol. 112**: p. 80-92.

[104] Ko, J.M. and Y.Q. Ni (2005). *Technology developments in structural health monitoring of large-scale bridges.* Engineering Structures. **Vol. 27**(12): p. 1715-1725.

[105] Ko, J.M., Y.Q. Ni, H.F. Zhou, J.Y. Wang, and X.T. Zhou (2009). *Investigation concerning structural health monitoring of an instrumented cable-stayed bridge.* Structure and Infrastructure Engineering. **Vol. 5**(6): p. 497-513.

[106] Koo, K.Y., J.M.W. Brownjohn, D.I. List, and R. Cole (2013). *Structural health monitoring of the Tamar suspension bridge.* Structural Control and Health Monitoring. **Vol. 20**(4): p. 609-625.

[107] Kostić, B. and M. Gül (2017). *Vibration-Based Damage Detection of Bridges under Varying Temperature Effects Using Time-Series Analysis and Artificial Neural Networks.* Journal of Bridge Engineering. **Vol. 22**(10).

[108] Krishnan Nair, K. and A.S. Kiremidjian (2006). *Time Series Based Structural Damage Detection Algorithm Using Gaussian Mixtures Modeling.* Journal of Dynamic Systems, Measurement, and Control. **Vol. 129**(3): p. 285-293.

[109] Kromanis, R. and P. Kripakaran (2013). *Support vector regression for anomaly detection from measurement histories.* Advanced Engineering Informatics. **Vol. 27**(4): p. 486-495.

[110] Kromanis, R. and P. Kripakaran (2014). *Predicting thermal response of bridges using regression models derived from measurement histories.* Computers & Structures. **Vol. 136**: p. 64-77.

[111] Kromanis, R., P. Kripakaran, and B. Harvey (2015). *Long-term structural health monitoring of the Cleddau bridge: evaluation of quasi-static temperature effects on bearing movements.* Structure and Infrastructure Engineering. **Vol. 12**(10): p. 1-14.

[112] Kromanis, R. and P. Kripakaran (2016). *SHM of bridges: characterising thermal response and detecting anomaly events using a temperature-based measurement interpretation approach.* Journal of Civil Structural Health Monitoring. **Vol. 6**(2): p. 237-254.

[113] Kromanis, R. and P. Kripakaran (2017). *Data-driven approaches for measurement interpretation: analysing integrated thermal and vehicular response in bridge structural health monitoring.* Advanced Engineering Informatics. **Vol. 34**: p. 46-59.

[114] Kullaa, J. (2003). *Damage Detection of the Z24 Bridge Using Control Charts.* Mechanical Systems and Signal Processing. **Vol. 17**(1): p. 163-170.

[115] Lanata, F. and A.D. Grosso (2006). *Damage detection and localization for continuous static monitoring of structures using a proper orthogonal decomposition of signals.* Smart Materials and Structures. **Vol. 15**(6): p. 1811-1829.

[116] Laory, I., T.N. Trinh, and I.F.C. Smith (2011). *Evaluating two model-free data interpretation methods for measurements that are influenced by temperature.* Advanced Engineering Informatics. **Vol. 25**(3): p. 495-506.

[117] Larsson, O. and R. Karoumi (2011). *Modelling of climatic thermal actions in hollow concrete box cross-sections.* Structural Engineering International: Journal of the International Association for Bridge and Structural Engineering (IABSE). **Vol. 21**(1): p. 74-79.

[118] Larsson, O. (2012). *Climate Related Thermal Actions for Reliable Design of Concrete Structures*. Lund University, Doctoral Thesis, 158 p.

[119] Larsson, O. and S. Thelandersson (2012). *Transverse thermal stresses in concrete box cross-sections due to climatic exposure.* Structural Concrete. **Vol. 13**(4): p. 227-235.

[120] Li, F., Z. Wang, and G. Liu (2013). *Towards an Error Correction Model for dam monitoring data analysis based on Cointegration Theory.* Structural Safety. **Vol. 43**: p. 12-20.

[121] Li, H.-N., T.-H. Yi, L. Ren, D.-S. Li, and L.-S. Huo (2014). *Reviews on innovations and applications in structural health monitoring for infrastructures.* Structural Monitoring and Maintenance. **Vol. 1**(1): p. 1-45.

[122] Li, H.-N., L. Ren, Z.-G. Jia, T.-H. Yi, and D.-S. Li (2015). *State-of-the-art in structural health monitoring of large and complex civil infrastructures.* Journal of Civil Structural Health Monitoring. **Vol. 6**(1): p. 3-16.

[123] Li, H.-N., D.-S. Li, L. Ren, T.-H. Yi, Z.-G. Jia, and K.-P. Li (2016). *Structural health monitoring of innovative civil engineering structures in Mainland China.* Structural Monitoring and Maintenance. **Vol. 3**(1): p. 1-32.

[124] Li, H., S. Li, J. Ou, and H. Li (2010). *Modal identification of bridges under varying environmental conditions: Temperature and wind effects.* Structural Control and Health Monitoring. **Vol. 17**(5): p. 495-512.

[125] Li, H. and J. Ou (2015). *The state of the art in structural health monitoring of cable-stayed bridges.* Journal of Civil Structural Health Monitoring. **Vol. 6**(1): p. 43-67.

[126] Li, M., Y. Jiang, and C.F.M. Coimbra (2017). *On the determination of atmospheric longwave irradiance under all-sky conditions.* Solar Energy. **Vol. 144**: p. 40-48.

[127] Li, S., H. Li, Y. Liu, C. Lan, W. Zhou, and J. Ou (2014). *SMC structural health monitoring benchmark problem using monitored data from an actual cable-stayed bridge.* Structural Control and Health Monitoring. **Vol. 21**(2): p. 156-172.

[128] Liang, G., Y. Hu, and Q. Li (2018). *Safety Monitoring of High Arch Dams in Initial Operation Period Using Vector Error Correction Model.* Rock Mechanics and Rock Engineering. **Vol. 51**(8): p. 2469-2481.

[129] Liang, Y., D. Li, G. Song, and Q. Feng (2018). *Frequency Co-integration-based*

damage detection for bridges under the influence of environmental temperature variation. Measurement. **Vol. 125**: p. 163-175.

[130] Liao, W.Y., Y.Q. Ni, and G. Zheng (2012). *Tension Force and Structural Parameter Identification of Bridge Cables.* Advances in Structural Engineering. **Vol. 15**(6): p. 983-996.

[131] Maddala, G.S. and I.M. Kim (1998). *Unit Roots, Cointegration, and Structural Change*: Cambridge University Press.

[132] Magalhães, F., Á. Cunha, and E. Caetano (2009). *Online automatic identification of the modal parameters of a long span arch bridge.* Mechanical Systems and Signal Processing. **Vol. 23**(2): p. 316-329.

[133] Magalhães, F., A. Cunha, and E. Caetano (2012). *Vibration based structural health monitoring of an arch bridge: From automated OMA to damage detection.* Mechanical Systems and Signal Processing. **Vol. 28**: p. 212-228.

[134] Magalhães, F.M.R.L.d. (2004). *Identificação modal estocástica para validação experimental de modelos numéricos*. Faculdade de Engenharia da Universidade do Porto, Tese de Mestrado.

[135] Mata, J. (2011). *Interpretation of concrete dam behaviour with artificial neural network and multiple linear regression models.* Engineering Structures. **Vol. 33**(3): p. 903-910.

[136] Mattson, S.G. and S.M. Pandit (2006). *Statistical moments of autoregressive model residuals for damage localisation.* Mechanical Systems and Signal Processing. **Vol. 20**(3): p. 627-645.

[137] Mehrabi, A.B. and H. Tabatabai (1998). *Unified finite difference formulation for free vibration of cables.* Journal of structural engineering New York, N.Y. **Vol. 124**(11): p. 1313-1322.

[138] Mendes, P. (1989). *Acção Térmica Diferencial em Pontes de Betão*. IST, Master Thesis.

[139] Mirambell, E. and A. Aguado (1990). *Temperature and Stress Distributions in Concrete Box Girder Bridges.* Journal of Structural Engineering. **Vol. 116 - nº9**.

[140] Moaveni, B., J.P. Conte, and F.M. Hemez (2009). *Uncertainty and Sensitivity Analysis of Damage Identification Results Obtained Using Finite Element Model Updating.* Computer-Aided Civil and Infrastructure Engineering. **Vol. 24**(5): p. 320-334.

[141] Montgomery, D.C. (2009). *Introduction to Statistical Quality Control*. Sixth edition ed, ed. Wiley, Jefferson City.

[142] Montgomery, D.C. and G.C. Runger (2011). *Applied statistics and probability for engineers - fifth edition*, USA: John Wiley and Sons, Inc.

[143] Mordini, A., K. Savov, and H. Wenzel (2008). *Damage detection on stay cables using*

an open source-based framework for finite element model updating. Structural Health Monitoring. **Vol. 7**(2): p. 91-102.

[144] Mufti, A. (2001). *Guidelines for structural health monitoring.* Design manual, Winnipeg, Manitoba: ISIS Canada Corporation. pag. var.-pag. var.

[145] Mujica, L., J. Rodellar, A. Fernandez, and A. Guemes (2010). *Q-statistic and T2-statistic PCA-based measures for damage assessment in structures.* Structural Health Monitoring. **Vol. 10**(5): p. 539-553.

[146] NewMENSUS (2015). *Sistema de Monitorização Estrutural e de Durabilidade do Viaduto do Corgo: Manual de Utilização*, NewMENSUS: Porto.

[147] Ni, Y., H. Zhou, and J. Ko (2009). *Generalization Capability of Neural Network Models for Temperature-Frequency Correlation Using Monitoring Data.* Journal of Structural Engineering. **Vol. 135**(10): p. 1290-1300.

[148] Ni, Y.Q., X.G. Hua, K.Q. Fan, and J.M. Ko (2005). *Correlating modal properties with temperature using long-term monitoring data and support vector machine technique.* Engineering Structures. **Vol. 27**(12): p. 1762-1773.

[149] Oh, C.K., H. Sohn, and I.-H. Bae (2009). *Statistical novelty detection within the Yeongjong suspension bridge under environmental and operational variations.* Smart Materials and Structures. **Vol. 18**(12): p. 125022.

[150] Omenzetter, P. and J.M.W. Brownjohn (2006). *Application of time series analysis for bridge monitoring.* Smart Materials and Structures. **Vol. 15**(1): p. 129-138.

[151] Ou, J. and H. Li (2010). *Structural Health Monitoring in mainland China: Review and Future Trends.* Structural Health Monitoring. **Vol. 9**(3): p. 219-231.

[152] Pan, H., M. Azimi, F. Yan, and Z. Lin (2018). *Time-Frequency-Based Data-Driven Structural Diagnosis and Damage Detection for Cable-Stayed Bridges.* Journal of Bridge Engineering. **Vol. 23**(6).

[153] Peres-Neto, P.R., D.A. Jackson, and K.M. Somers (2005). *How many principal components? stopping rules for determining the number of non-trivial axes revisited.* Computational Statistics & Data Analysis. **Vol. 49**(4): p. 974-997.

[154] Perez, R., P. Ineichen, R. Seals, J. Michalsky, and R. Stewart (1990). *Modeling daylight availability and irradiance components from direct and global irradiance.* Solar Energy. **Vol. 44**(5): p. 271-289.

[155] Pimentel, M., E. Brühwiler, and J. Figueiras (2014). *Safety examination of existing concrete structures using the global resistance safety factor concept.* Engineering Structures. **Vol. 70**: p. 130-143.

[156] Posenato, D., F. Lanata, D. Inaudi, and I.F.C. Smith (2008). *Model-free data interpretation for continuous monitoring of complex structures.* Advanced Engineering Informatics. **Vol. 22**(1): p. 135-144.

[157] Posenato, D. (2009). *Model-free Data Interpretation for Continuous Monitoring of Complex Structures*. École Polytechnique Fédérale de Lausanne, Doctoral Thesis, 155 p.

[158] Posenato, D., P. Kripakaran, D. Inaudi, and I.F.C. Smith (2010). *Methodologies for model-free data interpretation of civil engineering structures.* Computers & Structures. **Vol. 88**(7-8): p. 467-482.

[159] Potgieter, I.C. and W.L. Gamble (1989). *Nonlinear temperature distributions in bridges at different locations in the united states.* PCI Journal. **Vol.**: p. 80-103.

[160] Rageh, A., D.G. Linzell, and S. Eftekhar Azam (2018). *Automated, strain-based, output-only bridge damage detection.* Journal of Civil Structural Health Monitoring. **Vol. 8**(5): p. 833-846.

[161] Rainieri, C., F. Magalhaes, D. Gargaro, G. Fabbrocino, and A. Cunha (2019). *Predicting the variability of natural frequencies and its causes by Second-Order Blind Identification.* Structural Health Monitoring. **Vol. 18**(2): p. 486-507.

[162] Rama Mohan Rao, A., K. Lakshmi, and D. Venkatachalam (2012). *Damage diagnostic technique for structural health monitoring using POD and self adaptive differential evolution algorithm.* Computers & Structures. **Vol. 106-107**: p. 228-244.

[163] Ren, W.X., G. Chen, and W.H. Hu (2005). *Empirical formulas to estimate cable tension by cable fundamental frequency.* Structural Engineering and Mechanics. **Vol. 20**(3): p. 363-380.

[164] Reynders, E., G. Wursten, and G. De Roeck (2013). *Output-only structural health monitoring in changing environmental conditions by means of nonlinear system identification.* Structural Health Monitoring. **Vol. 13**(1): p. 82-93.

[165] Rodrigues, C., C. Félix, A. Lage, and J. Figueiras (2010). *Development of a long-term monitoring system based on FBG sensors applied to concrete bridges.* Engineering Structures. **Vol. 32**(8): p. 1993-2002.

[166] Rodrigues, J. (2004). *Identificação modal estocástica Métodos de análise e aplicações em estruturas de engenharia civil*. Faculdade de Engenharia da Universidade do Porto, Doctoral Thesis.

[167] Rytter, A. (1993). *Vibrational Based Inspection of Civil Engineering Structures*. Aalborg University, Doctoral Thesis.

[168] Santos, A., E. Figueiredo, M. Silva, R. Santos, C. Sales, and J.C.W.A. Costa (2017). *Genetic-based EM algorithm to improve the robustness of Gaussian mixture models for damage detection in bridges.* Structural Control and Health Monitoring. **Vol. 24**(3).

[169] Santos, J.P., C. Crémona, A.D. Orcesi, and P. Silveira (2013). *Multivariate statistical analysis for early damage detection.* Engineering Structures. **Vol. 56**: p. 273-285.

[170] Santos, J.P. (2014). *Smart structural health monitoring techniques for novelty identification in civil engineering structures*. Instituto Superior Técnico - Universidade de Lisboa, Doctoral Thesis.

[171] Santos, J.P., C. Crémona, L. Calado, P. Silveira, and A.D. Orcesi (2015). *On-line unsupervised detection of early damage.* Structural Control and Health Monitoring. **Vol. 23**(7): p. 1047-1069.

[172] Santos, J.P., C. Crémona, A.P.C.d. Silveira, and L.C.d.O. Martins (2016). *Real-time damage detection based on pattern recognition.* Structural Concrete. **Vol. 17**(3): p. 338-354.

[173] Scalea, F.L.d., P. Rizzo, and F. Seible (2003). *Stress Measurement and Defect Detection in Steel Strands by Guided Stress Waves.* Journal of Materials in Civil Engineering. **Vol. 15**(3): p. 219-227.

[174] Schwert, G.W. (1989). *Tests For Unit Roots: A Monte Carlo Investigation.* Journal of Business & Economic Statistics. **Vol. 7**(2): p. 147-159.

[175] SENER and LCW (2010). *Subconcessão Auto-Estrada Transmontana. A4/IP4 - Vila Real (Parada de Cunhos)/Quintanilha. Lote 1. Projecto de Execução. Obras de Arte Especiais. Viaduto do Corgo: Memória Descritiva e Justificativa*: Lisbon.

[176] Seo, J., J. Hu, and J. Lee (2015). *Summary Review of Structural Health Monitoring Applications for Highway Bridges.* Journal of Performance of Constructed Facilities. **Vol.**: p. 04015072.

[177] Shi, H., K. Worden, and E.J. Cross (2016). *A nonlinear cointegration approach with applications to structural health monitoring.* Journal of Physics: Conference Series. **Vol. 744**.

[178] Shi, H., K. Worden, and E.J. Cross (2018). *A regime-switching cointegration approach for removing environmental and operational variations in structural health monitoring.* Mechanical Systems and Signal Processing. **Vol. 103**: p. 381-397.

[179] Shi, H., K. Worden, and E.J. Cross (2019). *A cointegration approach for heteroscedastic data based on a time series decomposition: An application to structural health monitoring.* Mechanical Systems and Signal Processing. **Vol. 120**: p. 16-31.

[180] Smith, I.F.C., J.-A. Goulet, and I. Laory (2013). *Structural Identification Methods for Full-Scale Bridges*. in *Structures Congress 2013*. Pittsburrgh, Pennsylvania, United States.

[181] SNIRH (2016). *Sistema Nacional de Informação de Recurso Hídricos*. Access Date: March 2016. Available from: www.snirh.pt.

[182] Sohn, H. and C.R. Farrar (2001). *Damage diagnosis using time series analysis of vibration signals.* Smart Materials and Structures. **Vol. 10**(3): p. 446.

[183] Sohn, H., C.R. Farrar, F.M. Hemez, D.D. Shunk, D.W. Stinemates, B.R. Nadler, and

J.J. Czarnecki (2004). *A Review of Structural Health Monitoring Literature: 1996-2001*, Los Alamos National Laboratory.

[184] Sohn, H. (2007). *Effects of environmental and operational variability on structural health monitoring.* Philos Trans A Math Phys Eng Sci. **Vol. 365**(1851): p. 539-60.

[185] Song, Z., J. Xiao, and L. Shen (2012). *On Temperature Gradients in High-Performance Concrete Box Girder under Solar Radiation.* Advances in Structural Engineering. **Vol. 15**(3): p. 399-416.

[186] Soo Lon Wah, W., Y.-T. Chen, G.W. Roberts, and A. Elamin (2018). *Separating damage from environmental effects affecting civil structures for near real-time damage detection.* Structural Health Monitoring. **Vol. 17**(4): p. 850-868.

[187] Sousa, H., C. Félix, J. Bento, and J. Figueiras (2011). *Design and implementation of a monitoring system applied to a long-span prestressed concrete bridge.* Structural Concrete. **Vol. 12**(2): p. 82-93.

[188] Sousa, H., F. Cavadas, A. Henriques, J. Bento, and J. Figueiras (2013). *Bridge deflection evaluation using strain and rotation measurements.* Smart Structures and Systems. **Vol. 11**(4): p. 365-386.

[189] Sousa, H., J. Bento, and J. Figueiras (2014). *Assessment and Management of Concrete Bridges Supported by Monitoring Data-Based Finite-Element Modeling.* Journal of Bridge Engineering. **Vol. 19**(6): p. 05014002.

[190] Sousa Tomé, E. (2012). *Modelação do Faseamento Construtivo do Sub-viaduto Central do Viaduto do Corgo em Vila Real*. Faculdade de Engenharia da Universidade do Porto, Master Thesis.

[191] Sousa Tomé, E., M. Ferraz, R.C.d. Barros, and J. Figueiras (2012). *Modelação do faseamento construtivo do Sub-viaduto Central do Viaduto do Corgo em Vila Real*. in *Encontro Nacional Betão Estrutural 2012*. Porto: FEUP/GPBE.

[192] Sousa Tomé, E., A. Lage, and J. Figueiras (2013). *STayMensus - Manual de Instalação e Utilização*, Porto: FEUP/LABEST.

[193] Sousa Tomé, E., A. Lage, M. Pimentel, and J. Figueiras (2013). *STayMensus: A tool for Acquisition and Analysis of Tension Forces in Stay Cables*. in *55º Congresso Brasileiro do Concreto*. Gramado.

[194] Sousa Tomé, E., R.d. Faria, M. Pimentel, C. Félix, and J. Figueiras (2014). *Ensaios de Receção ao Viaduto sobre o Vale do Rio Corgo: Relatório Técnico*, LABEST/FEUP: Porto. 201 p.

[195] Sousa Tomé, E., M. Pimentel, M. Ferraz, R.d. Faria, C. Félix, and J. Figueiras (2014). *Structural assessment of a cable-stayed bridge during a load test.* in *56º Congresso Brasileiro do Concreto*. Natal.

[196] Sousa Tomé, E., M. Pimentel, M. Ferraz, R.d. Faria, C. Félix, J. Figueiras, V. Barata,

and L. Afonso (2014). *Ensaio de carga ao Viaduto do Corgo.* in *5º Jornadas Portuguesas de Engenharia de Estruturas.* Lisboa.

[197] Sousa Tomé, E., M. Pimentel, and J. Figueiras (2015). *Viaduto do Corgo: Sistema de monitorização dos tirantes, ensaio de carga, movimentos de apoio e modelo multi-regressivo para a estimativa de deslocamentos no topo dos mastros*, LABEST/CONSTRUCT/FEUP: Porto. 126 p.

[198] Sousa Tomé, E., M. Pimentel, and J. Figueiras (2018). *Structural response of a concrete cable-stayed bridge under thermal loads.* Engineering Structures. **Vol. 176**: p. 652-672.

[199] Spencer, J.W. (1971). *Fourier series representation of the position of the sun.* Search. **Vol. 2**(5): p. 172.

[200] Sridhar, V. and R.L. Elliott (2002). *On the development of a simple downwelling longwave radiation scheme.* Agricultural and Forest Meteorology. **Vol. 112**(3): p. 237-243.

[201] Su, Z., X. Wang, L. Cheng, L. Yu, and Z. Chen (2009). *On Selection of Data Fusion Schemes for Structural Damage Evaluation.* Structural Health Monitoring. **Vol. 8**(3): p. 223-241.

[202] Taha, M.M.R., A. Noureldin, J.L. Lucero, and T.J. Baca (2006). *Wavelet Transform for Structural Health Monitoring: A Compendium of Uses and Features.* Structural Health Monitoring. **Vol. 5**(3): p. 267-295.

[203] Teughels, A. and G. De Roeck (2004). *Structural damage identification of the highway bridge Z24 by FE model updating.* Journal of Sound and Vibration. **Vol. 278**(3): p. 589-610.

[204] TNO DIANA (2015). *Diana 9.6 User's Manual* Delft.

[205] Vall, S. and A. Castell (2017). *Radiative cooling as low-grade energy source: A literature review.* Renewable and Sustainable Energy Reviews. **Vol. 77**: p. 803-820.

[206] Vardanega, P.J., G.T. Webb, P.R.A. Fidler, and C.R. Middleton (2016). *Assessing the potential value of bridge monitoring systems.* Proceedings of the Institution of Civil Engineers - Bridge Engineering. **Vol. 0**(0): p. 1-13.

[207] Vasarevicius, D. and R. Martavicius (2011). *Solar irradiance model for solar electric panels and solar thermal collectors in lithuania.* Elektronika ir Elektrotechnika. **Vol.** (2): p. 3-6.

[208] Wang, H., Y.-M. Zhang, J.-X. Mao, H.-P. Wan, T.-Y. Tao, and Q.-X. Zhu (2019). *Modeling and forecasting of temperature-induced strain of a long-span bridge using an improved Bayesian dynamic linear model.* Engineering Structures. **Vol. 192**: p. 220-232.

[209] Webb, G.T., P.J. Vardanega, and C.R. Middleton (2014). *Categories of SHM*

Deployments: Technologies and Capabilities. Journal of Bridge Engineering. **Vol. 20**(11): p. 04014118.

[210] Welch, P.D. (1967). *The Use of Fast Fourier Transform for the Estimation of Power Spectra: A Method Based on Time Averaging Over Short, Modified Peridograms.* IEEE Transaction on Audio and Electroacoust. **Vol. AU-15**: p. 70-73.

[211] Wenzel, H. (2009). *Health Monitoring of Bridges*: Wiley.

[212] Westgate, R., K.-Y. Koo, and J. Brownjohn (2015). *Effect of Solar Radiation on Suspension Bridge Performance.* Journal of Bridge Engineering. **Vol. 20**(5): p. 04014077.

[213] Worden, K., G. Manson, and N.R.J. Fieller (2000). *Damage Detection Using Outlier Analysis.* Journal of Sound and Vibration. **Vol. 229**(3): p. 647-667.

[214] Worden, K. and J.M. Dulieu-Barton (2004). *An Overview of Intelligent Fault Detection in Systems and Structures.* Structural Health Monitoring. **Vol. 3**(1): p. 85-98.

[215] Worden, K., C.R. Farrar, G. Manson, and G. Park (2007). *The fundamental axioms of structural health monitoring.* Proceedings of the Royal Society A: Mathematical, Physical and Engineering Sciences. **Vol. 463**(2082): p. 1639-1664.

[216] Worden, K. and G. Manson (2007). *The application of machine learning to structural health monitoring.* Philos Trans A Math Phys Eng Sci. **Vol. 365**(1851): p. 515-37.

[217] Worden, K. and M.I. Friswell (2009). *Modal–Vibration-Based Damage Identification.* Encyclopedia of Structural Health Monitoring. **Vol.**

[218] Worden, K., W.J. Staszewski, and J.J. Hensman (2011). *Natural computing for mechanical systems research: A tutorial overview.* Mechanical Systems and Signal Processing. **Vol. 25**(1): p. 4-111.

[219] Worden, K., E.J. Cross, I. Antoniadou, and A. Kyprianou (2014). *A multiresolution approach to cointegration for enhanced SHM of structures under varying conditions – An exploratory study.* Mechanical Systems and Signal Processing. **Vol. 47**(1-2): p. 243-262.

[220] Xia, Y., B. Chen, X.-q. Zhou, and Y.-l. Xu (2013). *Field monitoring and numerical analysis of Tsing Ma Suspension Bridge temperature behavior.* Structural Control and Health Monitoring. **Vol. 20**(4): p. 560-575.

[221] XU, Y.-L. and Y. Xia (2012). *Structural Health Monitoring of Long-Spam Suspension Bridges*, Oxon: Spon Press.

[222] Xu, Y.-L. (2018). *Making good use of structural health monitoring systems of long-span cable-supported bridges.* Journal of Civil Structural Health Monitoring. **Vol. 8**(3): p. 477-497.

[223] Xu, Z.-D. and Zhishen Wu (2007). *Simulation of the Effect of Temperature Variation on Damage Detection in a Long-span Cable-stayed Bridge.* Structural Health Monitoring. **Vol. 6**(3): p. 177-189.

[224] Yan, A.M., G. Kerschen, P. De Boe, and J.C. Golinval (2005). *Structural damage diagnosis under varying environmental conditions—Part I: A linear analysis.* Mechanical Systems and Signal Processing. **Vol. 19**(4): p. 847-864.

[225] Yan, A.M., G. Kerschen, P. De Boe, and J.C. Golinval (2005). *Structural damage diagnosis under varying environmental conditions—part II: local PCA for non-linear cases.* Mechanical Systems and Signal Processing. **Vol. 19**(4): p. 865-880.

[226] Yang, Y. and S. Nagarajaiah (2014). *Blind identification of damage in time-varying systems using independent component analysis with wavelet transform.* Mechanical Systems and Signal Processing. **Vol. 47**(1-2): p. 3-20.

[227] Yarnold, M. and N.C. Dubbs (2015). *Bearing Assessment with Periodic Temperature-Based Measurements.* Transportation Research Record: Journal of the Transportation Research Board. **Vol. 2481**: p. 115-123.

[228] Zang, C., M.I. Friswell, and M. Imregun (2004). *Structural Damage Detection using Independent Component Analysis.* Structural Health Monitoring. **Vol. 3**(1): p. 69-83.

[229] Zhang, Q. and Y. Zhou (2007). *Investigation of the applicability of current bridge health monitoring technology.* Structure and Infrastructure Engineering. **Vol. 3**(2): p. 159-168.

[230] Zhou, G.-D., T.-H. Yi, B. Chen, and X. Chen (2018). *Modeling Deformation Induced by Thermal Loading Using Long-Term Bridge Monitoring Data.* Journal of Performance of Constructed Facilities. **Vol. 32**(3).

[231] Zhou, H.F., Y.Q. Ni, and J.M. Ko (2010). *Constructing input to neural networks for modeling temperature-caused modal variability: Mean temperatures, effective temperatures, and principal components of temperatures.* Engineering Structures. **Vol. 32**(6): p. 1747-1759.

[232] Zhou, H.F., Y.Q. Ni, and J.M. Ko (2011). *Structural damage alarming using auto-associative neural network technique: Exploration of environment-tolerant capacity and setup of alarming threshold.* Mechanical Systems and Signal Processing. **Vol. 25**(5): p. 1508-1526.

[233] Zhou, H.F., Y.Q. Ni, and J.M. Ko (2011). *Eliminating Temperature Effect in Vibration-Based Structural Damage Detection.* Journal of Engineering Mechanics. **Vol. 137**(12): p. 785-796.

[234] Zhou, L., Y. Xia, J.M.W. Brownjohn, and K.Y. Koo (2016). *Temperature Analysis of a Long-Span Suspension Bridge Based on Field Monitoring and Numerical Simulation.* Journal of Bridge Engineering. **Vol. 21**(1): p. 04015027.

[235] Zhu, J. and Q. Meng (2017). *Effective and Fine Analysis for Temperature Effect of Bridges in Natural Environments.* Journal of Bridge Engineering. **Vol. 22**(6): p. 04017017.

[236] Zhu, Y., Y.-Q. Ni, A. Jesus, J. Liu, and I. Laory (2018). *Thermal strain extraction methodologies for bridge structural condition assessment.* Smart Materials and Structures. **Vol.**

[237] Zhu, Y., Y.-Q. Ni, H. Jin, D. Inaudi, and I. Laory (2019). *A temperature-driven MPCA method for structural anomaly detection.* Engineering Structures. **Vol. 190**: p. 447-458.

[238] Zivot, E. and J. Wang (2003). *Modeling Financial Time Series with S-Plus*: Springer.

[239] Zolna, K., P.B. Dao, W.J. Staszewski, and T. Barszcz (2015). *Nonlinear Cointegration Approach for Condition Monitoring of Wind Turbines.* Mathematical Problems in Engineering. **Vol. 2015**: p. 1-11.

[240] Zolna, K., P.B. Dao, W.J. Staszewski, and T. Barszcz (2016). *Towards homoscedastic nonlinear cointegration for structural health monitoring.* Mechanical Systems and Signal Processing. **Vol. 75**: p. 94-108.

APPENDIXES

Appendix A

EXPERIMENTAL RAW TIME SERIES OF TEMPERATURES, GIRDER DEFLECTIONS AND STAY CABLE FORCES

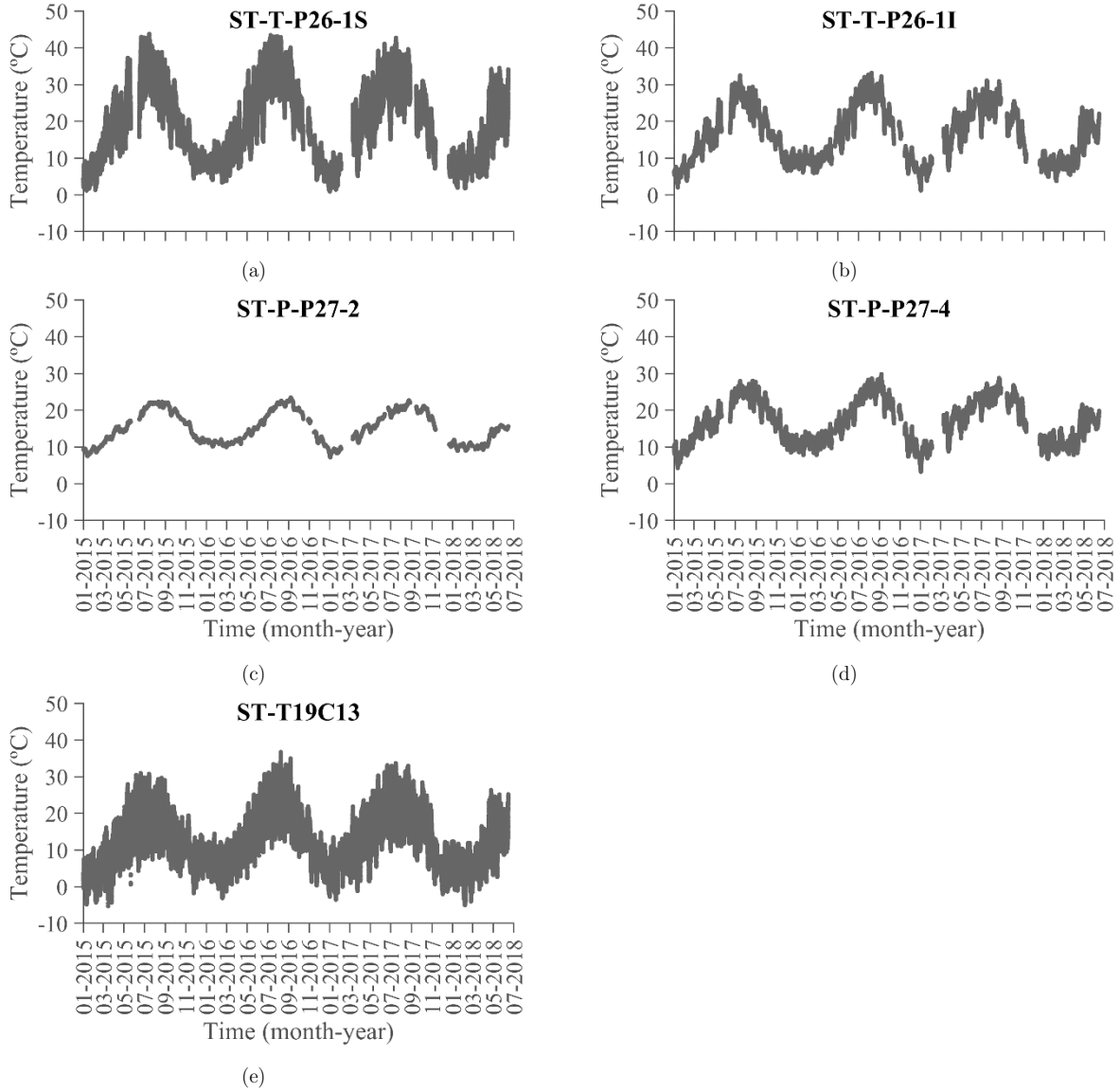

Figure A.1– Raw temperature time series: (a) ST-T-P26-1S, (b) ST-T-P26-1I, (c) ST-P-P27-2. (d) ST-P-P27-4 and (e) ST-T19C13.

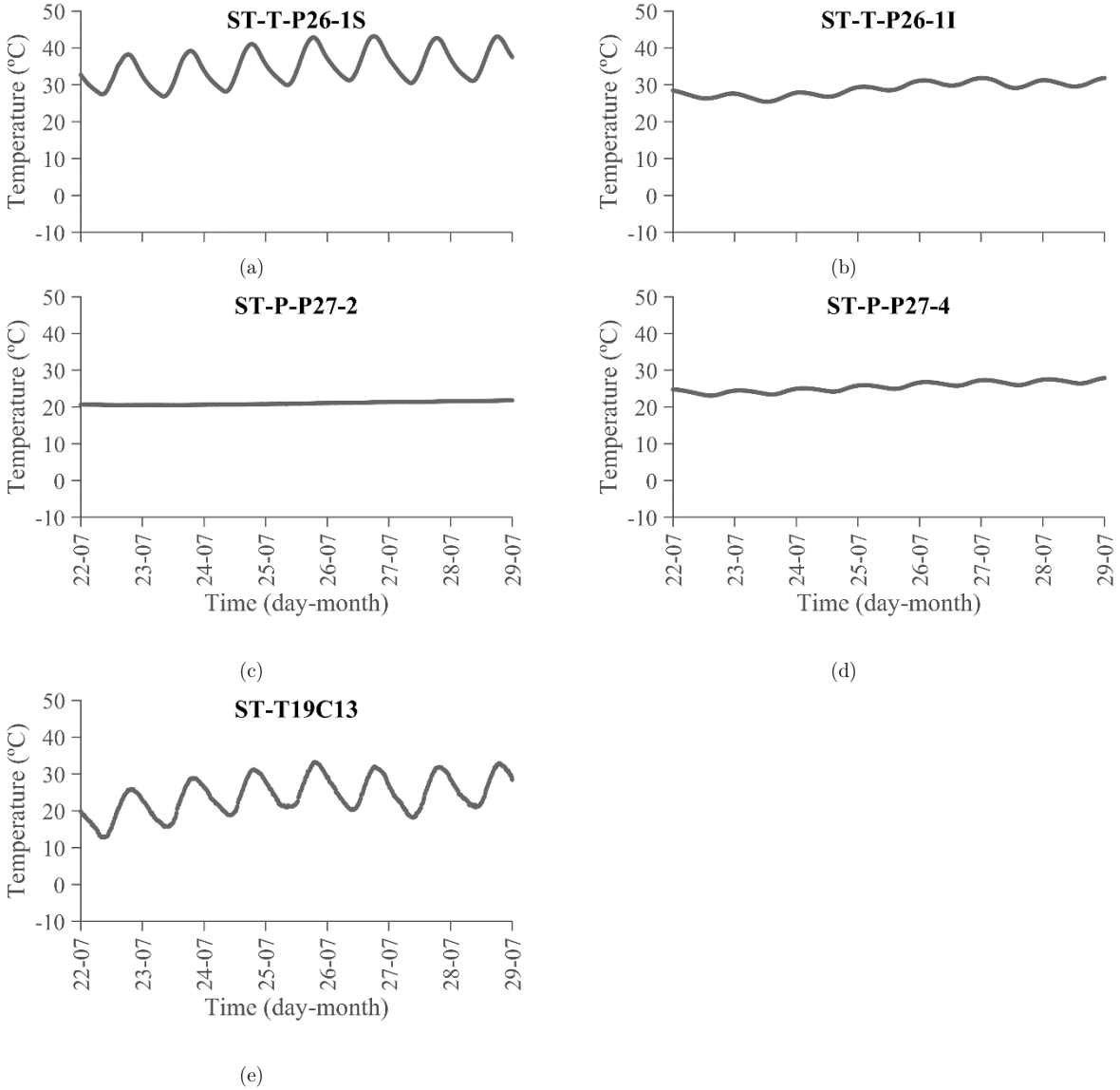

Figure A.2 – Raw temperature time series between 22nd and 29th July 2016: (a) ST-T-P26-1S, (b) ST-T-P26-1I, (c) ST-P-P27-2. (d) ST-P-P27-4 and (e) ST-T19C13.

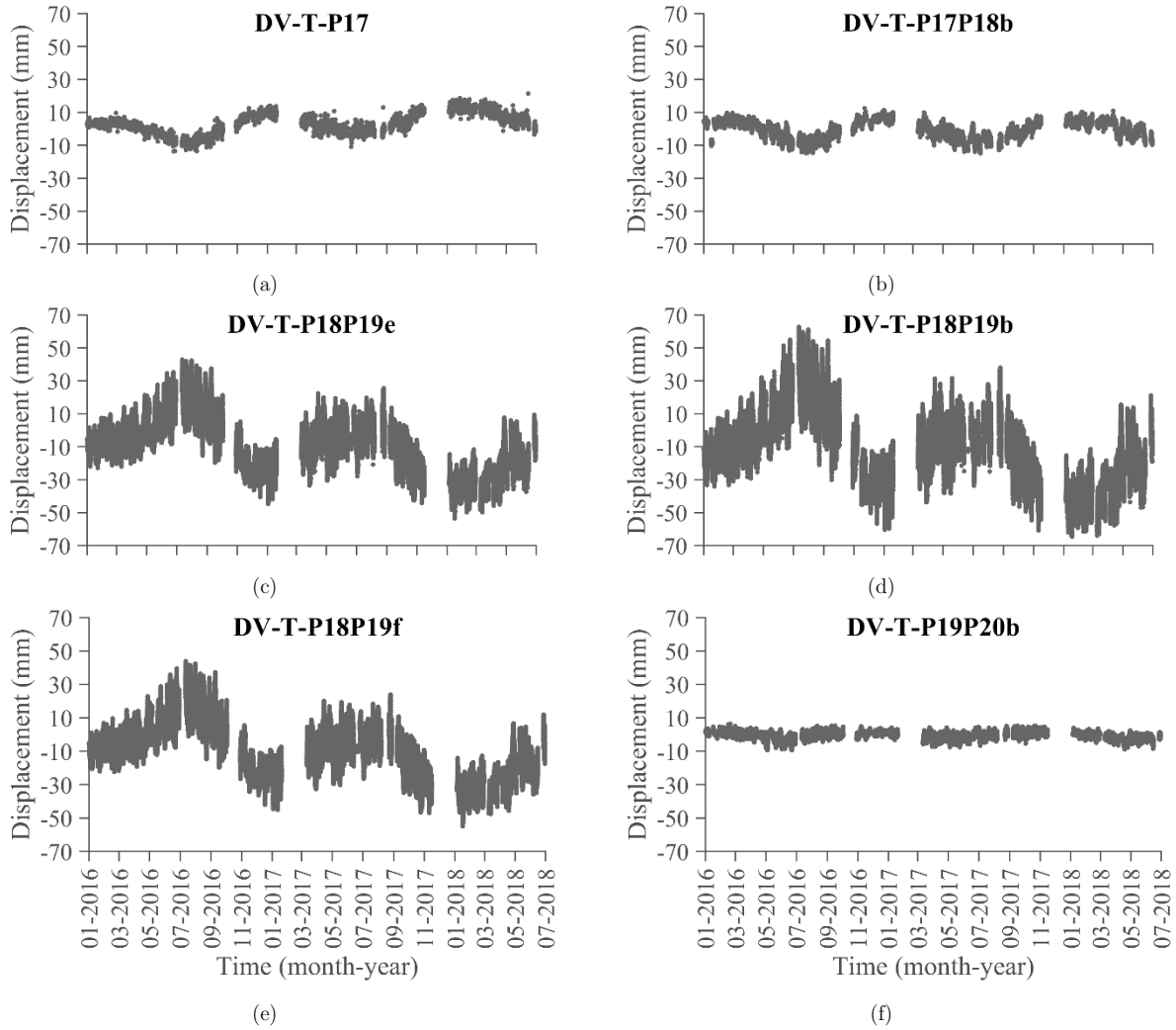

Figure A.3 – Raw experimental time series of the girder deflections: (a) DV-T-P17, (b) DV-T-P17P18b, (c) DV-T-P18P19e, (d) DV-T-P18P19b, (e) DV-T-P18P19f and (f) DV-T-P19P20b.

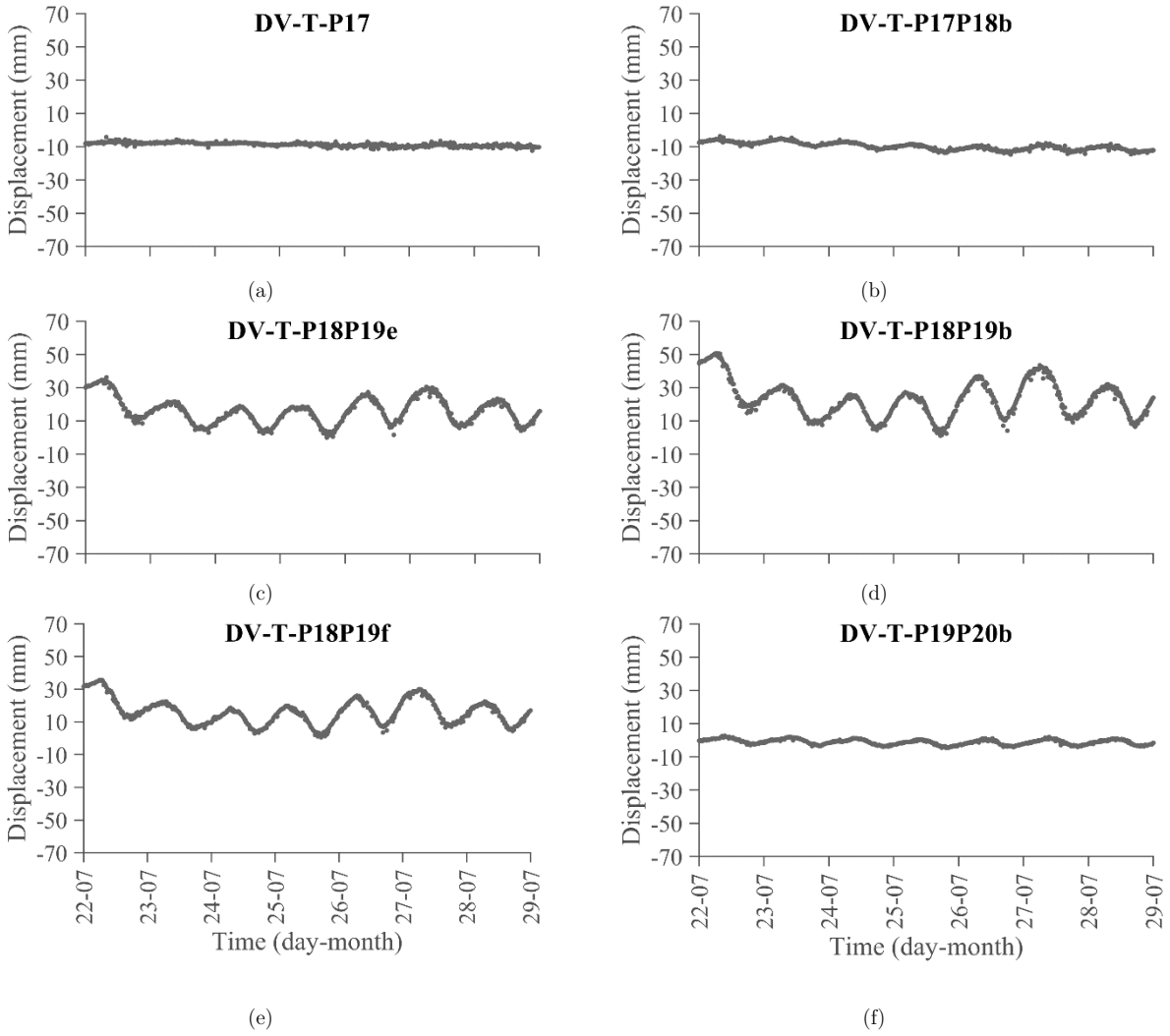

Figure A.4 – Raw experimental time series of the girder deflections between 22nd and 29th July 2016: (a) DV-T-P17, (b) DV-T-P17P18b, (c) DV-T-P18P19e, (d) DV-T-P18P19b, (e) DV-T-P18P19f and (f) DV-T-P19P20b.

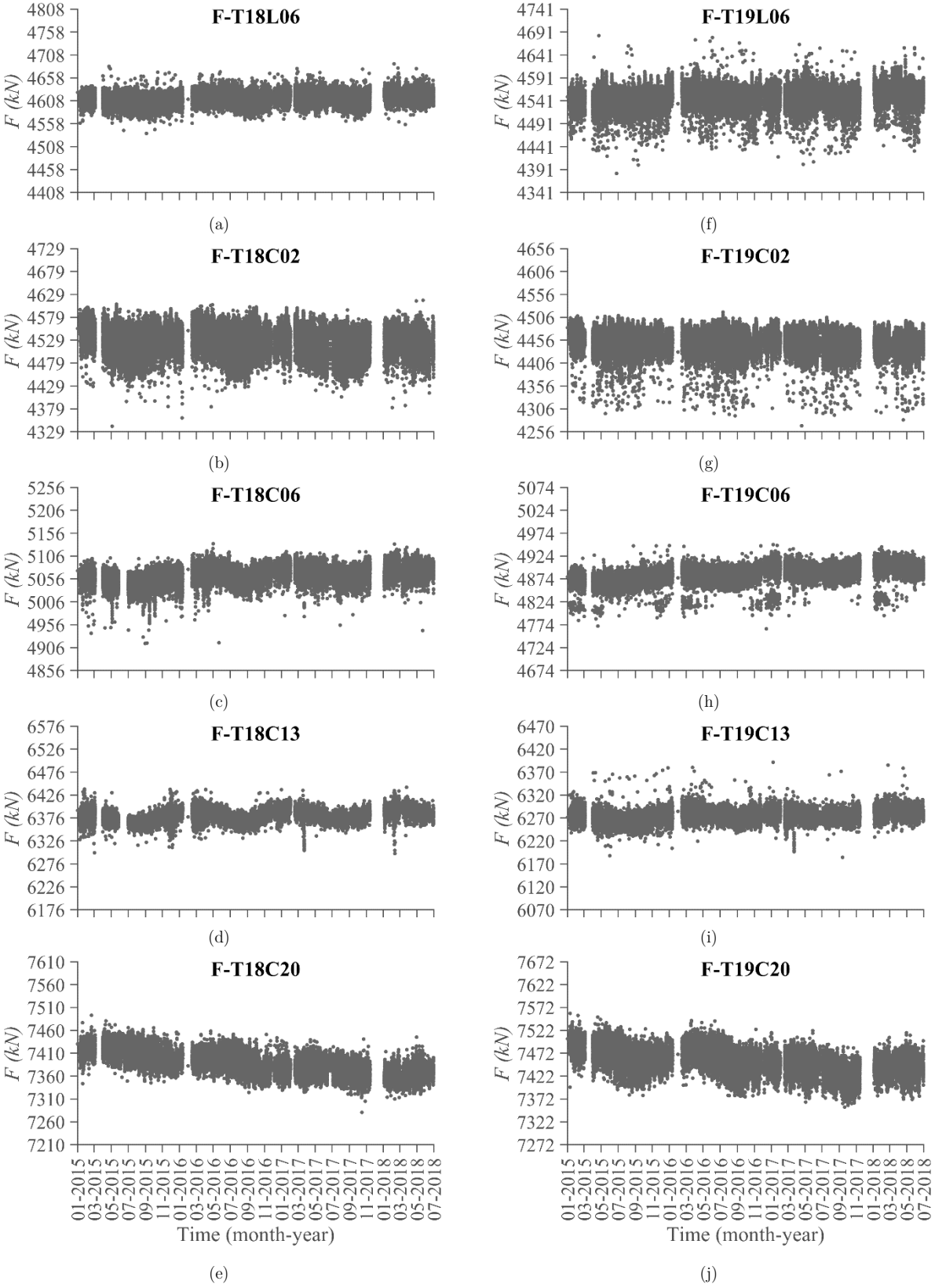

Figure A.5 – Raw experimental time series of the stay cable forces (computed using f_2): (a) F-T18L06, (b) F-T18C02, (c) F-T18C06, (d) F-T18C13, (e) F-T18C20, (f) F-T19L06, (g) F-T19C02, (h) F-T19C06, (i) F-T19C13 and (j) F-T19C20.

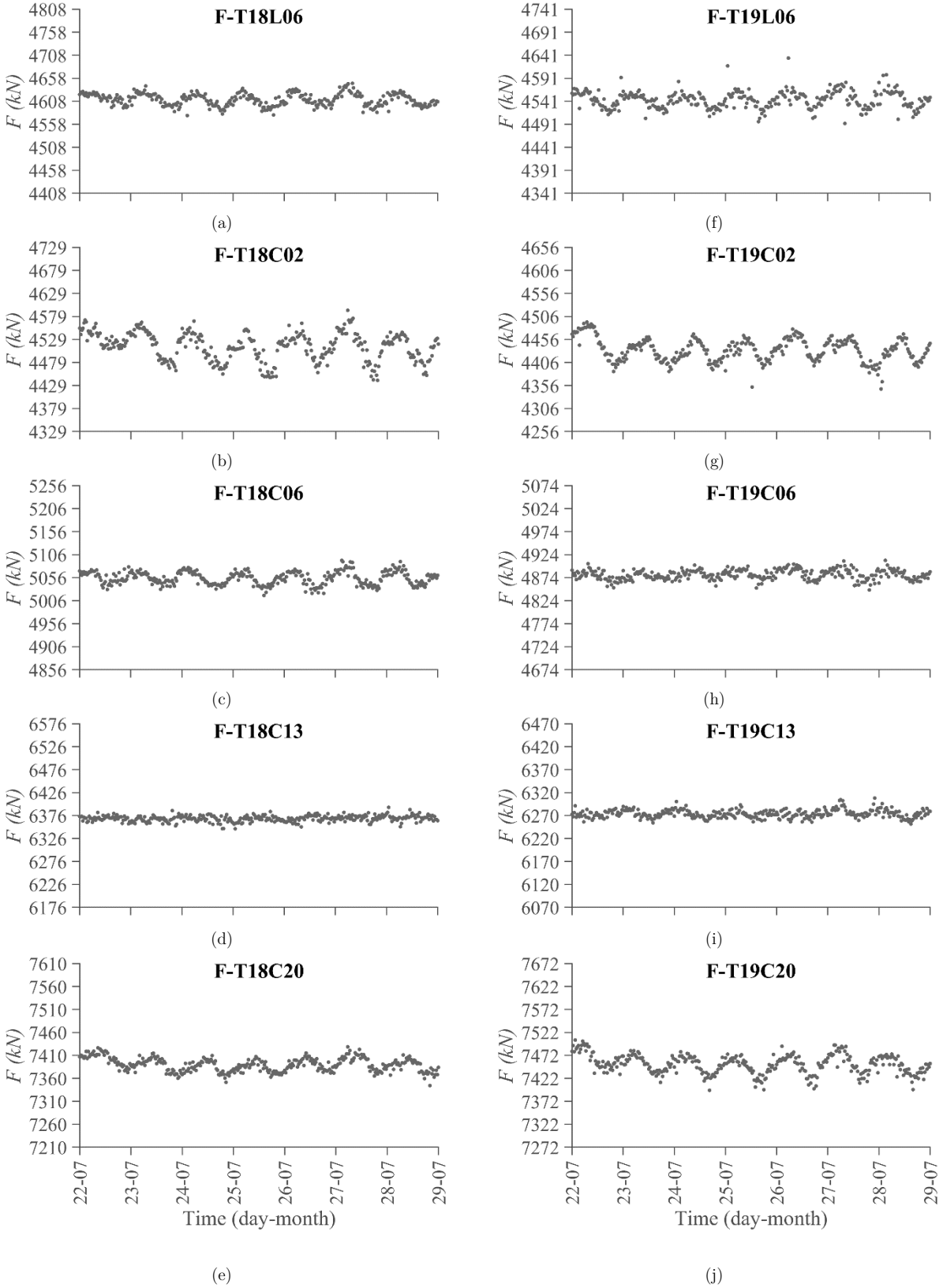

Figure A.6 – Raw experimental time series of the stay cables (computed using f_2) between 22nd and 29th July 2016: (a) F-T18L06, (b) F-T18C02, (c) F-T18C06, (d) F-T18C13, (e) F-T18C20, (f) F-T19L06, (g) F-T19C02, (h) F-T19C06, (i) F-T19C13 and (j) F-T19C20.

Appendix B

EFFECTIVE SKY TEMPERATURE

The effective sky temperature (T_{sky}) was estimated according to the following empirical model proposed by Sridhar and Elliott [200]:

$$T_{sky} = \left[1.31 \left(\frac{0.01 e_0}{T_a} \right)^{1/7} \right]^{1/4} T_a \tag{B.1}$$

where T_a is the ambient temperature [K] and e_0 is the partial pressure of water vapour [Pa], which can be estimated using the Magus equation [3]:

$$e_0 = 610.94 \left(\frac{RH}{100} \right) \exp \left(\frac{17.625(T_a - 273.15)}{T_a - 30.11} \right) \tag{B.2}$$

being RH the relative humidity [%]. In the present work both RH and T_a were measured by the bridge structural health monitoring system.

Appendix C

SOLAR GEOMETRIC RELATIONS

The total solar radiation on an arbitrary inclined surface depends on the geometric relationships between the surface and the earth and between the surface and the sun, which can be described by angles depicted in Figures C.1 and C.2 [47]:

- α_s is the solar altitude angle [º], i.e., the angle between the horizontal and the line to the sun;
- β is the surface angle relative to the horizontal plane $[0º \leq \beta \leq 180º]$;
- γ is the surface azimuth angle [º], i.e., the deviation from the local meridian of the projection on a horizontal plane of the normal to the surface – 0º means south, 90º means east, 180º means north and 270º means west;
- γ_s is the solar azimuth angle [º], i.e., the angular displacement from south of the projection of beam radiation on the horizontal plane;
- δ is the declination [º], i.e., the angular position of the sun at solar noon with respect to the plane of the equator;
- θ is the angle of incidence [º], i.e., the angle between the beam radiation on a surface

and the normal to that surface. For horizontal surfaces, $\theta = \theta_z$;

- θ_z is the zenith angle [º], i.e., the angle between the vertical and the line to the sun, that is, the complement of the solar altitude angle;
- ω is the hour angle [º], i.e., the angular displacement of the sun east or west of the local meridian due to rotation of the earth at 15º per hour (Figure C.2). It takes negative values in the morning and positive values in the afternoon.

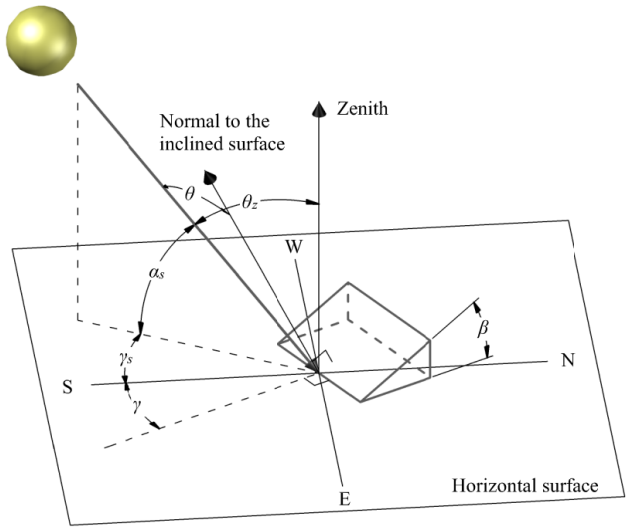

Figure C.1 – (a) Zenith angle (θ_z), solar altitude angle (α_s), solar azimuth angle (γ_s), surface azimuth angle (γ) and surface angle (β). (Adapted from Duffie and Beckman [56]).

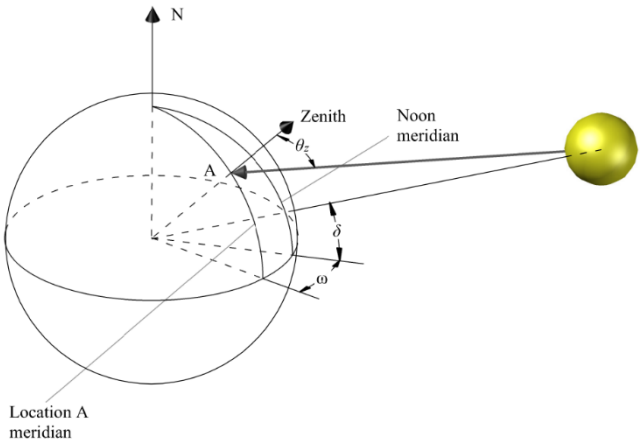

Figure C.2 – Hour angle (ω), declination (δ) and zenith angle (θ_z). (Adapted from Vasarevicius and Martavicius [207]).

The declination δ may be obtained from the equation proposed by Cooper [38]:

$$\delta = 23.45 \sin\left(360 \frac{284+n}{365}\right) \tag{C.1}$$

or from a more accurate equation proposed by Spencer [199] (maximum absolute error of 0.035º):

$$\begin{aligned}\delta = \frac{180}{\pi}(&0.006918 - 0.399912\cos B + 0.070257\sin B - 0.006758\cos(2B) \\ &+ 0.000907\sin(2B) - 0.002697\cos(3B) + 0.00148\sin(3B))\end{aligned} \tag{C.2}$$

with B given by:

$$B = (n-1)\frac{360}{365} \tag{C.3}$$

where n is the day of the year (with $n=1$ for January1st). The angle of incidence θ can be obtained from one of the following two equations:

$$\begin{aligned}\cos\theta = &\sin\delta\sin\phi\cos\beta - \sin\delta\cos\phi\sin\beta\cos\gamma + \cos\delta\cos\phi\cos\beta\cos\omega \\ &+ \cos\delta\sin\phi\sin\beta\cos\gamma\cos\omega + \cos\delta\sin\beta\sin\gamma\sin\omega\end{aligned} \tag{C.4}$$

$$\cos\theta = \cos\theta_z cos\beta + \sin\theta_z \sin\beta\cos(\gamma_s - \gamma) \tag{C.5}$$

where ϕ is the latitude (in degrees). For a horizontal surface $\theta = \theta_z$ and $\beta = 0$, the equation (C.4)becomes:

$$\cos\theta_z = \cos\phi\cos\delta\cos\omega + \sin\phi\sin\delta \tag{C.6}$$

It should be borne in mind that the angle of incidence θ may be higher than 90º when the sun is behind the surface. Therefore, the cosine of the angle of incidence should be positive and the hour angle ω should be between the sunrise and sunset. At the sunset hour, the azimuth angle θ_z is 90º. Therefore, from equation (C.6) the sunset angle ω_{ss} can be obtained from:

$$\cos\omega_{ss} = -\frac{\sin\phi\sin\delta}{\cos\phi\cos\delta} = -\tan\phi\tan\delta \tag{C.7}$$

The sunrise angle is the negative of the sunset angle. As the earth rotates at an angular velocity of 15º/h, the hour angle ω is given by:

$$\omega = 15 h_{solar} \tag{C.8}$$

where h_{solar} is the solar time that have values between -12 and 12. Solar time can be obtained from standard time $h_{standard} \in [0,24]$ using the following equation:

$$h_{solar} = h_{standard} + \frac{4(L_{st} + L_{loc}) + E}{60} - 12 \tag{C.9}$$

where L_{st} is the standard median for the local time zone, L_{loc} is the longitude of the location in question and E is the equation of time (in minutes). The latter can be calculated from [199]:

$$\begin{aligned} E = 229.2(&0.000075 + 0.001868\cos B - 0.032077\sin B \\ &- 0.014615\cos(2B) - 0.04089\sin(2B)) \end{aligned} \tag{C.10}$$

where B is obtained from equation (C.3). The solar azimuth angle γ_s can vary between 0º and 360º and is given by [56]:

$$\gamma_s = \mathrm{s}ign(\omega)\left|\cos^{-1}\left(\frac{\cos\theta_z \sin\phi - \sin\delta}{\sin\theta_z \cos\phi}\right)\right| \tag{C.11}$$

Appendix D

ISOTROPIC DIFUSE MODEL

The solar constant $G_{sc} = 1367\ \mathrm{W/m^2}$ is the average energy received from the sun per unit of time by a unit surface area perpendicular to the radiation and located at the earth mean distance from the sun [56, 75]. However, the amount of energy from the Sun that reaches the outer layers of the earth atmosphere (extra-terrestrial radiation, G_{on}) varies due to the variation in the radiation emitted by the sun and to the elliptic earth orbit around the sun (and consequent variation of the Earth-Sun distance). While the former can be ignored for engineering proposes, the latter leads to variations in the range $\pm 3.3\%$ [56]. Therefore, the extra-terrestrial solar radiation G_{on} may be obtained from:

$$G_{on} = G_{sc}\left(1 + 0.033\cos\frac{360n}{365}\right) \tag{D.1}$$

As the solar radiation is scattered or absorbed during the passage through the atmosphere, only a part of the extraterrestrial solar radiation G_{on} reaches the earth surface. The amount of solar radiation that reaches a horizontal plane at the earth surface is called total solar radiation (or global radiation) I and it can be divided in beam or direct radiation I_b and

diffuse radiation I_d. The former refers to the solar radiation received from the sum without being scattered by the atmosphere and the latter refers to the solar radiation that results from scattering of the sun beams. In a clear day, the diffuse radiation is about 10 to 15% of the total solar radiation. When the sun is obscured by thick clouds the direct radiation is null and the total solar radiation is equal to the diffuse radiation.

The total, beam and diffuse solar radiation can be obtained through empirical formulae, such as those found in Duffie and Beckman [56], or from field measurements. In the scope of this work the total solar radiation acting on the tilted surfaces of the structural elements of the Corgo Bridge was obtained from field measurements of the total solar radiation on a horizontal surface, *I*, using the isotropic diffuse model. In this work *I* was measured by a meteorological station located 40 kilometres east from the Corgo Bridge

According to the isotropic diffuse model, the total solar radiation on a tilted plane I_T can be split in three components: beam, isotropic and solar radiation diffusely reflected from the ground which are, respectively, the first, second and third terms of the following equation [56]:

$$I_T = I_b \cdot R_b + I_d \left(\frac{1+\cos(\beta)}{2} \right) + I \cdot \rho_g \left(\frac{1-\cos(\beta)}{2} \right) \tag{D.2}$$

where I_b is the beam solar radiation on a horizontal plane [W/m^2], I_d is the diffuse solar radiation on a horizontal plane [W/m^2], β is the surface angle relative to the horizontal plane $(0° \leq \beta \leq 180°)$, I is the total solar radiation [W/m^2] on a horizontal plane (measured), ρ_g is the albedo or reflection coefficient of the ground and R_b is the ratio of beam radiation on a tilted plane ($I_{b,T}$) to that on a horizontal plane. R_b is obtained from [56]:

$$R_b = \frac{a}{b} \tag{D.3}$$

where

$$\begin{aligned} a = {} & (\sin\delta\sin\phi\cos\beta - \sin\delta\cos\phi\sin\beta\cos\gamma)\times\frac{1}{180}(\omega_2-\omega_1)\pi \\ & + (\cos\delta\cos\phi\cos\beta + \cos\delta\sin\phi\sin\beta\cos\gamma)\times(\sin\omega_2 - \sin\omega_1) \\ & - (\cos\delta\sin\beta\sin\gamma)\times(\cos\omega_2 - \cos\omega_1) \end{aligned} \tag{D.4}$$

and

$$b = (\cos\phi\cos\delta)\times(\sin\omega_2 - \sin\omega_1) + (\sin\phi\sin\delta)\times\frac{1}{180}(\omega_2-\omega_1)\pi \tag{D.5}$$

where ω_1 and ω_2 are two adjacent hours. The ratio between diffuse and total solar radiation on a horizontal plane may be obtained from the correlation proposed by Erbs *et al.* [62]:

$$\frac{I_d}{I} = \begin{cases} 1.0 - 0.09k_T & \text{for } k_T \le 0.22 \\ 0.9511 - 0.1604k_T + 4.388k_T^2 - 16.638k_T^3 + 12.336k_T^4 & \text{for } 0.22 < k_T \le 0.8 \\ 0.165 & \text{for } k_T > 0.8 \end{cases} \tag{D.6}$$

where k_T is the hourly clearness index:

$$k_T = \frac{I}{I_o} \tag{D.7}$$

where I_o is the extra-terrestrial radiation on a horizontal surface for an hour period:

$$I_o = \frac{12}{\pi}G_{on}\times\left[\cos\phi\cos\delta(\sin\omega_2 - \sin\omega_1) + \frac{\pi(\omega_2-\omega_1)}{180}\sin\phi\sin\delta\right] \tag{D.8}$$

In the scope of this work, an albedo of 0.2 was adopted. Although the isotropic diffuse model is easy to understand, it is reported to have a tendency to underestimate the total solar radiation on a tilted surface I_T [56]. Other improved models like the anisotropic diffuse models, such as the HDKR model and the Perez Model [154], may be found, for instance, in Duffie and Beckman [56]. However, in the scope of the present work no significant differences were found when the HDKR model was used.

Appendix E

TEMPERATURE DISTRIBUTION DECOMPOSITION

For a cross section discretized in n finite elements e [138]:

$$T_u = \frac{1}{n}\sum_{e=1}^{n} T_{m,e} \tag{E.1}$$

$$y_G = \frac{\sum_{e=1}^{n} A_e \cdot y_{G,e}}{\sum_{e=1}^{n} A_e} \tag{E.2}$$

$$z_G = \frac{\sum_{e=1}^{n} A_e \cdot z_{G,e}}{\sum_{e=1}^{n} A_e} \tag{E.3}$$

$$I_y = \sum_{e=1}^{n} [I_{\varepsilon y,e} + A_e \cdot (z_G - z_{G,e})^2] \tag{E.4}$$

$$I_z = \sum_{e=1}^{n} [I_{\varepsilon z,e} + A_e \cdot (y_G - y_{G,e})^2] \tag{E.5}$$

$$\int T \cdot (y - y_G)\, dA = \sum_{e=1}^{n} [T_{m,e} \cdot (y_{G,e} - y_G) \cdot A_e] \tag{E.6}$$

$$\int T \cdot (z - z_G)\, dA = \sum_{e=1}^{n} [T_{m,e} \cdot (z_{G,e} - z_G) \cdot A_e] \tag{E.7}$$

where $\Delta T_{m,e}$ is the average temperature of the finite element e, A_e is the area of the finite element e, $y_{G,e}$ and $z_{G,e}$ are the coordinates of the centre of gravity of the finite element e and $I_{\varepsilon y,e}$ and $I_{\varepsilon z,e}$ are the moments of inertia about the axes εy and εz which are parallel to the principal axes of inertia of the cross-section y and z, respectively.

For triangular finite elements with area A_e and nodes ijk (Figure D.1):

$$T_{m,e} = \frac{1}{3}(T_i + T_j + T_k) \tag{E.8}$$

$$A_e = \frac{1}{2}(c_k b_j - c_j b_k) \tag{E.9}$$

$$y_{G,e} = \frac{1}{3}(y_i + y_j + y_k) \tag{E.10}$$

$$z_{G,e} = \frac{1}{3}(z_i + z_j + z_k) \tag{E.11}$$

where

$$a_i = y_j z_k - y_k z_j \quad b_i = z_j - z_k \quad c_i = y_k - y_j \tag{E.12}$$

$$a_j = y_k z_i - y_i z_k \quad b_j = z_k - z_i \quad c_j = y_i - y_k \tag{E.13}$$

$$a_k = y_i z_j - y_j z_i \quad b_k = z_i - z_k \quad c_k = y_j - y_i \tag{E.14}$$

and y_i, y_j, y_k, z_i, z_j and z_k are the coordinates of the nodes i, j and k. The moment of inertia of a finite element e in relation to a generic axis ζ is:

$$I_{\zeta,e} = \int_{A_e} d^2\, dA \tag{E.15}$$

Where d is the distance to the axis ζ:

$$d = \mathbf{N}^T \mathbf{d}_e \tag{E.16}$$

where $\mathbf{d}_e$ is the vector with the distances between the axis ζ and the nodes i, j and k, and $\mathbf{N}$ are the shape functions:

$$\mathbf{N} = \begin{bmatrix} N_i \\ N_j \\ N_k \end{bmatrix} = \frac{1}{2A_e} \begin{bmatrix} a_i + b_i y + c_i z \\ a_j + b_j y + c_j z \\ a_k + b_k y + c_k z \end{bmatrix} \tag{E.17}$$

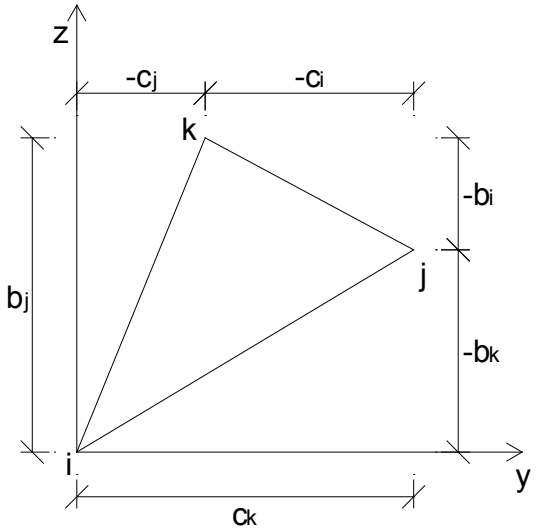

Figure D.1 – Triangular finite element.

In compliance with Eisenberg and Malvern [58] [138]:

$$\int_{A_e} (N_i)^p \left(N_j\right)^q \left(N_k\right)^r dA_e = \frac{p!q!r!}{\left(p+q+r+2\right)!} 2A_e \tag{E.18}$$

Therefore,

$$\begin{aligned} I_{\zeta,e} &= \mathbf{d}_e^T \int_{A_e} \mathbf{N} \cdot \mathbf{N}^T \, dA_e \, \mathbf{d}_e = \\ &= \frac{A_e}{6} (d_i^2 + d_j^2 + d_k^2 + d_i d_j + d_i d_k + d_j d_k) \end{aligned} \tag{E.19}$$

In relation to the principal axis of inertia of the finite element, εy:

$$I_{\varepsilon y,e} = \frac{A_e}{6} (\eta_i^2 + \eta_j^2 + \eta_k^2 + \eta_i \eta_j + \eta_i \eta_k + \eta_j \eta_k) \tag{E.20}$$

where

$$\eta_m = z_m - z_{G,e} \quad \text{for} \quad m = i, j \text{ or } k \tag{E.21}$$

Appendix F

THEORETICAL BACKGROUND OF THE JOHANSEN'S COINTEGRATION PRODECURE

Johansen's procedure applies maximum likelihood to the VAR model, assuming that the errors are Gaussian [131]. Therefore, the probability density function of $\boldsymbol{\varepsilon}_t$ is:

$$p(\boldsymbol{\varepsilon}_t) = \frac{1}{\sqrt{(2\pi)^T \left|\boldsymbol{\Omega}\right|}} \exp\left(-\frac{1}{2} \boldsymbol{\varepsilon}_t{}^{\mathrm{T}} \boldsymbol{\Omega}^{-1} \boldsymbol{\varepsilon}_t \right) \tag{F.1}$$

where $\boldsymbol{\Omega}$ is the covariance of $\boldsymbol{\varepsilon}_t$ and T is the number of observations. The likelihood function L is then given by:

$$L(\boldsymbol{\Psi}, \mathbf{A}, \mathbf{B}, \boldsymbol{\Omega}) = \prod_{t=1}^{T} p(\boldsymbol{\varepsilon}_t) = \frac{1}{\left[(2\pi)^T \left|\boldsymbol{\Omega}\right|\right]^{T/2}} \exp\left(-\frac{1}{2} \sum_{i=1}^{T} \boldsymbol{\varepsilon}_t{}^{\mathrm{T}} \boldsymbol{\Omega}^{-1} \boldsymbol{\varepsilon}_t \right) \tag{F.2}$$

and the log likelihood function $logL$ is given by:

$$logL(\boldsymbol{\Psi}, \mathbf{A}, \mathbf{B}, \boldsymbol{\Omega}) = -\frac{1}{2} T \log\left((2\pi)^T\right) - \frac{1}{2} T \log\left(\left|\boldsymbol{\Omega}\right|\right) - \frac{1}{2} \sum_{i=1}^{T} \boldsymbol{\varepsilon}_t{}^{\mathrm{T}} \boldsymbol{\Omega}^{-1} \boldsymbol{\varepsilon}_t \tag{F.3}$$

Defining $\mathbf{u}_{0,t} = \boldsymbol{\Delta}\mathbf{y}_t$, $\mathbf{u}_{1,t} = \mathbf{y}_{t-1}$, $\mathbf{u}_{2,t} = \left[\boldsymbol{\Delta}\mathbf{y}_{t-1}{}^{\mathrm{T}}, \boldsymbol{\Delta}\mathbf{y}_{t-2}{}^{\mathrm{T}}, ..., \boldsymbol{\Delta}\mathbf{y}_{t-k}{}^{\mathrm{T}}, \mathbf{d}_t{}^{\mathrm{T}} \right]^{\mathrm{T}}$ and

$\boldsymbol{\Psi} = \left[\boldsymbol{\Gamma}_1, \boldsymbol{\Gamma}_2, ..., \boldsymbol{\Gamma}_{k-1}, \boldsymbol{\Phi}\right]$, equation (6.7) can be rewritten as [98]:

$$\mathbf{u}_{0,t} = \mathbf{A}\mathbf{B}^{\mathrm{T}}\mathbf{u}_{1,t} + \boldsymbol{\Psi}\mathbf{u}_{2,t} + \boldsymbol{\varepsilon}_t \tag{F.4}$$

Substituting equation (F.4) into equation (F.3), the log likelihood function $logL$ can be written as:

$$\begin{aligned} logL(\boldsymbol{\Psi}, \mathbf{A}, \mathbf{B}, \boldsymbol{\Omega}) = &-\frac{1}{2}T\log\left((2\pi)^T\right) - \frac{1}{2}T\log\left(\left|\boldsymbol{\Omega}\right|\right) - \\ &-\frac{1}{2}\sum_{i=1}^{T}\left(\mathbf{u}_{0,t} - \mathbf{A}\mathbf{B}^{\mathrm{T}}\mathbf{u}_{1,t} - \boldsymbol{\Psi}\mathbf{u}_{2,t}\right)^{\mathrm{T}}\boldsymbol{\Omega}^{-1}\left(\mathbf{u}_{0,t} - \mathbf{A}\mathbf{B}^{\mathrm{T}}\mathbf{u}_{1,t} - \boldsymbol{\Psi}\mathbf{u}_{2,t}\right) \end{aligned} \tag{F.5}$$

The log likelihood function $logL$ is then used to estimate $\boldsymbol{\Psi}$ by calculating [98]:

$$\frac{\partial logL}{\partial \boldsymbol{\Psi}} = 0 \tag{F.6}$$

which leads to [98]:

$$\sum_{i=1}^{T}\left(\mathbf{u}_{0,t} - \mathbf{A}\mathbf{B}^{\mathrm{T}}\mathbf{u}_{1,t} - \hat{\boldsymbol{\Psi}}\mathbf{u}_{2,t}\right)\mathbf{u}_{2,t}{}^{\mathrm{T}} = 0 \tag{F.7}$$

Introducing the notation for the product-moment matrices [98]:

$$\mathbf{M}_{ij} = \frac{1}{T}\sum_{t=1}^{T}\mathbf{u}_{it}\mathbf{u}_{jt}{}^{\mathrm{T}}, i, j = 0,1,2 \tag{F.8}$$

being

$$\mathbf{M}_{ij} = \mathbf{M}_{ji}{}^{\mathrm{T}}, i, j = 0,1,2 \tag{F.9}$$

The equation (F.7) can then be written as:

$$\mathbf{M}_{02} = \mathbf{A}\mathbf{B}^{\mathrm{T}}\mathbf{M}_{12} + \hat{\boldsymbol{\Psi}}\mathbf{M}_{22} \tag{F.10}$$

such that [98]

$$\hat{\boldsymbol{\Psi}}(\mathbf{A}, \mathbf{B}) = \mathbf{M}_{02}\mathbf{M}_{22}^{-1} - \mathbf{A}\mathbf{B}^{\mathrm{T}}\mathbf{M}_{12}\mathbf{M}_{22}^{-1} \tag{F.11}$$

Substituting equation (F.11) into equation (F.4):

$$\boldsymbol{\varepsilon}_t = \mathbf{u}_{0,t} - \mathbf{A}\mathbf{B}^{\mathrm{T}}\mathbf{u}_{1,t} - \mathbf{M}_{02}\mathbf{M}_{22}^{-1}\mathbf{u}_{2,t} + \mathbf{A}\mathbf{B}^{\mathrm{T}}\mathbf{M}_{12}\mathbf{M}_{22}^{-1}\mathbf{u}_{2,t} \tag{F.12}$$

this leads to the definition of the residuals [98]:

$$\mathbf{r}_{0,t} = \mathbf{u}_{0,t} - \mathbf{C}_1\mathbf{u}_{2,t} \tag{F.13}$$

$$\mathbf{r}_{1,t} = \mathbf{u}_{1,t} - \mathbf{C}_2\mathbf{u}_{2,t} \tag{F.14}$$

being the coefficient matrixes $\mathbf{C}_1 = \mathbf{M}_{02}\mathbf{M}_{22}^{-1}$ and $\mathbf{C}_2 = \mathbf{M}_{12}\mathbf{M}_{22}^{-1}$ obtained by ordinary least squares. These are the residuals obtained by regressing $\mathbf{u}_{0,t}$ and $\mathbf{u}_{1,t}$ on $\mathbf{u}_{2,t}$. Then, equation (F.12) becomes:

$$\boldsymbol{\varepsilon}_t = \mathbf{r}_{0,t} - \mathbf{A}\mathbf{B}^{\mathrm{T}}\mathbf{r}_{1,t} \tag{F.15}$$

and the log likelihood function can then be rewritten as:

$$\begin{aligned} logL(\boldsymbol{\Psi}, \mathbf{A}, \mathbf{B}, \boldsymbol{\Omega}) = &-\frac{1}{2}T\log\left((2\pi)^T\right) - \frac{1}{2}T\log\left(\left|\boldsymbol{\Omega}\right|\right) - \\ &-\frac{1}{2}\sum_{i=1}^{T}\left(\mathbf{r}_{0,t} - \mathbf{A}\mathbf{B}^{\mathrm{T}}\mathbf{r}_{1,t}\right)^{\mathrm{T}}\boldsymbol{\Omega}^{-1}\left(\mathbf{r}_{0,t} - \mathbf{A}\mathbf{B}^{\mathrm{T}}\mathbf{r}_{1,t}\right) \end{aligned} \tag{F.16}$$

and the term $\boldsymbol{\Psi}\mathbf{u}_{2,t}$ has been concentrated out [40].

The residual vectors $\mathbf{r}_{0t}$ and $\mathbf{r}_{1t}$ can be used to form residual product-moment matrixes:

$$\mathbf{S}_{ij} = \frac{1}{T}\sum_{t=1}^{T}\mathbf{r}_{it}\mathbf{r}_{jt}^{\mathrm{T}} \qquad i, j = 0,1 \tag{F.17}$$

For fixed $\mathbf{B}$, the maximum likelihood estimates of $\mathbf{A}$ and $\boldsymbol{\Omega}$ can be found by regressing $\mathbf{r}_{0,t}$ on $\mathbf{B}^{\mathrm{T}}\mathbf{r}_{1,t}$. Therefore, from ordinary least squares:

$$\hat{\mathbf{A}}(\mathbf{B}) = \left(\sum_{t=1}^{T}\mathbf{B}^{\mathrm{T}}\mathbf{r}_{1,t}\mathbf{r}_{1,t}{}^{\mathrm{T}}\mathbf{B}\right)^{-1}\sum_{t=1}^{T}\mathbf{B}^{\mathrm{T}}\mathbf{r}_{1,t}\mathbf{r}_{0,t}{}^{\mathrm{T}} \tag{F.18}$$

substituting equation (F.17) into (F.18) and after the necessary matrix calculus and careful

rearrangement, the estimate of $\mathbf{A}$ can be expressed as:

$$\hat{\mathbf{A}}(\mathbf{B}) = \mathbf{S}_{01}\mathbf{B}(\mathbf{B}^{\mathrm{T}}\mathbf{S}_{11}\mathbf{B})^{-1} \tag{F.19}$$

Since

$$\hat{\boldsymbol{\Omega}}(\mathbf{B}) = \frac{1}{T}\sum_{t=1}^{T}\boldsymbol{\varepsilon}_t\boldsymbol{\varepsilon}_t{}^{\mathrm{T}} \tag{F.20}$$

substituting equation (F.15) into (F.20):

$$\hat{\boldsymbol{\Omega}}(\mathbf{B}) = \frac{1}{T}\sum_{t=1}^{T}\left(\mathbf{r}_{0,t} - \mathbf{A}\mathbf{B}^{\mathrm{T}}\mathbf{r}_{1,t}\right)\left(\mathbf{r}_{0,t} - \mathbf{A}\mathbf{B}^{\mathrm{T}}\mathbf{r}_{1,t}\right)^{\mathrm{T}} \tag{F.21}$$

After the necessary matrix calculus and careful rearrangement, taking in consideration equations (F.17) and (F.19), the estimate of $\boldsymbol{\Omega}$ can be expressed as:

$$\hat{\boldsymbol{\Omega}}(\mathbf{B}) = \mathbf{S}_{00} - \mathbf{S}_{10}\mathbf{B}(\mathbf{B}^{\mathrm{T}}\mathbf{S}_{11}\mathbf{B})^{-1}\mathbf{B}^{\mathrm{T}}\mathbf{S}_{10} \tag{F.22}$$

All the parameters of $\boldsymbol{\varepsilon}_t$ have now been expressed in terms of $\mathbf{B}$, which is still to be estimated [40]. Using the Lemma A.15 from Johansen [98], the maximum likelihood function of independent identically distributed Gaussian variables is given by [131]:

$$\left[L(\mathbf{B})\right]^{-2/T} = |\,\hat{\boldsymbol{\Omega}}\,| = |\,\mathbf{S}_{00} - \mathbf{S}_{01}\mathbf{B}\left(\mathbf{B}^{\mathrm{T}}\mathbf{S}_{11}\mathbf{B}\right)^{-1}\mathbf{B}^{\mathrm{T}}\mathbf{S}_{10}\,| \tag{F.23}$$

Maximization of the likelihood function with respect to $\mathbf{B}$ implies minimization of this determinant with respect to $\mathbf{B}$ [131]. Considering the identity [98, 131]

$$\left|\mathbf{F} - \mathbf{E}^{\mathrm{T}}\mathbf{D}\mathbf{E}\right| = \frac{|\,\mathbf{D} - \mathbf{E}\mathbf{F}^{-1}\mathbf{B}^{\mathrm{T}}\,| \cdot |\,\mathbf{F}\,|}{|\,\mathbf{D}\,|} \tag{F.24}$$

with $\mathbf{F} = \mathbf{S}_{00}$, $\mathbf{D} = \mathbf{B}^{\mathrm{T}}\mathbf{S}_{11}\mathbf{B}$ and $\mathbf{E} = \mathbf{B}^{\mathrm{T}}\mathbf{S}_{10}$, the following expression have to be minimized:

$$\frac{|\,\mathbf{B}^{\mathrm{T}}\mathbf{S}_{11}\mathbf{B} - \mathbf{B}^{\mathrm{T}}\mathbf{S}_{10}\mathbf{S}_{00}^{-1}\mathbf{S}_{01}\mathbf{B}\,| \cdot |\,\mathbf{S}_{00}\,|}{|\,\mathbf{B}^{\mathrm{T}}\mathbf{S}_{11}\mathbf{B}\,|} \tag{F.25}$$

Since $\mathbf{S}_{00}$ is fixed, the minimization of (F.25) is given by the minimization of [131]

$$\frac{|\mathbf{B}^{\mathrm{T}}(\mathbf{S}_{11}-\mathbf{S}_{10}\mathbf{S}_{00}^{-1}\mathbf{S}_{01})\mathbf{B}|}{|\mathbf{B}^{\mathrm{T}}\mathbf{S}_{11}\mathbf{B}|} \tag{F.26}$$

which is given by solving the eigenvalue problem (Lemma A.8 from Johansen [98]):

$$\left|\lambda\mathbf{S}_{11}-\mathbf{S}_{10}\mathbf{S}_{00}^{-1}\mathbf{S}_{01}\right|=0 \tag{F.27}$$

being the eigenvectors the cointegrating vectors $\mathbf{B}$.